Imperial College London
Department of Mechanical Engineering

Optimum Battery Capacity for Electric Vehicles with Particular Focus on Battery Degradation

Clemens Friedrich Lorf

April 10, 2014

Submitted in part fulfilment of the requirements for the degree of
Doctor of Philosophy in Mechanical Engineering of Imperial College London
and the Diploma of Imperial College London

Abstract

Electric vehicles (EVs) are seen as a key future trend in the automotive industry. These vehicles rely on rechargeable batteries to store energy on board. The optimum size of this energy store, often referred to as the battery capacity measured in ampere-hours (Ah) or kilowatt-hours (kWh), depends on the specific application, design limitations, costs and the degradation of the particular battery pack.

Validated by 'real-world' driving data from the Imperial College *Racing Green Endurance (RGE)* flagship electric supercar, the SRZero, a software model following a quasi-steady, backward-forward facing and equivalent circuit approach is introduced. This model is also supported by the results of the 2010, 2011 and 2012 RAC *Future Car Challenges* as well as by battery life testing from a lab environment. Furthermore, travel surveys from the United Kingdom (UK), Germany and the United States (US) have been analysed and then converted into input parameters for this algorithm. The work considers five different electric vehicle classes ranging from mini cars to sport utility vehicles (SUVs).

Results show that varying kerb weights combined with differing levels of driving resistances (aerodynamic drag, rolling resistance, climbing resistance, etc.) lead to reference 'driving forces' of 70-290 Wh/km for the five reference vehicle classes. On average, SUVs consume more than four times as much energy per unit distance as mini cars. Also, driving behaviour has a significant impact on energy consumption and thus on the optimum nominal battery capacity. Empirical data has shown that the mean driving force can vary up to 23% between drivers who follow exactly the same route at comparable traffic conditions and driving another vehicle of exactly the same make and model. Daily range requirements of EVs vary between 150-700 km based on the 95$^{\text{th}}$ percentile of the number of all daily trips or the cumulative distance of all trips combined for the UK, Germany and the US. Thus, optimum nominal battery capacities range between 11-203 kWh.

In addition, it is shown that the optimum actual size of a battery pack for an electric vehicle depends on the battery's degradation as well. Over time and number of cycles the available capacity as well as the available power fades. This is mainly due to the effects of increased internal resistance, polarisation, corrosion and passivation. Therefore, first it is recommended to reduce the depth of discharge (DOD) to 80% when the battery is in use. Second, a spare capacity at the beginning of life of around 20-40% is recommended in order to satisfy range and power requirements also towards the end of the EVs lifetime. It follows that the optimum actual battery capacity is around 1.25-1.75 times the optimum nominal battery capacity for an EV.

Declaration

I herewith certify that all material in this dissertation, which is not my own work, has been properly acknowledged.

Clemens Friedrich Lorf

The copyright of this thesis rests with the author and is made available under a Creative Commons Attribution Non-Commercial No Derivatives licence. Researchers are free to copy, distribute or transmit the thesis on the condition that they attribute it, that they do not use it for commercial purposes and that they do not alter, transform or build upon it. For any reuse or redistribution, researchers must make clear to others the licence terms of this work.

Acknowledgement

First and foremost I would like thank my main supervisor Prof. Ricardo Martínez-Botas for his continuous support, his critical challenges and his strong commitment to perfection. His trust in my work combined with permanent questioning as well as his patience cannot be praised highly enough. I would also like to thank my second supervisor Prof. Nigel Brandon for his strong belief in and his backing of the *Racing Green Endurance (RGE)* project, without which my dissertation would have been impossible.

My gratitude also goes to the *Grantham Institute of Climate Climate Change*, which generously sponsored me for the duration of 39 months. My office companions including Peter, Nicola, Adam, Colin, Pablo, Haz, Owen, Jonathan, Minyang, Masa and Lawrence were always there for insightful discussions and new directions of thought. Dr. Mardit Matian, Dr. Vladimir Yufit, Dr. David Howey, Dr. Alessandro Romagnoli, Dr. Apostolos Pesiridis, Dr. Robin North and Dr. Srithar Rajoo have passed on valuable senior experience and knowledge to me, for which I am very thankful. Dr. Scott Le Vine introduced me to the world of travel surveys. Many thanks also to Toby Schulz, Luca Lytton, Peter Newton and Adam Malloy for proofreading as well as correcting parts or all of my thesis.

The RGE team members including Alex, Toby, Nik, Andy, Pambo, Aran, Alec and Celine helped to make my PhD experience one like no other PhD experience. Harriet von Zitzewitz made sure that I would not lose track of the industrial angle of my dissertation. My flatmate and close friend Maya Marescotti as well as Katerina Giannini and Adriano Menicanti on the other hand looked after my social balance and that I would not be writing up forever, all for which I am enormously grateful.

The basic layout and the formatting of this dissertation is based on the work of Daniel Wagner © 2008 (available from: *www.PrettyPrinting.net/Imperial*).

Finally, I would like to thank my family for their unconditional love and support. This work is dedicated to Thomas, Kerstin, Caroline-Christiane and Alexander Lorf.

Unser Leben führt uns mit raschen Schritten von der Geburt bis zum Tode. In dieser kurzen Zeitspanne ist es die Bestimmung des Menschen, für das Wohl der Gemeinschaft, deren Mitglied er ist, zu arbeiten.

Friedrich der Große (1711-1786)

Contents

Abstract 2

Declaration 3

Acknowledgement 4

Dedication 5

Table of Contents 6

List of Figures 9

List of Tables 13

Glossary 15

Nomenclature 17

1. Introduction 19
- 1.1. Background 19
- 1.2. Rationale 22
- 1.3. Problem Statement 23
- 1.4. Outline 24

2. Fundamentals & Literature Review 25
- 2.1. Terminology 25
- 2.2. Electric Vehicles 26
  - 2.2.1. History of Electric Vehicles 26
  - 2.2.2. Fundamentals of Electric Vehicles 31
  - 2.2.3. Modelling of Electric Vehicles 34
  - 2.2.4. Interim Summary 41
- 2.3. Batteries for Electric Vehicles 42
  - 2.3.1. History of Batteries 42
  - 2.3.2. Fundamentals of Batteries 45
  - 2.3.3. Battery Degradation 54

    - 2.3.4. Modelling of Batteries 58
    - 2.3.5. Interim Summary 66
  - 2.4. Summary & Conclusions from Literature Review 66

3. Methodology **68**
  - 3.1. Assumptions 69
  - 3.2. Modelling & Simulation 70
  - 3.3. Experimental Methods 70
    - 3.3.1. Racing Green Endurance (RGE) 70
    - 3.3.2. Future Car Challenge (FCC) 76
    - 3.3.3. Travel Survey Analysis 79
    - 3.3.4. Battery Testing 81
  - 3.4. Conclusions 85

4. Nominal Energy Requirements of Electric Vehicles **86**
  - 4.1. Electric Vehicle Driving Forces 86
    - 4.1.1. Theoretical Driving Force 86
    - 4.1.2. 'Real' Driving Force 102
    - 4.1.3. Interim Conclusion 114
  - 4.2. Range Requirements for Electric Vehicles 117
    - 4.2.1. General Travel Trends 117
    - 4.2.2. United Kingdom 118
    - 4.2.3. Germany 123
    - 4.2.4. United States 126
    - 4.2.5. Interim Conclusion 129
  - 4.3. Discussion & Summary 130

5. Performance & Degradation Characteristics of EV Traction Batteries **133**
  - 5.1. Performance Characteristics of EV Traction Batteries 134
    - 5.1.1. Steady Battery Behaviour 134
    - 5.1.2. Dynamic Battery Behaviour 139
    - 5.1.3. Interim Conclusion 152
  - 5.2. Battery Degradation 154
    - 5.2.1. Empirical Evidence of Battery Degradation 154
    - 5.2.2. Empirical Modelling of Battery Degradation 162
    - 5.2.3. Interim Conclusion 169
  - 5.3. Discussion & Summary 172

6. Discussion **175**

6.1. Optimum Nominal Battery Capacity 175
  6.1.1. Mean Driving Force 175
  6.1.2. Range 177
  6.1.3. Conclusion 178
6.2. Battery Performance & Degradation 179
  6.2.1. Battery Performance 179
  6.2.2. Battery Degradation 179
6.3. Limitations 181
  6.3.1. Assumptions 181
  6.3.2. Validation Methods 182
  6.3.3. Physical Limitations 182
  6.3.4. Financial Limitations 184

7. Conclusions & Further Work **185**

7.1. Conclusions 185
7.2. Further Work 186

Bibliography **187**

Appendices **202**

A. Publications **203**

B. SRZero Battery Specifications **204**

C. Racing Green Endurance Itinerary **206**

D. International Driving Cycles **208**

E. 2011 FCC - EV Specifications **209**

F. Battery Statistics from the RGE Trip **210**

List of Figures

1.1. Yearly Averaged Crude Oil Prices per Barrel in 2011 USD [2] 19
1.2. Global Energy-Related CO_2 Emissions in 2008 [7] 20
1.3. Fleet Average CO_2 Emissions for Medium-Sized Passenger Vehicles [8] 21
1.4. World Population Trends [10] 21
1.5. Factors Influencing Optimum Battery Capacity for EVs 23

2.1. Electric Vehicle Hype Cycle (adapted from [15]) 26
2.2. Jedlik's Electric Vehicle Model from 1828 [16] 27
2.3. Jenatzy's Record Breaking '*Jamais Contente*' from 1899 [20] 28
2.4. Power Train Types in the US in 1900 [21] 28
2.5. Typical Milk Float [24] 29
2.6. Basic Vehicle Power Train Configurations [32] 32
2.7. Representative Energy Flow of an ICEV During an Urban Drive Cycle [33] . . . 32
2.8. Basic EV Configuration [34] 33
2.9. Representative Energy Flow of an EV During an Urban Drive Cycle [37]-[39] . . 34
2.10. Forward-Facing EV Software Schematic 35
2.11. Backward-Facing EV Software Schematic 37
2.12. Top Level Block Diagram for a HEV in QSS [58] 38
2.13. ADVISOR 2.1 Vehicle Input Screen [60] 39
2.14. ADVISOR's Top Level Block Diagram for an EV [60] 40
2.15. V-Elph's Top Level Block Diagram [63] 41
2.16. Baghdad Battery with Copper Cylinder and Iron Rod [68] 42
2.17. Voltaic Pile [69] 43
2.18. Global Battery Market Share by Chemistry in 2009 [73] 45
2.19. Lithium-Ion Cell Schematic [12] 46
2.20. Series Cell Arrangement for a Battery 47
2.21. Parallel Cell Arrangement for a Battery 47
2.22. Electric-Hydraulic Analogy [82] 47
2.23. Capacity Rate Effect 49
2.24. Voltage Relaxation Effect 50
2.25. Peridodic Table of Elements (adapted from [84]) 51
2.26. Ragone Plot (adapted from [89]) 53

2.27. Lithium-Ion Battery Chemistry Roadmap [90] (** in development) 54
2.28. Nissan Leaf Battery Capacity Fade (adapted from [95]) 55
2.29. Battery Modelling Logic 58
2.30. Internal Resistance Model 61
2.31. Thévenin Model 62
2.32. Battery Electrochemical Impedance Spectroscopy (EIS) Schematic 62
2.33. PNGV Model 63
2.34. Resistor Capacitor (RC) Model 63
2.35. MATLAB/Simulink Battery Model [117] 64
2.36. Matlab/Simulink Model Parameters [117] 65

3.1. Research Process & Expected Outcomes 68
3.2. Analytical Structure 69
3.3. Major Cities Along the Pan-American Highway 71
3.4. SRZero Schematic View 71
3.5. SRZero Motor Efficiency Map 73
3.6. Field Weakening Schematic 73
3.7. SRZero Power Train Layout 74
3.8. SRZero in Patagonia, Argentina 76
3.9. SRZero at the 2011 Future Car Challenge 79
3.10. Exemplary Daily Trip Distribution 80
3.11. Battery Cycling Schematic 81
3.12. SRZero Battery Pack with BMS and Heat Sink in early 2010 82

4.1. Measured Drag Coefficients for Various Shapes [140] 87
4.2. Road Grade Schematic 88
4.3. Traction Ratio Applied to NEDC for a Medium Sized Car 91
4.4. Theoretical Vehicle Driving Force at Steady Speed and Zero Incline 92
4.5. Total and Constituent Theoretical Vehicle Driving Powers at Steady Speed for a Medium-Sized Car 94
4.6. Theoretical Energy Consumption for Driving 1 km at Steady Speed 95
4.7. Theoretical Driving Powers at Varying Speeds and Accelerations 96
4.8. Theoretical Driving Powers at Varying Speeds and Road Grades 96
4.9. Theoretical NEDC Driving Powers with Full Recuperation 98
4.10. Sensitivities of the Mean Driving Force with Respect to Vehicle Parameters . . . 101
4.11. Speed Distribution for SRZero 102
4.12. Acceleration Distribution for SRZero 103
4.13. MC Output Currents vs. Output Torque Values 104
4.14. Torque Distribution for SRZero 105
4.15. Driving Force Requirements vs. Distance for SRZero 106

4.16. 2010-2011 FCC Route [144] 107
4.17. 2010-2011 FCC Altitude Profile [144]-[145] 107
4.18. 2010 FCC EV Driving Forces 108
4.19. 2011 FCC Individual and Mean Power Consumption 109
4.20. 2011 FCC EV Absolute Regenerative Braking Benefits 110
4.21. 2011 FCC EV Driving Forces 110
4.22. 2012 FCC Route [144] 112
4.23. 2012 FCC Altitude Profile [144]-[145] 113
4.24. 2012 FCC EV Driving Forces 113
4.25. Modal Share in the UK, Germany and the US [137]-[139] 117
4.26. Individual Trip Distances in the UK 118
4.27. Car Activity According to the Day of Week in the UK 119
4.28. Car Activity According to Vehicle Category in the UK 120
4.29. UK Vehicle Registrations According to Vehicle Category [153] 120
4.30. Daily Driving Distances in the UK 121
4.31. Car Activity According to the Day of Week in Germany 123
4.32. Car Activity According to Vehicle Category in Germany 124
4.33. Daily Driving Distances in Germany 124
4.34. Car Activity According to the Day of Week in the US 126
4.35. Car Activity According to Vehicle Category in the US 127
4.36. Daily Driving Distances in the US 127
4.37. Battery Capacity for Range Requirements in the UK 131
4.38. Battery Capacity for Range Requirements in Germany 131
4.39. Battery Capacity for Range Requirements in the US 131

5.1. Capacity Fade Schematic 133
5.2. Published Discharge Curves of SRZero Battery Cells (see appendix B) 134
5.3. Initial Charge and Discharge Curves of a Single SRZero Battery Cell 135
5.4. GEIS Voltage and Current History 136
5.5. Measured and Modelled Values for the OCV vs. SOC Relationship 138
5.6. Simplified Power Flow for EV Power Train 139
5.7. Sample SRZero Drive Cycle 140
5.8. Sample SRZero Acceleration Profile 140
5.9. Theoretical and Measured Torque Values 141
5.10. Total Requested Torque Values of SRZero During Test Drive 142
5.11. Theoretical and Measured AC Motor Controller Current Values 142
5.12. SRZero Inverter AC Output Currents vs. DC Inverter Input Currents 143
5.13. Theoretical and Measured Requested MC DC Currents 144
5.14. Combined SRZero DC Motor Controller Current Values 144

5.15. SRZero Traction Battery Current 145
5.16. OCV & SOC vs. Time for Sample Drive Cycle 147
5.17. Comparison of Various Battery Models Applied to SRZero Drive Cycle 150
5.18. SRZero Traction Voltage 151
5.19. SRZero Traction Voltage vs. Current 151
5.20. SRZero Battery Power Output 152
5.21. Discharge Capacity as a Function of Battery Cycles for Sample SRZero Cell . . . 154
5.22. Cell Voltage as a Function of Capacity During Long-Term Cycling 155
5.23. Coefficients for Custom Model of OCV vs. SOC Relationship 156
5.24. Cell Voltage as a Function of Capacity During Short-Term Cycling 157
5.25. Galvanostatic Electrochemical Impedance Spectroscopy Test Results 158
5.26. Resistance Values as a Function of Battery Cycles for Sample SRZero Cell 159
5.27. Discharge Capacity as a Function of Battery Cycles for Low-Capacity Cell 160
5.28. Initial and Final SOC Values Individual Cycles along SRZero Trip 161
5.29. Traction Voltage as a Function of Capacity for SRZero Battery Pack 161
5.30. Annual Mileages in Germany and the UK 162
5.31. Random Stress Fluctuation with Time 164
5.32. Rainflow Pagoda Roof 165
5.33. Sample Rainflow-Counting Cycles 165
5.34. SRZero Energy and Capacity Extreme Values 166
5.35. Rainflow-Counting Histogram of SRZero Charge/Discharge History 169

6.1. Battery Capacity Ratio for Various EVs 184

D.1. New European Driving Cycle (NEDC) [143] 208
D.2. US Federal Testing Procedure (FTP-75) [143] 208
D.3. Japanese 10-15 Mode [143] 208

List of Tables

2.1. Selection of Commercially Available EVs as of December 2012 [30] 31
2.2. Electric and Hydraulic Circuit Equivalents 48
2.3. Rechargeable Battery Chemistries and Practical Properties ([74, 76, 77, 85]) . . . 52
2.4. Equivalent Circuit Elements and Their Physical Meaning 61

3.1. Technical Specifications of SRZero 74
3.2. Racing Green Endurance Log File Information 75
3.3. Future Car Challenge Entry Classes [132] 77
3.4. Future Car Challenge Data Log Information 77
3.5. Battery Cycling Procedure 83
3.6. Electrochemical Impedance Spectroscopy Procedure 84

4.1. Traction Force Parameters and Typical Values [57, 141] 89
4.2. Vehicle Classes and Representative Parameter Values [57],[141] 89
4.3. Power Train Operating Modes 90
4.4. Theoretical Driving Forces at Different Steady Speeds 93
4.5. Assumed Mean Auxiliary Powers 93
4.6. Theoretical Driving Powers at Different Steady Speeds 94
4.7. Theoretical Power Requirements for Gradeability Test 97
4.8. International Drive Cycle Parameters [143] 97
4.9. Theoretical Driving Forces (NEDC) 98
4.10. Relative Recuperation Benefits for Different Drive Cycles 99
4.11. Partial Derivatives for the Mean Driving Force Applied to the NEDC 101
4.12. Relative Recuperation Benefits for Different Vehicle Classes at the 2011 FCC . . 110
4.13. Driving Behaviour Comparison for 2011 FCC 111
4.14. Mean Driving Forces for Different Vehicle Categories 116
4.15. Transportation Comparison for the UK, Germany and the US [9],[150] 118
4.16. Daily Distance Statistics for the UK 122
4.17. Daily Distance Statistics for Germany 125
4.18. Daily Distance Statistics for the US 128
4.19. Summary of EV Driving Forces 130
4.20. EV Battery Capacity Requirements According to Driving Force and Range . . . 132

5.1. Goodness of Fit for Various Models to Represent OCV vs. SOC Relationship . . 137
5.2. Coefficients for Custom Model of OCV vs. SOC Relationship 138
5.3. Comparison of Various Battery Models Applied to SRZero Drive Cycle 150
5.4. Battery Cycle Requirements 163
5.5. Rainflow-Counting Equivalent Cycles of SRZero Charge/Discharge History . . . 167

6.1. Vehicle Classes and Representative Parameter Values 175
6.2. Mean Driving Forces for Different Vehicle Categories 177
6.3. EV Battery Capacity Requirements According to Driving Force and Range . . . 178
6.4. Battery Pack Mass According to Specific Energy and Capacity 183
6.5. Upper Battery Capacity Limits According to Weight 183

Glossary

A/C	Air Conditioning
AC	Alternating Current
ADC	Analog-to-Digital Converter
ADVISOR	Advanced Vehicle Simulator
AER	All Electric Range
AFM	Axial Flux Motor
APU	Auxiliary Power Unit
ARC	Accelerated Rate Calorimetry
BBC	British Broadcasting Corporation
bbl	Oil Barrel (≈159 litres)
BEV	Battery Electric Vehicle
bhp	Brake Horsepower
BMS	Battery Management System
CAD	Computer Aided Design
CAN	Controller Area Network
CARB	California Air Resources Board
CCC	Committee on Climate Change
CTS	Centre for Transport Studies
CVT	Continuously Variable Transmission
DC	Direct Current
DECC	Department of Energy and Climate Change (UK)
DEFRA	Department for Environment, Food and Rural Affairs (UK)
DfT	Department for Transport
DOD	Depth of Discharge
DOE	Department of Energy (US)
DOS	Disk Operating System
DST	Dynamic Stress Test
DUKES	Digest of UK Energy Statistics
ECU	Engine Control Unit
EES	Electrochemical Energy Storage
EFL	Energy Futures Lab
e.g.	exempli gratia ('for example')
EIS	Electrochemical Impedance Spectroscopy
EKF	Extended Kalman Filter
EM	Electric Motor
EMF	Electromotive Force
EPA	Environmental Protection Agency (US)
ESDS	Economic and Social Data Service
ESE	Department of Earth Science & Engineering
ESO	European Southern Observatory
ESS	Energy Storage System
etc.	Et Cetera ('and so forth')
EU	European Union
EV	Electric Vehicle
FCC	Future Car Challenge
FCEV	Fuel Cell Electric Vehicle
FORTRAN	Formula Translating System
FPGA	Field-Programmable Gate Array
FTP-75	Federal Testing Procedure 75
GCPL	Galvanostatic Cycling with Potential Limitation
GEIS	Galvano-Electrochemical Impedance Spectroscopy
GHG	Greenhouse Gas
GM	General Motors
GPS	Global Positioning System
GUI	Graphical User Interface
HDV	Heavy-Duty Vehicle
HEV	Hybrid Electric Vehicle
HHV	Higher Heating Value
HiL	Hardware-in-the-loop
HMI	Human Machine Interface
HPC	High-Performance Computing
HPPC	Hybrid Pulse Power Characterisation

HV	High Voltage
IC	Integrated Circuit
ICCT	International Council on Clean Transportation
ICE	Internal Combustion Engine
ICEV	Internal Combustion Engine Vehicle
ICL	Imperial College London
i.e.	id est ('that is')
iea	International Energy Agency
Inc.	Incorporation
IP	Intellectual Property
ISA	International Standard Atmosphere
IVA	Individual Vehicle Approval
JAMA	Japan Automobile Manufacturers Association
KERS	Kinetic Energy Recovery System
KF	Kalman Filter
LCD	Liquid Crystal Display
LCV	Light Commercial Vehicle
LDV	Light Duty Vehicle
LHV	Lower Heating Value
LPF	Low-Pass Filter
MC	Motor Controller
MH	Metal Hydride
MOP	Mobility Panel (Germany)
MPG	Miles per Gallon
n/a	Not Available
NDA	Non-Disclosure Agreement
NEDC	New European Driving Cycle
NEV	Neighbourhood Electric Vehicle
NHTS	National Household Travel Survey (US)
NI	National Instruments
NREL	National Renewable Energy Laboratory
NTS	National Travel Survey (UK)
OBD	On-Board Diagnostics
OCV	Open Circuit Voltage
ODE	Ordinary Differential Equation
OEM	Original Equipment Manufacturer
PC	Personal Computer
PHEV	Plug-In Hybrid Electric Vehicle
PID	Proportional Integral Derivative
PM	Permanent Magnet (Motor)
PNGV	Partnership for a New Generation of Vehicles
RAC	Royal Automobile Club
REEV	Range Extended Electric Vehicle
RGE	Racing Green Endurance
RMS	Root Mean Square (Value)
RPM	Revolutions per Minute
SAE	Society of Automotive Engineers (US)
SD	Standard Deviation
SEI	Solid Electrolyte Interphase
SI	Système International d'Unités
SLI	Start, Light & Ignition
SOC	State of Charge
SOH	State of Health
SOL	State of Life
SOP	State of Power
STW	Source-to-Wheel
SUV	Sport Utility Vehicle
TCO	Total Cost of Ownership
UCSD	University of California, San Diego
UDDS	Urban Dynamometer Driving Schedule
UK	United Kingdom
UNFCCC	United Nations Framework Convention on Climate Change
US	United States of America
USD	US Dollar
V2G	Vehicle to Grid
VMT	Vehicle Miles Travelled
VTB	Virtual Test Bed
w/o	without
WIPO	World Intellectual Property Organization
WTW	Well-to-Wheel
yrs	Years
ZEV	Zero Emissions Vehicle

Nomenclature

Symbol	**Description**	**Unit**
$\oslash$	Average	[-]
α	Angle of Inclination	[°]
η	Activation Overpotential	[V]
η	Efficiency	[%]
ρ	Density	[kg/m^3]
ρ_{air}	Density of Ambient Air	[kg/m^3]
σ	Standard Deviation	[-]
τ	Torque	[Nm]
ω	Rotational Speed	[rad/s]
a	Acceleration	[m/s^2]
A	Area	[m^2]
A_a	Pre-Exponential Arrhenius Factor	[-]
A_f	Frontal Vehicle Area	[m^2]
C	Capacitance	[F]
C_d	Aerodynamic Drag Coefficient	[-]
C_r	Rolling Resistance Coefficient	[-]
C_B	Bulk Capacitance	[F]
C_S	Surface Capacitance	[F]
C_{Th}	Thévenin Capacitance	[F]
$\mathrm{CH_4}$	Methane	[-]
$\mathrm{CO_2}$	Carbon Dioxide	[-]
d	Diameter	[m]
E	Energy	[J] or [kWh]
E^0	Standard Electrode Potential	[V]
E_a	Activation Energy	[kJ/mol]
f	Frequency	[Hz]
F	Force	[N]
F_a	Aerodynamic Drag Force	[N]
F_c	Climbing Force	[N]
F_d	Driving Force	[N]
F_i	Inertial Force	[N]
F_r	Rolling Resistance Force	[N]
F_t	Traction Force	[N]
g	Gravitational Constant (≈ 9.81)	[m/s^2]
I	Current	[A]
k	Peukert Constant	[-]

Symbol	**Description**	**Unit**
K_E	Voltage Constant	[Vs/rad]
K_T	Torque Constant	[Nm/A]
L	Length	[m]
Li	Lithium	[-]
Li^+	Lithium-Ion	[-]
$\mathrm{LiCoO_2}$	Lithium Cobalt Oxide	[-]
$\mathrm{LiFePO_4}$	Lithium Iron Phosphate	[-]
$\mathrm{LiMn_2O_4}$	Lithium-Manganese Oxide	[-]
m	Mass	[kg]
n	Number of Cycles	[-]
n_{eol}	End of Life Number of Cycles	[-]
$\mathrm{N_2O}$	Nitrous Oxide	[-]
$\mathrm{O_2}$	Oxygen	[-]
P	Power	[W]
P_{aux}	Auxiliary Power	[W]
P_{loss}	Power Loss	[W]
Q	Electric Charge	[C]
Q_{fuel}	Volumetric Fuel Flow Rate	[$\mathrm{m^3/s}$]
Q_{bat}	Battery Capacity	[Ah]
$Q_{bat,0}$	Initial Battery Capacity	[Ah]
Q_{loss}	Capacity Loss	[Ah]
r_r	Reaction Rate Constant	[-]
r_w	Wheel Radius	[m]
R	Electrical Resistance	[Ω]
$\bar{R}$	Universal Gas Constant (≈8.31)	[J/(mol K)]
R_{ct}	Charge Transfer Resistance	[Ω]
R_{diff}	Diffusion Resistance	[Ω]
R_{int}	Internal Resistance	[Ω]
R_{pol}	Polarisation Resistance	[Ω]
s	Range	[km]
$\mathrm{SF_6}$	Sulphur Hexafluoride	[-]
t	Time	[s]
T	Temperature	[°C] or [K]
TR	Traction Ratio	[-]
v	Velocity	[m/s]
v_c	Coasting Velocity	[m/s]
V	Electric Potential = Voltage	[V]
V	Volume	[$\mathrm{m^3}$]
V_{nom}	Nominal Voltage	[V]
V_{OC}	Open Circuit Voltage	[V]
V_T	Terminal Voltage	[V]
Z	Electrical Impedance	[Ω]

1. Introduction

Road transport describes the movement of people and goods from one location to another by the means of automobiles, buses, trucks, motorcycles and other road-worthy vehicles. It is important for economic growth as well as for quality of life, enabling international trade and worldwide travel. In 2011 the global vehicle fleet for the first time surpassed one billion units [1]. The following sections highlight the present challenges facing the road transport sector (1.1), make the case for electric vehicles, justify the need for an in-depth analysis of the sizing and the degradation of batteries for electric vehicles (1.2) and finally define the research problem (1.3).

1.1. Background

Currently, the traditional road transport sector is being challenged in multiple ways:

- Fuel prices are expected to keep rising
- Governments around the world are increasingly tightening emission and safety standards
- Continuing urbanisation is leading to new road transport requirements

Oil prices, which alongside taxation dominate global petrol and diesel prices, have seen a rising trend for the past 14 years. This is illustrated in figure 1.1, which shows the inflation-adjusted crude oil price over time. Three remarkable peaks stand out. First, in 1864 a combination of

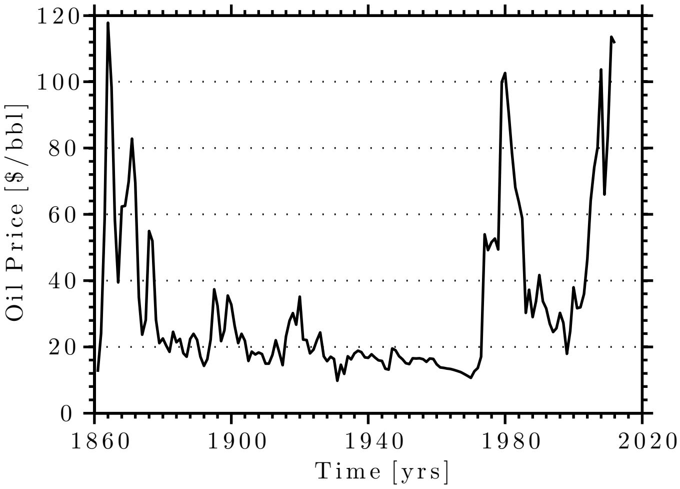

Figure 1.1.: Yearly Averaged Crude Oil Prices per Barrel in 2011 USD [2]

short-time short supply and great demand led to the oil price's all-time high of \$115.45 per barrel. In 1980 the second oil crisis caused the oil price to peak at \$100.54. Since then prices were falling until 1998. The average oil price from 2011 presents the third oil price peak. At \$111.26 the 2011 price is just below the all-time high of 1864. Economists argue that oil prices are very likely to continue rising as the oil supply will decline in the foreseeable future while, due to a growing world population (see figure 1.4) and booming emerging markets, the demand for fuel is expected to increase.

Rising fuel prices lead to growing economic concerns about the impacts of road transport [3]. In addition, road transport is considered to cause environmental damage [4] and bring about harmful health-related side-effects for society [5]. Internal combustion engines (ICE), which in 2011 powered 97% of the global vehicle fleet [6], convert chemical into kinetic energy by means of combustion. In the ideal case of complete combustion of gasoline and oxygen (O_2) a hydrocarbon (C_nH_{2n+2}) is converted into water (H_2O) and carbon dioxide (CO_2) (equation 1.1). In reality, carbon monoxide (CO) and pure carbon (C) in the form of soot are also emitted.

$$2C_8H_{18} + 25O_2 \rightarrow 16CO_2 + 18H_2O \tag{1.1}$$

It follows from equation 1.1 that fuel consumption and CO_2 emission levels of an ICE are proportional. Consequently, fuel efficiency and CO_2 emissions are inversely proportional. CO_2 emissions lead to localised pollution of the air and on a bigger scale are believed to cause global warming. Figures from the International Energy Agency (iea) show that the transport sector accounts for almost ¼ (23%) of global energy-related CO_2 emissions [7]. Road transport in particular is responsible for more than ⅙ (17%) of global energy-related CO_2 emissions as can be seen from figure 1.2. Consequently, governments around the world put **regulatory pressure** on the vehicle manufacturing industry to develop more fuel efficient vehicles. Strict emission standards are in line with energy policies of most governments, who seek to provide secure, clean and affordable energy. Since 2000 CO_2 emission levels for passenger vehicles in the major

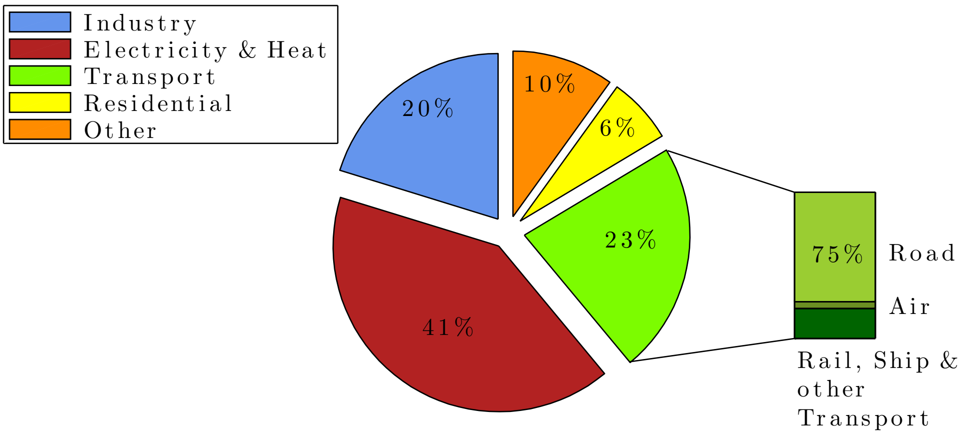

Figure 1.2.: Global Energy-Related CO_2 Emissions in 2008 [7]

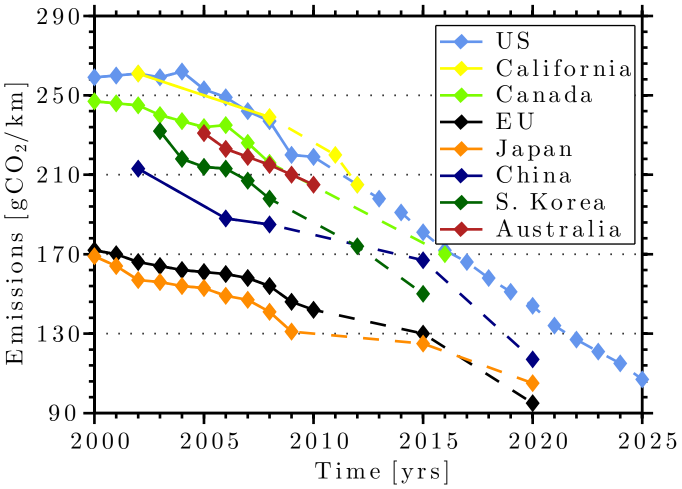

Figure 1.3.: Fleet Average CO_2 Emissions for Medium-Sized Passenger Vehicles [8]

vehicle markets have been decreasing continuously. This is illustrated by the solid lines in figure 1.3, which represent historical performance. The figure shows past, present and expected future fleet average CO_2 tailpipe emission levels for medium-sized passenger vehicles based on the New European Driving Cycle (NEDC) [8]. In the European Union (EU) for instance average CO_2 emission levels have been reduced by almost 18% from 2000 to 2010. Any emission level data points after 2011, shown with dashed lines, represent either enacted or proposed future targets. Ambitious reduction targets can be observed in China, Europe, Japan and the United States (US). From 2015 until 2020 these countries on average aim to lower their fleet average by 7 gCO_2/km per year.

While CO_2 emissions for individual passenger vehicles have been brought down over the last decade, the total amount of CO_2 emissions stemming from road transport has been rising [7]. This is owed to an increasing global vehicle fleet, which in turn is caused by two major trends.

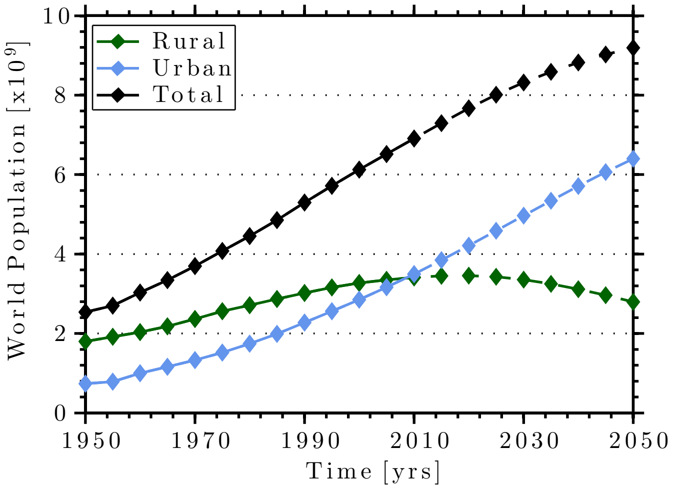

Figure 1.4.: World Population Trends [10]

First, thanks to growing prosperity in developing countries, vehicle ownership per capita has been rising in these countries [9]. Secondly, the world population has been growing too (see figure 1.4). Thus, improving individual vehicles' fuel efficiency alone will not reduce emissions from road transport. Figure 1.4 also shows that since 2007 more people have been living in cities than in rural areas. According to the United Nations (UN) **urbanisation** is likely to progress for the next couple of decades [10]. Urbanisation has profound implications on road transport as well. In order to cope with an increasing vehicle fleet and rising emissions, many major city councils have introduced low-emission zones, congestion charge zones, and/or designated parking areas for low/zero-emission and/or car sharing vehicles only.

To conclude, the road transport sector is currently facing rising fossil fuel prices, increasing emission standards and urban driving as well as parking restrictions. Electric vehicles (EVs) charged from renewable energy sources (e.g. hydro, solar, wind and/or geothermal) do not rely on fossil fuels while driving. They offer zero tailpipe emissions at all times and, if charged from non-fossil fuel based energy sources, even zero well-to-wheel emissions. Consequently, EVs present one possible solution to overcoming the aforementioned challenges.

However EVs themselves pose new challenges for both battery and vehicle manufacturers. Each of the vehicle parameters must be selected for an exceptional dynamic performance, outstanding drivability, improved safety, and better fuel economy, all at a competitive price for the consumer [11]. In particular energy density, power density, durability and costs of traction batteries are presently seen as major bottlenecks for the mass-commercialisation of electric vehicles.

1.2. Rationale

Electric vehicles rely on rechargeable batteries to store energy on board. Lithium-ion (Li-ion) type batteries are the preferred choice of energy storage for EVs at the moment because of their relatively high specific energy, no memory effect and a slow self-discharge rate. Research into Li-ion batteries for electric vehicles so far has concentrated on improving safety and durability, on widening the operational temperature range and on increasing both the volumetric and the gravimetric energy density while at the same time reducing costs [12]. Thus, the focus has for long been on the microscopic level looking at electrochemical processes and structures. This has led to major breakthroughs since 1976 when the Li-ion battery was first discovered. However, there remains a vacuum with regards to the macroscopic inspection of batteries for electric vehicles. The question is: What is the optimum battery capacity for electric vehicles with particular focus on battery degradation?

Automotive manufacturers intending to introduce a new electric vehicle model first work out the total energy requirement in order to size the battery pack. But, as most automotive manufacturers are planning for a ten-year vehicle life span covering around 100,000-250,000 km ($\approx 10^6$ km for lorries) [13], they need to take account for expected battery degradation as well. For example, an original equipment manufacturer (OEM), whose electric city car nominally requires a 15 kWh battery, is likely to specify a 25 kWh battery instead, so that after ten years and 40% performance degradation, the battery will still have sufficient energy capacity for unrestricted operation. This may be too much, exactly right or just not enough. At the moment there is still relatively big uncertainty as to how much exactly the capacity and power fades under differing conditions. Consequently, there is a need for the detailed analysis of the optimum battery size for electric vehicles, which draws particular attention to battery degradation.

1.3. Problem Statement

Sizing traction battery packs for electric vehicles is a complex and multi-disciplinary task. Figure 1.5 shows a selection of factors that affect the optimum battery capacity. The main factors include the individual vehicle's energy consumption, the battery's intrinsic properties, the battery's reliability, design constraints within the vehicle, safety considerations, environmental aspects, costs and the available infrastructure. Several more lead to these main factors. Many considerations also correlate with each other. A bigger battery pack due to the effects of battery degradation for instance will have an impact on the battery pack's weight and volume

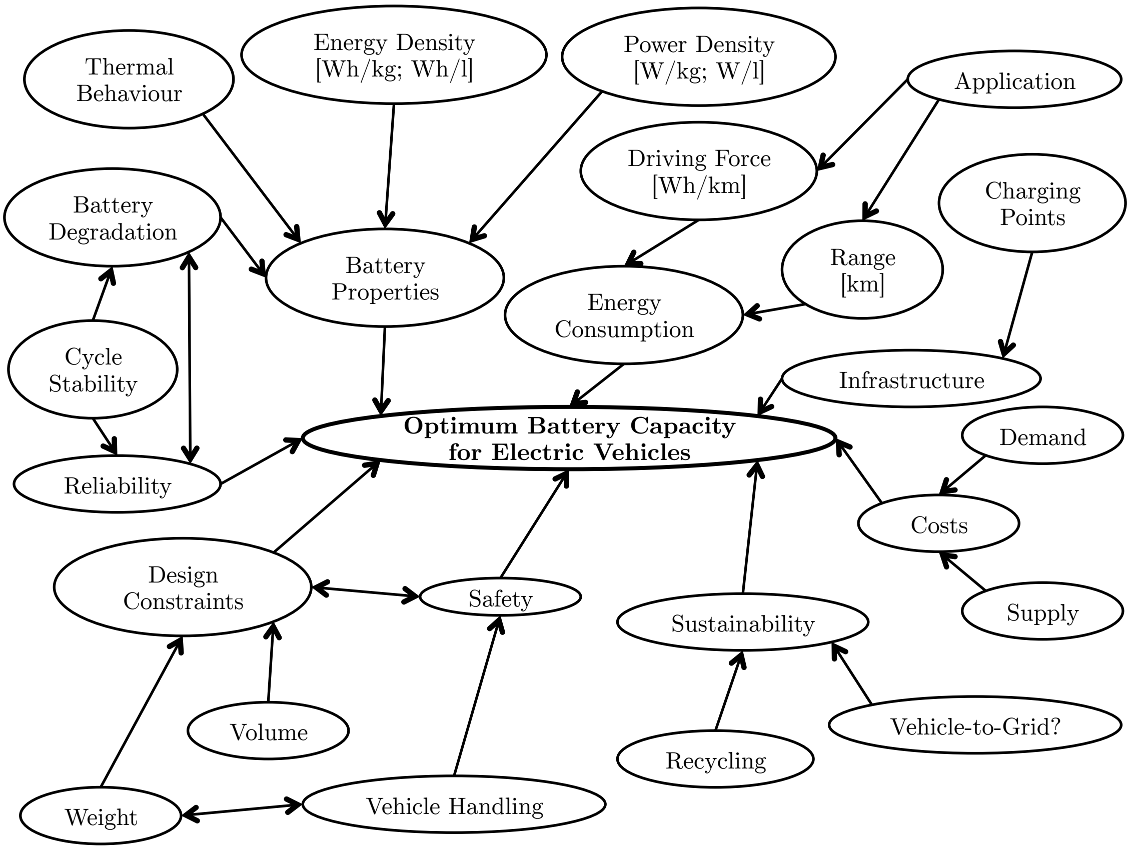
Thermal Behaviour
Energy Density [Wh/kg; Wh/l]
Power Density [W/kg; W/l]
Application
Driving Force [Wh/km]
Battery Degradation
Charging Points
Battery Properties
Range [km]
Energy Consumption
Cycle Stability
Infrastructure
Optimum Battery Capacity for Electric Vehicles
Demand
Reliability
Costs
Design Constraints
Safety
Supply
Sustainability
Volume
Vehicle-to-Grid?
Recycling
Weight
Vehicle Handling

Figure 1.5.: Factors Influencing Optimum Battery Capacity for EVs

and also on the vehicle's energy consumption. This work focuses on the individual vehicle's energy consumption and the battery's degradation. The aim is to accurately predict an effective and efficient battery size, which ultimately saves volume, weight, and costs for automobile manufacturers. In particular it intends to answer the following questions:

- What does 'optimum battery capacity' mean in the electric vehicle context?
- Which are the main factors that affect the optimum battery size and how?
- What is the expected lifetime of an EV and therefore of its battery pack?
- What does battery degradation mean?
- How does battery degradation affect the sizing of a traction battery for EVs?

1.4. Outline

The rest of this work is divided into five chapters. The following chapter (2) is devoted to an outline of the fundamentals and a comprehensive literature review. It first lays out the basics of electric vehicles and batteries. Second, it reviews and critically assesses the available literature on electric vehicles as well as on batteries for electric vehicles. At the end of this chapter knowledge gaps as well as modelling gaps concerning the optimum battery capacity for electric vehicles are identified. Chapter 3 explains the methodologies applied for this work. Specifically, it outlines the main underlying assumptions, modelling and simulation tools used as well as the validation techniques. The chapter on the nominal energy requirements of electric vehicles (4) brings together two key elements, which affect the optimum battery size: driving force and range. It concludes with the optimum battery capacity for various vehicle categories while neglecting battery degradation. Chapter 5 ties in with the latter. It deals with battery performance and degradation and their implications for the optimum battery capacity. The penultimate chapter (6) discusses the main findings of this work and brings them together. It identifies the optimum battery capacity for electric vehicles with particular focus on battery degradation. The final chapter (7) concludes this work and suggests areas for further work.

2. Fundamentals & Literature Review

The objective of this work is concerned with two main areas of research: electric vehicles and batteries. Therefore, after a very short discourse on the terminology (2.1), sections 2.2-2.3 lay out the basics and review the currently available literature about electric vehicles and about traction batteries for electric vehicles respectively. The two sections are linked and thus several cross-references are made. Both sections are divided into subsections that describe the particular history, fundamentals as well as software models and close with a short summary. The history outlines the main technological advancements of the past and the challenges, which still lie ahead. Basic functionalities are explained in the subsections dealing with fundamentals. Major software models for both EVs and batteries are introduced, analysed and critically assessed. Ultimately, their gaps are identified.

2.1. Terminology

Software models and simulations will be reviewed, analysed and applied extensively for this work. Consequently, it is important to define the common terms used in modelling and simulation. These have been defined by P. Fritzson of Linköping University in Sweden [14] and extended by [11]:

System:	The object or collection of objects the software designer wishes to study
Inputs:	The variables of the environment that influence the behaviour of the system. These inputs may or may not be controllable by the designer
Outputs:	The variables that are determined by the system and may influence the surrounding environment
Experiment:	The process of extracting information from a system by exercising its inputs
Model:	Anything an 'experiment' can be applied to in order to answer questions about that system
Simulation:	An experiment performed on a model
Modelling:	The process of building a model that sufficiently represents a system
Simulator:	A computer program capable of executing a simulation

2.2. Electric Vehicles

Electric vehicles are not new. They have been commercially available for more than 115 years. The idea of a vehicle being propelled by electricity is in fact older than that of internal combustion engine vehicles (ICEVs). Consequently, the literature available about electric vehicles is both broad and solid. In the following, the history of electric vehicles is outlined. This is followed by an explanation of the basic principles of this alternative power train type. Subsection 2.2.3 is devoted to the modelling of EVs, which also leads to the summary of this section (2.2.4).

2.2.1. History of Electric Vehicles

The history of electric vehicles is best characterised by an initial excitement during the turn from the 19th to the 20th century, which is followed by a steep loss of interest until the early 1980s. After this, the interest in EVs has continuously been picking up again. Figure 2.1 depicts these three phases, which are described in detail in the following paragraphs.

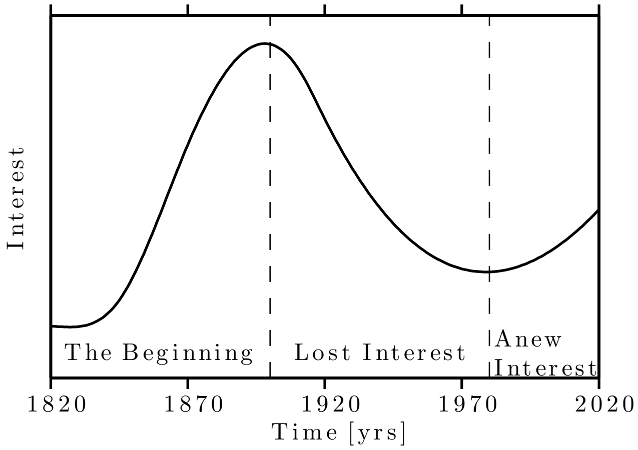

Figure 2.1.: Electric Vehicle Hype Cycle (adapted from [15])

The Beginning (1828-1900)

The groundwork for electric vehicles was laid in 1800 when the Italian Alessandro Volta demonstrated that electric energy could be stored chemically. In 1821 the Briton Michael Faraday developed the first electric motor/generator. Who invented the very first electric vehicle remains uncertain and several inventors have been given credit. In 1828 the Hungarian Ányos Jedlik developed an early type of electric motor that powered a very small model car shown in figure 2.2. Around the same time, in 1829, the Englishman Robert Stephenson assembled the most advanced steam locomotive of its day, *Stephenson's Rocket*. Three years later the Frenchman Hippolyte Pixii demonstrated an operating electric motor at the Académie des Sciences in Paris [17]. Between 1832 and 1839 Robert Anderson, a Scottish inventor, came up with the '*first crude electric carriage*', which attained a speed of 6.4 km/h [18]. In 1835 Thomas Davenport,

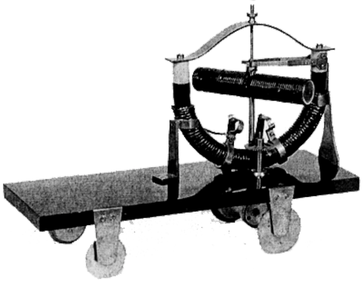

Figure 2.2.: Jedlik's Electric Vehicle Model from 1828 [16]

the inventor of the first American direct current (DC) motor, presented a small electric car running on a short circular electrified track. Similar to Jedlik's device and in the same year of Davenport's discovery Sibrandus Stratingh and his assistant designed a small-scale electric car that first used primary (i.e. non-rechargeable) cells as the on-board energy storage device. Stratingh's car is considered to be the first battery electric vehicle (BEV).

Reliable secondary (i.e. rechargeable) cells only became available in 1859 thanks to the works of the French chemist Gaston Planté. For more details on the history of traction batteries for electric vehicles see section 2.3. Exploiting these scientific developments, the French inventor Gustave Trouvé presented the first fully working full-scale three-wheeled electric vehicle at the International Exhibition of Electricity in Paris in 1881. It was also during this show that electrical engineers and scientists from around the world agreed on a standardised terminology for this new area of research. The units included Ampere (current), Faraday (capacity), Gauss (magnetic flux), Henry (magnetic inductance), Ørsted (magnetic intensity), Ohm (resistance) and Watt (power), honouring the respective electrical experimenters [17].

Thanks to them operating independently of precious oxygen (O_2), electric vehicles soon after were deployed as trolleys in coal mines. Until the early 1880s electric motors were struggling with reliability. Nikola Tesla, a Serbian-American engineer and scientist, is credited with overcoming this issue by developing the first induction motor in 1883. This also fuelled the development of a six-passenger electric wagon capable of reaching a speed of 23 km/h by the American William Morrison in 1891. The first commercially available automobile however, presented in 1895 by the German Carl Benz, was propelled by an internal combustion engine. EVs saw their first commercial application in 1897 with the introduction of an electric vehicle taxi fleet in New York. Thanks to their quiet, odourless, non-vibrating, and gearless operation this seemed an ideal application for these low-range vehicles. Changing gears and hand-cranking in order to start the engine were the most difficult tasks related to early ICEVs. Neither was required for EVs, which greatly enhanced the ease of operation for women as well. Consequently, EVs soon were perceived as '*women's cars*'. Their limited range was quickly identified as the biggest drawback. Thus, as early as 1896 an exchangeable battery service was proposed [19].

In 1899, it was an electric vehicle developed by the Frenchman Camille Jenatzy that would be the first vehicle to go faster than 100 km/h. The '*Jamais Contente*' (English: '*The Never*

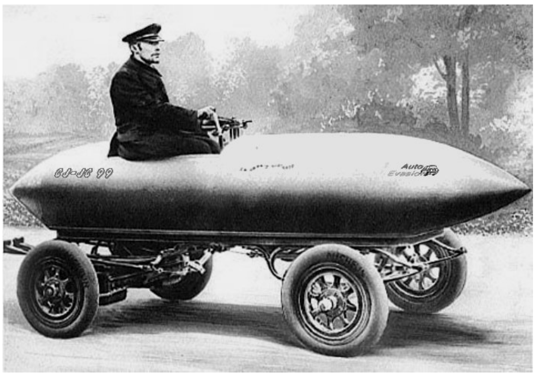

Figure 2.3.: Jenatzy's Record Breaking '*Jamais Contente*' from 1899 [20]

Satisfied'), pictured in figure 2.3, reached a top speed of 105.88 km/h. Certainly by the end of the 19th century the millennia-long land transport domination of the horse-drawn carriage was brought to an end. Steam, petrol and electric driven vehicles were taking over instead and would coin the so-called '*horseless age*'. The share of electric vehicles as part of the total vehicle fleet rose to 38% in 1900 in the US, the country where electric vehicles were most popular. This is illustrated in figure 2.4.

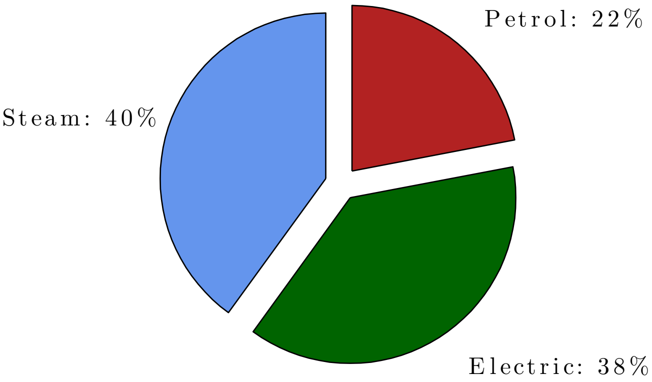

Figure 2.4.: Power Train Types in the US in 1900 [21]

Lost Interest (1900-1980)

For a number of reasons electric vehicles lost their appeal at the beginning of the 20th century. An improved road infrastructure connecting major cities both in the US and Europe meant that in the absence of a battery-charging infrastructure vehicles with a greater range were sought after. Due to their limited range (50-65 km), relatively low top speed (24-32 km/h) and long charging time, electric vehicles remained limited to urban use. In addition, economic reasons led to a losing interest in electric vehicles. During the 1910s and the 1920s the American Henry Ford popularised mass production for petrol cars, which led to steep price cuts. In 1912 an electric roadster sold for $1,750, while a petrol car cost $650 [22]. Dropping petrol prices during the early years of the 20th century (see figure 1.1) also played in the hands of petrol cars. Finally, in 1912 the American Charles Kettering came up with the electric self-starter, an application of battery power. It eliminated the difficult hand-cranking for petrol cars and thus enabled their use for women as well [21].

Beginning with the 1920s electric vehicles would only cater for a very small share of a rapidly growing passenger car market. Only a few manufacturers offered them on special order until World War II [21]. During the war, both the Allies and the Axis were struggling with fuel shortages. Especially at the home fronts they increased efforts to avoid the use of petrol. This led to the development of electric milk floats in Great Britain (see figure 2.5), '*the most long-lived fleet of electric vehicles the world has ever seen*' [23]. However, compared with the total passenger vehicle market, the share was insignificant. Electric vehicles remained popular only for a very limited range of applications. These mainly included the aforementioned milk floats, forklifts and golf buggies.

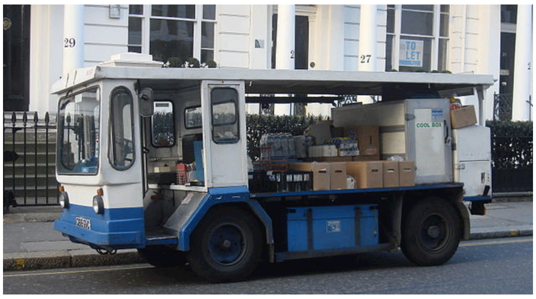

Figure 2.5.: Typical Milk Float [24]

After World War II several attempts by different car manufacturers have been made to revive the electric car. One example is the '*Henney Kilowatt*' which was introduced in the US in 1959. It featured a top speed of 96 km/h and a range of over 97 km. Despite these significant performance improvements compared with earlier electric cars, the '*Henney Kilowatt*' proved to be too expensive to penetrate the market. Several similar projects were also cancelled due to excessive costs, unsatisfying range and/or performance. EVs remained niche products, exemplified by the first manned vehicle on the moon during the Apollo 15 mission of 1971.

Anew Interest (1980-today)

The oil shocks during the 1970s and the 1980s (see figure 1.1) caused a renewed interest in electric vehicles. California's Air Resources Board (CARB) was among the first governmental institutions to incentivise zero-emission vehicles (ZEV) in 1990 [25]. Despite an initial success with carmakers developing a range of ZEVs including the Chrysler TEVan, the Ford Ranger EV pickup and the GM EV1, the ZEV initiative got overturned in Federal Court in 2001. Chrysler, Toyota, and a group of GM dealers successfully sued CARB alleging '*the new ZEV rules violate a federal law barring states from regulating fuel economy in any way*' [26].

In 1997 the Kyoto Protocol was adopted in order to stabilise '*greenhouse gas concentrations in the atmosphere at a level that would prevent dangerous anthropogenic interference with the climate system*' [27]. Under the Protocol, 37 countries including Australia, Canada, China, the EU, Japan and South Korea but excluding the US commit themselves to a significant reduction of four greenhouse gases: carbon dioxide (CO_2), methane (CH_4), nitrous oxide (N_2O) and sulphur hexafluoride (SF_6). Since road transport emissions present a major share of total greenhouse gas emissions (see figure 1.2), worldwide emission standards for road vehicle have been becoming stricter ever since (see figure 1.3). As a consequence car manufacturer have been introducing more low-emission vehicles. These include pure EVs, fuel cell electric vehicles (FCEVs), range-extended electric vehicles (REEVs), plug-in hybrid electric vehicles (PHEVs), hybrid electric vehicles (HEVs) and downsized internal combustion engine vehicles. The most prominent low-emission vehicles during the 1990s have been the Toyota Prius and the Honda Insight, both hybrid electric vehicles [23].

During the 1990s and the 2000s most major car manufacturers did not offer EVs for sale. Instead they have been focussing on the development and selling of internal combustion engine vehicles and some hybrid electric vehicles. Consequently, small companies have filled the gap of developing and selling EVs. In 2001, after seven years of research and development the REVA Electric Car Company of India launched the REVAi, a small micro electric car. In the United Kingdom (UK) it is known as G-Wiz and has become particularly popular in urban spaces. Due to safety concerns in many countries it does not qualify as a highway-capable motor vehicle. Instead it is classified as a neighbourhood electric vehicle (NEV), which can only be driven on roads with speed limits of up to 72 km/h depending on local regulations. According to Pike Research, globally there were 475,000 NEVs registered in 2011 [28]. NEVs, which also include electric fork lifts, golf carts and milk floats, constitute the largest share of commercially available EVs.

As of December 2012 the number of commercially available and highway-capable EVs is limited. Table 2.1 lists a selection of currently commercially available and highway-capable EVs. Out of 28.4 million cars registered in the UK in December 2012 around 2,000 are fully electric, i.e. 0.007% [29]. The Tesla Roadster, the Tesla Model S and the Nissan LEAF (leading, environmentally friendly, affordable family car) are the two most prominent electric vehicles of the 2000s and 2010s so far.

The main technical challenges facing EV development today have broadly remained the same over the past century. They include limited range, deteriorating range (as a function of time, number of driving cycles, temperature, etc.), accurate and real-time predictions of the remaining energy level, high capital costs and an insufficient charging infrastructure. However, most of these (range, energy level and costs) are directly related to the traction battery.

Table 2.1.: Selection of Commercially Available EVs as of December 2012 [30]

Make	**Model**	**Vehicle Mass [kg]**	**Peak Power [kW]**	**Top Speed [km/h]**	**Range[1] [km]**	**Battery Capacity [kWh]**	**Price [$]**
BMW	ActiveE[2]	1,800	125	140	151	32.0	n/a
BMW	Mini E[2]	1,465	150	150	153	35.0	n/a
Bollor	Bluecar	1,120	50	110	150	30.0	n/a
BYD	e6	2,020	200	140	300	48.0	35,000
Citroën	C1 ev'ie	890	30	100	100	16.0	30,890
Coda	Sedan	1,660	100	130	142	31.0	38,000
Ford	Focus Electric	1,674	107	135	122	23.0	36,000
Kewet	Buddy	994	13	80	100	15.0	35,000
Lumeneo	Smera	550	30	110	100	9.3	33,000
Mercedes-Benz	Vito E-Cell	2,275	60	89	100	36.0	30,000
Mia	electric	764	9.7	100	130	8.0	33,700
Mitsubishi	i-MiEV	1,080	47	130	100	16.0	45,100
Nissan	Leaf	1,521	80	150	120	24.0	32,780
Renault	Fluence ZE	1,543	70	135	185	22.0	32,000
Renault	Zoe	1,392	65	135	210	22.0	25,000
REVA	i	665	13	80	80	9.6	12,000
REVA	L-ion	565	13	80	120	9.6	n/a
Smart	ED	870	30	100	135	16.5	20,000
Tazzari	Zero	542	15	100	140	12.3	29,900
Tesla	Roadster	1,235	215	200	240	56.0	92,000
Tesla	Model S	2,108	310	200	393	85.0	95,400
Th!ink	City	1,038	34	110	160	23.0	30,000
Toyota	RAV4 EV	1,830	115	137	148	41.8	49,800
Wheego	Whip LiFe	1,284	45	95	160	30.0	32,995
	⊘	**1287**	**80**	**122**	**156**	**27.13**	**38,428**

2.2.2. Fundamentals of Electric Vehicles

The following paragraphs first explain the basic working principles of ICEVs, HEVs and PHEVs and then describe the functionality of an EV in more detail.

Working Principle of ICEVs, HEVs and PHEVs

The power train of an EV differs significantly from that of a conventional internal combustion engine vehicle. Figure 2.6 shows the basic power train layouts for different types of vehicles. The ICEV power train layout, shown on the far right, solely relies on fossil fuels as energy source. The most commonly used fuels for ICEVs, petrol and diesel, have approximate energy contents (gross calorific values) of 13,083 Wh/kg and 12,663 Wh/kg respectively [31]. The fuel is burnt in the internal combustion engine, which results in relatively high rotational speeds (1,000-8000 rpm) of the crankshaft. The crankshaft is connected to a gear box, which converts speed and

---

[1] based on both NEDC and US FTP-75

[2] demonstration fleet

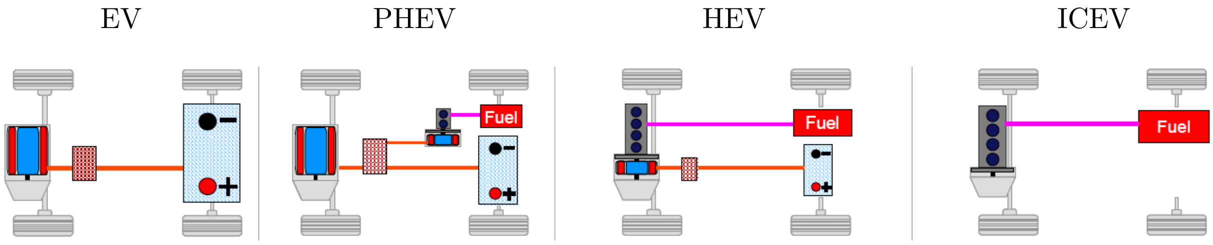

Figure 2.6.: Basic Vehicle Power Train Configurations [32]

torque while keeping the power coming from the ICE constant. This description ignores losses, which for an ICEV are relatively high. Figure 2.7 demonstrates that for a mid-sized ICEV during an urban cycle less than ⅕ of the fuel energy is converted into useful propulsion energy. More than ⅗ of the initial fuel energy is lost in the ICE in form of heat.

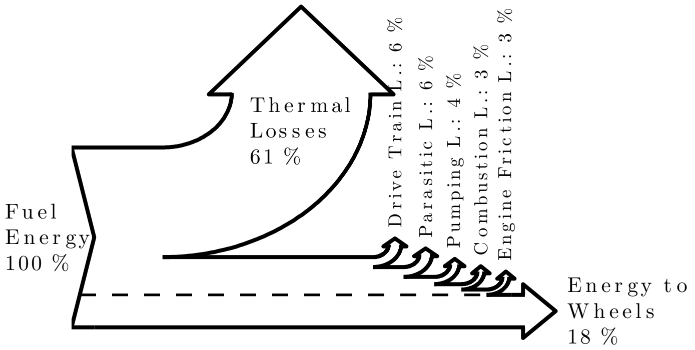

Figure 2.7.: Representative Energy Flow of an ICEV During an Urban Drive Cycle [33]

A typical parallel hybrid electric power train layout is shown on the left of the ICEV power train layout in figure 2.6. It features an ICEV power train in parallel with an electric power train with a relatively small battery pack (≈ 1-2 kWh), power electronics and one or several electric motor(s). Both power trains can power the vehicle either individually or together. The series hybrid electric power train on the left of that has a relatively larger battery pack (≈ 4-5 kWh). Only the electric motors power the drive train, whereas the ICE works as a generator to charge the battery pack. For a series HEV the battery cannot be charged externally, whereas for a PHEV it can.

Working Principle of EVs

The EV drive train, illustrated on the far left in figure 2.6, exclusively takes its energy from the battery pack. Consequently, the EV's battery pack is the largest (≈ 10-100 kWh) and usually is also bigger and heavier than the fuel tank of a comparable ICEV. This is due to the relatively low specific energy of modern lithium-ion batteries, which currently ranges in between 100-250 Wh/kg [12] (see also figure 2.26). EVs do not necessarily require a transmission like ICEVs as their power electronics can match speed and torque requirements accordingly. Also, they can have one, two, three or four electric motors installed. Figure 2.8 illustrates how the power electronics including the electronic controller and the motor controller(s) manage the energy flow from the AC power source to the wheels. Thick arrows represent energy flows, thin ones stand for electronic signals. First, the EV is charged from an alternating current (AC) power source (e.g. power socket or charging point). The on-board battery charger acts as a rectifier converting AC to DC power. The battery pack usually operates at a relatively high voltage (75-600 V) in order to avoid high currents, which cause increased ohmic losses. Most current commercial EVs operate at a pack voltage of in between 300-400 V, which allows lower currents for the same power level. Equation 2.1 clarifies the relationship between current and heat loss.

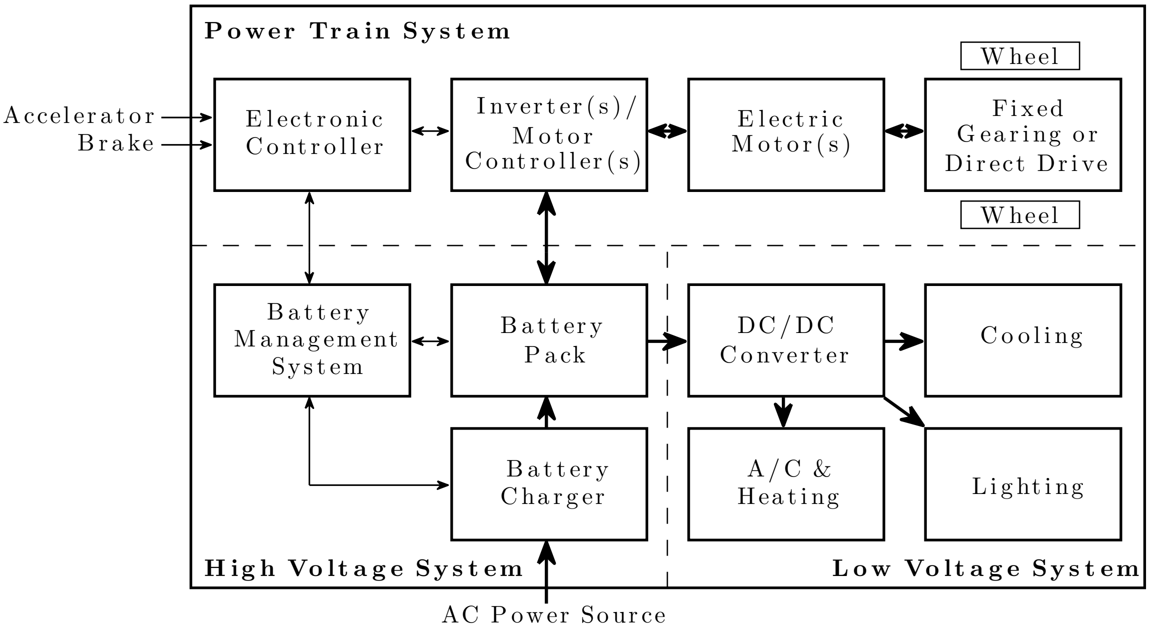
Power Train System
Wheel
Accelerator
Brake
Electronic Controller
Inverter(s)/ Motor Controller(s)
Electric Motor(s)
Fixed Gearing or Direct Drive
Wheel
Battery Management System
Battery Pack
DC/DC Converter
Cooling
Battery Charger
A/C & Heating
Lighting
High Voltage System
Low Voltage System
AC Power Source

Figure 2.8.: Basic EV Configuration [34]

$$P_{loss} = I^2 R \tag{2.1}$$

The ohmic power loss P_{loss} is proportional to the square of the current I. Depending on the type of electric motor(s), the use of inverters may be necessary. Despite their increased control requirements and the need for inverters, AC motors are the preferred choice over direct DC motors, because of their superior power and energy density. In this example (figure 2.8) an AC motor is applied. From the DC battery pack the electric potential energy is transferred to one or several inverters which convert the DC power back into AC power. At the same time the inverters act as motor controllers by adjusting voltage and current in order to cater for the requested speed and torque values respectively. Finally, depending on the layout, one or more electric motors apply a traction force to the wheels. For a direct-drive design this is done immediately, alternatively a gear box can be added in between. The all-electric Nissan Leaf and Tesla Roadster feature final gear ratios of 7.98 and 8.28 respectively [35]. In addition to the high voltage system and the power train system there usually is a low voltage system (≈ 12 V) as well. A DC/DC converter reduces the high system voltage to approximately 12 V. The low voltage system, which typically consumes only about 2% of the total available power [36], caters for the starting, lighting and cooling requirements of the vehicle as well as for auxiliary needs such as radio, air conditioning (A/C) and heating. Losses of electric power trains are significantly smaller compared to those of ICEV drive trains. Figure 2.9 demonstrates that more than 3/5 of the input grid energy is converted into useful propulsion energy at the wheels.

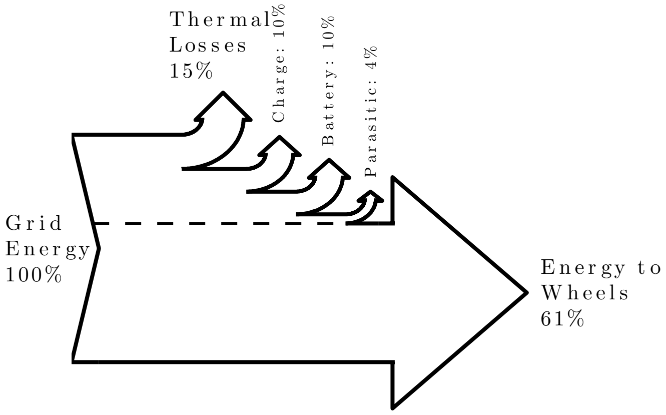

Figure 2.9.: Representative Energy Flow of an EV During an Urban Drive Cycle [37]-[39]

2.2.3. Modelling of Electric Vehicles

The modelling of EVs is as old as the EV itself [40]. However, due to the prevalence of the internal combustion engine vehicle during the 20th century (see section 2.2.1), simulation software for ICEVs and in particular internal combustion engine modelling has advanced far beyond electric vehicle and its component modelling. The following paragraphs present an overview and a critical appraisal of the currently available and most popular software models for electric vehicles.

Most modern vehicle simulations can be categorised according to two parameters; direction and accuracy of modelling [11]. First, depending on the direction of the simulation, vehicle models can be forward-facing, backward-facing or a combination of the two. Secondly, depending on the level of details, vehicle models may be steady-state, quasi-steady, or dynamic. Here, forward-facing models are considered first, then backward-facing and finally mixed models are examined. Some models were first developed more than 20 years ago, but have been updated continually since.

Forward-Facing Models

Forward-facing vehicle models describe simulations which use control signals like the driver stepping on the accelerator or brake as inputs (see figure 2.10). This means that the physical causality is respected. If the vehicle is required to follow a speed-time trace, a drive cycle, the forward-facing model derives the required control signals [41]. Typically, this is done via a proportional-integral-derivative (PID) controller [42]. The control signals are then used to determine the required torque and speed values from the electric motor(s). These values are then used as inputs for the transmission system, which again are used as inputs for calculating the speed and torque of the wheels. The resulting layout, which is similar to that in figure 2.8, has one direction of information/simulation flow only. The forward-facing approach is very beneficial for a detailed causality analysis and in order to work out maximum speed and acceleration. Practically, it calculates the effect at the wheel caused by the driver's inputs. Thus, the forward-facing modelling approach has distinct benefits:

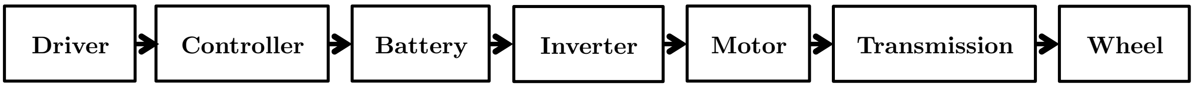

Figure 2.10.: Forward-Facing EV Software Schematic

- Follows physical causality
- Quick and computationally easy integration with vehicle control systems (e.g. LabVIEW [43] or MATLAB/Simulink [44])
- Good dynamic response

However, for the detailed analysis of power train components such as the electric motor or the battery pack the forward-facing approach has disadvantages:

- Most validated component models are defined as backward-facing only
- Exact knowledge of control inputs requires expensive and complicated sensor equipment

In the following six well-established forward-facing vehicle simulation models that also cover electric vehicles are presented in alphabetical order.

Autonomie , the successor software of *PSAT*, was developed by the Argonne National Laboratory (ANL) and General Motors (GM) in 2007. As a forward-facing simulation it predicts and analyses fuel efficiency and performance of various power train types [45]. *Autonomie* determines system hardware and software requirements, which concentrate on component control parameters regarding variation and/or robustness.

AVL CRUISE is a commercial power train simulation software developed by the Austrian automotive consultancy AVL List GmbH [46]. *CRUISE* follows an object-oriented forward-facing physical modelling approach. It can be linked with other simulation tools such as *AVL DRIVE* (driving dynamics and comfort), *Flowmaster*, *Kuli* (both cooling fluid simulations), *AVL InMotion* (hardware-in-the-loop (HiL) simulation), *MATLAB/Simulink* (control simulation) and Microsoft Excel. *CRUISE* supports conventional ICEV modelling as well as PHEV/HEV and EV modelling for optimisation of fuel efficiency, emissions, performance and drivability.

Dymola is a commercial modelling and simulation environment for engineering applications based on the the open-source *Modelica* modelling language [47]. Developed by the French software specialist Dassault Systèmes, *Dymola* features model libraries which cover systems like power trains, vehicle dynamics and electric drives. Thanks to the use of open software, users are free to create their own model libraries or to modify the ready made model libraries to better match their unique modelling and simulation needs. The smart electric drives library focuses on the simulation of hybrid vehicles and not pure electric vehicles.

Modelica is an object-oriented, equation based modelling language for complex systems [48]. *Dymola* is one of its many simulation environments. The other environment that can be used for power train analysis is *CATIA* (Computer Aided Three-Dimensional Interactive Application), although its focus lies on computer-aided design (CAD). In addition to the libraries available to *Dymola*, *Modelica* libraries feature more than 1,200 model components and over 900 functions.

PSAT describes the *Powertrain System Analysis Toolkit* first developed by ANL in 1999 [49]. At the price of a relatively high computing power input *PSAT* allows for the development of realistic control strategies for internal combustion engine vehicles as well as for advanced power train types including electric vehicles. *PSAT* follows a quasi-steady approach and in 2007 it was overhauled in order to develop *Autonomie*.

SimDriveline is one of many commercial library extensions of the MATLAB/Simulink environment [50]. Unlike the conventional Simulink blocks which represent mathematical operations or operates on signals, *SimDriveline* models an entire vehicle drive train system. At best, these models represent steady-state relationships [51]. *SimDriveline*'s focus is on conventional ICE power train configurations and vehicle dynamics.

Backward-Facing Models

Backward-facing vehicle models run in the opposite direction of forward-facing vehicle models, which means that the physical causality is not respected (see figure 2.11). They typically use a drive cycle and vehicle parameters as input in order to deliver specific component behaviour like that of the traction battery as output. It follows that the backward-facing approach calculates

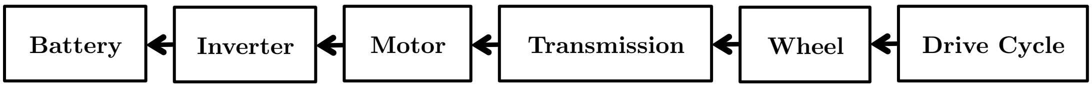

Figure 2.11.: Backward-Facing EV Software Schematic

the power input given the power output. This leads to a number of benefits, which are closely related to the drawbacks of the forward-facing approach:

- Most component models which include steady or dynamic efficiency maps are defined in terms of output speed and torque.
- Vehicle performance benchmarking for fuel/energy consumption and CO_2 emissions is normally performed through standard drive cycles like the European NEDC, the American FTP-75 or the Japanese 10-15 mode (see appendix D).
- Computation time can be reduced significantly since standard integration routines can be used with the relatively large (often $t = 1$ s) time steps of drive cycles [52].

There are also disadvantages associated with the backward-facing approach:

- It assumes that the speed-time trace (drive cycle) is achieved by both the driver and the vehicle.
- The approach fails to directly predict vehicle performance including climbing ability, maximum acceleration or speed.
- Modelling and developing a control system is not possible.

The following paragraphs are dedicated to popular applications of the backward-facing approach.

CarSim was first developed by AeroVironment, Inc. in 1992 [53]. It features a similar functionality as that of *SIMPLEV*, emissions however cannot be predicted. *CarSim*'s focus lies on vehicle dynamics and drivability, with detailed driver control, aerodynamic, 3D geometry, friction, suspension, steering, brake and tyre models [54]. It offers interfaces with MATLAB/Simulink, LabView and AVL Cruise.

JANUS is a road vehicle simulation package, first developed at the Engineering Department of Durham University [55] in 1985. Written in the Fortran programming language, it allows different power train types including electric ones to be simulated. Standard input parameters are regulatory drive cycles and typical outputs include fuel/energy consumption.

MARVEL is a software written for the more holistic evaluation of electric and hybrid electric vehicles [56]. First developed at ANL in 1991, it is a backward-facing model, which provides relatively little flexibility. Its aim is to provide life-cycle cost evaluations. In order to achieve this, it includes extensive modelling of the inter-relationships among battery parameters.

QSS is the open *Quasi-Static Simulation* designed by the Institute for Dynamic Systems and Control of the Swiss Federal Institute of Technology Zurich in 2007 [57, 58]. It is based on the MATLAB/Simulink platform, which provides the user with great design flexibility. Its input variables are speed, acceleration and the road gradient. With this information and the vehicle's main parameters, the required tractive force for the chosen profile can be calculated. The vehicle parameters consist of the frontal area, the aerodynamic drag coefficient, the rolling resistance coefficient and the vehicle mass. Quasi-static in the context of this approach means that the velocities and accelerations are assumed to be constant for a given time step. The time interval has to be chosen small enough in order to satisfy this assumption. Thus, for the main regulatory drive cycles (see appendix D) this is equal to 1 s. The quasi-static approach presents a compromise between the fast steady (or average-operating-point) approach and the mathematically 'correct' but computationally intensive dynamic approach. *QSS* is relatively accurate for long time intervals (i.e. $t \geq 1$ s), but substantially inaccurate for short time intervals (i.e. $t < 1$ s) [57]. The *QSS* battery model is presented in section 2.3.4.

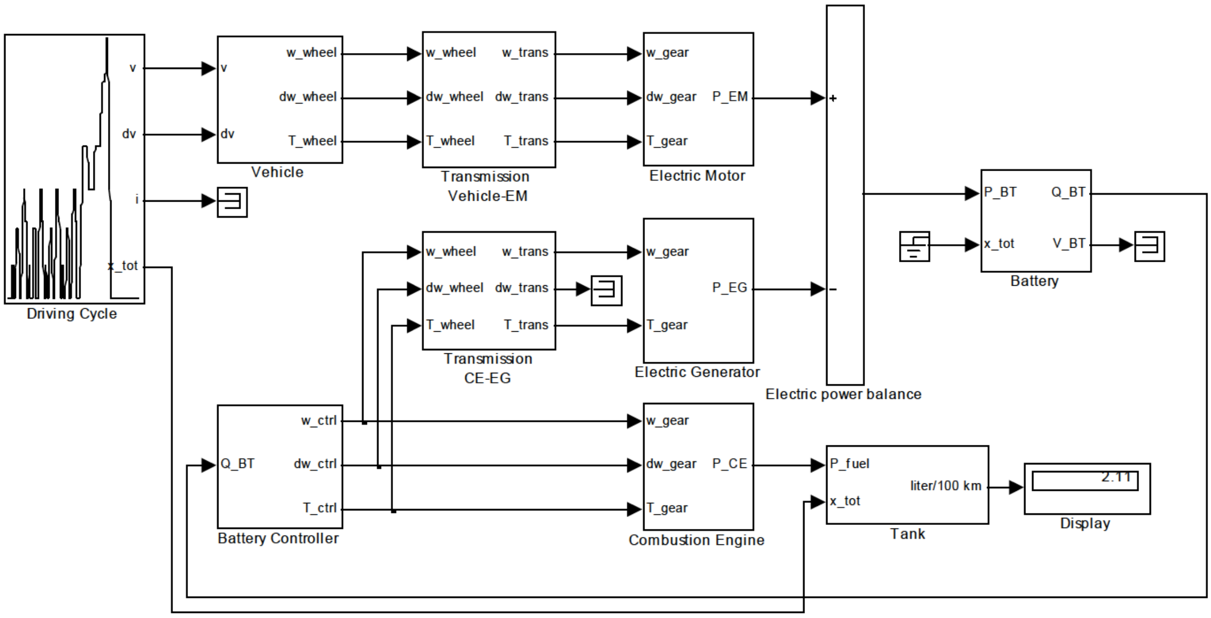
v
dv
i
x_tot
Driving Cycle
v
dv
w_wheel
dw_wheel
T_wheel
Vehicle
w_wheel
dw_wheel
T_wheel
w_trans
dw_trans
T_trans
Transmission
Vehicle-EM
w_gear
dw_gear
T_gear
P_EM
Electric Motor
+
-
Electric power balance
w_wheel
dw_wheel
T_wheel
w_trans
dw_trans
T_trans
Transmission
CE-EG
w_gear
T_gear
P_EG
Electric Generator
P_BT
x_tot
Q_BT
V_BT
Battery
Q_BT
w_ctrl
dw_ctrl
T_ctrl
Battery Controller
w_gear
dw_gear
T_gear
P_CE
Combustion Engine
P_fuel
x_tot
liter/100 km
Tank
2.11
Display

Figure 2.12.: Top Level Block Diagram for a HEV in QSS [58]

SIMPLEV describes the *Simple Electric Vehicle* simulation program first developed at the Idaho National Engineering & Environmental Laboratory in 1991 [59]. It is strictly backward-facing, features a basic interface based on the disk operating system (DOS) and can plot typical output results like energy consumption, and well-to-wheel emissions.

Combined Models

Forward-facing vehicle models are powerful tools for vehicle performance analysis (e.g. climbing ability, maximum speed and acceleration) and for control design, the processing time however is long. Backward-facing vehicle models are convincing instruments for energy consumption and emissions analysis as well as for the examination of individual component behaviour, but the physical causality is neglected. Most of the time vehicle designers need to have overall vehicle performance as well as individual component data available to them. Preferably for them, the simulation is fast and also reflects real system setup. Consequently, software designers have come up with hybrid models, which combine forward- and backward facing vehicle models. These hybrid models are considered to be state of the art of electric vehicle modelling. The following paragraphs introduce four popular ones.

ADVISOR is the *Advanced Vehicle Simulator* first developed by the National Renewable Energy Laboratory (NREL) as a commercial software in 1994 [52]. Between 1998 and 2003 *ADVISOR* was made available free of charge before AVL, the company behind *AVL Cruise*, licensed it until 2012. Since then the simulator is distributed under a permissive open-source license and can be downloaded from [60]. In contrast to most of the other simulators presented, *ADVISOR* includes all elements of the source code. This provides a high level of modelling flexibility for the user. *ADVISOR* features a powerful graphical user interface (GUI) shown in figure 2.13. The vehicle power train layout, in this case an EV, is shown on the top left hand corner. Specific empirical component characteristics (in this case the variation of the battery's internal resistance with state of charge (SOC)) are mapped on the bottom left hand corner. The right hand side of the input screen allows the user to manually change vehicle, energy storage, transmission, wheel, accessory and control parameters. Fundamentally, *ADVISOR* is an empirical backward-forward facing model, relying on static maps that reflect steady-state behaviour of vehicle subsystems. Although the backward-facing approach is dominant (see

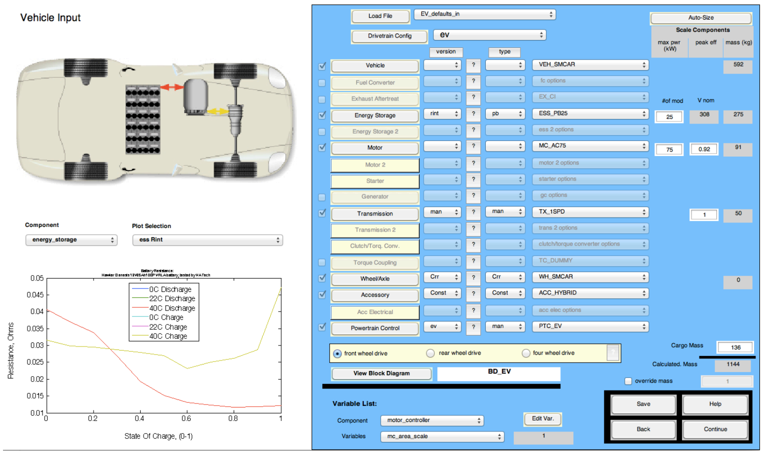
Vehicle Input
Battery Resistance:
Hawker Genesis 12V26Ah10EP VRLA battery, tested by VA Tech
0C Discharge
22C Discharge
40C Discharge
0C Charge
22C Charge
40C Charge
Resistance, Ohms
State Of Charge, (0-1)
0.05
0.045
0.04
0.035
0.03
0.025
0.02
0.015
0.01
0
0.2
0.4
0.6
0.8
1
Load File
Drivetrain Config
version
type
?
Auto-Size
Scale Components
Fuel Converter
Exhaust Aftertreat
Energy Storage 2
Motor 2
Starter
Generator
Transmission 2
Clutch/Torq. Conv.
Torque Coupling
Acc Electrical
fc options
EX_CI
ess 2 options
motor 2 options
starter options
gc options
trans 2 options
clutch/torque converter options
TC_DUMMY
acc elec options
View Block Diagram
Edit Var.
Save
Help
Back
Continue

Component: energy_storage
Plot Selection: ess Rint

Load File: EV_defaults_in
Drivetrain Config: ev

	version	type		#of mod / max pwr (kW)	V nom / peak eff	mass (kg)
☑ Vehicle			VEH_SMCAR			592
☑ Energy Storage	rint	pb	ESS_PB25	25	308	275
☑ Motor			MC_AC75	75	0.92	91
☑ Transmission	man	man	TX_1SPD		1	50
☑ Wheel/Axle	Crr	Crr	WH_SMCAR			0
☑ Accessory	Const	Const	ACC_HYBRID			
☑ Powertrain Control	ev	man	PTC_EV			

● front wheel drive ○ rear wheel drive ○ four wheel drive

BD_EV

Cargo Mass: 136
Calculated. Mass: 1144
☐ override mass: 1

Variable List:
Component: motor_controller
Variables: mc_area_scale 1

Figure 2.13.: ADVISOR 2.1 Vehicle Input Screen [60]

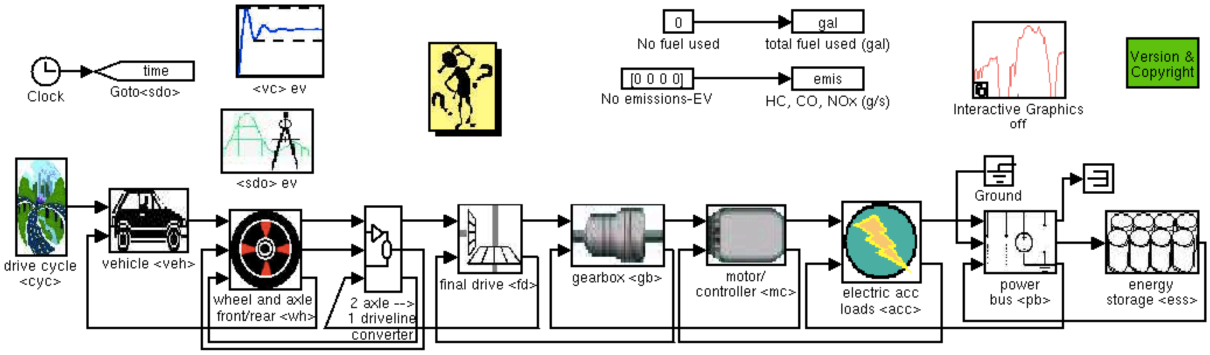
Clock
time
Goto<sdo>
<vc> ev
<sdo> ev
0
No fuel used
gal
total fuel used (gal)
[0 0 0 0]
No emissions-EV
emis
HC, CO, NOx (g/s)
Interactive Graphics off
Version & Copyright
drive cycle <cyc>
vehicle <veh>
wheel and axle front/rear <wh>
2 axle --> 1 driveline converter
final drive <fd>
gearbox <gb>
motor/ controller <mc>
electric acc loads <acc>
Ground
power bus <pb>
energy storage <ess>

Figure 2.14.: ADVISOR's Top Level Block Diagram for an EV [60]

figure 2.14), feedback loops in the opposite direction represent forward-facing modelling. Two assumptions are overriding *ADVISOR*'s modelling architecture. First, no drive train component requires more power from its upstream (i.e. backward-facing) neighbour than it can use. Once a component operating limit is reached, the input speed is either lowered or increased. Operating limits include wheel slip, maximum engine speed, maximum torque at different speeds, maximum controller current, minimum controller voltage, maximum and minimum battery voltage as well as maximum battery current. Secondly, individual component efficiencies are the same for both the forward- and the backward facing simulation. Using a standard personal computer (PC) *ADVISOR*'s solution speed is on the order of $^1/_{75}$ of real time [61]. It features five battery models, two of which are only applicable to lead-acid batteries. The remaining three are introduced in section 2.3.4.

FASTSim stands for the *Future Automotive Systems Technology Simulator* also developed at NREL [62]. It aims at quickly evaluating the impact of technology improvements on vehicle efficiency, performance, cost, and battery life in conventional vehicles, hybrid electric vehicles, plug-in hybrid electric vehicles, as well as electric vehicles (EVs). *FASTSim* is written in Microsoft Excel and features a user-friendly interface. Inputs include engine power, battery power and vehicle mass which lead to typical outputs like energy/fuel consumption, emissions and costs. The battery model, which also estimates battery life time, is described in section 2.3.4.

V-Elph is a system-level modelling, simulation, and analysis package first developed by a Masters student at Texas A&M University in 1996 [63]. It is based on MATLAB/Simulink and uses visual programming techniques. *V-Elph* calculates parameters like energy efficiency, fuel economy, and vehicle emissions. It aides designers for hybrid electric and electric vehicles with component sizing, energy management strategies, and general optimisation. The schematic shown in figure 2.15 is remarkably similar to that of *ADVISOR*, however less complex (see figure 2.14).

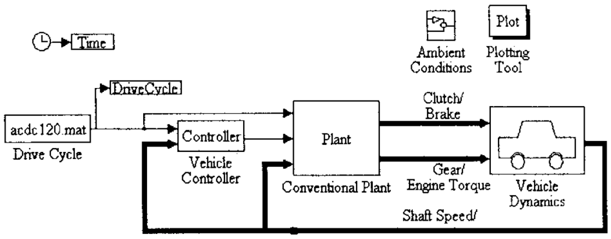

Figure 2.15.: V-Elph's Top Level Block Diagram [63]

Other Models

In addition to the aforementioned vehicle simulations, which basically pass on power requirements up and/or down the power train, more complex vehicle modelling platforms exist. The Virtual Test Bed (VTB) from the University of South Carolina (USC) is designed for the prototyping of large-scale, multi-disciplined dynamic systems [64]. Its focus lies on advanced power systems, especially on hybrid or fully electric land, air and sea vehicles. Individual component models can be integrated as 'black box' models into a system without passing on valuable intellectual property (IP) to other contributors. Similarly, *PSIM* is a simulation software for complex systems, focussing on power electronics and motor control [65].

2.2.4. Interim Summary

Electric vehicles have been around for more than 100 years. They have been particularly popular in the US around 1900 where they made up more than ⅓ of the vehicle fleet. Dropping petrol prices, mass manufacturing and the limited range of electric vehicles amongst other factors led to the dominance of internal combustion engine vehicles during the 20th century. This also led to significant advances in the modelling of combustion engine vehicles compared with electric vehicles. At the beginning of the 21st century several alternative power train types including EVs, FCEVs, PHEVs and HEVs have become commercially available. Thus, the need to accurately model and simulate alternative power train types is evident.

Vehicle simulators can be categorised according to the level of accuracy and according to the direction of simulation. With the exception of *AVL Cruise*, *Dymola*, the *VTB* and *PSIM* all presented vehicle simulations are either based on steady or quasi-steady assumptions. Dynamic models are often limited to individual components like the internal combustion engine, electric motors or the battery pack. Most dynamic power train models, which usually are formulated using sets of ordinary differential equations (ODEs), cannot be executed in real-time [66]. They suffer from the 'curse of dimensionality', i.e. from a rapid increase in complexity with an increasing number of dimensions. Steady and quasi-steady models can be computed in real time or faster and apply empirical data, engineering assumptions, and physics-based algorithms. Their main advantage is fast computation. Forward-facing models, which simulate the vehicle starting with the driver input down to the forces at the wheels, are more accurate than backward-facing models. They are particularly powerful tools for the development of an effective control strategy. On the other hand, their high level of complexity leads to increased computational time. In contrast, backward-facing models are typically much faster. Hybrid models like *ADVISOR*, which form the state of the art of electric vehicle modelling, are aimed at combining the strengths of each approach.

The aim of this work is to establish a battery sizing model for electric vehicles, which also considers battery degradation. None of the presented electric vehicle models currently incorporates such a component model. Both *ADVISOR* and *QSS* feature the most detailed battery models out of the envisaged ones, which could be expanded for this purpose. Therefore, the proposed component model needs to be mainly backward-facing with iterative loops in the forward-direction in order to be incorporated into either *ADVISOR* or *QSS*.

2.3. Batteries for Electric Vehicles

An electrical battery describes one or more electrochemical cells that convert stored chemical energy into electrical energy. Since its discovery it has become a common power source for both stationary and mobile applications. The following paragraphs first outline the history of batteries and then explain the fundamentals of batteries including battery degradation. These are followed by paragraphs that outline the main modelling approaches regarding batteries and a summary at the end of this section.

2.3.1. History of Batteries

The first batteries are considered to be more than 2,000 years old. In 1938 archaeologists uncovered a set of clay jars near Baghdad in Iraq, each containing a copper cylinder that encased an iron rod [67]. Replicas of the so called 'Baghdad Battery', illustrated in figure 2.16, work and can produce voltages from 0.8 to nearly 2.0 V. Scientists assume that a common food acid such as lemon juice, wine or vinegar could have served as electrolyte.

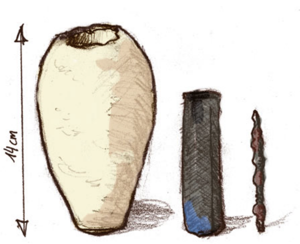

Figure 2.16.: Baghdad Battery with Copper Cylinder and Iron Rod [68]

The first successful scientific examination of electricity in the modern sense was undertaken by the American polymath Benjamin Franklin in 1749 nearly 30 years before the United States declaration of independence. He coined the term 'battery' by linking an array of capacitors with electricity. He used charged glass plates as capacitors. In 1780 the Italian physician and physicist Luigi Galvani discovered 'animal electricity' by twitching a frog's leg, which was affixed by a brass hook, with his iron scalpel. It took his friend Alessandro Volta more than 10 years to prove Galvani wrong. Volta argued that the mysterious twitching of the frog's leg was caused by two different metals joined together by a moist intermediary instead. In order to verify his hypothesis, Volta built an arrangement of pairs of copper and zinc discs stacked on top of each other. This is known as the voltaic pile (figure 2.17). He used a layer of cloth soaked in brine in order to separate the two metals. Thus, he identified the frog's leg in Galvani's case and the moist cloth in his own experiment as essential in order to produce continuous electric currents and voltages. Today, this separator is known as the electrolyte (see section 2.3.2). Volta continually improved his experimental setup and found that zinc and silver would give him the best results. He also sealed his pile to prevent acid electrolyte leakage. Still, his voltaic pile could only deliver an electric current for a relatively short period of time (up to one hour).

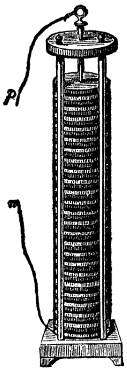

Figure 2.17.: Voltaic Pile [69]

In 1836 the Englishman John Daniell improved Volta's design significantly by introducing a second electrolyte. He used zinc ($ZnSO_4$) and copper sulphate ($CuSO_4$) to separate metallic zinc and copper. The role of the second electrolyte was to absorb the hydrogen (H_2) produced from the reaction with the first (aqueous) electrolyte. Before, hydrogen caused a steep increase in internal resistance. This would drastically reduce the lifespan of the voltaic pile. Consequently, the Daniell cell could deliver electric currents for prolonged periods of time. This led to the application of the Daniell cell in telegraphs, telephones and doorbells for more than 100 years.

Using the same basic principles of electrochemistry as for batteries, the Welsh physicist William Grove developed the first fuel cell in 1839. It combines oxygen (O_2) and hydrogen (H_2) in order to produce water (H_2O) and electricity via reverse electrolysis. Grove also came up with an improved battery design, using a zinc anode dipped in sulphuric acid (H_2SO_4) and a platinum cathode dipped in nitric acid (HNO_3). The Grove cell featured a porous earthenware to separate the two electrodes. Despite providing higher power than the Daniell cell, the Grove cell emitted poisonous nitric oxide (NO), which prevented its mass commercialisation.

Up to this point, the electrochemical reaction in the electrochemical cells were irreversible and thus non-rechargeable. These cells are referred to as primary cells. Only with the invention of the lead-acid battery by the Frenchmen Gaston Planté in 1859, electrochemical cells became rechargeable. Thus, lead-acid cells, which today are mainly used as starting, lighting and ignition (SLI) batteries in vehicles, were the first secondary cells. Their working principle is explained in the following subsection. The first lead-acid cells were struggling with reliability, which meant that primary cells continued to be the batteries of choice. During the 1860s the Frenchman Callaud patented an electrochemical cell similar to the Daniell cell. In comparison, it was less complex and featured a lower internal resistance. It was called the gravity cell, because zinc sulphate crystals would be separated from copper sulphate crystals in a glass jar by their different densities and the polarity of the cell.

In 1866 the French engineer Georges Leclanché invented the carbon-zinc cell. This cell provided a voltage of 1.4 V, but only for a relatively short period. Side reactions caused the internal resistance to rise. In the following years a lot of research effort went into developing a dry cell, because earlier cells with a moist electrolyte were leaking and also caused unwanted side reactions. These efforts were finally successful in 1886, when the German scientist Carl Gassner patented a dry variant of the Leclanché cell. Instead of a liquid electrolyte he used a paste based on gypsum plaster and ammonium chloride (NH_4Cl). Soon after in 1899, the Swedish scientist Waldemar Jungner came up with the first battery that was both dry and rechargeable. His nickel-cadmium (NiCd) battery was the first one to use nickel and alkaline electrodes. The first NiCd batteries were more reliable and featured a higher energy density than lead-acid batteries. The main disadvantage was their high price. Jungner also worked on a nickel-iron battery, but it produced hydrogen like early primary cells. Thomas Edison, the American inventor and businessman, sought to improve Jungner's nickel-iron battery in order to replace the relatively heavy and unreliable lead-acid batteries for electric vehicles.

Thanks to the creative work of the Canadian chemical engineer Lewis Urry alkaline batteries for the first time became cost competitive in 1959. He improved Jungner's work on alkaline batteries by implementing a manganese dioxide cathode and a powdered zinc anode. The first nickel-hydrogen battery was brought into service in 1977 for commercial communication satellites. Similar in design, nickel-metal hydride batteries (NiMH) entered the commercial market in 1989. NiMH batteries have a longer battery life and are considered to be more environmentally friendly than NiCd batteries [70]. Although early experiments with lithium batteries date back to the beginning of the 20th century, it was only in 1991 that Sony commercialised the first lithium-ion battery. The American chemist John Goodenough contributed the $LiCoO_2$ cathode [71], whereas the French scientist Rachid Yazami discovered the electrochemical intercalation of lithium into graphite on the anode side [72].

In 2009, the global battery market was worth $47.5 billion [73] and split according to figure 2.18. Primary batteries, which are mainly used in watches, remote controls and toys, made up less than a quarter of that. Their share is expected to further diminish in the future. Rechargeable lithium-ion batteries are the preferred choice for portable electronics like laptops

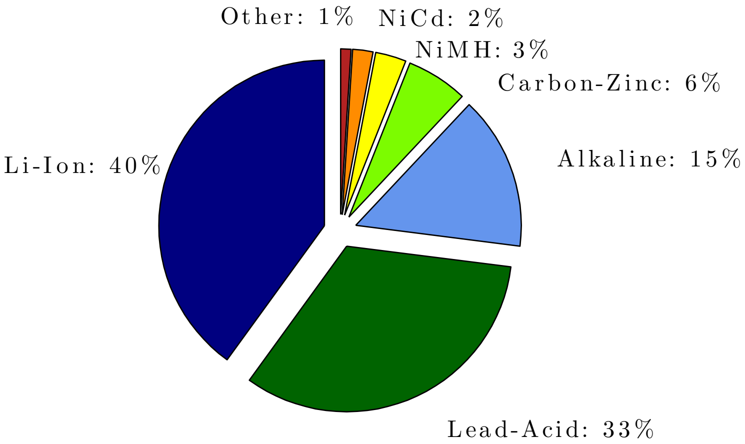

Figure 2.18.: Global Battery Market Share by Chemistry in 2009 [73]

and mobile phones, but also for EVs, PHEVs and HEVs. Lead-acid batteries are mainly used as SLI batteries in the automotive industry. Typically, batteries are available as coin (e.g. in watches), pouch (e.g. in cell phones), cylindrical (e.g. in laptops) and prismatic cells (e.g. in EVs).

Today's research efforts regarding batteries for electric vehicles mainly focus on improving their predictability, energy density, power density, cycle life, safety and cost effectiveness. This work aims to improve the long-term predictability of batteries for electric vehicles in order to suggest optimum battery capacities.

2.3.2. Fundamentals of Batteries

The following paragraphs explain the basic working principles of batteries, their main constituents, performance characteristics, degradation and the recycling thereof. This subsection deliberately ignores detailed electrochemistry. Readers interested in more electrochemical details of modern batteries are referred to [74]-[78].

Working Principle

An electrochemical cell converts chemical energy stored in its two electrodes into all-purpose electrical energy. The negative electrode (the anode) shown on the left-hand side in figure 2.19 is the reductant, i.e. it transfers electrons to the cathode during discharge while it is being oxidised. The positive electrode (the cathode) shown on the right-hand side is the oxidant, i.e. it gains electrons while it is being reduced. Consequently, there is a continuous oxidation-reduction (redox) reaction between the two electrodes. Primary cells cannot be recharged as their electrochemical reaction is irreversible. Secondary cells can restore the chemical energy by applying a charging current, which reverses the reaction [79]. In the case of lithium-ion cells, the working ion is Li^+. Lithium-type batteries take advantage of the so-called intercalation or insertion reaction,

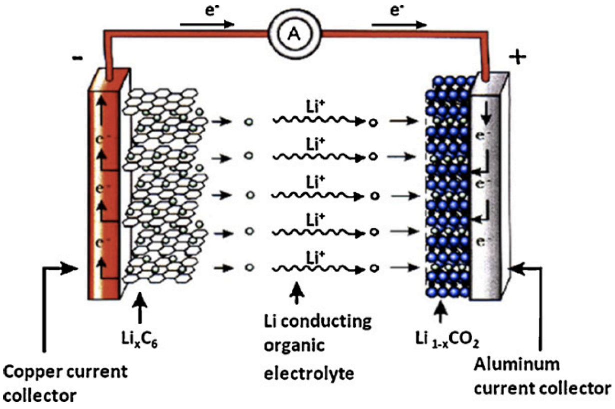

Figure 2.19.: Lithium-Ion Cell Schematic [12]

which means that lithium-ions can migrate into or out of the respective electrode [76]. Once an external load (A) is connected, the lithium-ions get extracted (de-intercalation) from the anode on the left hand-side, then move to the right hand-side and get inserted (intercalation) into the cathode. The reverse happens during the charging process. This alternating insertion and extraction process in lithium-type batteries led to them being dubbed '*rocking-chair*' batteries [80]. The solid layer, which is electrically insulating yet provides sufficient ionic conductivity, is referred to as the solid electrolyte interphase (SEI). To counterbalance the ion movement, electrons (e^-) flow from the anode to the cathode as well, and back when charging. When the battery is fully charged, there is a surplus of electrons on the anode giving it a negative charge and a deficit on the cathode giving it a positive charge resulting in a potential difference across the cell. This potential difference is called voltage or electromotive force (EMF). Contact resistances along the electrical circuit (internal resistances R_{int}), charge transfer resistances (R_{ct}) and diffusion resistances to the transfer of lithium-ions across the electrodes and through the electrolyte (R_{diff}) cause a voltage loss, the steady-state activation overpotential η. It is the difference of the electrochemical potentials of the electrodes or the open-circuit voltage V_{OC} and the terminal voltage V as illustrated in equation 2.2.

$$\eta(t) = I(t) \times (R_{diff}(t) + R_{int}(t) + R_{ct}(t)) = V_{OC}(t) - V(t) \tag{2.2}$$

Depending on the system's voltage and capacity requirements, several individual cells can be connected in a series or a parallel arrangement, or a combination of both in order to form a battery. The etymological roots of the word '*battery*' are French and in military terms refer to a coordinated group of artillery. Similarly, in electrical terms a battery describes a coordinated group of cells. A battery pack's voltage in a series arrangement is the sum of the individual cell voltages as illustrated in figure 2.20. In a parallel arrangement (shown in figure 2.21) in contrast, the individual cell voltages are the same as the total battery pack voltage. The total resistance in series networks is equal to the sum of the individual cell resistances. In parallel networks, the total resistance is the reciprocal of the sum of the individual cell resistance's reciprocals.

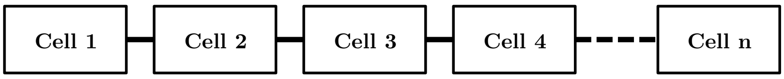

$$\begin{aligned} V_{tot} &= V_1 + V_2 + V_3 + V_4 + V_n \\ I_{tot} &= I_1 = I_2 = I_3 = I_4 = I_n \\ R_{tot} &= R_1 + R_2 + R_3 + R_4 + R_n \end{aligned} \tag{2.3}$$

Figure 2.20.: Series Cell Arrangement for a Battery

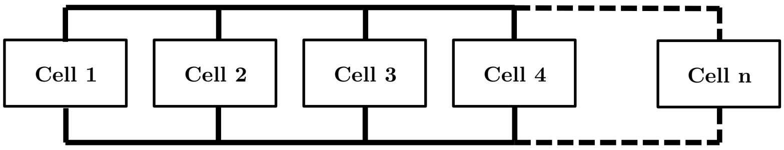

$$\begin{aligned} V_{tot} &= V_1 = V_2 = V_3 = V_4 = V_n \\ I_{tot} &= I_1 + I_2 + I_3 + I_4 + I_n \\ \frac{1}{R_{tot}} &= \frac{1}{R_1} + \frac{1}{R_2} + \frac{1}{R_3} + \frac{1}{R_4} + \frac{1}{R_n} \end{aligned} \tag{2.4}$$

Figure 2.21.: Parallel Cell Arrangement for a Battery

An alternative and more mechanical way of looking at a battery is via the electric-hydraulic analogy. The hydraulic analogy, first proposed by Oliver Heaviside in 1893 [81], facilitates the understanding of a battery from a mechanical engineering point of view. The hydraulic circuit shown in figure 2.22b is analogous to the electric circuit shown in figure 2.22a. Large tanks of water (A & B) contain potential energy. Thus, the hydraulic head between the two presents a varying pressure source.

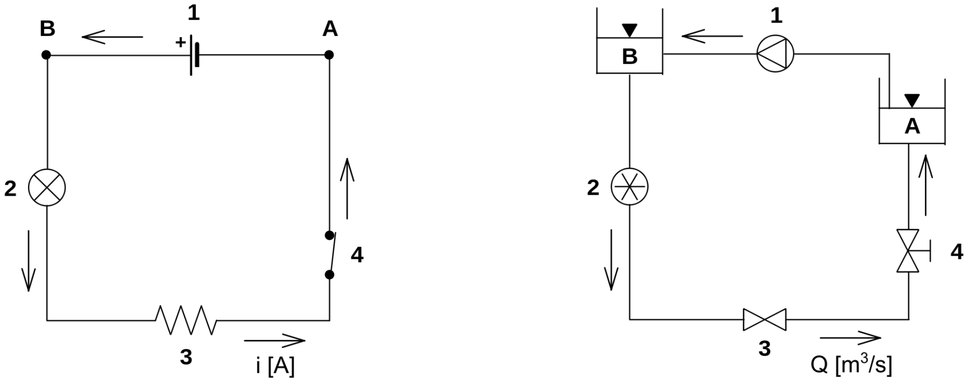

(a) Electric Circuit **(b) Hydraulic Circuit**

Figure 2.22.: Electric-Hydraulic Analogy [82]

In contrast, the ideal battery is supposed to be an ideal voltage source. This means that in theory it should deliver a constant voltage regardless of the current drawn. The hydraulic equivalent of the ideal voltage source/battery is a dynamic pump with feedback control in order to keep the pressure difference between A and B constant. Real-world battery behaviour is more complex and requires additional linear and non-linear effects to be factored in. This is addressed in the following paragraph and a selection of available battery models is introduced in section 2.3.4.

Table 2.2 lists important electric circuit elements and their hydraulic circuit equivalents. Most analogies including electric charge, electric potential, voltage, current and the wire are straightforward. The resistor and capacitor hydraulic equivalent however may need further explanation as they also describe important real-world battery behaviour.

Table 2.2.: Electric and Hydraulic Circuit Equivalents

Electric Circuit	**Description**	**Hydraulic Circuit**
Electric Charge [C]	Similar to magnetic charge, it causes a force when exposed to electrically charged matter.	Quantity of water [m^3]
Electric Potential [V]	Electric potential energy.	Hydraulic head [Pa]
Voltage [V]	Refers to the *potential difference* between two points, usually with the ground as reference.	Pressure difference [ΔPa]
Current [A]	Flow of electric charge through a conductive medium.	Volumetric flow rate [m^3/s]
Wire	Conductive, i.e. electrically non-insulating charge transfer medium.	Simple pipe completely filled with water.
Resistor	Causes electrical resistance R measured in Ohm [Ω].	Simple pipe with constricted cross-section.
Capacitor	Characterised by its capacitance (C) measured in [F], it stores energy in an electric field.	Rubber diaphragm sealed inside a pipe.

Electrical resistance (R) describes the opposition of an electrical element (resistor) to the transfer of electric current though it. As mentioned earlier (equation 2.2), resistances inside the electrochemical cell cause the voltage to drop from the open-circuit voltage to the terminal voltage. The hydraulic equivalent of electrical resistance is a simple straight pipe with a constricted cross section like in a venturi meter. The restriction of the flow results in a pressure drop of the system.

Capacitance describes the ability of an element to store electrical charge (capacity) Q. In other words, it is the charge a capacitor will accept for the potential across it to increase by 1 V. Electric charge causes a force (EMF) when exposed to electrically charged matter and is measured in Coulomb [1 C = 1 As], although the use of ampere-hour [Ah] is more common when referring to batteries. Capacitance C on the contrary is measured in Farad [$1\ \mathrm{F} = 1\ \frac{\mathrm{C}}{\mathrm{V}} = 1\ \frac{\mathrm{As}}{\mathrm{V}}$]. Any element that is capable of being charged with electricity exhibits capacitance. Thus, any electrochemical cell also features capacitative attributes. A capacitor is an electrical component that stores energy in an electric field.

The hydraulic equivalent of a capacitor is a flexible and impermeable rubber diaphragm sealed inside a straight pipe. Energy is stored by the bi-directional stretching of the diaphragm. When the flow rate (current) increases, the back pressure on the rubber (voltage) increases as well. Consequently, current leads voltage in a capacitor. Also, as the back pressure reaches the limiting value of the applied pressure, the flow rate is reduced. This leads to the diaphragm acting like a filter. Constant low-frequency pressure differences (low changing voltages) are filtered out while high-frequency varying pressure differences (high changing voltages) are passed on to the next stage in the circuit. This is analogous to the capacitor being charged and discharged by the flow of current and explains its relatively high power as well as its relatively low energy density compared with other electrochemical energy storage devices (see figure 2.26).

Ideal vs. Real Battery Behaviour

In the ideal case, as mentioned before, the battery acts as an ideal voltage source keeping a constant voltage during discharge. Only after having consumed all available energy, i.e. when the state of charge is equal to zero, there is an instantaneous voltage drop to zero in this hypothetical case. In crude terms, the state of charge (SOC) is a measure of the charge level still left in the battery. More precisely, it is the ratio between the available battery capacity Q_{bat} after time t and the original capacity $Q_{bat,0}$ at $t = 0$ as shown in equation 2.5.

$$SOC(t) = 100\frac{Q_{bat}(t)}{Q_{bat,0}} \qquad [\%] \tag{2.5}$$

Also, the ideal battery capacity would be constant for all discharge rates [83].

Real battery behaviour is more complex and differs significantly regarding various aspects. First, real battery cell voltage drops slowly during discharge. Second, the effective capacity is lower for high discharge rates compared with low discharge rates. This means that when the battery is discharged faster, the total capacity is reduced, because the lower voltage limit is reached earlier. The *capacity rate effect* is illustrated in figure 2.23. Third, the battery can

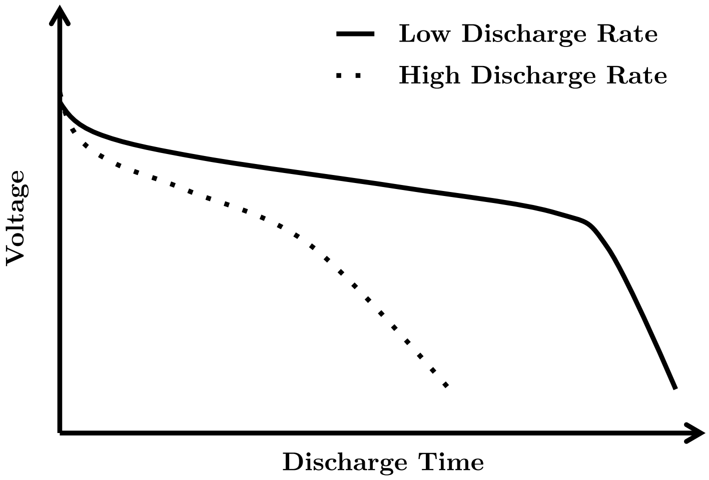

Figure 2.23.: Capacity Rate Effect

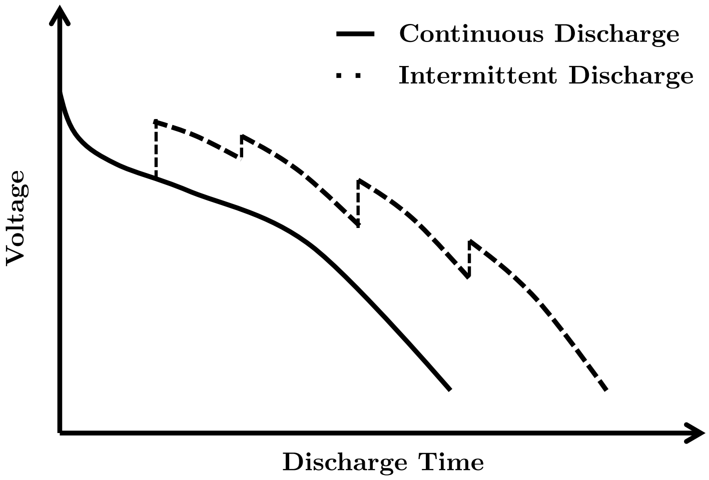

Figure 2.24.: Voltage Relaxation Effect

'recover' some capacity during periods of very low currents or when no current is drawn at all. Usually this happens when a period of high discharge rates is followed by a sustained period of very low or zero current draw. The *voltage relaxation effect* can be observed in figure 2.24. Additionally, polarisation, corrosion and passivation phenomena occur in electrochemical cells. Polarisation refers to the depletion of reactants (electrons and ions) leading to a voltage drop. Corrosion is the successive destruction of materials in general by chemical (redox) reaction with its environment. Passivation describes the process of the active materials becoming '*passive*', i.e. becoming less affected by environmental factors. With varying extents these effects can be observed in all practical battery types [83]. The modelling approaches presented in section 2.3.4 to varying degrees accommodate for them.

Constituents and Performance Characteristics

Any electrochemical cell features three main constituents: anode, cathode and the electrolyte. Differences between cell types only arise from varying electrode and electrolyte materials. These materials are typically selected for their voltage, charge capacity, conductivity, weight, cost, reactivity with other components, longevity, ease of handling, ease of manufacturing, etc. [74]. In the case of an electric vehicle traction battery this means combining the individual materials in order to achieve a maximum specific power density, a maximum specific energy density, a maximum volumetric energy density with a maximum cycle life without sacrificing inherent safety at minimum costs.

Figure 2.25 shows the standard periodic table of elements with general trends of electron affinity. Reducing agents have surplus electrons in their outer molecular shell, which they donate in a redox reaction and thus become oxidised. Consequently, elements on the left hand-side in figure 2.25 tend to qualify for good anode materials. Oxidising agents have a deficit of electrons in their outer molecular shell. Thus, they accept electrons in the redox reaction and

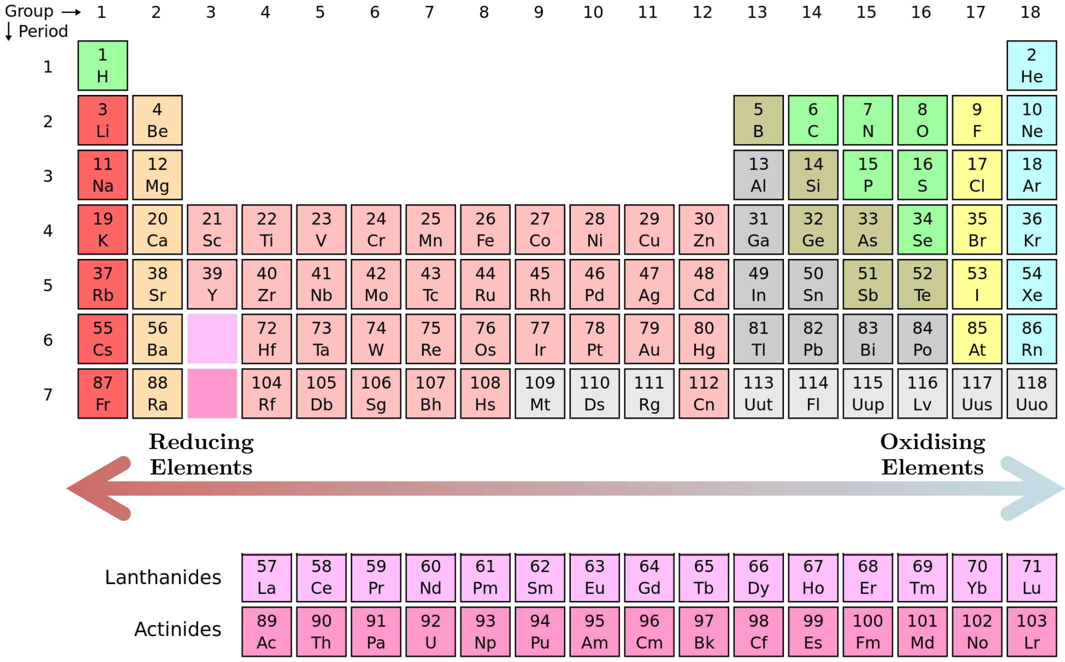

Figure 2.25.: Peridodic Table of Elements (adapted from [84])

become reduced. They tend to be on the right hand-side of the periodic table. The strongest reducing agent, i.e. the one with the lowest standard electrode potential E^0 is lithium (Li). The strongest oxidising agent, i.e. the one with the greatest standard electrode potential is fluorine (F). Practically, however, not any potential reducing agent can be combined with any oxidising agent. Not all electrode pairs can react reversibly, i.e. they cannot be used for rechargeable batteries. Also, strong reducing/oxidising agents are highly reactive and thus tend to undergo undesirable side reactions which lead to increased cell degradation. Electrolyte materials vary greatly among cell types and depend upon the electrode materials chosen.

Table 2.3 lists some practically feasible and commercially viable combinations of anode and cathode materials as of 2013 in order to form rechargeable cells. The table also depicts practical properties that are relevant for any electric vehicle traction battery. Even though sodium type batteries feature a relatively high energy density fabricated from inexpensive materials, their high operating temperature (300-350 ℃) only allows for stationary applications. Lead acid batteries are still dominating as SLI batteries in vehicles despite their relatively low specific and volumetric energy densities. This is because of their ability to provide high surge currents at very low costs. Nickel-type batteries have the lowest nominal voltage, whereas the three lithium-type batteries have the highest nominal voltage thanks to lithium being the the strongest reductant (-3.01 V vs. standard hydrogen electrode) in the periodic table [86]. Cell voltages for lithium-ion type batteries are larger than the potential at which standard aqueous electrolytes can electrolyse. Additionally, lithium is highly reactive to water. Consequently, non-aqueous

Table 2.3.: Rechargeable Battery Chemistries and Practical Properties ([74, 76, 77, 85])

Cell Type	Anode	Cathode	Nominal Voltage [V]	Specific Energy [Wh/kg]	Energy Density [Wh/L]
Alkaline	Zn	MnO_2	1.5	85	250
Lead-acid	Pb	PbO_2	2.0	35	70
Lithium cobalt oxide ($LiCoO_2$)	Graphite	$LiCoO_2$	3.7	250	630
Lithium manganese oxide (spinel)	Graphite	$LiMn_2O_4$	3.9	150	420
Lithium iron phosphate ($LiFePO_4$)	Graphite	$LiFePO_4$	3.3	90-150	333
Nickel-cadmium (NiCd)	Cd	Ni oxide	1.2	35	100
Nickel-metal hydride (NiMH)	MH	Ni oxide	1.2	75	240
Nickel-zinc (NiZn)	Zn	Ni oxide	1.6	60	120
Sodium-nickel chloride	Na	$NiCl_2$	2.6	115	190
Sodium-sulfur	Na	S	2.0	170	345

electrolyte solutions are used for lithium-ion type batteries. These include liquid electrolytes like lithium salts in an organic solvent. A high nominal battery voltage for an electric vehicle is not only required from an energy/power density point of view. In addition, high nominal voltages make sure that at a low state of charge (SOC), the battery can still deliver sufficient power.

Lithium-type batteries have the highest specific energy with up to 250 Wh/kg, because of lithium being the lightest (6.94 g/mol) metal. This makes them an attractive choice for portable consumer electronics including mobile phones and laptops, but also for power tools. Because of its relative maturity $LiCoO_2$ has been the preferred cathode material for these applications for the past decade. Lead-acid and NiCd batteries have the lowest energy density compared with lithium-type batteries, which demonstrate the highest energy density.

Overall, the best performance characteristics relevant for electric vehicle applications are demonstrated by the lithium-type batteries. By examining table 2.3 the lithium-polymer battery ($LiCoO_2$) seems to be the ideal EV traction battery. However, lithium-cobalt-oxide ($LiCoO_2$) is relatively rare, expensive, partially toxic and thermally unstable. That is why lithium iron phosphate ($LiFePO_4$) and lithium manganese oxide ($LiMn_2O_4$) are seen as its ideal substitute in the near- to medium-term future [12]. The biggest drawback of $LiMn_2O_4$ batteries is manganese dissolution into the electrolyte during cycling, especially at temperatures above ambient [87]. This results in a relatively poor cycle life of $LiMn_2O_4$ as illustrated by figure 2.28. Despite these disadvantages NISSAN uses this technology for its all-electric '*Leaf*'. As a cathode material $LiFePO_4$ is considered to be safer and cheaper than both $LiCoO_2$ and $LiMn_2O_4$. Its main disadvantage is its relatively low specific energy and its relatively low energy density compared with the other lithium-type batteries.

In 1995 Abraham & Jiang first proposed the design of a lithium-air cell [88]. This technology offers practical specific energies of up to 1,000 Wh/kg, which is still more than one order of magnitude below the specific energy of diesel (12,663 Wh/kg [31]) or petrol (13,083 Wh/kg [31]).

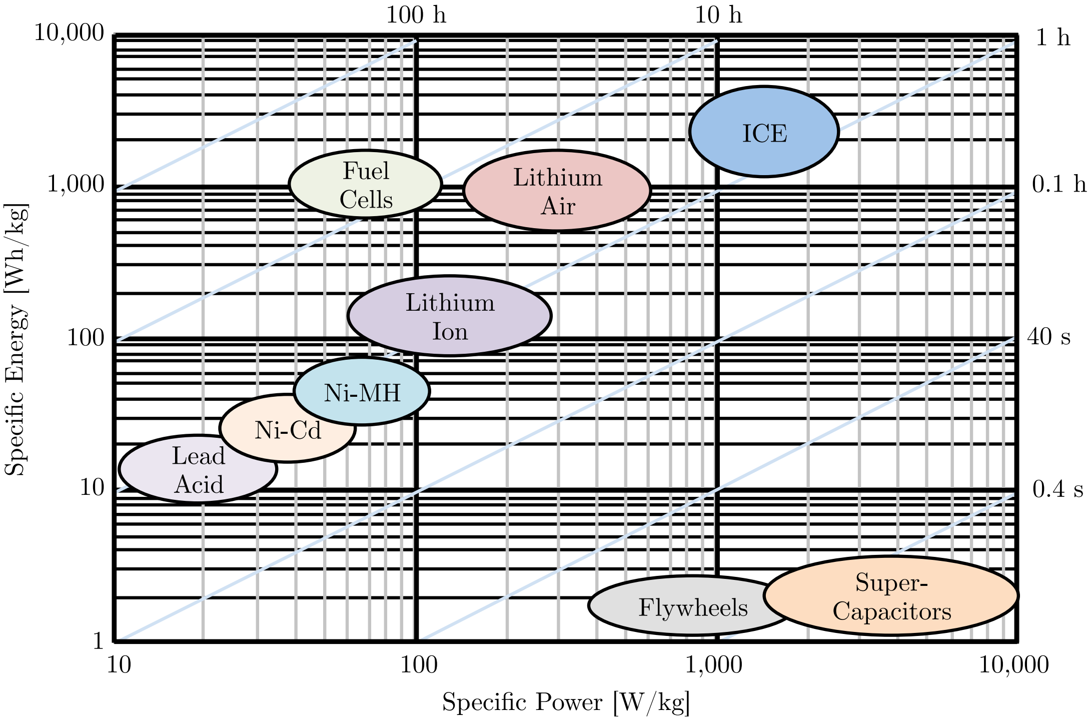

Figure 2.26.: Ragone Plot (adapted from [89])

Also, there are still many challenges to overcome, '*from designing their cathode structure, to optimizing their electrolyte compositions and elucidating the complex chemical reactions that occur during charge and discharge*' before these cells can be realized as high performance, commercially viable products [89]. Figure 2.26 puts into perspective specific powers as well as specific energies for different practical energy storage/conversion options. The diagonal lines indicate discharge times, with high discharge rates displayed at the bottom right corner of the so-called Ragone plot. It shows that the internal combustion engine still features the best combination of power and energy per unit mass, which explains the existing prevalence of ICEVs.

However, battery technology has improved over time and currently lithium-type batteries promise to become the most effective and efficient energy storage systems (ESS). Still, this requires breakthroughs regarding innovative chemistries for both the electrode and electrolyte components. These must overcome low specific energies and powers, limited temperature ranges and degradation effects. Some current and future potential materials are listed in figure 2.27.

Recycling

Recycling refers to the processing of used materials (waste) into new products. There are several drivers for recycling including the prevention of wasting potentially useful materials, the reduction of the consumption of fresh raw materials, the reduction of waste and the reduction of pollution from landfill or incineration. Battery recycling in particular is topical as they

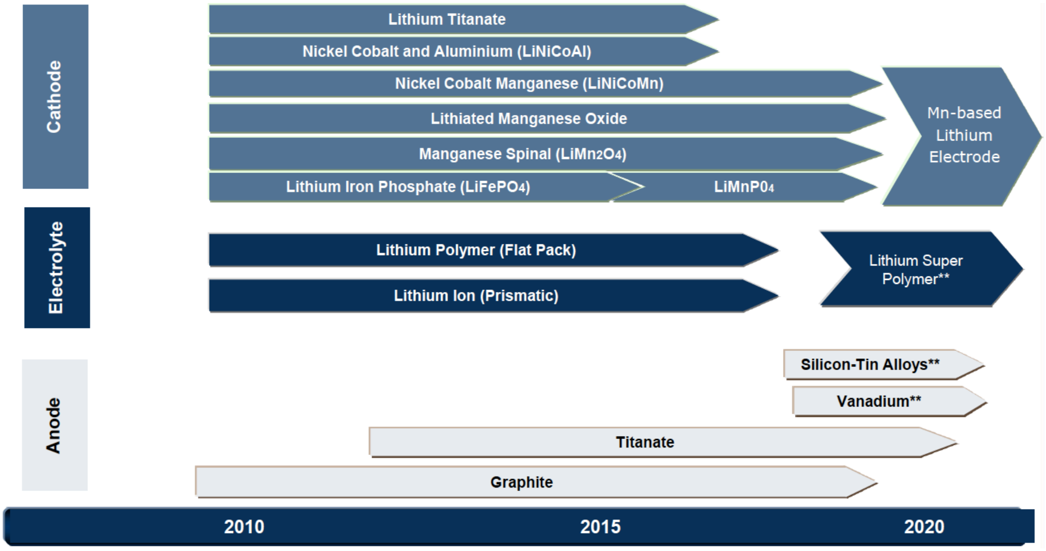
Cathode
Electrolyte
Anode
Lithium Titanate
Nickel Cobalt and Aluminium (LiNiCoAl)
Nickel Cobalt Manganese (LiNiCoMn)
Lithiated Manganese Oxide
Manganese Spinal (LiMn2O4)
Lithium Iron Phosphate (LiFePO4)
LiMnP04
Mn-based Lithium Electrode
Lithium Polymer (Flat Pack)
Lithium Ion (Prismatic)
Lithium Super Polymer**
Silicon-Tin Alloys**
Vanadium**
Titanate
Graphite
2010
2015
2020

Figure 2.27.: Lithium-Ion Battery Chemistry Roadmap [90] (in development)**

contain a number of heavy metals and toxic chemicals. Lead acid batteries are recycled by first grinding them, neutralising the acid and separating the polymers from the lead [91]. Modern lead acid factories can recover enough lead from one recycled SLI battery in order to manufacture one new one thanks to improved recycling and battery technology. Recycling of lithium-type batteries is not as common as lead acid battery recycling but nevertheless possible. Vacuum distillation facilitates the recovery of nickel-containing iron, ferro-manganese, cobalt and copper when lithium is being used as reductant [92].

2.3.3. Battery Degradation

The cycle life of an electric vehicle traction battery is based on the cumulative number of charge/discharge cycles during which the battery is capable of retaining at least 80% of its original capacity $Q_{bat,0}$ measured in ampere-hours [Ah]. Alongside specific energy, energy density, specific power, safety, recyclability and cost, the cycle life is one of the most important features of a traction battery for EVs. Due to degradation and ageing the cycle life of a battery cell is limited. Today's ICEVs are designed for a lifetime of around ten years and a service life of 100,000-250,000 km [13]. In order to be competitive EVs must reach similar values. In terms of a battery cycle life, this roughly equates to 150-1,700 cycles depending on the individual battery's capacity and charging/driving behaviour.

Degradation and ageing describe electrochemical phenomena, which modify a cell's inherent properties with time and use. Because of the relatively large variety of lithium-ion cells and thus the relative large number of ageing reactions likely to occur, it is almost impossible to give an exhaustive picture of all degradation mechanisms [93]. This work focuses on the physical consequences of degradation and ageing in lithium-ion batteries with regards to battery sizing rather than on the electrochemical processes. The three most problematic symptoms of a degraded cell are capacity loss, power loss and loss of integrity (i.e. cell damage or leakage) [34], which are explained in the following.

Capacity Fade

The capacity of a battery cell Q_{bat} is a measure of the maximum constant current I_{max} that a new cell can supply for 20 hours at 20 ℃. Typically, the capacity for an entire battery pack of an EV is expressed in kilowatt-hours (kWh), which is the ampere-hour rating multiplied by the nominal voltage V_{nom} of the entire battery pack. Capacity loss in a cell and consequently in a battery pack can result from irreversible loss of recyclable and electrochemically active lithium, referred to as de-lithiation [94]. This can result from both cycling and resting (self-discharge). With cumulative cycles the solid electrolyte interphase (SEI) layer between the functional graphite at the anode and the electrolyte can grow due to side reactions which consume active Li^+ [93]. Additionally, capacity loss can be caused by the ageing, transformation or reaction of non-active materials like for instance binders, conductors and current collectors as well as by mechanical modification of the composite electrode structure due to volume changes during cycling. A rise in impedance, which is the AC circuit equivalent to resistance R explained in the previous section (2.3.2), indicates this capacity loss. Capacity loss for an EV traction battery, which is also referred to as capacity fade, is exhibited in figure 2.28. The figure shows the typical cycling behaviour of $LiMn_2O_4$ cells used by Nissan for their all-electric LEAF model. Nissan assumes an annual mileage of about 20,000 km (12,500 mi), which according to their claimed range (76-169 km) translates into 119-265 cycles per year. Thus, after 5 years and only about 595-1325 cycles their battery has already lost about 20% of its initial capacity. The figure demonstrates that with an increasing operating/cycle life the capacity decreases. However, the capacity fade rate decreases with an increasing number of cycles. This is in accordance with the theory of a growing SEI layer that consumes active Li^+ during cycling. In exceptional circumstances, with

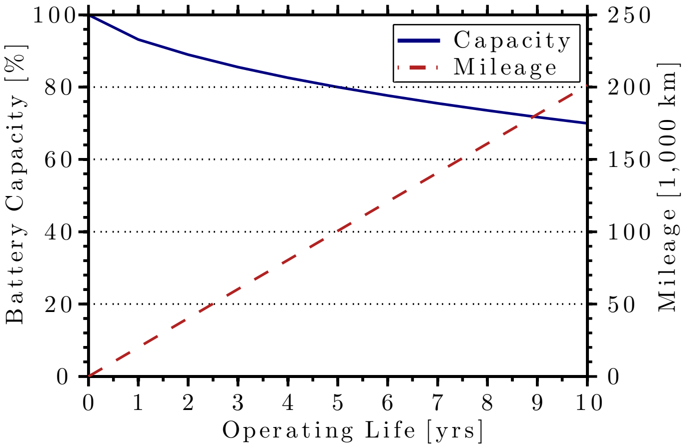

Figure 2.28.: Nissan Leaf Battery Capacity Fade (adapted from [95])

an increasing number of cycles the capacity fade rate may also increase. This can happen when Li^+ starts to plate significantly [93]. Lithium plating is the surface covering of the electrode material with Li^+. This causes the Li^+ to become inactive, the electrode surfaces to clog and ultimately the electrode surfaces to lose porosity. Lithium plating is assumed to be very temperature sensitive with low temperatures encouraging the capacity fading rate [93]. On the other hand, moderately low temperatures allow for high local current densities. Thus, there is a trade-off between moderately low operating temperatures allowing for high local current densities and moderately high operating temperatures avoiding lithium plating. For lithium-ion batteries temperatures above 30 ℃ are considered to be high and temperatures below 10 ℃ are referred to be low. The basic Arrhenius law for chemical reactions in equation 2.6 underlines the temperature dependence of chemical reactions.

$$r = A_a e^{-\frac{E_a}{\bar{R}T}} \tag{2.6}$$

All else being equal, the speed of any chemical reaction (rate constant) r increases with an increasing temperature T. A_a is the pre-exponential Arrhenius factor, E_a the activation energy and $\bar{R}$ the universal gas constant. Consequently, for chemical reactions like those occurring at room temperature in lithium-ion cells, the reaction rate doubles for every 10 ℃ increase in temperature. This means that electrical conductivity as well as ionic diffusivity is greatly enhanced at higher temperatures, which results in high power availability at high temperatures. At the same time, reversible side reactions are also encouraged by high temperatures which promote degradation [96]. At the upper extreme the active chemicals may break down.

This leads to the conclusion that moderately high temperatures are generally more favourable than low temperatures for the capacity retention of lithium-ion batteries provided that high temperature operation is not continuous throughout. In addition, the capacity of a battery pack is believed to be better retained at low depths of discharge (DOD). The relation between the state of charge (SOC) and depth of discharge (DOD) is illustrated in equation 2.7.

$$DOD(t) = 100 - SOC(t) \qquad [\%] \tag{2.7}$$

The DOD describes the discharged capacity divided by the original capacity. Usually the maximum recommended DOD for lithium-ion batteries before recharging is 80-90% in order to limit capacity fade. EVs may provide electricity not only for vehicle use, but also for vehicle-to-grid (V2G) services. The idea is that electric vehicle traction batteries 'communicate' with the power grid and deliver electricity or reduce their charging rate in order to level the power grid. It is suggested that V2G energy incurs approximately half the capacity loss per unit energy processed compared to that of regular vehicle use [97]. The disadvantage is that with V2G the processed energy is higher and thus degradation with respect to the car's mileage is increased.

Several authors ([93],[94] & [96]) agree that lithium-ion cells degrade in response to capacity (Ah) processed. However, the exact correlation is not known and depends on several other factors as well. 100 Ah for instance can be consumed very quickly in a moderate temperature environment or very slowly in a hot temperature environment. The exact difference between the two regarding capacity fade is yet to be established. In terms of the hydraulic analogy, the effect of capacity fade can be compared to that of a leak in the system, which accumulates (unusable) water with time. It follows that the capacity fade Q_{loss} is some function of time t (self-discharge), capacity processed $\int_0^t I(t)dt$, rate of charge/discharge $\frac{dI}{dt}$ and temperature T as illustrated in equation 2.8.

$$Q_{loss} = f(t, \int_0^t I(t)\,dt, \frac{dI}{dt}, T) \tag{2.8}$$

Power Fade

The second problematic symptom of a degraded and an aged battery cell is power loss. The maximum power P_{max} of a cell is measured in watts [W] or kilowatts [kW], which is the product of the nominal voltage V_{nom} and the maximum current I_{max}. The main sources for power fade are an increased resistance due to the growth of the SEI layer and an increased electrolyte resistance [98]. Like with any other electrochemical cell, lithium-ion cells have a limited maximum discharge current I_{max} increasing with temperature. The maximum current I_{max} also limits the maximum power output P_{max}. Battery manufacturers use the so-called 'C-rate' to categorise the rate of charge/discharge currents. Most batteries are rated at 1 C and can take up to 20 C impulse currents. Ignoring the capacity rate effect, this means that a 100 Ah battery would provide 100 A for one hour if discharged at 1 C rate. The same battery discharged at 0.5 C would provide 50 A for two hours. At 2 C, the 100 Ah battery would deliver 200 A in half an hour. Going beyond the maximum current may lead to serious degradation and even damage. The maximum current is limited by the discharge resistance R_{dis} which increases with cycle number and a lower temperature.

Zhang et al. conclude that power fade at low temperatures rather than capacity fade is the more serious performance limitation of $LiFePO_4$ cells [98]. Also, the discharge resistance slowly increases with the duration of the applied current. They found that electronic resistance of electrode particles is dominant in the discharge resistance for a fresh cell whereas increasing electrolyte resistance is dominant after considerable cycling resulting from lithium loss. Broussely et al. suggest that power loss is directly related to impedance growth as well and that this can be overcome by doping [93]. Doping in this context is adding impurities into the electrodes in order to change their electrical properties. Consequently, power fade P_{loss} is very closely related to capacity fade, but with a stronger dependence on resistance. The effect of power fade can be compared to that of fouling in hydraulic systems, whereby the flow of water is increasingly impeded by the build-up of a growing layer inside the pipes (compare with table 2.2). Hence, power fade P_{loss} is some function of the battery's resistance R, which in turn is also some function of time t (self-discharge), capacity processed $\int_0^t I(t)dt$, rate of charge/discharge

$\frac{dI}{dt}$ and temperature T as illustrated in equation 2.9.

$$P_{loss} = f(R(t, \int_0^t I(t)\,dt, \frac{dI}{dt}, T)) \tag{2.9}$$

Cell Disintegration

The third problematic symptom of a degraded and an aged battery cell is loss of integrity of the cell. This means that the battery cell is suffering from severe damage or leakage due to cycling. Loss of integrity is usually caused exclusively by cycling and not by resting. Cycling adds kinetically induced effects such as volume variations through swelling or contraction of the electrodes. Concentration gradients of Li^+ may also have a similar effect. These effects may lead to severe damage or leakage. Blaiszik et al. claim that a cell's anode, which swells while charging and then shrinks during discharge, can eventually crack and thus lead to its disintegration [99]. Overcharging can also lead to severe damage of Li-ion batteries [100]. In hydraulic terms cell disintegration can be compared with the bursting of a pipe leaving the system unable to function anymore. Cell disintegration $Cell_{dis}$ is primarily a function of capacity processed $\int_0^t I(t)dt$ and the rate of charge/discharge $\frac{dI}{dt}$ as exemplified by equation 2.10.

$$Cell_{dis} = f(\int_0^t I(t)\,\mathrm{d}t, \frac{\mathrm{d}I}{\mathrm{d}t}) \tag{2.10}$$

Extreme operating conditions can lead to thermal runaway and thus to disintegration of a battery as shown by the Boeing 787 lithium battery fire incidents in early 2013. More detailed information on battery failure modes and their prevention mechanisms can be found in [101].

2.3.4. Modelling of Batteries

Like vehicle simulations, battery simulations can be categorised according to their accuracy. However, the direction of battery models, which are relevant for EVs, is the same. As explained in section 2.2.3, EV traction battery models work out the battery's power output given the requested power. Hence, they are backward-facing. Figure 2.29 illustrates this modelling logic, which forms the basis of the following paragraphs.

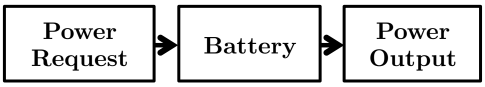

Figure 2.29.: Battery Modelling Logic

The modelling of batteries goes back to the first academic thoughts on electricity by Volta (see section 2.3.1). However, the wide variety of electrochemical cells, their various parameters and their inherent complexity make it very difficult to model batteries. The following paragraphs present an overview and a critical appraisal of the currently available and most popular software models for batteries. They mainly include analytical models, electrochemical models, equivalent circuit models and thermal models.

Analytical Modelling

The Shepherd equation is probably the best known and most simplistic battery model. The equation describes the electrochemical behaviour of the battery directly in terms of voltage and current [102]:

$$V(t) = V_{OC} - R_{pol} I(t) \left(\frac{1}{1 - SOC(t)} \right) - R_{int} I(t) \tag{2.11}$$

The Shepherd equation extends the model for the overpotential η introduced with equation 2.2. According to the Shepherd model, the terminal voltage V is obtained by subtracting the polarisation loss V_{pol} and the voltage loss caused by internal resistance R_{int} from the open circuit voltage V_{OC}. Shepherd refers to the SOC in the same way as defined in equation 2.5. The model accounts for an increase in polarisation resistance with a decreasing SOC. The Shepherd model is often used in conjunction with Peukert's law, which expresses the capacity of a lead-acid battery in terms of the rate at which it is discharged [55].

$$Q_{bat}(t) = I(t)^k t \tag{2.12}$$

For constant discharge rates the Peukert constant k accounts for the capacity rate effect. Peukert's law can also be applied to Li-ion batteries when making sure that both the ambient temperature and the discharge current is held constant [103]. It is applied in the JANUS vehicle simulation.

The major advantages associated with analytical battery models are as follows:

- Mathematically simple
- Computationally easy to implement

The major disadvantages of analytical battery models:

- Only valid for constant discharge currents
- Very inaccurate

Electrochemical Modelling

Electrochemical cell modelling refers to the modelling of batteries from a very detailed chemical perspective. Ion and electron transfer processes are described in great detail. Consequently, these models are very accurate, highly complex, difficult to configure and usually require high processing power.

In [104]-[106], Doyle, Fuller & Newman from the University of California, Berkeley, have developed the most popular electrochemical model for lithium-ion batteries. Their model, which they refer to as '*dualfoil*', is also available as a FORTRAN software download from [107]. The model inputs include more than 60 battery parameters like diffusion coefficients, electronic conductivities, and the entropy of reaction for the cell. Six coupled and non-linear differential equations take these inputs in order to solve for various outputs. Amongst other outputs, dualfoil very accurately predicts heat and entropy generation, voltage and current values as a function of time. With heat and entropy values one can work out losses and long term degradation.

Other electrochemical models that also consider degradation include crack propagation models [108], porous electrodes and concentrated solution models [75], single particle models [109], lumped parameter lithium-ion models [110] and lithium corrosion kinetic models [111]. They are similar in their nature compared to the dualfoil model, but often concentrate on one very specific aspect. The dualfoil model in contrast is probably one of the most comprehensive electrochemical models as it is being used as reference model for its accuracy. Therefore, the dualfoil model is regarded as the state of the art of battery modelling. It is estimated that even more detailed electrochemical models, which lead to a better understanding and thus better handling of batteries, can reduce the costs of batteries by 25% and cut recharging times in half [112].

To summarise, these are the main advantages of electrochemical battery models:

- Very accurate
- Large set of output variables e.g. heat and entropy generation

On the other hand, there are also significant disadvantages associated with electrochemical models:

- Difficult to configure
- Require high computer processing power
- Require detailed knowledge about electrochemistry
- Cannot be performed in real-time
- Poor robustness under extrapolation conditions

Equivalent Circuit Modelling

Equivalent circuit battery models are lumped parameter models putting together relatively few individual circuit elements in order to form an equivalent circuit. This is the same approach as with the hydraulic analogy (see section 2.3.2), however focussing on electrical circuit elements. These circuits obey the laws of series and parallel networks explained in equations 2.3 and 2.4. Table 2.4 lists the most important equivalent circuit elements and their respective physical meaning. They include a capacitor, a resistor, a voltage source and a wire. In [113], Hu, Li &

Table 2.4.: Equivalent Circuit Elements and Their Physical Meaning

Circuit Element	Description	Symbol
Capacitor	Represents the capacity Q_{bat} in amp-hours [Ah] of battery	
Resistor	Stands for the various battery's resistances R in [Ω]	
Voltage Source	Usually represents the open circuit voltage V_{OC}	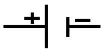
Wire	Describes the ion/electron transfer without losses	—

Peng give a very good overview of equivalent circuit models for Li-ion batteries. In the following, four of the most widely used equivalent circuit models for batteries are presented.

The **Internal Resistance Model** shown in figure 2.30 simply combines an ideal voltage source in series with a resistor, representing the internal resistance of the battery. Both the internal resistance R_{int} and the open-circuit voltage R_{OC} are usually modelled as functions of SOC only. Additionally, they can be modelled as a function of temperature as well. The current I has a positive value during discharge and a negative one during charge. The terminal voltage V is plainly the difference between V_{OC} and the voltage drop due to internal resistance as expressed in equation 2.13. The internal resistance model is included in the ADVISOR energy storage <ess> library (see figure 2.14) [114].

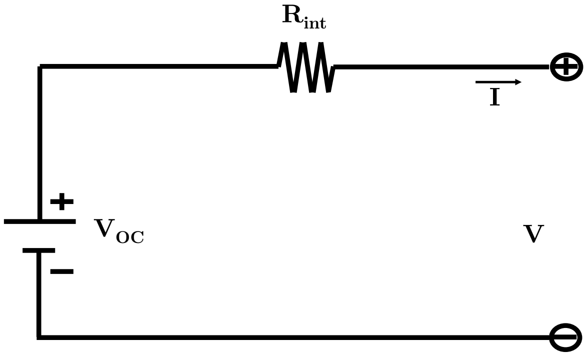

$$V(t) = V_{OC} - R_{int} I(t) \tag{2.13}$$

Figure 2.30.: Internal Resistance Model

The **Thévenin Model** extends the simple internal resistance model by adding an additional resistor placed in parallel with a capacitor. The additional resistance R_{pol} represents polarisation resistance. The capacitance induced by the extra capacitor is representative of the transient effects [115], which can be compared to that of a sealed diaphragm in a closed hydraulic system (see section 2.3.2). Equations 2.14-2.15 summarise the electrical responses. The physical meaning of the resistance R_{pol} placed in parallel with the capacitance C_{Th}, also referred to as RC ladder, is explained in figure 2.32. Electrochemical impedance spectroscopy (EIS) is a means

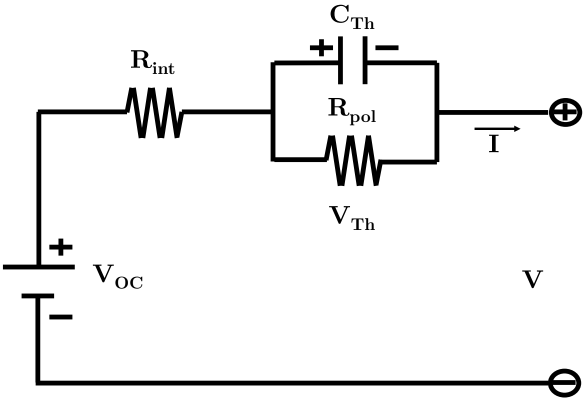

$$\dot{V}_{Th}(t) = -\frac{V_{Th}}{R_{pol}C_{Th}} + \frac{I(t)}{C_{Th}} \tag{2.14}$$

$$V(t) = V_{OC} - V_{Th} - R_{int}I(t) \tag{2.15}$$

Figure 2.31.: Thévenin Model

of measuring polarisation (impedance) as a function of frequency ω for electrochemical devices such as batteries. The figure shows negative imaginary impedance on the y-axis versus real impedance (resistance) on the x-axis. The frequency is increasing to the left on figure 2.32. The three parameters R_{int}, R_{pol} and C_{Th} from figure 2.31 can be identified in figure 2.32.

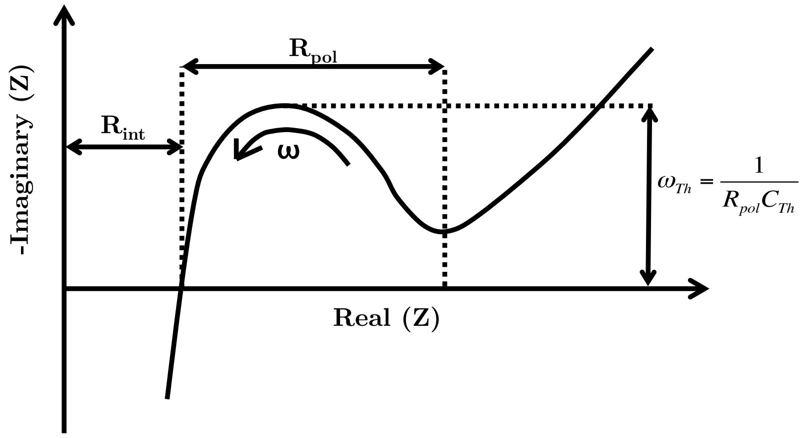

Figure 2.32.: Battery Electrochemical Impedance Spectroscopy (EIS) Schematic

The US Partnership for a New Generation of Vehicles (PNGV), which was cancelled in 2001 (see section 2.2.1), has extended the Thévenin model by adding a capacitor in series with the internal resistance R_{int} (see figure 2.33). The additional element in the **PNGV Model** adjusts the open-circuit voltage V_{OC} according to the current drawn. It also forms part of the ADVISOR library [114].

The **Resistor Capacitor (RC) Model** illustrated in figure 2.34 was first developed by

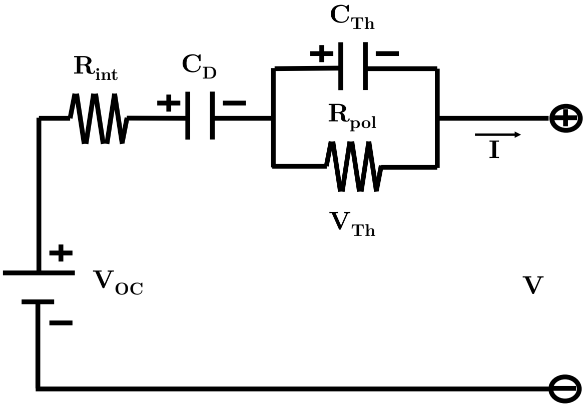

$$\dot{V}_D = V_{OC} \tag{2.16}$$

$$\dot{V}_{Th} = -\frac{V_{Th}}{R_{Th}C_{Th}} + \frac{I}{C_{Th}} \tag{2.17}$$

$$V = V_{OC} - V_D - V_{Th} - R_{int}I \tag{2.18}$$

Figure 2.33.: PNGV Model

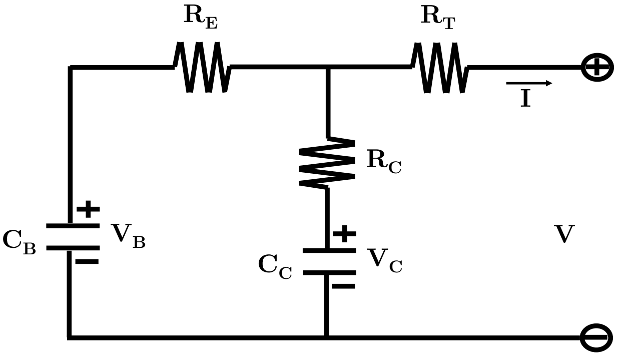

$$\begin{bmatrix}\dot{V}_B\\ \dot{V}_C\end{bmatrix} = \begin{bmatrix}\dfrac{-1}{C_B\left(R_E+R_C\right)} & \dfrac{1}{C_B\left(R_E+R_C\right)}\\ \dfrac{1}{C_C\left(R_E+R_C\right)} & \dfrac{-1}{C_C\left(R_E+R_C\right)}\end{bmatrix}\begin{bmatrix}V_B\\ V_C\end{bmatrix} + \begin{bmatrix}\dfrac{-R_C}{C_B\left(R_E+R_C\right)}\\ \dfrac{-R_C}{C_C\left(R_E+R_C\right)}\end{bmatrix}\left[I\right] \tag{2.19}$$

$$\left[V\right] = \begin{bmatrix}\dfrac{R_C}{\left(R_E+R_C\right)} & \dfrac{R_E}{\left(R_E+R_C\right)}\end{bmatrix}\begin{bmatrix}V_B\\ V_C\end{bmatrix} + \begin{bmatrix}-R_T - \dfrac{R_CR_E}{\left(R_E+R_C\right)}\end{bmatrix}\left[I\right] \tag{2.20}$$

Figure 2.34.: Resistor Capacitor (RC) Model

SAFT, a French battery company. Unlike the previous models, the RC model does not feature an ideal voltage source. Instead, in addition to wires connecting the individual elements, the RC model only features resistors and capacitors in a mix of series and parallel arrangements. Two capacitors are arranged in parallel. The bulk capacitor shown on the left hand-side features a relatively large (bulk) capacitance C_B, which represents the battery's capability to store electrical charge. The surface capacitor shown in the middle reflects surface effects of the cell. Hence, its capacitance C_S is significantly smaller than C_B. The electrical behaviour is summarised in equations 2.19-2.20. More complicated RC models with additional combinations of resistors and capacitors have been suggested in [94] and [116]. While they can achieve better accuracy, they are computationally more complicated and they tend to show little robustness outside their validated range according to [113]. The RC model is also included in the ADVISOR energy storage <ess> library (see figure 2.14) [114].

The **MATLAB/Simulink Model** developed by two Canadian engineers is mainly an equivalent circuit model based on the internal resistance model (figure 2.30), but with added analytical terms as shown in figure 2.35. It is the custom battery model used by MATLAB/Simulink in

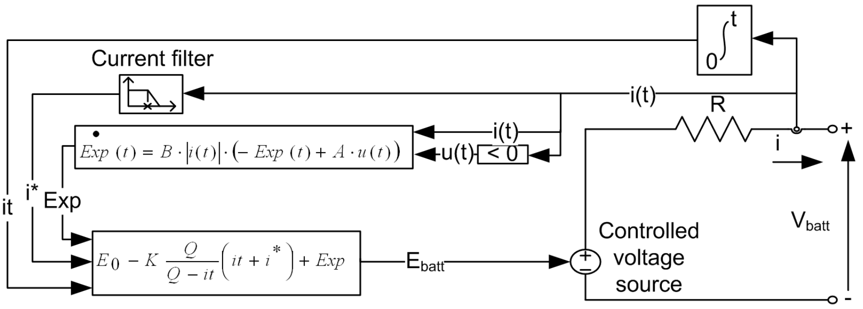
t
0
Current filter
i(t)
R
i(t)
$\dot{Exp}(t) = B \cdot |i(t)| \cdot (-Exp(t) + A \cdot u(t))$
u(t)
< 0
+
i
it
i*
Exp
$E_0 - K\frac{Q}{Q-it}\left(it + i^*\right) + Exp$
E_{batt}
Controlled voltage source
V_{batt}
-

$$V_{discharge} = V_{oc} - R_{int}I - K\frac{Q}{Q - \int_0^t Idt}\left(\int_0^t Idt + I^*\right) + Ae^{-B\int_0^t Idt} \tag{2.21}$$

$$V_{charge} = V_{oc} - R_{int}I - K\frac{Q}{\int_0^t Idt - 0.1Q}I^* - K\frac{Q}{Q - \int_0^t Idt}\int_0^t Idt + Ae^{-B\int_0^t Idt} \tag{2.22}$$

Figure 2.35.: MATLAB/Simulink Battery Model [117]

order to simulate power systems. The symbols used in the figure have been changed for equations 2.21-2.22 in order to be consistent with the notation used in this work. The model applies parameters, which are illustrated in figure 2.36, in order to work out the voltage during charge and discharge respectively. According to [117] the lithium-ion battery discharge curve can be divided into three distinct areas. First, the exponential area, which ranges from the voltage of a fully charged battery V_{full} to the exponential voltage at V_{exp}. Second, the almost linear nominal area that starts at V_{exp} and finishes at the nominal voltage V_{nom}. The last area is irrelevant as below V_{nom} the capacity is dropping at an accelerated rate. These characteristics are reflected in equations 2.21-2.22. However, temperature effects are not considered in this

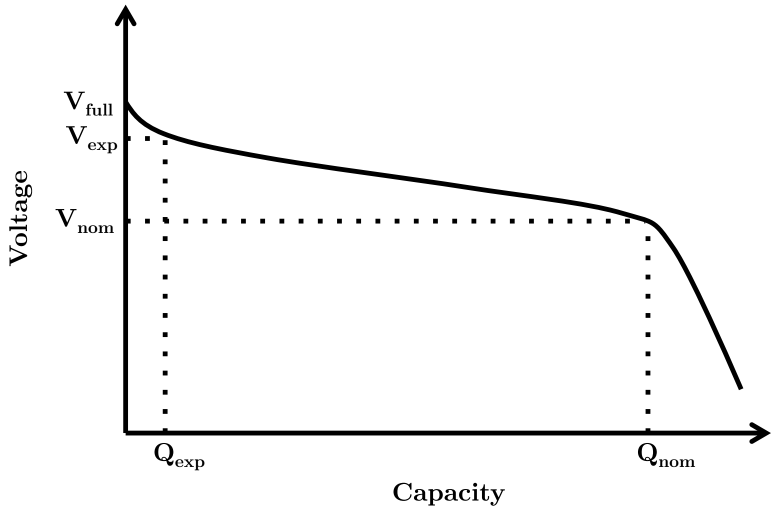

Figure 2.36.: Matlab/Simulink Model Parameters [117]

model. The strength of this model is its intuitive and simple configuration on the basis of only three data points from manufacturer's data sheets. This means that experimental configuration of the parameters is not necessary.

All presented equivalent circuit models assume the OCV to be a function of SOC, which is calculated either via a look-up table or a piecewise linear function [113]. The OCV vs. SOC relationship is not affected by degradation and/or temperature effects as demonstrated in [118] and [119]. This leads to it being one of the most fundamental relationships in battery modelling.

Traditionally, the SOC has been established either by a method called '*coulomb-counting*' or simply by waiting for the fluctuating terminal voltage V to 'relax' until its equilibrium state V_{OC} is reached. Coulomb-counting means that the current drawn over time is integrated with respect to time. Both methods, coulomb-counting and the voltage-relaxation method are mathematically simple and computationally easy to implement. Their accuracy, however, can be quite low especially in highly dynamic systems and where there is no time for the battery to 'relax'. Consequently, adaptive methods and extended Kalman filtering (EKF) has been proposed in order to overcome these limitations. A detailed description of the use of EKF for SOC estimation can be found in [120]-[122]. In [118], Pop et al. suggest that EKF provides the best long-term SOC estimation.

The main advantages of equivalent circuit models are summarised below:

- Relatively easy to implement
- Real-time results
- Good accuracy
- Relatively robust

Equivalent circuit models for simulating battery behaviour also bears disadvantages:

- Lower accuracy compared with electrochemical models
- Oversimplification
- Results usually only include voltage and current values

Thermal Modelling and Others

In addition to the aforementioned battery models, thermal and other models co-exist. Thermal models ([97] & [123]-[126]) are typically used for efficiency optimisation and cooling loop design. Other commercial models include the Battery Design Studio from ANSYS [127] or COMSOL [128], which integrates finite element models based on the dualfoil model.

2.3.5. Interim Summary

Battery models can be divided into analytical models, electrochemical models, equivalent circuit models, thermal models and others. While analytical models are mostly mathematically simple and easy to implement, they lack accuracy and robustness. Electrochemical models on the contrary are the most accurate models, but they are difficult to configure and require detailed knowledge about electrochemistry. Usually, they cannot be performed in real-time, which is crucial for on-board vehicle applications. Equivalent circuit models may lack accuracy, but they can be performed in real-time and therefore are the preferred choice for vehicle simulations. They are accurate enough, yet not unnecessarily complicated.

Subsection 2.2.4 concluded that there is a knowledge and modelling gap regarding the sizing of EV traction batteries, which also considers battery degradation for generic power train models. This section has introduced and critically assessed available battery models. It was shown that detailed battery degradation models exist, but not for the purpose of sizing an EV traction battery pack. Existing battery degradation models are mainly electrochemical models. Therefore, there is a modelling and knowledge gap regarding a battery sizing model, which is quick, mathematically simple, easy to implement and also considers degradation.

2.4. Summary & Conclusions from Literature Review

This chapter has summarised, critically assessed and reviewed the developments of electric vehicles and batteries. First, an historical outline of electric vehicles was presented highlighting that EVs have been commercially available for more than 115 years and that their spread was greatest around 1900 in the US. Since then ICEVs have been dominating road transport for reasons of costs and range. Today, EVs are gaining interest again because of rising fuel prices and stricter emission standards for passenger vehicles. Compared to that of ICEVs, the power train configuration of EVs is relatively simple leading to significantly higher 'tank-to-wheel' efficiencies and lower maintenance efforts. Electric vehicle simulations are either forward- or backward-facing, or a combination of both. Thanks to their physical sequence of events, forward-facing vehicle models are usually preferred for control design and performance analysis such as maximum speed. Backward-facing simulations in contrast are preferred for individual component analysis such as that of the battery. Hybrid models like ADVISOR combine the two approaches to allow for individual component analysis as well as for overall system performance analysis. They present the state of the art of electric vehicle modelling. Consequently, ADVISOR is the preferred vehicle simulation underpinning this work.

The second part of this chapter was devoted to batteries. It was shown that electricity was discovered by accident, when Volta made experiments with twitching frog's legs. Batteries are devices, which convert electrochemical energy into electrical energy. They mainly consist of a negative electrode (anode), a positive electrode (cathode) and an electrolyte, which separates the two electrodes. The electrolyte needs to permeable for ions to move bi-directionally between the electrodes, but impermeable for electrons, which have to flow through an external circuit. The external circuit is connected to a load, which can use the applied current. Battery design is mainly about choosing the best combinations of materials for the electrodes and the electrolyte in order to achieve long-term high energy and power densities at low costs and with inherent safety. Models that describe the complex battery behaviour can be categorised into analytical, electrochemical, equivalent circuit and thermal models. Analytical models are too simplistic and not accurate enough for highly dynamic applications like that in an EV. Electrochemical models, which are the state of the art of battery modelling, are very accurate, however they cannot be performed in real-time for vehicle applications. Equivalent circuit models offer a good comprise for providing sufficient accuracy while not being too overcomplicated.

To some extent the existing equivalent circuit models can predict the relationship between SOC, cycle life and the resulting loss of capacity quite accurately. However, most of these models are either limited to experimental single cells and not entire battery packs, exclusively focus on capacity fade and not on power fade as well, centre on very narrow temperature ranges (i.e. 20-30 ℃) only, address solely very low discharge currents (i.e. 1-3 C), ignore unsteady discharge behaviour or disregard other influences like charging of the battery through regenerative braking and humidity for example. Consequently, a new approach is required in order to find the optimum battery size for electric vehicles with particular focus on battery degradation.

3. Methodology

This chapter outlines the scientific approach taken in order to find solutions for the research problem introduced in section 1.3. The aim is to find the optimum battery capacity for electric vehicles with particular focus on battery degradation through iterative steps as illustrated in figure 3.1.

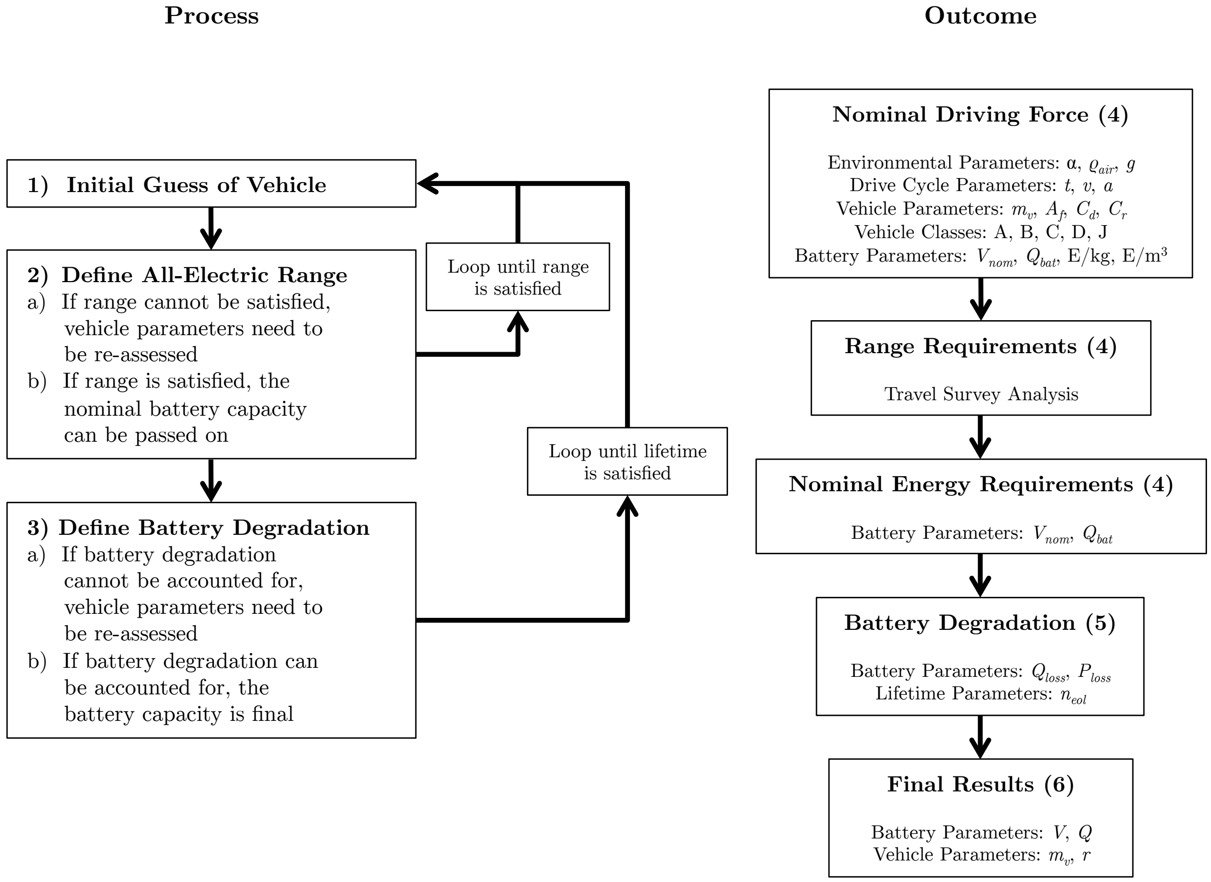
Process
Outcome
1) Initial Guess of Vehicle
2) Define All-Electric Range
a) If range cannot be satisfied, vehicle parameters need to be re-assessed
b) If range is satisfied, the nominal battery capacity can be passed on
3) Define Battery Degradation
a) If battery degradation cannot be accounted for, vehicle parameters need to be re-assessed
b) If battery degradation can be accounted for, the battery capacity is final
Loop until range is satisfied
Loop until lifetime is satisfied
Nominal Driving Force (4)
Environmental Parameters: α, ϱ_{air}, g
Drive Cycle Parameters: t, v, a
Vehicle Parameters: m_v, A_f, C_d, C_r
Vehicle Classes: A, B, C, D, J
Battery Parameters: V_{nom}, Q_{bat}, E/kg, E/m^3
Range Requirements (4)
Travel Survey Analysis
Nominal Energy Requirements (4)
Battery Parameters: V_{nom}, Q_{bat}
Battery Degradation (5)
Battery Parameters: Q_{loss}, P_{loss}
Lifetime Parameters: n_{eol}
Final Results (6)
Battery Parameters: V, Q
Vehicle Parameters: m_v, r

Figure 3.1.: Research Process & Expected Outcomes

First, with initial estimates the nominal driving force of EVs is calculated by considering environmental, drive cycle, vehicle and battery parameters. Most parameters have a specific range of possible values from very low extremes to very high extremes. Together with the vehicle's range requirements, the nominal energy requirements for the on-board traction battery is worked out through an iterative process. This process is explained in detail in chapter 4 as indicated by the numbers in brackets. The next step, working out the battery performance and degradation, is dealt with in chapter 5. Finally, the penultimate chapter (6) brings together these findings and discusses their implications. The last chapter (7) summarises the main conclusions and suggests areas for further work.

In crude terms, the optimum battery capacity is the product of driving force, range and battery degradation as illustrated in figure 3.2. Therefore, each of the three headings in figure 3.2 presents a multiplier, which is the result of several individual analyses also listed in figure 3.2.

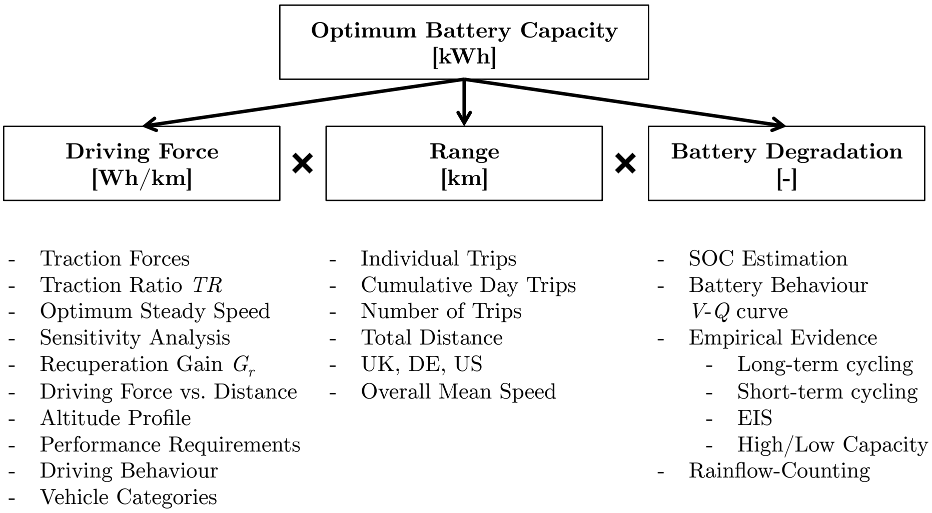
Optimum Battery Capacity [kWh]
Driving Force [Wh/km]
×
Range [km]
×
Battery Degradation [-]
- Traction Forces
- Traction Ratio TR
- Optimum Steady Speed
- Sensitivity Analysis
- Recuperation Gain G_r
- Driving Force vs. Distance
- Altitude Profile
- Performance Requirements
- Driving Behaviour
- Vehicle Categories
- Individual Trips
- Cumulative Day Trips
- Number of Trips
- Total Distance
- UK, DE, US
- Overall Mean Speed
- SOC Estimation
- Battery Behaviour V-Q curve
- Empirical Evidence
- Long-term cycling
- Short-term cycling
- EIS
- High/Low Capacity
- Rainflow-Counting

Figure 3.2.: Analytical Structure

The following sections of this chapter explain the main assumptions for the software model, introduce the software environment itself and present the validation techniques.

3.1. Assumptions

First, vehicle dynamics are only assessed along the vehicle's longitudinal axis, i.e. transverse vehicle dynamics such as sideslip are ignored throughout this analysis. Second, vehicle as well as battery characteristics are assumed to be 'steady' for the duration of one second. This means, a quasi-steady approach (introduced in section 2.2.3) is adopted. Third, this work takes a mechanical engineering viewpoint of the battery sizing problem. Political, economic or social analyses are mainly omitted. Also, electrochemical details affecting the functionality of batteries, which are explained in section 2.3.2, are mostly ignored for the analysis. Fourth, the terminal voltage is assumed to be in electrochemical equilibrium ($V_T = V_{OC}$) after a minimum of 30 minutes under the no-load condition. This means, battery dynamics are ignored when the last current draw occurred 30 minutes ago or even earlier.

3.2. Modelling & Simulation

The modelling and simulation environment chosen for this work is MATLAB and MATLAB-Simulink. The commercial software enables the quick execution of algorithms and the visualisation of their results. It is particularly useful for the analysis and interpretation of large data sets including log files from the Racing Green Endurance (RGE) project, the Future Car Challenge (FCC) and travel surveys.

3.3. Experimental Methods

This section introduces and explains the experimental methods used within this work. First, the RGE project is presented. This is followed by an introduction of the Future Car Challenge (FCC) and an explanation of the use of travel surveys. Finally, the battery testing procedures are commented on.

3.3.1. Racing Green Endurance (RGE)

From December 2008 until December 2010 the Racing Green Endurance (RGE) team, which the author is part of, has been working towards developing an electric supercar and driving it down the Pan-American Highway as shown in Figure 3.3. The mission was to disprove common perceptions about electric vehicles, which include that they are slow, boring and of short range. In particular, it was about demonstrating the viability of electric vehicles as an alternative to conventional ICEVs. The project was based upon four aims. First, to show that sustainable transport is possible. Second, to help encourage the next generation of scientists and engineers to keep challenging common wisdom. Third, to excite people by being adventurous. And fourth, to collect valuable real-world and long-term data from an electric vehicle, which without industrial collaborations is very difficult to obtain.

Design

After the successful award of the required financial and in-kind sponsorship in August 2009, the first task was to design the vehicle. Thanks to Radical Sportscars Ltd., the team was donated a chassis of a SR8 racing car, which would form the basis of the new SRZero (zero emission). The remarkable design (see Figure 3.4) deliberately would catch the attention of other drivers and pedestrians along the way. Consequently, the team's task was to design the entire power train and not the exterior of the vehicle. The overriding design parameter for the SRZero was range. Early research has shown that the longest stretches along the Pan-American Highway without a built infrastructure are in the Chilean Atacama Desert and more than 400 km long. Thus, the SRZero needed to have an all-electric range (AER) of at least 400 km in order to be charged locally. The team decided that charging from a mobile generator would defeat the purpose of promoting sustainability.

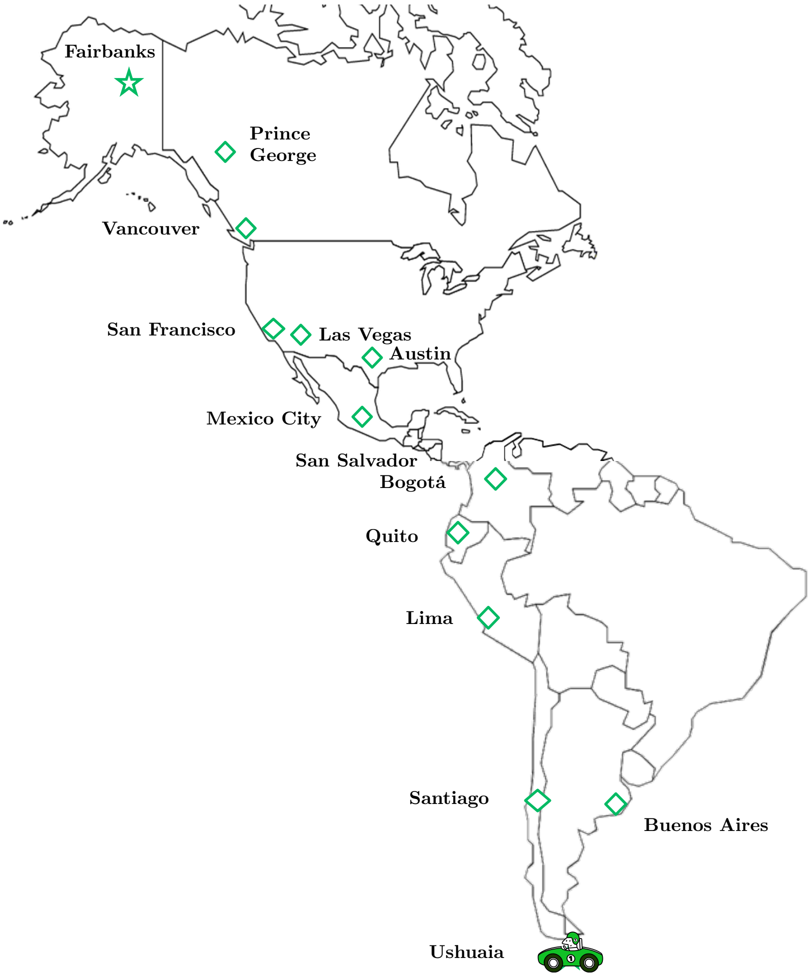
Fairbanks
Prince George
Vancouver
San Francisco
Las Vegas
Austin
Mexico City
San Salvador
Bogotá
Quito
Lima
Santiago
Buenos Aires
Ushuaia

Figure 3.3.: Major Cities Along the Pan-American Highway

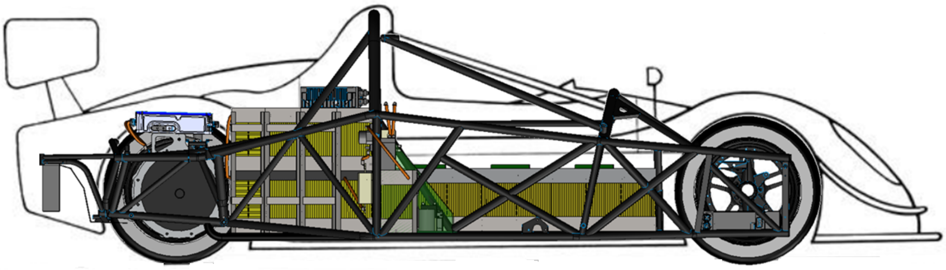

Figure 3.4.: SRZero Schematic View

Using initial estimates and iterative algorithms, which are presented in chapter 4, the required battery capacity was found to be 54 kWh. In order to keep the maximum currents low, it was decided to combine 164 lithium-iron phosphate ($LiFePO_4$) cells with a nominal voltage of 3.3 V and a rated capacity of 100 Ah in a series arrangement. This 164S0P configuration resulted in a relatively high nominal battery pack voltage of 541.2 V and a rated capacity of 100 Ah. As explained in section 2.2.2 high system voltages (>200 V) are usually favoured over low system voltages in order to reduce the losses associated with high currents (see equation 2.9). Also, the team decided to use $LiFePO_4$ cells instead of $LiCoO_2$ or $LiMn_2O_4$ cells. As discussed in section 2.3.2 '*temperatures of these cells during thermal runaway are unlikely to cause hot surface ignition of the vent gases*' and thus are comparatively safe without the need for active cooling [101]. Their main disadvantage is their comparatively low specific energy and their comparatively low energy density. The cells were donated by the Chinese battery manufacturer ThunderSky Ltd. (now Winston Battery Ltd.). More details on the exact battery specifications can be found in appendix B.

The battery pack was placed at the rear directly behind the driver's and the co-pilot's seat and in the two sidepods of the open-cockpit sportscar. In Figure 3.4 the individual battery cells are shown in yellow. The high-capacity prismatic cells featured fins on the outer casing in order to facilitate convective air (passive) cooling.

The electrical energy in the battery cells was converted from DC to AC power via two inverters in parallel, mounted above the rear axle on top of two three-phase AC permanent magnet (PM) motors [129]. The small and lightweight inverters were also used as motor controllers for the electric axial flux motors mentioned above. Conversion of power is always associated with losses. Consequently, inverter efficiencies are always <100% regardless of the direction of power flow. In this case inverter losses are associated with the conversion loss from DC to AC power and vice versa. During normal operation, when the power flow is from the battery to the wheels (i.e. torque values are positive), DC power values are greater than the resulting AC power values. On the contrary, during recuperation when kinetic energy from the wheels is fed back to the battery, AC power values are greater than resulting DC power values. Equation 3.1 clarifies this relationship.

$$P_{DC} = \frac{P_{AC}}{\eta_{inverter}} \tag{3.1}$$

The axial flux motors, which were provided by EVO Electric Ltd., have a relatively high power density of 3.6 kW/kg and allow for cruising speed efficiencies of >95% thanks to a custom design. The electric motors are custom-wound (i.e. their peak efficiency is at lower speeds than normal) for a nominal driving speed of ≈80 km/h (713 rpm in this case) as illustrated in figure 3.5. The motors can run up to speeds of 1,800 rpm (202 km/h) and achieve a combined maximum torque of 1,300 Nm, but experience field weakening at speeds above 1,500 rpm. Field weakening in AC motors, the effect of which cannot be shown in figure 3.5, appears once the voltage remains constant and the frequency increases. Then, the torque decreases in proportion to the increasing

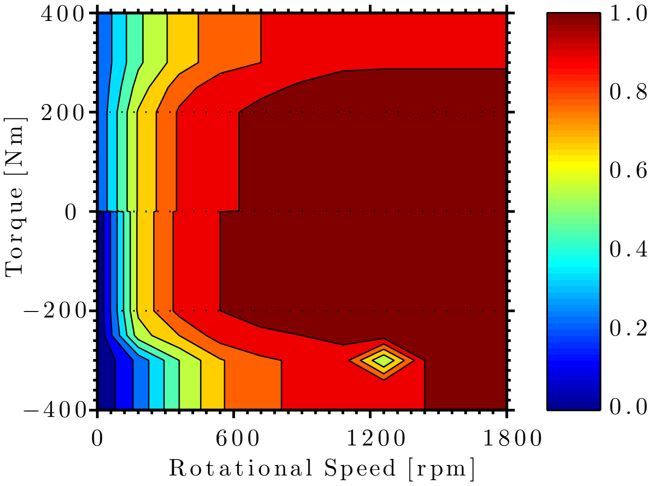

Figure 3.5.: SRZero Motor Efficiency Map

speed and the power remains constant (see figure 3.6). This means that at high speeds only low torque is available. That is why very high speeds shall be avoided with this design. The motors also act as generators while the SRZero is recuperating energy from deceleration and/or braking. They are cooled using a water/glycol mixture.

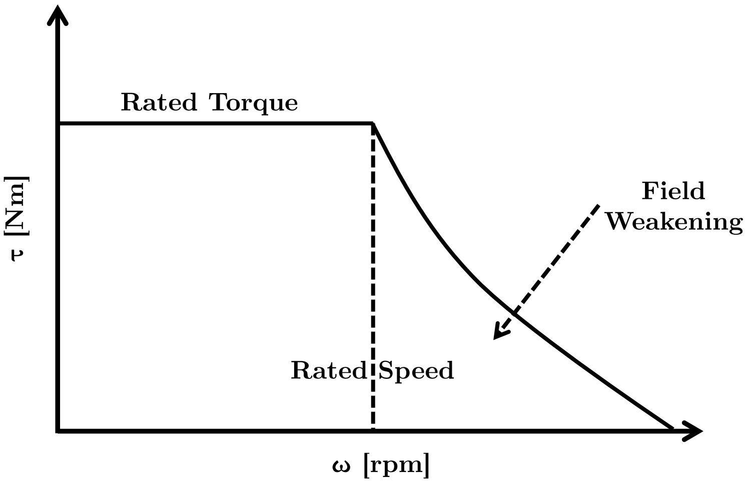

Figure 3.6.: Field Weakening Schematic

The supervisory control is carried out by a real-time controller, a CompactRIO which was donated by the National Instruments Corporation (NI). The vehicle supervisory system follows a torque control approach. Figure 3.7 illustrates this power train setup.

The relatively long range requirement not only demands a relatively large battery pack, but also a highly efficient and robust power train. This leads to an additional design priority, favouring endurance over speed. Thus, the two motor shafts are directly connected to the wheels. It is only possible to leave out a gear box if the required combinations of torque and

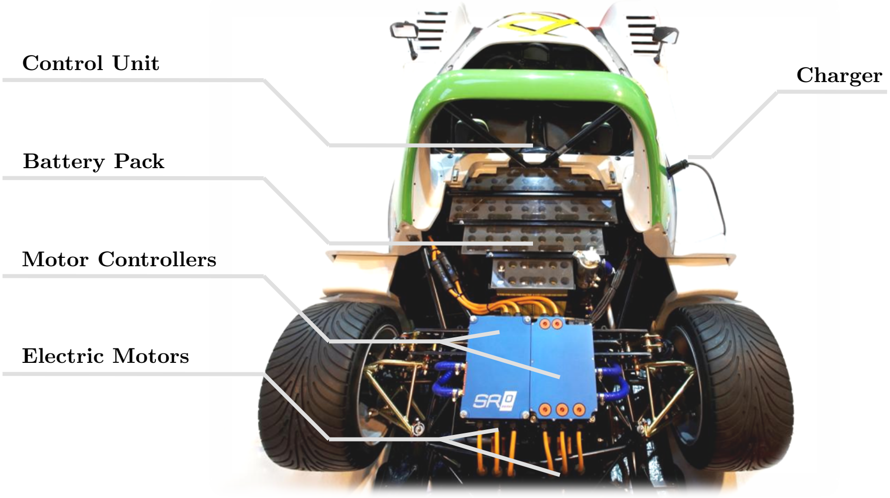

Figure 3.7.: SRZero Power Train Layout

speed values can be attained by the electric motors alone. Usually, this requires the motors to be custom-wound for the specific application (see previous paragraph). In the absence of a gear box losses associated with friction are reduced, also weight and volume can be saved.

On top of this, the SRZero only features the most basic auxiliaries. These include lighting,

Table 3.1.: Technical Specifications of SRZero

Attribute	Value
Rated Battery Capacity	100 Ah (54.12 kWh)
Battery Chemistry	$LiFePO_4$
Number of Cells	164
Nominal System Voltage	541.2 V
Battery Pack Mass	574 kg
Motor Type	3-Phase AC PM
Max. Power Output	300 kW (400 bhp)
Max. Torque Output	1,300 Nm
Number of Motors	2
Drive System	Rear Wheel Direct Drive
Kerb Weight	1,150 kg
Length	4.2 m
Width	1.8 m
Height	0.8 m
Wheel Diameter	0.5955 m
Frontal Area	1.44 m^2
Drag Coefficient (C_d)	0.38 (estimated)
Rolling Resistance (C_r)	0.011 (estimated)
Range	>515 km
Top Speed	190 km/h
Acceleration (0-100 km/h)	7 s

a liquid crystal display (LCD) and radio communication powered by a 12 V battery. The low voltage battery is also used to initialise the control system, which starts the car (compare with figure 2.8 about the system layout). Air conditioning, heating and entertainment systems are omitted. Detailed technical specifications of the SRZero are listed in table 3.1.

Data Collection

The CompactRIO, simultaneously serving as a real-time controller and also as a field-programmable gate array (FPGA), is used to implement an efficient and robust vehicle control system [129]. It executes the vehicle's battery management system (BMS) and additionally manages the motor controllers, driver interface and safety systems. Most relevant in the context of this work is the controller's ability to store real-time data. The data logs sampled at a frequency of 1 Hz include analogue and error state data, records from the chargers, the BMS, motor controllers and motors. More specifically, table 3.2 lists the available log file information in alphabetical order. This information is used to validate the results from the software model introduced in chapters 4-5. However, not all information such as individual cell temperatures is available for the entire length of the trip. Approximately 15% of all data logs are not readable because they are corrupted. More than 70% of the temperature logs are also corrupted.

Table 3.2.: Racing Green Endurance Log File Information

Information	Sign	Unit
Auxiliary Voltage	V_{aux}	V
Cell Temperature	T_{cell}	°C
Cell Voltage	V_{cell}	V
Current (fast ⊘)	I_{fast}	A
Current (slow ⊘)	I_{slow}	A
Feedback Torque	τ_{out}	Nm
Inverter Current (AC)	I_{mc_ac}	A
Inverter Current (DC)	I_{mc_dc}	A
Inverter Voltage (AC)	V_{mc_ac}	V
Inverter Voltage (DC)	V_{mc_dc}	V
Motor Speed	ω_{motor}	rev/min
Motor Temperature	T_{motor}	°C
Requested Torque	τ_{req}	Nm
State of Charge	SOC	%
Time	t	s
Traction Voltage	V_{trac}	V
Vehicle Speed	v	km/h

After nine months of design and manufacture and after having passed the individual vehicle approval (IVA) for the SRZero in the UK in early May 2010, the team was ready to start the record-breaking journey (no other team has ever done something similar before) along the Pan-American Highway on July 4th 2010. After 71 drive cycles, 87 battery cycles and a cumulative distance of 26,500 km (see appendix C for a detailed itinerary) the team accomplished its mission and arrived at the southernmost city in the world, Ushuaia, on November 16th 2010. In the meantime, the car withstood two accidents, three broken chargers, four broken shock absorbers, a fire, after which the BMS was destroyed, and very rough road conditions. Figure 3.8 depicts the SRZero in Patagonia, Argentina. More information on the RGE project as well as access to the BBC World Documentary about the project is available from *www.RacingGreenEndurance.com*.

Figure 3.8.: SRZero in Patagonia, Argentina

3.3.2. Future Car Challenge (FCC)

The Future Car Challenge (FCC) is an annual motoring challenge organised on behalf of the Royal Automobile Club (RAC). Its debut was in November 2010 [130] and since then participants have been challenged to consume least energy while driving a 92-102 km route from Brighton to London in a given time frame. The FCC provides a unique opportunity to compare the energy consumption of different vehicle configurations on the same basis under real-world driving conditions [131].

All road-legal electric, fuel cell electric, plug-in hybrid electric, hybrid electric and up to 110 gCO_2/km (NEDC) internal combustion engine passenger motor cars and light commercial vehicles (LCVs) produced after January 1st 2001 are eligible for this competition [132]. A minimum time of 2 hours and 45 minutes and a maximum time of 3 hours and and 30 minutes are set including a 15-30 minute stop-over approximately half-way at Crawley. Two adult passengers have to be in the participating vehicles at all times. Vehicles are classed by power train type, vehicle size (Euro Car Segments [133]) and by the type of build as shown in table 3.3.

From 2010-2012 there are 51, 40 and 23 individual vehicle energy data logs available for comparison respectively. Table 3.4 lists the available energy consumption information for different power trains. Tickmarks indicate available information, whereas a cross indicates that this

Table 3.3.: Future Car Challenge Entry Classes [132]

Power Source	**Vehicle Size**	**Build**
Electric Vehicle (EV)	Small (A & B)	Prototype
Fuel Cell Electric Vehicle (FCEV)	Regular (C)	Production
Plug-In Hybrid Electric Vehicle (PHEV)	Large (D)	
Hybrid Electric Vehicle (HEV)	Sports (S)	
Internal Combustion Engine Vehicle (ICEV)	Multi-Purpose (M & J)	
	Light Commercial Vehicle (LCV)	

information is not available for this particular power train type. Pure EVs rely on electrical energy only for propulsion, whereas PHEVs may be powered by electrical as well as by chemical energy from liquid fossil fuels. HEVs can also be powered by electrical and chemical energy, but their battery cannot be charged externally. ICEVs exclusively depend on liquid (or gaseous) fossil fuels for motion. Consequently, the methods used for measuring electrical and chemical (fuel) energy are explained in the following two subsections. More detailed information on the methods for measuring the energy consumption for the FCC can be found in [130]. The last subsection describes how driving behaviour is assessed.

Table 3.4.: Future Car Challenge Data Log Information

	Traction Voltage [V(t)]	**Current [I(t)]**	**Fuel Flow [l/s (t)]**
EV	✓	✓	✗
FCEV	✓	✓	✓
PHEV	✓	✓	✓
HEV	✗	✗	✓
ICEV	✗	✗	✓

Electric Energy

The electric 'tank-to-wheel' energy consumption for EVs, FCEVs and PHEVs is calculated via the time integral of electric power consumption. For a fixed time step $\Delta t = 1/f$ this becomes a summation as illustrated in equation 3.2. The sampling frequency f varies within 1-100 Hz, depending on the power train type.

$$E_{el} = \frac{\sum V(t)I(t)\Delta t}{\eta_{charge}\eta_{battery}} \tag{3.2}$$

This also takes into account charging ($\eta_{charge} = 93\%$) and battery/coulombic ($\eta_{battery} = 99\%$) efficiencies. By convention, positive currents are defined as flowing out of the battery and negative currents as flowing into the battery.

EVs, FCEVs and PHEVs are fitted with a data logger, which records both traction voltage and current on the high voltage (HV) DC bus between the battery pack and the motor controllers. The loggers have been supplied by GEMS Ltd. Sensors include hall effect current sensors with a range of ±750 A [130] as well as high value resistors across the bus to generate a small leakage current, which is then measured using another current transducer giving a range of 0-450 V. Current and voltage signals are fed to a 10-bit analog-to-digital converter (ADC). The transducers used for current and voltage measurement are temperature compensated and individually calibrated before installation. For the challenges between 2010 and 2012 inclusively there are 16, 26 and 11 individual electric vehicle energy data logs available for comparison respectively.

Fuel Energy

The energy stored per unit volume in conventional liquid fossil fuels is based on the calorific value, also referred to as the heating value. The relative difference between the higher heating value (HHV) and the lower heating value (LHV) based on volume is 5.2% for petrol and 6.4% for diesel respectively [31]. As the HHV represents the maximum energy content stored in a fuel and official UK government publications (e.g. [134]) use the HHV when citing emission factors for businesses, the HHV is the preferred reference value over the LHV for this analysis. Diesel's energy density with respect to volume (10.60 kWh/l) is 10% higher than the equivalent of petrol (9.61 kWh/l) [31]. Hydrogen (H_2) has a specific energy density (HHV) of 39.33 kWh/kg [135]. The fuel 'tank-to-wheel' energy consumption for FCEVs, PHEVs, HEVs and ICEVs is described by the following equation:

$$E_{fuel} = HHV_{fuel} \sum Q_{fuel} \Delta t \tag{3.3}$$

It is equal to the product of the higher heating value (HHV) and the time integral of the volumetric fuel flow rate Q_{fuel}. The instantaneous volumetric fuel flow rate is retrieved from the vehicle's encrypted CAN bus message of the on-board diagnostics (OBD-II). Its time integral is compared against a brim-to-brim fuel measurement at each end of the challenge.

Driving Behaviour

Driving behaviour in the context of this analysis refers to the different individual speed and acceleration profiles of the vehicles. During the 2011 FCC for example more than ⅔ of participating vehicles (i.e. 27 of 40) were equipped with a Global Positioning System (GPS) receiver, which logged vehicle position at either 50 or 100 Hz with an accuracy of the receiver of about 10 m. This allows for the generation of relatively accurate speed and acceleration profiles for individual participants.

Relevance

The FCC data logs present a valuable validation source for the nominal energy consumption of various power train types and in particular of electric vehicles. With this information, the assumptions and calculations made in chapter 4 can be checked against real-world values. Additionally, the FCC logs present a valuable data source for the analysis of driving behaviour. For each of the past three FCCs at least two data sets are available for an EV with the exact same model and make. Thus, any difference in energy consumption for these vehicles can primarily be attributed to the driving behaviour. The most detailed and most comprehensive data set of the FCC with regards to EVs is available for 2011. During that year, the RGE SRZero also participated in the run (see figure 3.9). More information on the FCC can be found at *www.FutureCarChallenge.com*.

Brighton to London Future Car Challenge 2011
Start
RAC

Figure 3.9.: SRZero at the 2011 Future Car Challenge

3.3.3. Travel Survey Analysis

Travel surveys are studies of individual travel behaviour. Most travel surveys are large data sets (typically .txt or .csv files), which include socio-economic and demographic information about individuals and their household, information about their modes of transportation and typically a diary of their journeys on a given day. There are travel surveys on regional as well as on national levels. Three countries, for which relatively detailed national travel surveys exist, are analysed individually and compared against each other: the UK, Germany and the US.

The latest UK National Travel Survey (NTS) was published by the Department for Transport (DfT) on December 13th 2012 and can be downloaded from [136]. Raw data sets are available from the Economic and Social Data Service (ESDS) [137]. The latest German travel surveys (Mobilität in Deutschland 2008 & Deutsches Mobilitätspanel (MOP) 2011/2012) were published in 2009 and 2012 respectively. Their raw data sets can be ordered from [138]. For the United

States, the most recent study is the 2009 National Household Travel Survey (NHTS) and it's raw data can be downloaded from [139]. In order to have a comparable and sufficiently large sample size for averaging the results over a longer period of time and thus maximising the stability of data, data from 2008-2010 has been analysed for all three countries. Therefore, the sample sizes for the UK, Germany and the US are 409,770, 72,304 and 720,903 individual car journeys respectively.

As shown in figure 3.1 the travel survey analysis serves the purpose of establishing range requirements for electric vehicles. The underlying assumption is that private EVs are normally charged overnight at the owner's home and then discharged during the day. Also, it is assumed that travel patterns including the frequency of trips and the lengths of trips are independent of the vehicle power train type. Thus, using MATLAB, all raw data from the three surveys has been analysed and filtered for private cars with an identifiable driver only. This way duplicated journeys with the same vehicle but different passengers can be filtered out and information about the vehicle including size and annual mileage can also be obtained. Weights are included in the statistics in order to adjust for non-response, and also for drop-off in recording during the survey trial. Furthermore, all data has been cumulated for the duration of a single day. As shown in figure 3.10a, usually several individual journeys account for the total vehicle day distance. Following this example, one person might leave his/her home in the morning to go to work, leave work in the evening to go shopping before returning home. What is relevant here is that trips 1-3 are all undertaken using the same vehicle and the same driver. The example shown next to it in figure 3.10b demonstrates how one person might be going to the same places, but following different routes and using a second vehicle. The person might be using his/her car to go to work and back (trips 1-2), but his/her partner's car to go to the supermarket and

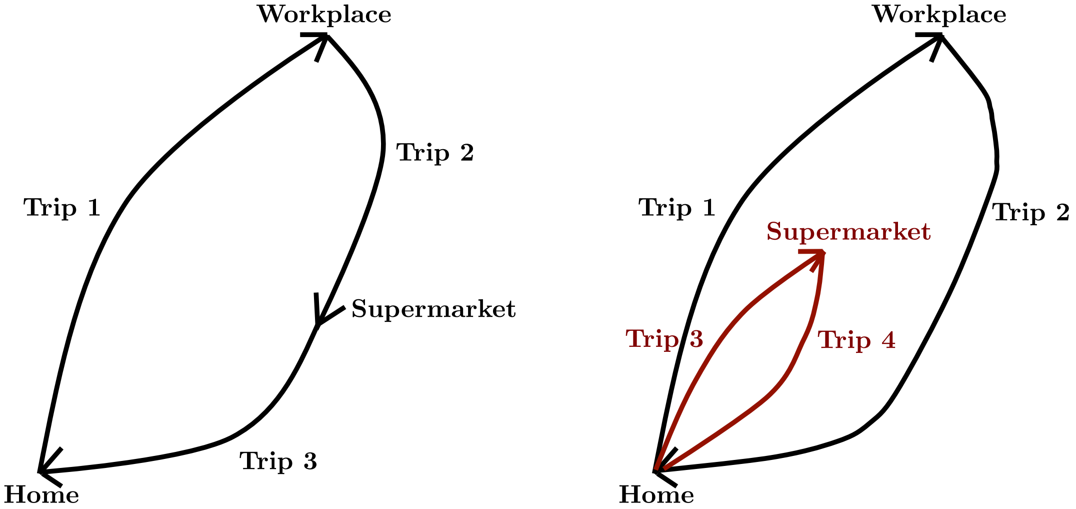

(a) One Vehicle **(b) Two Vehicles**

Figure 3.10.: Exemplary Daily Trip Distribution

back (trips 3-4). This is to demonstrate the importance of following an individual vehicle's path during the day rather than an individual person's path in order to establish daily range requirements for EVs.

3.3.4. Battery Testing

The final validation method associated with this work is related to experimental battery testing at Imperial College's fuel cell lab. This section is closely related to the Racing Green Endurance project introduced in section 3.3.1 as the battery cells in question are the traction batteries from the RGE project.

In the following, two methods of battery testing used for this work are explained and described: battery cycling and electrochemical impedance spectroscopy.

Battery Cycling

Battery cycling refers to the repeated charging and discharging of one or more battery cells under very specific conditions. It is used to identify performance characteristics such as capacity and nominal voltage and also to find faulty cells. Consequently, battery cycling is done prior to other battery testing methods. A procedural battery cycling schematic with two cycles is presented in figure 3.11. Real battery cycling tests can range within 1-10,000 cycles. The cell voltage is plotted against time. A typical battery cycle consists of a full charge followed by a full discharge. In figure 3.11 the charge is represented by an increasing voltage from the lower cut-off voltage V_{min} up until the upper cut-off voltage V_{max}. The cell's operating range is between V_{min} and V_{max}. During cycling a voltage increase is achieved through a constant current (galvanostatic) charge. After this the cell is further charged with currents being fed at a constant voltage V_{max} (potentiostatic charge) until the currents reach a minimum value I_{min}. The discharging process

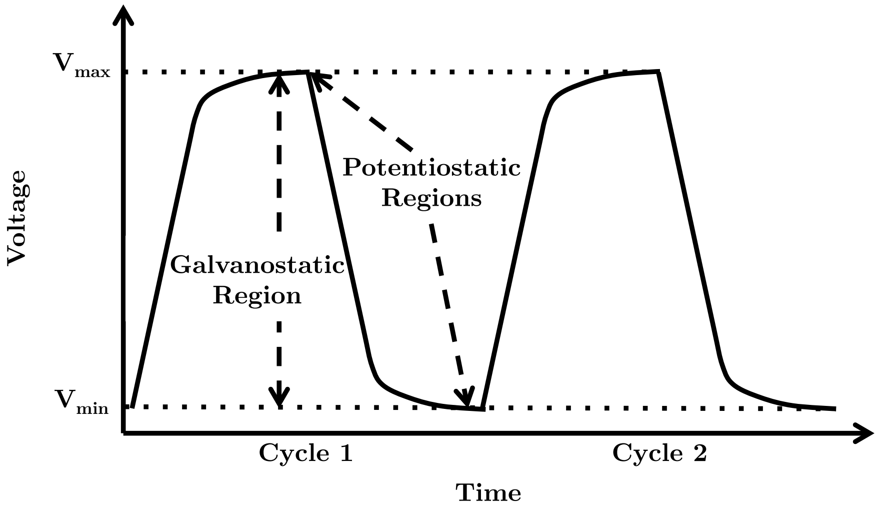

Figure 3.11.: Battery Cycling Schematic

is somewhat simpler as it only involves a constant current discharge until V_{min}. By increasing the charge/discharge currents as well as the ambient temperature, long-term heavy-duty cycles such as those occurring in EVs can be simulated at a fraction of real-time cycles. This method is called accelerated life testing.

Battery cycling in a lab environment for the RGE battery cells was carried out during the early months of 2010 and 2012 respectively. Basic battery cell parameters such as battery pack voltage and current (see section 3.3.1) are also available throughout the journey from July to November 2010. Thus, the battery characteristics before, during and after the drive down the Pan-American Highway are known.

The first cycling tests in early 2010 were completed at the grounds of Frazer Nash Research Ltd., the company which also sponsored the custom-made BMS and the three chargers for the RGE project. Their BMS and their chargers were used in conjunction with a load bank (heat sink) in order to cycle and balance all cells. Figure 3.12 shows this configuration. Cell balancing refers to the levelling of individual electric cell potentials (voltages) when several cells are combined to form a battery (pack). Ideally, each individual cell of a battery has the same voltage as all other cells.

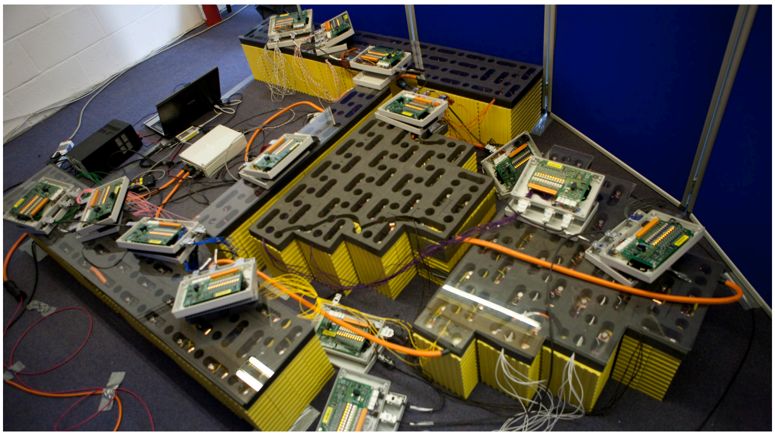

Figure 3.12.: SRZero Battery Pack with BMS and Heat Sink in early 2010

If, for example, in a series cell arrangement like that in figure 2.20 cell voltages are not balanced, then the resulting resistances vary as well. As explained in section 2.3.2 the polarisation resistance R_{pol} increases with a lower cell voltage, while the internal resistance R_{int} roughly stays the same. Assuming the same resistance characteristics for all cells, this leads to the conclusion that the cell with the lowest voltage has the highest resistance. According to Ohm's Law (see equation 3.4) the combination of a lower voltage V_{min} and a higher resistance R_{max} leads to a lower current.

$$I_{max} = \frac{V_{min}}{R_{max}} \tag{3.4}$$

Thus, the maximum current in a series cell arrangement is limited by the cell with the highest individual cell voltage. This has profound consequences for an EV, which needs to draw high currents while accelerating and/or ascending. Consequently, regular cell balancing is mandatory if the cell voltages are not levelled. Any active BMS balances cells during the charging process, while passive battery management systems only monitor the cell characteristics.

For the RGE project the 164 cells were balanced before the first use in the vehicle in early 2010. Also, during the journey the BMS was actively balancing until Cartagena in Colombia when the BMS was destroyed in a minor fire of the SRZero. Fortunately, the cells proved to be robust and stable enough to sustain the rest of the journey without the need of active balancing.

The cycling tests in 2012 on a single cell were completed using a Maccor 4300 desktop automated battery tester. Featuring up to eight ±5 Ampere channels the flexible testing unit can be programmed by the user in a similar way like a BMS and its comprehensive output data can be exported as text files. Despite the potentiostat being automated, the testing requires frequent and regular supervision. Disruptions for the tester include power outages, large ambient temperature variations and loosened sensors. The input parameters for the automated battery tester follow the same logic as illustrated in figure 3.11. The exact steps and their corresponding commands are listed in table 3.5.

Table 3.5.: Battery Cycling Procedure

Step	Description	Data Log Step
1	Rest period (30 minutes)	every 60 seconds
2	Constant current (10 A = 0.1 C) charge until $V_{max} \geq 3.9$ V	for every $\Delta V = 5$ mV
3	Constant voltage (3.9 V) charge until $I_{min} \leq 100$ mA	every 20 seconds
4	Rest period (30 minutes)	every 60 seconds
5	Constant current (10 A = 0.1 C) discharge until $V_{min} \leq 2.5$ V	for every $\Delta V = 5$ mV

This means that in accordance with the battery specifications listed in appendix B, an individual cell is considered to be fully charged at $V_{max} = 3.9$ V (also see figure 3.11). For the entire battery pack of the SRZero, which consists of 164 individual cells connected in series, this means that it is fully charged at 639.4 V. In addition, the cell is considered to be fully discharged at 2.5 V i.e. at 410.0 V for the battery pack. Maximum charging and discharging currents were constrained by the number of available channels (2). Thus, with a rated nominal capacity of 100 Ah, constant charge/discharge currents with a magnitude of 10 A had a comparatively low capacity rate of 0.1 C.

Rest periods of 30 minutes each (steps 1 and 4) after the charging and the discharging process made sure that the electrochemical cell would return back to its equilibrium state before being subjected to yet another charging or discharging process.

Table 3.5 also highlights that the data logs feature a non-uniform sampling interval. Only for rest periods (steps 1 and 4) and the constant voltage charge (step 3) data logs are generated linearly with time. For the galvanostatic charge and discharge processes (steps 2 and 5), a log is created for every incremental change of 5 mV of the cell voltage. Therefore, the data analysis needs to account for the non-linear and varying spacing of data logs. Three thermocouples also measured the ambient temperature and the surface temperatures on the front and back face of the cell.

Electrochemical Impedance Spectroscopy

Electrochemical impedance spectroscopy (EIS) as a means of measuring impedance (polarisation resistance) of electrochemical devices such as batteries was briefly introduced in section 2.3.4 (see figure 2.32). It is a non-invasive method, whereby a sinusoidal signal is induced into the electrochemical system. The response gives the difference in amplitude and phase between voltage and current at a given frequency. There are two types of impedance spectroscopy:

- galvanostatic: AC current is induced and the voltage response is measured
- potentiostatic: AC voltage is induced and the current response is measured

During the early months of 2012 several impedance spectroscopy measurements were carried out at Imperial College's fuel cell lab in order to establish various cell resistance values with time and number of cycles. For this purpose one cell was cycled according to the procedure listed in table 3.6. The procedure is principally the same as in table 3.5, but longer, more complex and includes impedance spectroscopy every time the cell is fully charged.

Table 3.6.: Electrochemical Impedance Spectroscopy Procedure

Step	Description	Data Log Step
1	Rest period (60 minutes)	every 120 seconds
2	Constant current (5 A = 0.05 C) charge until $V_{max} \geq 3.9$ V	for every $\Delta V = 5$ mV
3	Constant voltage (3.9 V) charge until $I_{min} \leq 0.1$ A	every 20 seconds
4	Rest period (60 minutes)	every 120 seconds
5	Constant current (5 A = 0.05 C) discharge until $V_{min} \leq 2.5$ V	for every $\Delta V = 5$ mV
	interrupted by six rest periods (30 minutes); each followed by	every 120 seconds
	constant current (0.4 mA) impedance spectroscopy for 51 frequencies (2,000-0.2 Hz)	for every frequency

First, the rest period of 60 minutes is longer, which further facilitates the cell's return to it's equilibrium state, i.e. its open-circuit voltage (OCV). Second, the galvanostatic charge/discharge is at a lower current (0.05 C). Third, the device, a galvanostatic impedance analyser, induces an AC current at 51 distinct low amplitude signals (2,000-0.2 Hz) when the cell is fully charged and also has rested sufficiently long. After the EIS, the cell is discharged with a pulsed load. This means that the load is not applied continuously during discharge. Instead, six rest periods, during which the cell voltage can return to its OCV, are included in the discharge procedure.

3.4. Conclusions

This chapter has introduced the scientific approach taken for this work. For each of the main chapters (4-5), a first principle analysis is compared against and adjusted to empirical test results from various validation techniques. First principle analyses are executed in the MATLAB and MATLAB Simulink programming environments. They usually follow a quasi-steady approach and ignore transverse vehicle dynamics as well as electrochemical details. The main experimental techniques for this work include the data logs of the *Racing Green Endurance* project, the 2010-2012 *Future Car Challenge*, travel surveys and battery testing data.

4. Nominal Energy Requirements of Electric Vehicles

This chapter deals with the nominal energy consumption of electric vehicles. Nominal energy consumption refers to the level of energy consumed for most of the driving. As illustrated in equation 4.1, energy is the product of force (F) and distance (d).

$$E = F(t)d \tag{4.1}$$

Consequently, the first section of this chapter is devoted to the vehicle driving force F_d. The second section deals with the range requirements of EVs. Finally, the last section concludes this chapter and makes the transition to the subject of the next chapter.

4.1. Electric Vehicle Driving Forces

The vehicle driving force is the force required to keep a road vehicle moving. Everything else being equal, it is independent of the power train type and thus applies to conventional ICEVs as well as to EVs. The following subsections first approximate the nominal vehicle driving force via theoretical assumptions. Then, these nominal driving force values are compared and contrasted with real values from the RGE project and the 2010-2012 Future Car Challenges.

4.1.1. Theoretical Driving Force

The driving force describes the distance-specific energy consumption of a vehicle. While the traction force describes an instantaneous force, the driving force is only valid over a certain distance. Theoretically, the vehicle driving force is influenced by traction forces, vehicle parameters, operating modes, steady and dynamic conditions, performance characteristics, auxiliaries as well as losses. Each are analysed in detail.

Traction Forces

Following Newton's second law of motion, the longitudinal dynamics of a vehicle can be described by the following equation:

$$F_i(t) = F_t(t) - [F_a(t) + F_r(t) + F_c(t)] \tag{4.2}$$

The inertial force of the vehicle F_i on the left hand-side of equation 4.2 is equal to the traction force F_t minus the sum of the aerodynamic drag force F_a, the rolling resistance force F_r and the climbing force F_c.

The inertial force F_i is described by the following ordinary differential equation (ODE):

$$F_i(t) = m_v \dot{v}(t) = m_v \frac{d}{dt} v(t) = m_v a(t) \tag{4.3}$$

The product of the vehicle mass m_v and the instantaneous acceleration *a(t)* is equal to the inertial force. It implies that large inertial forces need to be overcome for heavy vehicles and/or fast accelerations.

The aerodynamic drag force F_a is described by the following expression, which ignores possible headwind or tailwind:

$$F_a(t) = \frac{1}{2} \rho_{air} A_f C_d v(t)^2 \tag{4.4}$$

The density of the ambient air ρ_{air} decreases with an increasing altitude and/or a rise in temperature. Thus, ρ_{air} is greatest in cold climates at sea level and ρ_{air} is smallest in hot climates at

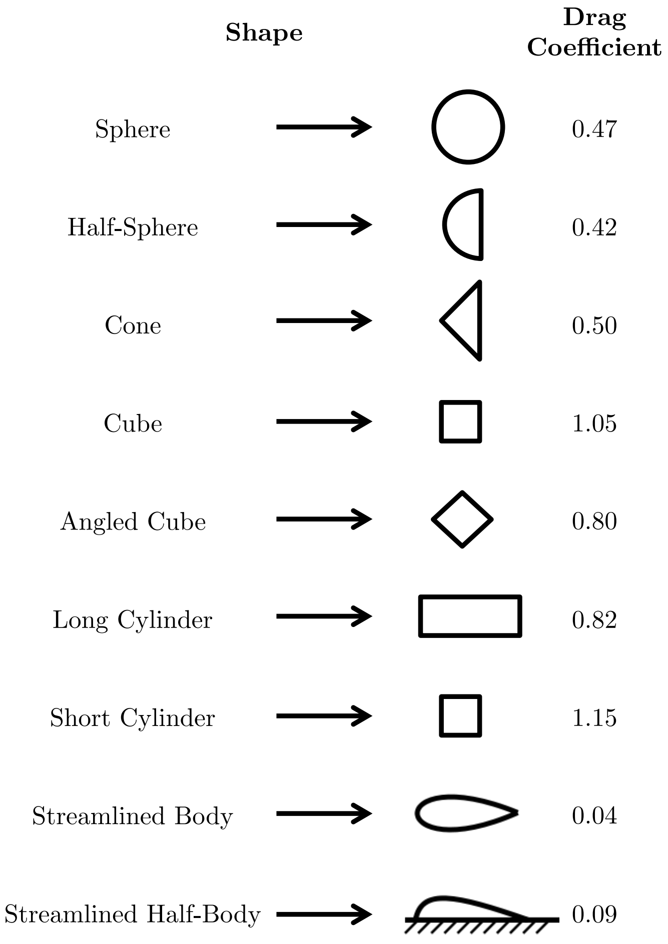
Shape
Drag Coefficient
Sphere
0.47
Half-Sphere
0.42
Cone
0.50
Cube
1.05
Angled Cube
0.80
Long Cylinder
0.82
Short Cylinder
1.15
Streamlined Body
0.04
Streamlined Half-Body
0.09

Figure 4.1.: Measured Drag Coefficients for Various Shapes [140]

high altitudes. At sea level and 15°C air has a density of approximately 1.225 kg/m^3 according to the International Standard Atmosphere (ISA). The frontal area of the vehicle A_f as well as the aerodynamic drag coefficient C_d highly depend upon the design and shape of the vehicle. Figure 4.1 shows the variation of the drag coefficient for different shapes with the same surface area. The experimentally determined C_d is always associated with a particular surface area A_f. For passenger vehicles the frontal area can be approximated:

$$A_f \approx 0.9 \times wheel\,track \times height \tag{4.5}$$

Together A_f and C_d determine how streamlined the vehicle is. The higher the speed, the proportionally bigger the aerodynamic drag force. For every doubling of the vehicle speed the aerodynamic drag force is increased fourfold. It follows that the aerodynamic drag force is smallest if the vehicle is streamlined with a relatively small frontal area and driven at relatively low speeds in high temperature climates at high altitudes. Typical values for the parameters are listed in table 4.1.

The rolling resistance force F_r is described by:

$$F_r(t) = m_v g C_r cos(\alpha) \tag{4.6}$$

F_r is a linear function of the vehicle mass m_v, the gravitational constant g, the rolling resistance coefficient C_r and the cosine of the angle of inclination α. C_r depends on the road surface, the tyre material, the contact area and tyre pressure. Typically, narrow large-diameter highly pressurised tyres have a low C_r. The cosine of α is the horizontal leg in figure 4.2. Thus, the rolling resistance force is minimised with a low vehicle mass, a low rolling resistance coefficient driving on an inclined road.

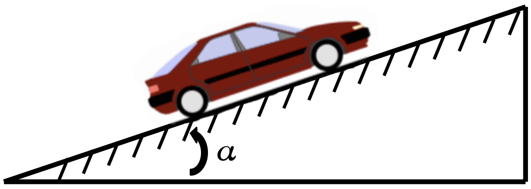

Figure 4.2.: Road Grade Schematic

The climbing force F_c proportionally depends upon the vehicle mass, the gravitational constant and the sine of α as shown in equation 4.7.

$$F_c(t) = m_v g sin(\alpha) \tag{4.7}$$

Demonstrated by equation 4.2, the traction force F_t is equal to the sum of the aerodynamic drag force F_d, the rolling resistance force F_r and the climbing force F_c if the vehicle is neither accelerating nor decelerating. If the vehicle changes its momentum, the inertial force F_i gets added on top. In either case, the traction force is smallest if the vehicle mass, the vehicle frontal area, the aerodynamic drag coefficient, the rolling resistance coefficient and the vehicle speed is minimised. Table 4.1 summarises all aforementioned parameters affecting the traction force and lists typical ranges. The gravitational constant g is assumed to be constant. Following a conservative approach, the air density is also assumed to be constant. Typically, the maximum grade, at which the vehicle can start from standstill, also called gradeability, is 30%. Following simple trigonometry (i.e. $\tan^{-1}(0.3)$), this translates into a 16.7° angle of inclination. For a conservative estimate, we assume 35% to be the maximum road grade.

Table 4.1.: Traction Force Parameters and Typical Values [57, 141]

Parameter	**Sign**	**Typical Value**			**Unit**
		Low		High	
Aerodynamic Drag Coefficient	C_d	0.2	-	0.5	-
Ambient Air Density	ρ_{air}	-	1.23	-	kg/m^3
Frontal Area	A_f	0.5	-	2.5	m^2
Gravitational Constant	g	-	9.81	-	m/s^2
Road Grade	-	0	-	35	%
Rolling Resistance Coefficient	C_r	0.008	-	0.013	-
Vehicle Acceleration	a	0	-	5.0	m/s^2
Vehicle Mass	m_v	750	-	2,000	kg
Vehicle Speed	v	0	-	200	km/h
Wheel Radius	r_w	0.27	-	0.37	m

Vehicle Classes

Based on the vehicle classes first introduced in section 3.3.2 and the parameters from table 4.1, representative vehicle specifications can be assigned. In alignment with the research aim of this work, only passenger road cars are analysed. These can be categorised into mini cars (e.g. Ford Ka or VW Up), small cars (e.g. Ford Fiesta or VW Polo), medium cars (e.g. Ford Focus or VW Golf), large cars (Ford Mondeo or VW Passat) and sport utility vehicles (SUVs) like the Range Rover or VW Touareg. Table 4.2 lists vehicle classes and representative parameter values. This table forms the basis for the following analysis on nominal driving force, range and battery degradation.

Table 4.2.: Vehicle Classes and Representative Parameter Values [57],[141]

	Mini Car	**Small Car**	**Medium Car**	**Large Car**	**SUV**
Euro Car Segment	A	B	C	D	J
m_v [kg]	750	1,000	1,200	1,500	2,000
C_dA_f [m^2]	0.3	0.6	0.7	0.8	1.2
C_r [-]	0.008	0.01	0.011	0.012	0.013

Operating Modes

The traction force required to keep the vehicle moving is only exerted when the vehicle is in traction mode. In theory, there are four possible operating modes for the vehicle power train as shown in table 4.3.

Table 4.3.: Power Train Operating Modes

Operating Mode	Description
Traction	The power source applies a driving force to the wheels
Braking	The mechanical brakes dissipate the kinetic energy of the decelerating vehicle as heat
Recuperating	The kinetic energy from the decelerating vehicle is (partly) recovered and transferred back to an energy storage device (battery, super capacitor, flywheel, etc.)
Coasting	The power source is disengaged and '*the resistance losses of the vehicle are exactly matched by the decrease of its kinetic energy*' [57]

Applying the traction force F_t over a distance d leads to the following expression for the theoretical nominal energy consumption E_{nom}:

$$E_{nom} = \sum F_t(t)d \tag{4.8}$$

Consequently, minimising both the magnitude of the traction force F_t and the relative time spent in traction mode reduces the vehicle's energy consumption for a given distance d. For this purpose we define the traction ratio TR as the relative time spent in traction mode. Practically, it is the time spent on the accelerator relative to driving time. We expect that a higher TR correlates with greater energy consumption and that a lower TR is associated with lower energy consumption. This hypothesis will be checked in section 4.1.2.

$$TR = \frac{Time\,spent\,in\,traction\,mode}{Total\,driving\,time} \tag{4.9}$$

The time spent in traction mode may be calculated by summing up the time steps from the drive cycle, at which the traction force F_t is greater than zero. Ideally, an exact i.e. analytical solution of the ODE introduced with equation 4.2 can be found for this purpose. However, two resistive forces are not explicit functions of time, namely the rolling and climbing resistances. They depend upon the slope of the road α, which varies with position s. Thus, [142] proposed the use of position s instead of time t as the independent variable. The disadvantage of this approach however, is that most sensing devices are time dependent. Therefore, in order for the model to be validated easily, time needs to remain the independent variable. In order to overcome the non-linearity of the rolling and climbing resistances, a piecewise (Δt = 1 s) analytical solution is proposed.

While the vehicle is coasting, the traction force must be equal to zero. Consequently, for the limiting case where $F_t = 0$, equation 4.2 may be rearranged in terms of the coasting velocity v_c.

$$\begin{aligned} \frac{d}{dt}v_c(t) &= -\frac{\rho_{air} A_f C_d \left(v_c(t)\right)^2}{2m_v} - g[cos(\alpha)C_r + sin(\alpha)] \\ &= -A^2 \left(v_c(t)\right)^2 - B^2 \end{aligned} \tag{4.10}$$

A and B are constants for the piecewise analytical solution. For $v_c > 0$ and $\alpha = 0$, equation 4.10 can be integrated in closed form. We extend this solution and also account for a varying road slope:

$$v_c(t) = \frac{B}{A} tan \left[tan^{-1} \left(\frac{B}{A} \right) v_c(0) - ABt \right] \tag{4.11}$$

The main advantage of this solution is that it can be solved analytically and is thus relatively precise for the respective time step. From this the vehicle is in traction mode if the vehicle speed v decreases less than the coasting velocity $v_c(t)$ would decrease when starting at the same initial speed $v_c(0)$. In contrast, the vehicle is in braking or recuperating mode if the vehicle speed v decreases more than the coasting velocity $v_c(t)$ would decrease when starting at the same initial speed $v_c(0)$.

Figure 4.3 shows how the traction ratio TR can be applied to the NEDC. The black line shows the speed vs. time trace of the NEDC, whereas the red line highlights when the traction mode is on ($y = 40$) or off ($y = 0$) for a medium-sized car based on the parameters of table 4.2. The upper and lower bounds for the red line are chosen arbitrarily and are for demonstration purposes only. Speed and acceleration time traces of the NEDC and other international driving cycles can be found in appendix D. Figure 4.3 shows that a medium-sized car following the NEDC is in traction mode for roughly 58% of the time. No time is spent coasting for this particular example. Thus, the remaining 42% of the time are spent braking. It also means that

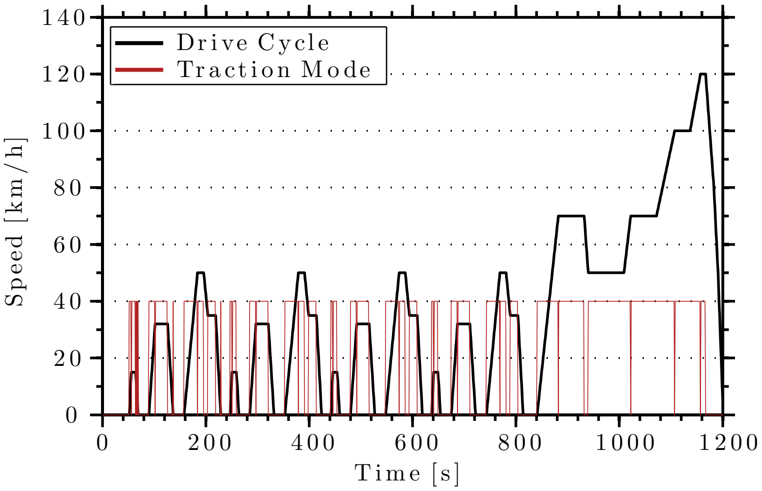

Figure 4.3.: Traction Ratio Applied to NEDC for a Medium Sized Car

the magnitude of the mean acceleration (0.53 m/s^2) is lower than the magnitude of the mean deceleration (0.82 m/s^2).

Steady Speed Conditions

This subsection works out the theoretical driving force requirements under steady speed conditions. On a horizontal road and at steady speed the traction ratio TR is equal to 1 throughout the drive cycle. This means that the vehicle is not cruising, recuperating or braking at any point in time. Also, inertial forces are irrelevant under these circumstances. For a mean steady speed and zero incline the mean traction force F_t, inertial and climbing forces can be ignored. Thus, under these circumstances only aerodynamic drag forces as well as rolling resistance forces are applied.

Figure 4.4 shows the forces required to keep different vehicle classes moving. Although the SI-unit for force is Newtons [N], it can also be expressed in terms of watt-hours per kilometre [Wh/km]. Watt-hours per kilometre will be used extensively in the forthcoming analysis as the normalised energy consumption unit for electric vehicles. It greatly simplifies the analysis of EV driving force and energy requirements. The equivalent units of Wh/km for ICEVs are miles per (Imperial) gallon (mpg_{imp}) in the UK, miles per (US) gallon (mpg_{US}) in the US and litres per 100 kilometres (l/100 km) in most of Europe and China.

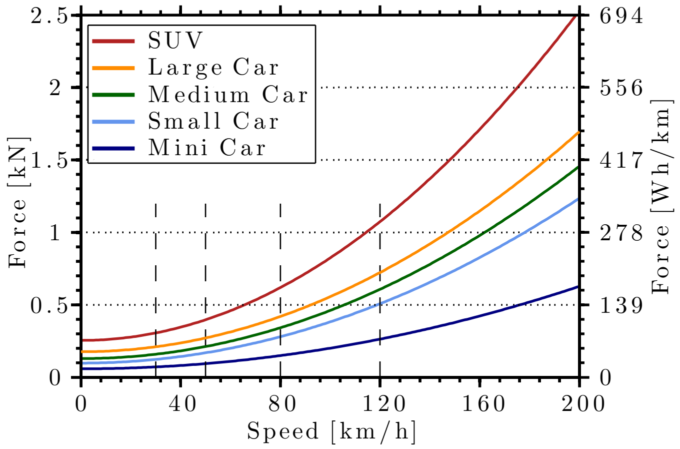

Figure 4.4.: Theoretical Vehicle Driving Force at Steady Speed and Zero Incline

The two units of force on the left and right hand-side in figure 4.4 are plotted against vehicle speed. It can be seen that the force increases quadratically with speed due to aerodynamic drag. For the frequent urban and suburban speed limits around 30, 50, 80 and 120 km/h the theoretical vehicle driving force for a medium-sized car ranges between 44-169 Wh/km. While at low speeds up to 25 km/h the ratio of the driving force between the biggest (SUV) and the smallest vehicle class (mini car) is about 4.3, this ratio decreases to about 4.0 at very high speeds around 200 km/h. This means that at low speeds the normalised energy consumption of SUVs compared with mini cars is proportionally larger than at high speeds. The reason for this is that the rolling resistance, which is predominant at low speeds (see figure 4.5), is exactly $4.\bar{3}$ times greater for the SUV than that of the mini car. The ratio of the two aerodynamic drag forces, which dominate at high speeds, is exactly 4.0. Also, the ratio of the theoretical driving forces at very high speeds (200 km/h) and at standstill (0 km/h) is about 10 for all vehicle classes. This implies one order of magnitude difference in distance-specific energy consumption at high and low speeds. Table 4.4 summarises traction forces for various vehicle sizes at different steady speeds.

Table 4.4.: Theoretical Driving Forces at Different Steady Speeds

Speed	**Driving Force [Wh/km]**				
[km/h]	**Mini Car**	**Small Car**	**Medium Car**	**Large Car**	**SUV**
0	16.35	27.25	35.97	49.05	70.85
30	19.91	34.37	44.27	58.54	85.09
50	26.24	47.02	59.04	75.41	110.39
80	41.66	77.87	95.02	116.54	172.09
120	73.29	141.14	168.84	200.90	298.63
150	105.33	205.20	243.58	286.32	426.75
200	174.53	343.61	405.05	470.86	703.57

Multiplying equation 4.2 with a mean velocity $\bar{v}$ and accounting for an average auxiliary power load $\bar{P}_{aux}$, which is independent of vehicle speed, yields the theoretical steady driving power.

Auxiliary systems in a vehicle are all appliances in a car, which consume energy but are not related to the propulsion of it. Due to an increasing demand for on-board safety, information, comfort and entertainment systems, auxiliary systems have become larger and more sophisticated. Typically, these include air conditioning (A/C), heating, power steering, power brakes, wipers, lights, window lifts, locks, navigation systems, damping systems, adjustable seats, audio and other entertainment systems. Because of its non-motive nature, auxiliary power is independent of vehicle speed. Consequently, mean auxiliary powers are assumed as listed in table 4.5:

Table 4.5.: Assumed Mean Auxiliary Powers

Mean Auxiliary Power [W]				
Mini Car	**Small Car**	**Medium Car**	**Large Car**	**SUV**
500	750	1,000	2,000	3,000

For a medium-sized car and assuming no losses and steady speed, the resulting total and constituent theoretical powers are shown in figure 4.5. There is a striking dependence of the total driving power on aerodynamic drag, especially at speeds above 60 km/h. At low speeds, here up to 30 km/h, driving power is controlled by the auxiliary load. At medium speeds, for this example between 30 and 60 km/h, the rolling resistance dominates. Any change in the

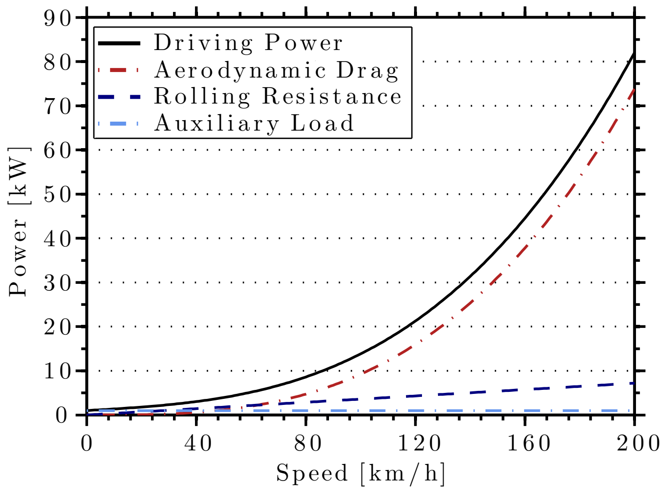

Figure 4.5.: Total and Constituent Theoretical Vehicle Driving Powers at Steady Speed for a Medium-Sized Car

vehicle parameters (m_v, $C_d A_f$, C_r and/or $\bar{P}_{aux}$) affects the exact speed ranges of the respective control regime, but not the general trend. For mountainous regions the climbing power is very significant as well. This means that for nominal driving, which we assume to be at medium speeds and with relatively low incline angles (<1°), we expect the rolling resistance to dominate the driving power at steady speed. The resulting driving powers for the different vehicle classes, which also consider mean auxiliary loads from table 4.5, are listed in table 4.6.

Table 4.6.: Theoretical Driving Powers at Different Steady Speeds

Speed [km/h]	Driving Power [kW] Mini Car	Small Car	Medium Car	Large Car	SUV
0	0.50	0.75	1.00	2.00	3.00
30	1.10	1.78	2.33	3.76	5.55
50	1.81	3.10	3.95	5.77	8.52
80	3.83	6.98	8.60	11.32	16.77
120	9.30	17.69	21.26	26.11	38.84
150	16.30	31.53	37.54	44.95	67.01
200	35.41	69.47	82.01	96.17	143.71

In a similar fashion, the energy consumption required to drive a certain distance can be calculated as a function of steady vehicle speed. Figure 4.6 compares the energy consumption at different steady speeds for various vehicle sizes introduced with table 4.2. It shows how for every combination of vehicle parameters there is an optimum steady speed, at which the vehicle consumes least energy. Interestingly, this speed for all vehicle sizes is around 40 km/h. The figure also demonstrates that at medium speeds between 20-100 km/h the energy consumption does not change significantly with speed. In contrast, at very low (<20 km/h) and at high speeds (>100 km/h) energy consumption is particular speed-sensitive.

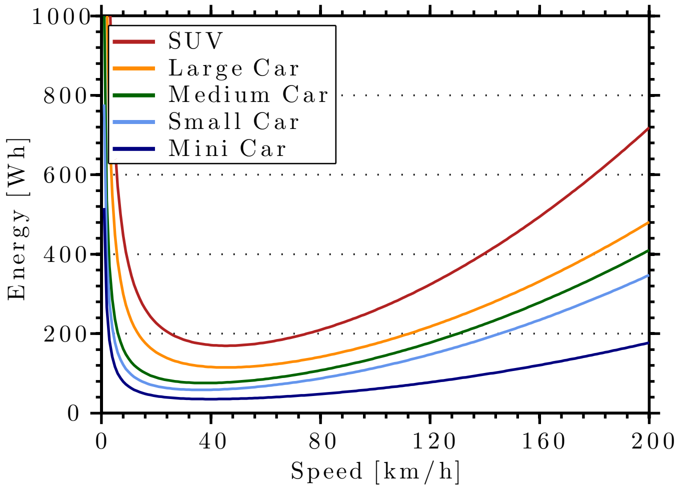

Figure 4.6.: Theoretical Energy Consumption for Driving 1 km at Steady Speed

Due to road speed limits, congestion and the assumption that most car journeys are relatively short (i.e. <50 km), we expect the nominal driving force for electric vehicles F_d to only have a relatively small standard deviation between different journeys. The standard deviation σ is a common metric to determine the variation of some data with respect to its mean. We also expect auxiliary loads to be dominant at very low steady speeds, rolling resistance to be overriding at medium steady speeds and aerodynamic drag to have a stronger impact at high steady speeds.

Variable Speed Conditions

The previous subsection ignored inertial forces, varying road gradients and assumed an uninterrupted application of the traction force. In contrast, this subsection deals with more realistic dynamic speed conditions with varying road grades, under which the traction force is applied only for a portion of the driving schedule. Referring back to equations 4.2, 4.3 and 4.7, dynamic driving forces can be computed. Figure 4.7 shows the potential impact of a range of accelerations applied at different speeds for the five vehicle classes introduced earlier. The maximum acceleration (5 m/s^2) corresponds to a vehicle accelerating from standstill to 100 km/h within roughly 5.6 seconds. Sports cars and other high performance may accelerate faster, but we expect maximum accelerations for the vehicle classes listed in table 4.2 to be less than 5 m/s^2. Moreover, we expect nominal accelerations to not exceed 2 m/s^2. For all five vehicle classes, the maximum theoretical driving powers (244, 347, 415, 513 and 699 kW) occur at the maximum speed combined with the maximum acceleration. However, we expect an inverse relationship between the frequency of high speed and high acceleration events for nominal driving; low speed events combined with high acceleration events or high speed events with low acceleration events to occur relatively frequently. Therefore, figure 4.7 should be treated with great caution. It only shows theoretical driving powers, which especially at the high end of the speed and acceleration ranges are unrealistic as evidenced by the following paragraphs.

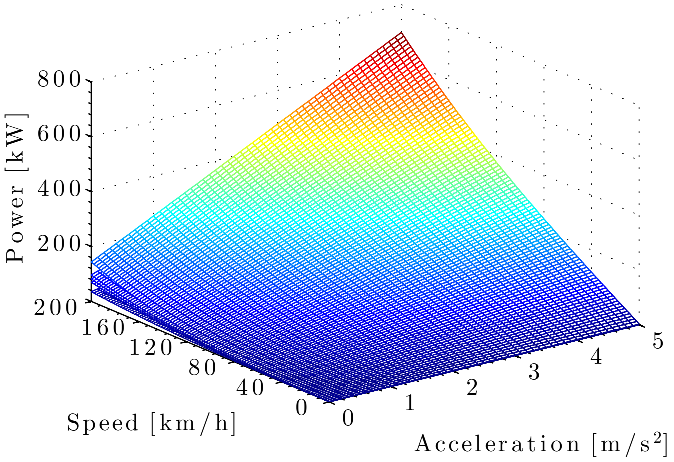

Figure 4.7.: Theoretical Driving Powers at Varying Speeds and Accelerations

Similarly, the theoretical driving powers at varying speeds and road grades can be computed. For a road grade range up to 35% figure 4.8 shows the resulting theoretical driving power requirements. Again, maximum values (170, 250, 298, 366 and 504 kW) are extremely high and occur at maximum speed combined with maximum road grade. Like with theoretical powers at varying speeds and accelerations, we expect high speed events to happen at low road gradients, and high road gradient events to happen at low speeds because of a combination of speed limits, congestion and safety concerns.

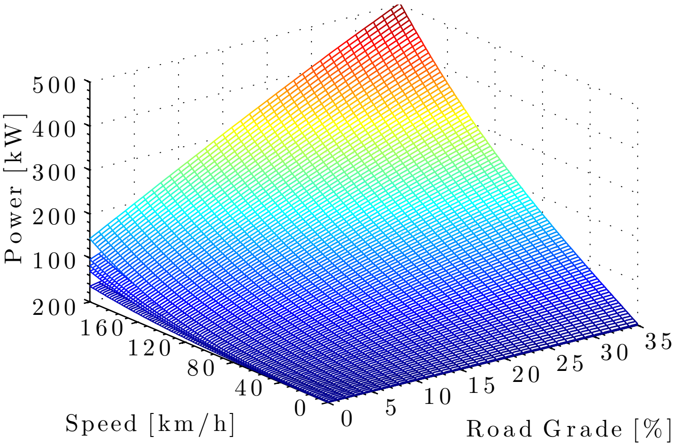

Figure 4.8.: Theoretical Driving Powers at Varying Speeds and Road Grades

More reasonable power requirements are retrieved from a simple gradeability analysis. In this scenario, the vehicle is accelerated from standstill to 35 km/h with an acceleration of 2 m/s^2 at an inclination of 30%. Table 4.7 lists the respective power requirements for the different vehicle categories.

In order to assess fuel/energy consumption requirements under dynamic conditions and on a comparable basis, standard drive cycles first introduced in section 2.2.3 are applied. For the

Table 4.7.: Theoretical Power Requirements for Gradeability Test

Efficiency [%]	**Power** [kW] **Mini Car**	**Small Car**	**Medium Car**	**Large Car**	**SUV**
100	36.36	48.85	58.82	74.37	99.75
90	40.39	54.28	65.36	82.64	110.84
80	45.44	61.07	73.53	92.96	124.69

European NEDC, the American FTP-75 and the Japanese 10-15 mode (see appendix D), table 4.8 lists some reference values. The table demonstrates how on average both mean vehicle speeds and mean accelerations for international drive cycles are comparatively low with the assumptions made in the previous paragraph. Only real-world test data (see section 4.1.2) can help in making a good estimate with regards to nominal speeds and accelerations. Most OEMs apply their own custom drive cycles in addition to the standard ones [13]. Meanwhile, the mean distance-specific energy consumption ($\bar{F_d}$ [Wh/km]) for different vehicle classes based on the NEDC as a reference dynamic cycle can be calculated.

Table 4.8.: International Drive Cycle Parameters [143]

	Mean Speed [km/h]	**STD Speed [km/h]**	**Mean Acceleration [m/s^2]**	**Maximum Acceleration [m/s^2]**	**Mean Deceleration [m/s^2]**	**Maximum Deceleration [m/s^2]**
NEDC	32.26	8.64	0.53	1.04	-0.82	-1.39
10-15 Mode	22.72	6.03	0.56	0.79	-0.65	-0.83
FTP-75	34.08	7.13	0.51	1.72	-0.58	-1.50
∅	**29.68**	**7.27**	**0.53**	**1.19**	**-0.68**	**-1.24**

Relating back to the traction ratio TR (see figure 4.3), two extreme scenarios may be thought of. First, the vehicle follows the drive cycle without recuperating inertial energy (no recuperation). Second, the vehicle recuperates all inertial energy (full recuperation, i.e. 100% conversion efficiency from kinetic into chemical, electrical or mechanical energy). Figure 4.9 shows the theoretical power distribution for different vehicle classes with parameters based on table 4.2 following the NEDC. Also, mean auxiliary powers based on table 4.5 are assumed. The figure shows that the theoretical maximum driving power required to follow this speed-time trace (56 kW for a SUV) is more than one magnitude below the maximum theoretical driving power at maximum speed and maximum acceleration (699 kW) from the previous paragraph. The resulting mean distance-specific energy consumptions ($\bar{F_d}$ in Wh/km) are listed in table 4.9. The table also considers mean losses in the vehicle's power train. Losses in the context of vehicle energy consumption refer to all inefficiencies of all power consumers, i.e. these include propulsion losses as well auxiliary losses. In general, propulsion losses include power conversion

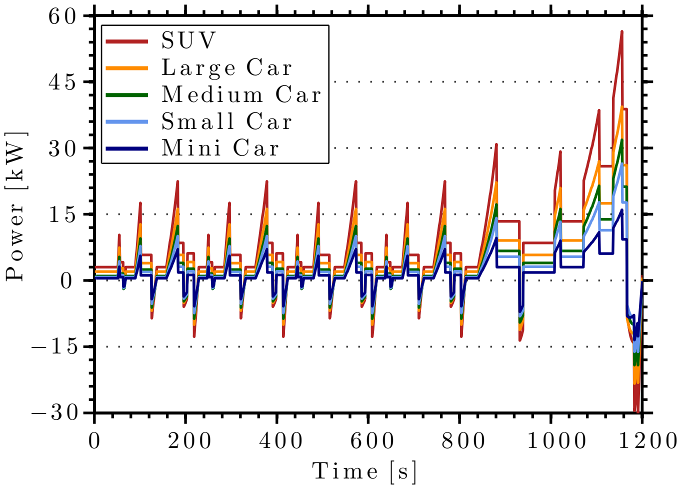

Figure 4.9.: Theoretical NEDC Driving Powers with Full Recuperation

Table 4.9.: Theoretical Driving Forces (NEDC)

Efficiency [%]	Recuperation	Mean Driving Force [Wh/km] Mini Car	Small Car	Medium Car	Large Car	SUV
100	None	67.15	107.11	133.23	189.22	274.10
	Full	55.63	92.83	116.32	167.30	245.45
90	None	74.61	119.01	148.04	210.24	304.56
	Full	61.81	103.15	129.25	185.89	272.72
80	None	83.93	133.89	166.54	236.53	342.63
	Full	69.54	116.04	145.40	209.13	306.81

losses, friction/heat losses, vehicle slip, transverse forces and damping. Electric vehicle power efficiencies are thus defined as the ratio of the useful power output (propulsion, lighting etc.) and the required power input (battery power).

From table 4.9 the respective relative recuperation gains G_r may be calculated according to the following relationship:

$$G_r = 100 \left(1 - \frac{\bar{F}_{d(\text{w. recuperation})}}{\bar{F}_{d(\text{w/o recuperation})}} \right) \qquad [\%] \tag{4.12}$$

Therefore, recuperation of inertial energy is most beneficial for a mini car and least beneficial for a SUV in relative terms as shown in table 4.10. Also, for other vehicle classes and applied to other driving cycles the trend is clear: The smaller the vehicle, the greater the relative effect of regenerative braking. The reasoning behind this counter-intuitive phenomenon is not straightforward. The magnitude of the positive traction power is significantly larger than the negative regenerative power (see figure 4.9) as neither the aerodynamic drag (P_a), nor the rolling resistance (P_r) or the mean auxiliary power ($\bar{P}_{aux}$) can be recuperated. Only inertial powers can be recuperated. Thus, in the absence of P_a, P_r and $\bar{P}_{aux}$ the relative recuperation benefits are the same for all vehicle categories. But since only inertial powers can be recuperated, the ratio of the driving force with recuperation and the driving force without recuperation widens across different vehicle categories.

Table 4.10.: Relative Recuperation Benefits for Different Drive Cycles[1]

	Relative Recuperation Benefit [%]				
	Mini Car	**Small Car**	**Medium Car**	**Large Car**	**SUV**
NEDC	17.15	13.33	12.69	11.58	10.45
10-15 Mode	30.46	25.34	23.90	20.58	18.74
FTP-75	12.18	5.97	3.69	1.57	0.13

Sensitivity Analysis

As seen from the previous paragraphs, the vehicle parameters (m_v, C_dA_f and C_r) introduced with table 4.2 as well as the mean auxiliary power $\bar{P}_{aux}$ significantly affect the mean driving force $\bar{F}_d$ required to keep a vehicle moving. Therefore, the mean driving force $\bar{F}_d$ for a particular drive cycle can be expressed in terms of these vehicle parameters only [57].

$$\bar{F}_d = \frac{1}{d_{tot}} \left(\frac{1}{2}\rho_{air} C_d A_f \sum_{i \in TR} v^3 t + m_v C_r g \sum_{i \in TR} vt + m_v \sum_{i \in TR} avt + \bar{P}_{aux} \sum t \right) \tag{4.13}$$

---

[1] based on equation 4.12

Equation 4.13 treats the drive cycle parameters (d_{tot}, $\sum\limits_{i\in TR} v^3t$, $\sum\limits_{i\in TR} vt$, $\sum\limits_{i\in TR} avt$ and $\sum t$) as constants. $\sum\limits_{i\in TR}$ refers to the partial summation of those instances, when the vehicle is in traction mode. The constants represent the total distance d_{tot} as well as the partial summations of time (t), speed (v) and acceleration (a) quantities only for the time intervals, during which the vehicle is in traction mode. The mean auxiliary power $\bar{P}_{aux}$ is assumed to be on for the entire duration of the drive cycle irrespective of the vehicle operation mode. Applying equation 4.13 to the NEDC and assuming a vehicle without an energy recuperation device (NR = no recuperation) leads to the following expression:

$$\bar{F}_{d,NEDC,NR} \approx 52.17 C_d A_f + 2.26 m_v C_r + 0.03 m_v + 0.03 \bar{P}_{aux} \qquad \text{[Wh/km]} \tag{4.14}$$

The equation simplifies the determination of driving force requirements for the NEDC without losing accuracy. The maximum relative difference between equation 4.14 and the values from table 4.9 is 0.05%. Mean efficiencies can be applied in a relatively straightforward manner and the results are expressed Wh/km.

For a vehicle with an ideal energy recuperation device ($\eta = 1$) the result changes slightly. Here, positive and negative inertial forces are exactly balanced and thus can be neglected. Both, the weight of the aerodynamic drag and that of the rolling resistance increases with respect to equation 4.14. Because the mean auxiliary power $\bar{P}_{aux}$ is still applied throughout the entire drive cycle, its weight does not change.

$$\bar{F}_{d,NEDC,FR} \approx 62.14 C_d A_f + 2.73 m_v C_r + 0.03 \bar{P}_{aux} \qquad \text{[Wh/km]} \tag{4.15}$$

The accuracy of this equation (FR = full recuperation) with regards to the reference values from table 4.9 is lower. The maximum error is 5.75%.

Based on equations 4.14-4.15, the relative influence of the aforementioned vehicle parameters can be evaluated on the basis of a sensitivity analysis. Equation 4.16 defines the sensitivity S_p of the mean driving force for the NEDC $\bar{F}_{d,NEDC}$ with respect to one of the vehicle parameters, denoted p.

$$S_p = \lim_{\delta p \to 0} \frac{\left[\bar{F}_{d,NEDC}(p+\delta p) - \bar{F}_{d,NEDC}(p)\right] / \bar{F}_{d,NEDC}(p)}{\delta p / p} \tag{4.16}$$

Equation 4.16 can be rearranged to:

$$S_p = \frac{\partial \bar{F}_{d,NEDC}}{\partial p}(p) \frac{p}{\bar{F}_{d,NEDC}(p)} \tag{4.17}$$

Thus, the variation of the mean driving force $\partial \bar{F}_{d,NEDC}$ divided by the variation of any of the parameter values ∂p (∂m_v, $\partial (C_d A_f)$, ∂C_r or $\partial \bar{P}_{aux}$) multiplied by the ratio of the parameter value p and the mean driving force $\bar{F}_{d,NEDC}$ yields the sensitivity S_p. The partial derivatives for both recuperation cases are listed in table 4.11. The full recuperation case considers the

Table 4.11.: Partial Derivatives for the Mean Driving Force Applied to the NEDC

No Recuperation	Full Recuperation
$\frac{\partial \bar{F}_{d,NEDC}}{\partial(m_v)} = 2.26C_r + 0.03$	$\frac{\partial \bar{F}_{d,NEDC}}{\partial(m_v)} = 2.73C_r$
$\frac{\partial \bar{F}_{d,NEDC}}{\partial(C_d A_f)} = 52.17$	$\frac{\partial \bar{F}_{d,NEDC}}{\partial(C_d A_f)} = 62.14$
$\frac{\partial \bar{F}_{d,NEDC}}{\partial(C_r)} = 2.26m_v$	$\frac{\partial \bar{F}_{d,NEDC}}{\partial(C_r)} = 2.73m_v$
$\frac{\partial \bar{F}_{d,NEDC}}{\partial(\bar{P}_{aux})} = 0.03$	$\frac{\partial \bar{F}_{d,NEDC}}{\partial(\bar{P}_{aux})} = 0.03$

entire drive cycle (i.e. positive and negative driving forces) while the no recuperation case only considers those instances, when the vehicle is in traction mode (i.e. when the driving force is positive).

With this information, equation 4.17 can be solved for the various vehicle sizes. Figure 4.10 shows the resulting four sensitivities for the non-recuperating case as well as for the full-recuperating case applied to mini cars, small cars, medium-sized cars, large cars and SUVs. For vehicles without recuperation capacity (4.10a) the sensitivity S_{m_v} is by far the most important for all vehicle classes. Thus, reducing the vehicle's mass has the single biggest energy saving potential for those vehicles. The smaller the vehicle the bigger the sensitivity of vehicle mass. Second, the sensitivity $S_{C_d A_f}$ is particularly important for small to medium-sized cars. For large cars and SUVs the sensitivity $S_{\bar{P}_{aux}}$ is very significant.

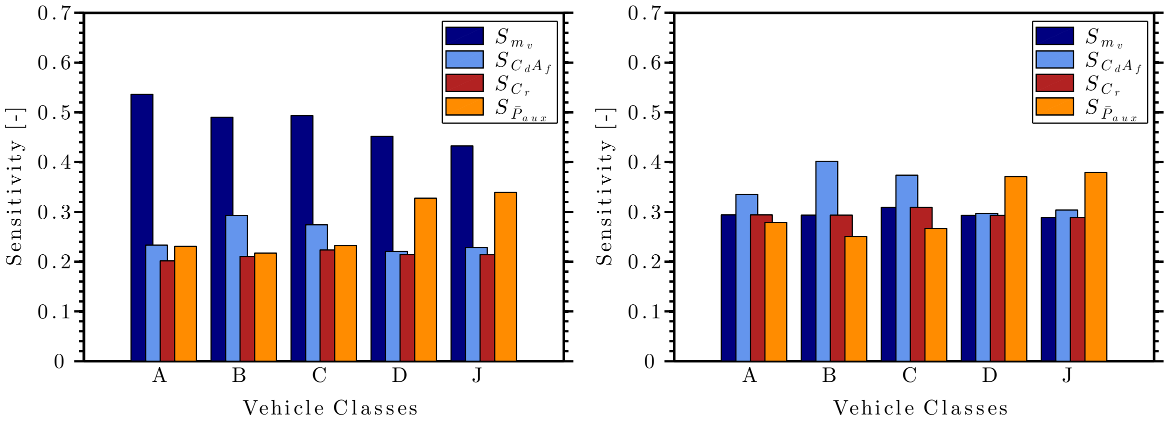

(a) No Recuperation **(b) Full Recuperation**

Figure 4.10.: Sensitivities of the Mean Driving Force with Respect to Vehicle Parameters

The mean driving force for vehicles with an ideal recuperation device is not as sensitive to vehicle mass changes as for vehicles without that capacity (see figure 4.10b). This is because inertial forces, which are very mass-dependent, are ignored for this calculation. For mini cars, small cars and medium-sized cars the sensitivity $S_{C_d A_f}$ is dominant. Again, for large cars and

SUVs the sensitivity $S_{\bar{P}_{aux}}$ is very significant.

4.1.2. 'Real' Driving Force

'Real' driving forces can vary significantly according to a number of parameters. In addition to the aforementioned traction force requirements, operating modes, steady and dynamic characteristics, auxiliary powers and losses, there are numerous more variables, which affect the total driving force. These include the local terrain, which may vary from being flat to very mountainous, and individual driving behaviour. The following paragraphs compare mean driving force $\bar{F}_d$ values from the RGE project and the 2010-2012 Future Car Challenges.

Racing Green Endurance

This subsection derives the nominal driving force of the SRZero required at its battery terminals. Even though the Racing Green Endurance (RGE) SRZero is designed to be a sports car, it can be best compared with a medium-sized car in terms of its specifications (compare with table 4.2). The SRZero is introduced in section 3.3.1 with its specifications listed in table 3.1. Its kerb mass (m_v = 1,150 kg) compares with an estimated vehicle mass for medium-sized cars of 1,200 kg. Also, its drag coefficient ($C_d A_f$ = 0.55) is smaller, but not far off from that of a medium sized car ($C_d A_f$ = 0.7). The rolling resistance coefficient C_r is 0.011 for both, but only an estimate as experimental data is unavailable.

Figure 4.11 shows the front wheel speed distribution. This information is retrieved from one Hall effect sensor placed at the front left wheel. The figure shows that during the RGE trip, the driving was relatively disciplined. This means that the vehicle was accelerated from standstill up to a cruising speed of ≈80 km/h and held there for most of the time. Speeds above 100 km/h are relatively rare (<0.5%), which is not surprising given the road conditions, speed limits

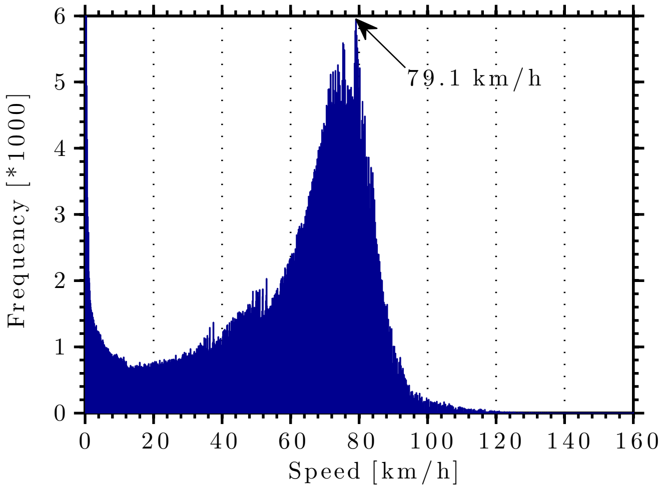

Figure 4.11.: Speed Distribution for SRZero

and congestion along the Pan-American Highway. The figure also reveals that speeds above 160 km/h are extremely rare in this case and that the initial guesses, which led to the custom-design of the electric motors, were relatively good. The electric motors have been custom-wound to achieve their peak efficiency at ≈80 km/h. If anything, this estimate was too high as the mean speed while driving was 51.49 km/h. Unfortunately, the speeds cannot be related to specific altitudes as the GPS tracker failed to function after two days of driving. Thus, it is assumed that the altitude profile for the RGE trip is flat on average.

Similarly, the acceleration distribution shows that much lower acceleration values were typically required than what was theoretically expected in the previous subsection (4.1.1). Figure 4.12 shows the acceleration distribution ranging from -2 to 2 m/s^2. The histogram is symmetric for positive accelerations and negative accelerations (decelerations). Accelerations above 2 m/s^2 only account for less than 0.04% of all occurrences. This may be attributed to the SRZero's relatively heavy weight, but also to gentle driving behaviour. Nevertheless, the SRZero participated in regular traffic conditions for more than 26,500 km (i.e. almost twice the average annual mileage in the UK; see table 4.15). This demonstrates that medium speed (v_{max} = 160 km/h) and acceleration (a_{max} = 2 m/s^2) performance characteristics can be regarded as sufficient for most driving conditions. For a medium-sized car this means to overcome a minimal translational inertial force:

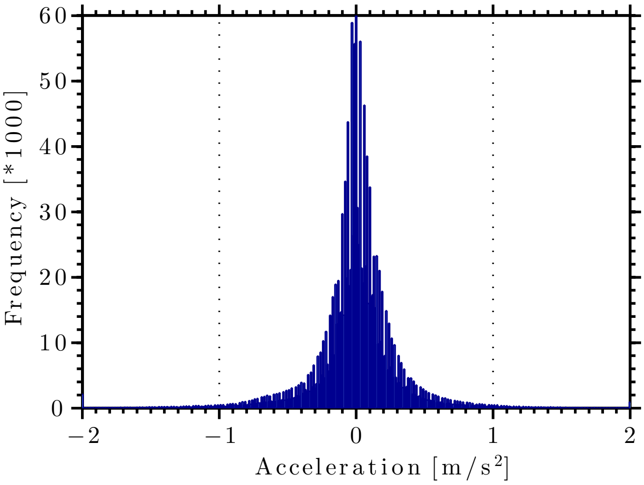

Figure 4.12.: Acceleration Distribution for SRZero

$$F_{i,min} = m_v a_{max} = 1,200 \text{ kg} \cdot 2 \text{ m/s}^2 = 2.4 \text{ kN (667 Wh/km)} \tag{4.18}$$

Equation 4.18 can be used to express the power train requirements in terms of rotational forces as well. Therefore, the minimum inertial torque for a medium-sized car with a total wheel radius of 32 cm can be approximated:

$$\tau_{i,min} = F_{i,min} r = 2,400 \text{ N} \cdot 0.32 \text{ m} = 768 \text{ Nm} \tag{4.19}$$

The required torque $\tau_{i,min}$ is distributed among the driving wheels, which usually are either the two front or the two rear wheels. Some vehicles are also equipped with a four-wheel drive system.

Dynamic torque values are difficult to obtain directly since electromagnetic effects constantly change the interaction between the rotating drive shaft of the electric motor and the 'static' vehicle chassis. Consequently, torque values are frequently estimated using constants. The torque constant K_T for electric motors is given by:

$$K_T = \frac{\tau}{I} \qquad [\mathrm{Nm/A}] \tag{4.20}$$

Thus, K_T can be experimentally determined from the ratio of the desired torque τ and the required current I at different temperatures. In the case of the SRZero, the motor input current I is assumed to be equal to the AC output current from the motor controller (MC) $I_{MC_{AC}}$. The AC output current from the motor controller again is an approximation:

$$I_{MC_{AC}} = \sqrt{\frac{I_q^2 + I_d^2}{2}} \tag{4.21}$$

It is the root mean square (RMS) value of the d- and q- axis (direct-quadrature-zero) component stator currents, which can be measured directly. By combining equations 4.20-4.21 the output torque τ_{out} may be calculated. The output torque, also referred to as the feedback torque, is the actual torque delivered at the wheels, which is different from the requested torque by the driver. The requested torque by the driver is proportional to the pedal position irrespective of the driving resistances.

Figure 4.13 shows the SRZero output torque range as a function of AC motor controller output current. While driving forward, the torque constant K_T is positive and equal to the slope of the nearly linear relationship between current and torque. Hence, the nominal torque constant

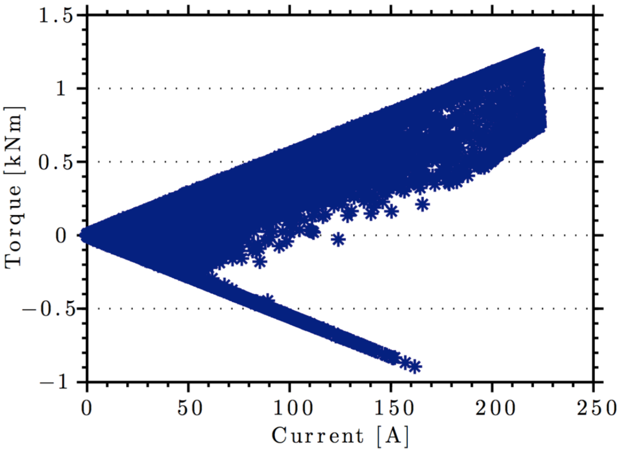

Figure 4.13.: MC Output Currents vs. Output Torque Values

value is equal to 5.5 Nm/A. While reversing, the torque constant has the same magnitude, but is negative. Figure 4.13 shows that the output torque ranges from zero up to 1,300 Nm, which is the maximum rated torque for the two electric motors combined. This value is almost twice as large as the minimum inertial torque calculated in equation 4.19. However, as shown in figure 4.14 the nominal output torque is only around 100 Nm. The figure illustrates the total torque distribution of the SRZero for the duration of the entire journey. Negative torque values indicate regenerative braking, positive ones indicate traction. Three peaks stand out: First, at around -240 Nm, when most regenerative braking is undertaken. Second, at zero Nm when the vehicle is in neutral mode (i.e. when the electric motors are electrically disconnected from the wheels) or the mechanical brakes are applied. And third, at roughly 100 Nm when the vehicle is cruising at its nominal speed of 80 km/h (compare with figure 4.11). Combined torque values above 500 Nm only occur for about 0.83% of the time. Thus, real nominal torque output values for medium-sized cars in standard driving conditions are relatively low (≈100 Nm). Despite this, high output torque values (>400 Nm) were crucial during the test drive across the Americas, especially when overtaking lorries at steep mountain passes.

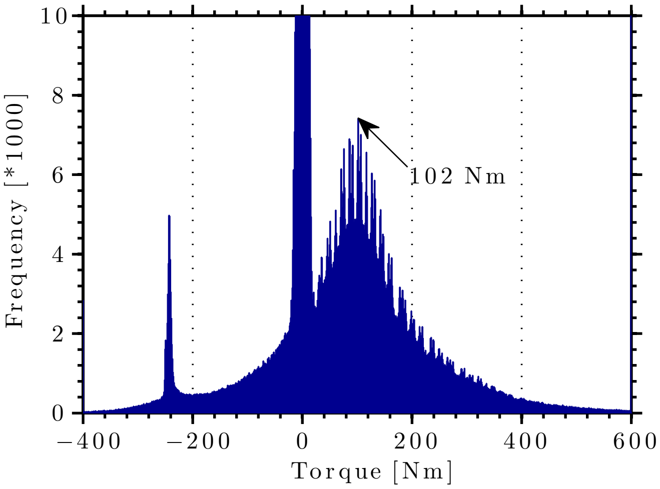

Figure 4.14.: Torque Distribution for SRZero

Similar to equation 3.2, the 'tank-to-wheel' electric distance-specific energy consumption or driving force requirements may be calculated as follows:

$$F_d = \frac{\sum V_{tot}(t) I_{DC}(t) \Delta t}{d} \tag{4.22}$$

The total instantaneous battery power is given by the product of the battery pack voltage $V_{tot}(t)$ and the DC battery current $I_{DC}(t)$. Its time integral yields the energy consumption. For discrete time intervals this can be simplified to a summation. Then, the energy consumed is divided by the distance d driven within that specific time frame.

Following this equation, figure 4.15 shows the driving force requirements for every single RGE

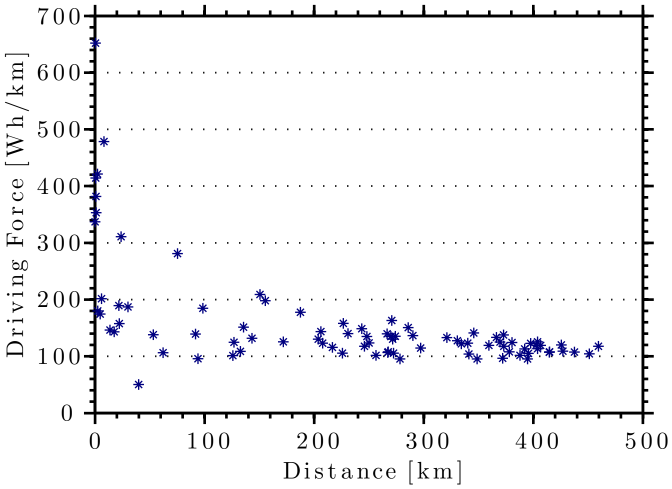

Figure 4.15.: Driving Force Requirements vs. Distance for SRZero

battery cycle as a function of distance. One battery cycle in this context refers to every partial or full charge followed by a partial or full discharge. Conventionally, the notation only refers to full charges and full discharges. However, under real driving conditions this is impossible to achieve for a number of reasons: First, due to degradation a 'full' charge/discharge decreases with time and number of cycles (see chapter 5). Second, driving distances, altitude profiles, road conditions and driving behaviour may vary significantly between cycles. And third, charging conditions (high/low charging power, reliability, current sensing tripping devices etc.) may vary significantly as well leading to alternating charges.

The obvious observation from figure 4.15 is that the driving force F_d is reduced with an increasing distance d. Therefore, the longer the distance driven, the lower the distance-specific energy consumption. Several reasons may explain this: First, the SRZero was designed as a long-distance EV (see section 3.3.1). Second, long distances are usually driven in rural environments on highways or other main roads at medium steady speeds (≈60-120 km/h). Third, the driving behaviour naturally changes a priori in anticipation of a long drive with an EV. Short journeys in contrast are often associated with urban driving, which involves very energy-intensive stop-and-go driving. Additionally, there have been several press and promotional events, during which the SRZero was driven very hard. Ignoring these sprint events (i.e. distances <10 km), the average driving force for the SRZero across all cycles was 131.43 Wh/km. The theoretical mean driving force for a medium-sized car with an efficiency of 90% ranges between 129.25-148.04 Wh/km (compare with table 4.9).

Future Car Challenge

The results of the 2010-2012 Future Car Challenges (FCC) offer the unique opportunity to compare the 'real-world' driving forces of 52 EVs ranging from mini cars up to light duty vehicles (LDVs). First, results from 2010-2011 are presented. Then, the results of the 2012

FCC, which featured a slightly different route, are introduced.

Both the inaugural 2010 FCC and the 2011 FCC took place along the same route shown in figure 4.16 on the first Saturday morning in November. Temperatures along the route on an early November morning are usually below 10 °C. The route covered city driving in Brighton, Crawley and London and followed the major A23 road for almost half of its distance. Therefore, rural and urban drives were included. No traffic restrictions were in place in order to keep the driving conditions as realistic as possible. Additionally, the 92 km long route included hill climbs of up to 154 m as shown in figure 4.17. It is expected that during descent from the four major elevations, the regenerative braking potential is greatest. The start of the FCC was at Madeira Drive in Brighton, which is right by the sea. The finish is at Waterloo Place in London, only 500 m away from the river Thames. Therefore, the total gain in altitude is minimal (5 m).

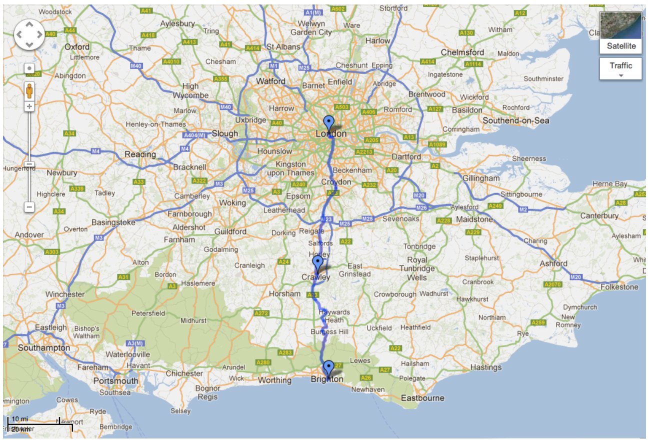

Figure 4.16.: 2010-2011 FCC Route [144]

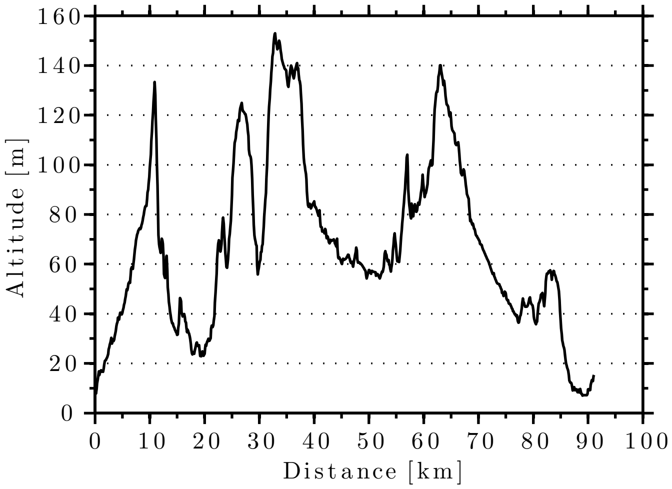

Figure 4.17.: 2010-2011 FCC Altitude Profile [144]-[145]

Figure 4.18 shows the distance-specific energy consumption for the 15 EVs that participated in the **2010 FCC**. The values have been calculated in exactly the same manner as in equation

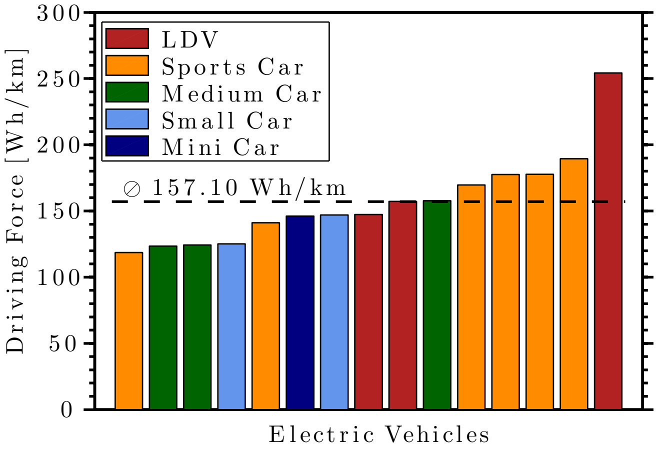

Figure 4.18.: 2010 FCC EV Driving Forces

4.22 from the previous subsection. They range between 119-254 Wh/km with a mean of 157.10 Wh/km. All vehicles are prototypes except for one production sports car at the high end of the driving force scale. LDVs as well as sports cars tend to consume more energy per kilometre than medium and small cars. However, this trend is not clear. The best performing EV is a sports car and the only mini car consumes more energy per unit distance than two sports cars and two medium cars. One explanation for this may be that the mini car was not equipped with a regenerative braking system while all other vehicles were. Nevertheless, the values still compare reasonably well with the predictions made in table 4.9. There, the driving force ranges between 103 Wh/km for a 90% efficient fully recuperating small car and 305 Wh/km for a 90% efficient SUV without regenerative braking.

In **2011** the number of participating electric vehicles rose by ⅔ to 25, which also included the RGE SRZero. Furthermore, 18 EVs (i.e. 72%) were equipped with GPS tracking devices allowing the driving behaviour to be analysed. Also, individual vehicle specifications are available and listed in appendix E. Hence, this run gives a more comprehensive picture about comparative energy consumption than the 2010 run.

The distance-specific energy consumption may be compared on the basis of the full run as shown in the previous paragraph (figure 4.18). However, more detailed insights can be gained from the comparative analysis of the energy/power requirements within the run. With a total number of 62 participants in 2011, starting intervals of >30 s, different driving behaviour and changing traffic conditions over time, vehicles may be apart from each other by up to two hours. Consequently, a comparison on the basis of time is not adequate.

In contrast, comparing power and/or energy values with respect to the distance driven allows for a more valid comparison. Thus, one can linearly interpolate instantaneous power values to get the power consumption at specific distance markers (100 m) along the route. Figure 4.19 shows the power requirements for all 18 EVs equipped with a GPS tracking device with respect to the distance driven. It was also checked that the vehicles followed the exact route outlined in

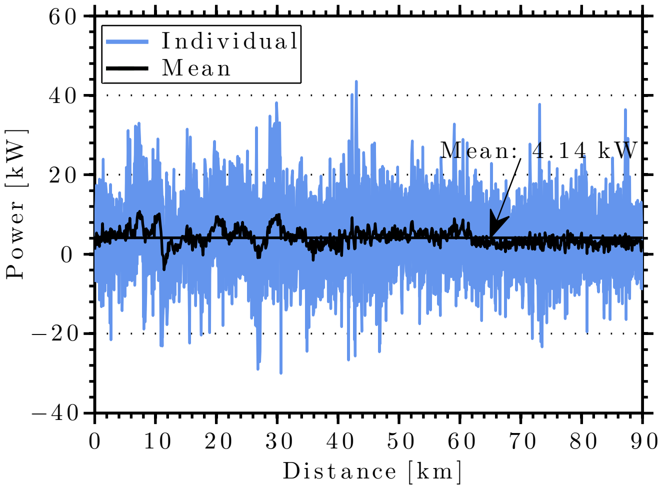

Figure 4.19.: 2011 FCC Individual and Mean Power Consumption

figure 4.16. Otherwise these vehicles would obscure the results. Individual power consumptions are stacked and shown in light blue, whereas the two mean values are shown in black. The oscillating mean value refers to the mean driving power of the 18 EVs at 100 m intervals. The other black line represents the overall mean power consumption along the route for the 18 EVs, which were investigated. Several observations can be made:

- The mean power consumption is very low (4.14 kW) compared to the mean rated power of the vehicles (78.72 kW)
- The maximum power required (43.50 kW) is only about 55% of the mean rated power of the vehicles (78.72 kW)
- The highest powers are required for ascents (km 7, 11, 24, 31 and 61; also compare with figure 4.17)
- The regenerative braking potential is greatest during descents (km 12, 27 and 36) and for stop-and-go city driving (km 64-90)

Overall, the mean absolute regenerative braking gain is 15.04 Wh/km as demonstrated by figure 4.20. This means that on average the relative regenerative braking gain G_r was almost 11%. Even though the theoretical relative recuperation potential is greatest for mini cars (see table 4.10), four mini cars were not equipped with a regenerative system at all. Medium-sized cars recuperated most energy in absolute terms. However, no general conclusions can be drawn from these results alone as the recuperative force also depends upon the efficiency of the system as well as the individual driving behaviour. Nevertheless, with the important exception of medium-sized cars, regenerative braking tends to be more beneficial for small cars than for large cars as illustrated in table 4.12. One reason why the hypothesis made in section 4.1.1 is not fully

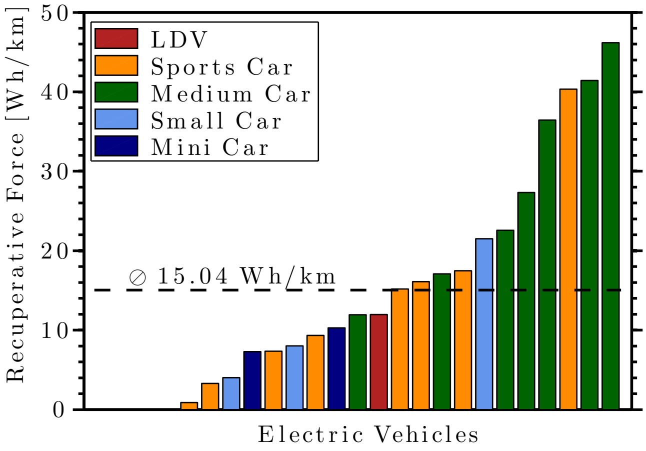

Figure 4.20.: 2011 FCC EV Absolute Regenerative Braking Benefits

validated may have to do with maturity of regenerative braking systems. All medium-sized cars were production vehicles while all other vehicles were prototypes.

Table 4.12.: Relative Recuperation Benefits for Different Vehicle Classes at the 2011 FCC

Recuperation Benefit [%][1]				
Mini Car	**Small Car**	**Medium Car**	**Sports Car**	**LDV**
11.17	8.63	18.29	9.34	8.32

Considering all 25 EVs participating in the 2011 FCC reveals that the mean driving force has been reduced by more than 22% to 122.52 Wh/km compared with the previous year. Figure 4.21 shows how the driving force varies for different vehicle categories during the 2011 FCC.

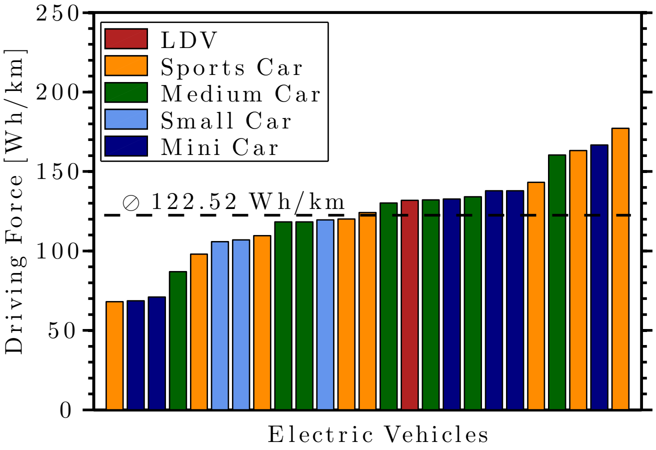

Figure 4.21.: 2011 FCC EV Driving Forces

---

[1] as defined in equation 4.12

While the number of LDVs has gone down from three to one, the number of mini cars has increased by a factor of six compared to the 2010 FCC. The relative share of medium-sized cars has also increased, while the share of sports cars has slightly decreased. The distance-specific energy consumption ranges between 68-177 Wh/km. Ironically, the SRZero was the worst performing EV during the 2011 FCC (177.17 Wh/km). This was mainly due to harsh driving and a relatively high current limit. Again, there is no clear correlation between vehicle class and driving force. Especially sports cars with a relatively wide range of vehicle parameters can be found throughout the driving force range. Fortunately, this time driving behaviour could be assessed.

The **driving behaviour** analysis is based on similar vehicles. There were four Nissan Leaf models with exactly the same specifications, also equipped with GPS, taking part in the 2011 FCC. As all four vehicles covered precisely the same route, any difference in energy consumption must be down to a difference in driving style. Table 4.13 compares these vehicles according to different parameters against each other and also against the mean values from those EVs with GPS. While the vehicle parameters, the number of passengers, the route and the distance covered are the same, the mean driving force for the four vehicles varies between 130-160 Wh/km. This means that in this particular case driving behaviour can result in energy consumption differences of more than 23%. The mean speed, which is relatively low for all participants, has no distinct effect on the mean driving force. Despite the highest relative mean speed (31.47 km/h), the biggest standard deviation of speed (21.92 km/h) and also the highest maximum speed (93.46 km/h), still vehicle 12 consumes about 16% less energy per unit distance compared with vehicle 36. Figure 4.6 from the previous subsection may explain this behaviour. There, we have seen

Table 4.13.: Driving Behaviour Comparison for 2011 FCC

Start Number	**30**	**56**	**12**	**36**	**⊘ All EVs[1]**
Make	Nissan	Nissan	Nissan	Nissan	-
Model	Leaf	Leaf	Leaf	Leaf	-
Euro Car Segment	C	C	C	C	-
# of Passengers	2	2	2	2	2
Mass [kg]	1,521	1,521	1,521	1,521	1,184
Peak Power [kW]	80	80	80	80	79
Battery Capacity [kWh]	24	24	24	24	23.89
Distance [km]	92	92	92	92	92
Mean Speed [km/h]	23.69	31.13	31.47	26.12	29.13
Maximum Speed [km/h]	77.91	92.05	93.46	67.65	83.79
SD Speed [km/h]	20.73	20.58	21.92	18.13	19.04
Traction Ratio [%]	69.52	72.07	73.04	77.41	71.76
Capacity per km [Ah/km]	0.35	0.36	0.36	0.43	0.44
Recuperative Force [Wh/km]	36.45	41.42	46.17	22.58	14.07
Driving Force [Wh/km]	**130.15**	**132.12**	**134.12**	**160.45**	**118.11**

---

[1] , which were equipped with GPS (18)

that at medium speeds (20-100 km/h) the energy consumption does not change markedly with speed.

In contrast, the traction ratio values highlighted in table 4.13 correlate almost linearly with driving force. The traction ratio TR (see section 4.1.1) for vehicles equipped with GPS was calculated based on the mean auxiliary power $\bar{P}_{aux}$. The mean power for driving events, when the vehicle speed was zero, was assumed to be equal to the mean auxiliary power $\bar{P}_{aux}$. For the Nissan Leafs $\bar{P}_{aux}$ was found to be 500 W, which is relatively low. However, given the nature of the event, participants were most probably keeping the use of auxiliaries to a minimum on purpose. Then, all events during which the instantaneous power consumption exceeded 500 W, were classified as traction events. Therefore all events during which the instantaneous power consumption is equal to or below 500 W, must be when the vehicle is either coasting, braking or recuperating. In other words, we assume that the driver has his/her foot on the accelerator only when the instantaneous power is greater than 500 W. It was found that none of the vehicles were coasting along the route. Again, this is logical from an energy-saving perspective as regenerative braking increases the range while coasting only preserves the range. The traction ratios are relatively high compared with the NEDC (see figure 4.3). In addition to the relatively low speeds and accelerations, the relatively low traction ratio can explain why fuel consumption values based on the NEDC are generally below 'real-world' fuel consumption figures.

Table 4.13 shows that a higher traction ratio ultimately leads to a higher capacity used per kilometre, which then leads to a higher driving force. While most vehicle as well as driving parameters are reasonably close to the mean of all 18 EVs equipped with GPS, the four Nissan Leafs outperform the remaining vehicles in terms of their recuperative force.

The **2012 FCC** saw several major changes compared with the 2010-2011 challenges. First, the route was altered in order to incorporate motorway-driving, which was expected to lead to a higher mean speed. Figure 4.22 shows the slightly altered route. The route from the start in Brighton to the stopover in Crawley remained unchanged. After this, the route was altered heading towards Reigate Hill, which also marked the new highest point of the route (see figure

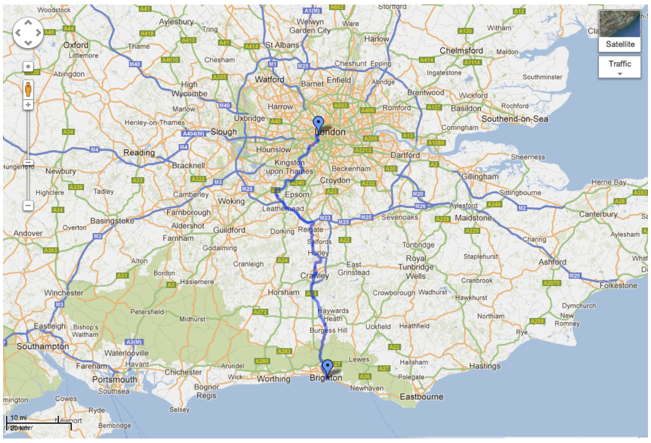

Figure 4.22.: 2012 FCC Route [144]

4.23). Following roughly 10 km on London's orbital M25 motorway, the route led to the new finish at Imperial College London in South Kensington. In total, the new route is approximately 102 km long.

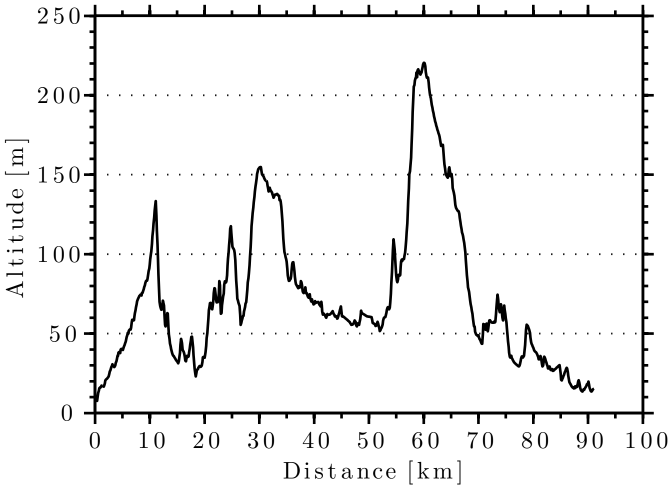

Figure 4.23.: 2012 FCC Altitude Profile [144]-[145]

In 2012, the number of participating EVs dropped by more than half to 10 compared to the previous year (25). The financial crisis, relatively long product development cycles for EVs, relatively high entry costs, a drop in public interest in EVs in 2012 and the fact that most available EVs have already competed in the 2010 and/or 2011 challenges may have led to the smaller number of EVs. Instead, the presence of PHEVs and HEVs increased significantly both in absolute and relative terms. Therefore, only brief comments are made about the driving force.

Figure 4.24 shows in rank-order the driving forces of the participating EVs according to vehicle classes. The data was acquired by Marie-Therese von Srbik [146]. The mean driving force increased by 8% to 132.59 Wh/km compared with the previous year (122.52 Wh/km). The

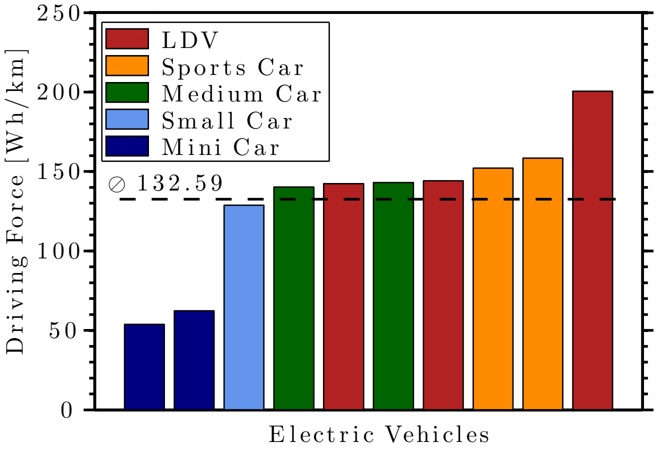

Figure 4.24.: 2012 FCC EV Driving Forces

winner, a micro car ($m_v = 300$ kg), consumed as little as 53.85 Wh/km. A LDV consumed most energy per unit distance (200.51 Wh/km). Compared with 2010-2011, the results of the 2012 FCC show a relatively strong correlation between vehicle category and driving force.

4.1.3. Interim Conclusion

The previous subsections have shown that the mean driving force $\bar{F}_d$ for EVs, defined as the total energy consumption normalised by the distance covered, can vary considerably according to a number of factors.

First, the mean driving force primarily depends upon vehicle parameters such as the vehicle's mass m_v, the aerodynamic drag coefficient C_d, the vehicle's frontal area A_f, the rolling resistance coefficient C_r, the mean auxiliary power $\bar{P}_{aux}$ and losses. These parameters may be grouped into representative vehicle categories: mini cars (e.g. Ford Ka or VW Up), small cars (Ford Fiesta or VW Polo), medium-sized cars (e.g. Ford Focus or VW Golf), large cars (e.g. Ford Mondeo or VW Passat) and SUVs like the Range Rover or VW Touareg. Therefore, all vehicle parameter values increase with vehicle size (see table 4.2). Additionally, environmental parameters like the ambient air density ρ_{air} and the road grade α affect the mean driving force. However, neither can be modified directly by the car manufacturer or by the driver.

Second, the magnitude of the mean driving force depends on whether the vehicle is in traction mode or not. Practically, a vehicle can be in four operating modes. During traction, when the driver puts down his/her foot on the accelerator, the motors apply a propulsion force to the wheels. During braking, when the driver puts down his/her foot on the brake, the kinetic energy of the decelerating vehicle is converted into heat. During recuperation, the kinetic energy from the decelerating vehicle is (partly) recovered and transferred back to an energy storage device. When coasting, the vehicle's resistance losses are exactly matched by the decrease of its kinetic energy. Thus, the mean driving force of a vehicle is reduced to its auxiliary load only, when the vehicle is not in traction mode. The traction ratio TR as a measure of the time spent in traction mode relative to driving time is derived for dynamic speed conditions and varying road grades (equations 4.9-4.11). In practice, traction ratios range between 55-75%. All else being equal, the mean driving force almost linearly depends upon TR (see table 4.13).

Third, the mean driving force is influenced by the driving parameters speed $v(t)$ and acceleration $a(t)$. For steady speeds, the energy consumption per unit distance is smallest at low medium speeds ($\approx$40 km/h) and ranges between 35 Wh/km for mini cars and 170 Wh/km for SUVs. At medium steady speeds (20-100 km/h) the mean driving force does not change markedly with speed. However, at very low speeds ($<$20 km/h) the driving force increases exponentially with decreasing speed due to the mean auxiliary power $\bar{P}_{aux}$. At high speeds ($>$100 km/h) the mean driving force increases quadratically with speed due to aerodynamic drag. Due to road speed limits, congestion and the assumption that most car journeys are relatively short (i.e. $<$50 km), we expect the variation of the mean driving force to be relatively small between different journeys. Dynamic driving involves a constant change of the vehicle's inertia. Nominal accelerations do not exceed 2 m/s^2.

Fourth, the mean driving force of an EV heavily depends upon its ability to recuperate kinetic energy. As kinetic energy is both a function of speed and mass, large and heavy vehicles can theoretically regain most energy in absolute terms through a regenerative braking system. However, the smaller (and thus the lighter) the vehicle, the greater the relative effect of regenerative braking. The relative recuperation gain G_r introduced with equation 4.12 applied to various drive cycles across different vehicle classes proves this point (see table 4.10). Furthermore, a sensitivity analysis (equations 4.13-4.17) has shown that for a vehicle with ideal recuperation the impact of vehicle mass on the mean driving force is greatly reduced compared to that of a vehicle without a regenerative braking system. Thus, a regenerative braking system is beneficial in two ways. It reduces the distance-specific energy consumption as well as its dependence on the vehicle's mass.

Fifth, the journey distance also affects the mean driving force. There is an empirical correlation that with longer journey distances, distance-specific energy consumption tends to be smaller (see figure 4.15). Long journeys are usually driven in rural environments on highways or other main roads at medium steady speeds ($\approx$60-120 km/h), at which the mean driving force is relatively low. In contrast, short journeys are often associated with urban driving, which involves very energy-intensive stop-and-go driving.

Sixth, the individual driving style has profound implications on the mean driving force. As evidenced by table 4.13 the mean driving force can vary up to 23% between different drivers who follow exactly the same route at comparable traffic conditions and driving another vehicle of exactly the same make and model.

There are shortcomings related to the validation techniques of the 'real' driving forces. First, the SRZero was designed as an endurance high performance sports car for long-distance driving. It was not designed for 'everyday' driving. Without space for more than two passengers, the lack of a boot and no real auxiliaries it was also never intended for that. However, its parameters (m_v, C_dA_f and C_r) are very close to that of a medium-sized car. Also, it's mean driving force (131.43 Wh/km) is within the theoretical range of that of a medium-sized car with an efficiency of 90% (129.25-148.04 Wh/km). Second, large EVs and electric SUVs did not compete during one of the FCCs, against which theoretical driving force values could be compared. Third, the FCC encourages low-energy driving. Thus, mean driving forces from the FCC tend to be an underestimation of 'real' values.

Nevertheless, subsection 4.1.2 about 'real' driving forces has broadly confirmed the assumptions made in the subsection about theoretical driving forces 4.1.1. These are corroborated by the published literature about the energy consumption of electric vehicles ([147]-[149]). The resulting reference values of table 4.14 are rounded values based on table 4.9, an overall vehicle efficiency of 90% and a regenerative braking efficiency of 50%.

Table 4.14.: Mean Driving Forces for Different Vehicle Categories

	Driving Force [Wh/km]				
	Mini Car	**Small Car**	**Medium Car**	**Large Car**	**SUV**
Analytical[1]	61.81-74.61	103.15-119.01	129.25-148.04	185.89-210.24	272.72-304.56
RGE SRZero	n/a	n/a	95.47-310.73	n/a	n/a
2010 FCC	146.18	125.19-146.94	124.32-157.66	n/a	n/a
2011 FCC	68.63-166.72	105.79-119.51	86.95-134.12	n/a	n/a
2012 FCC	53.85-62.33	128.81	140.25-143.01	n/a	n/a
Reference Values	**70.00**	**110.00**	**140.00**	**200.00**	**290.00**

---

[1] ranging from full recuperation to no recuperation with an energy efficiency of 90% (see table 4.9)

4.2. Range Requirements for Electric Vehicles

While the previous section looked at the first factor of the fundamental energy equation (4.1), the mean driving force $\bar{F}_d$, this section deals with the second factor, distance. Distance in an automobile context is also referred to as range. Depending on the fuel consumption, range for ICEVs can be up to 1,300 km. Typically, diesel cars have a longer range than comparable petrol cars. Also, HEVs can have longer ranges than comparable ICEVs. For EVs and PHEVs the all-electric range (AER) is of great importance as it is the measure for the distance between which the car needs to be charged. The charging time, depending on the battery capacity as well as the charging power, usually takes several hours. Therefore, a long all-electric range is desirable. As there is no alternative mode, in which an EV can operate other than the all-electric mode, range and all-electric range are the same for this analysis.

The following paragraphs establish range requirements for different vehicle classes and multiple geographies based on travel surveys. First, some general travel trends are derived. Then, car journeys across the UK, Germany and the US are investigated.

4.2.1. General Travel Trends

Car journeys are by far the most dominant mode of private transport (for journeys >1 km) for all investigated countries as can be seen from figure 4.25. However, the relative importance varies significantly. In the US, more than 83% of all journeys are with a car, while in the UK (64%) and in Germany (58%) this share is significantly lower. One major reason for this discrepancy is size. While Germany's total area is about 1.5 times bigger than that of the UK, the US is about 40 times larger than the UK. Therefore, distances between major cities tend to be larger within the US than within Europe. This leads to average distances travelled per car of 18,500 km in the US, 14,500 km in Germany and 14,000 km in the UK [150]. As the car most often also presents the cheapest method in order to cover long distances (>100 km), especially with full

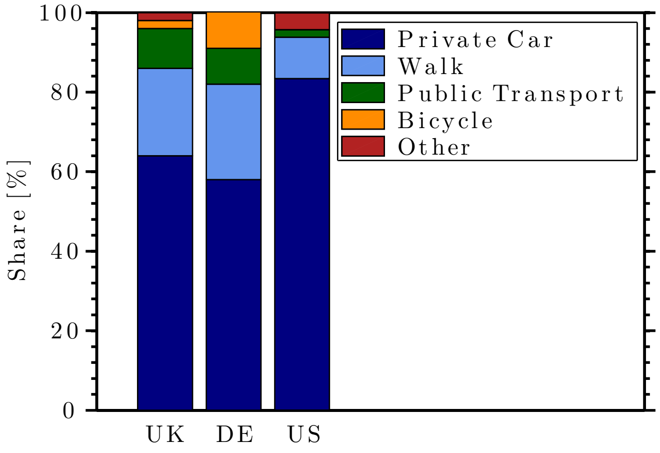

Figure 4.25.: Modal Share in the UK, Germany and the US [137]-[139]

occupancy, car journeys remain the preferred mode of transport. In addition, the US also has one of the highest numbers of motor vehicles per capita in the world (0.797). This compares to 0.519 vehicles per person in the UK and 0.572 in Germany [9]. Consequently, with a population of more than 315 million, there are around 250 million cars in the US. In the UK, there are more than 30 million cars, while in Germany this number is above 40 million. The main statistical parameters for these three countries are summarised in table 4.15, which are expanded in the following.

Table 4.15.: Transportation Comparison for the UK, Germany and the US [9],[150]

		UK	Germany	US
Population	**[10^6]**	63.18	81.80	315.60
Size	**[km^2]**	243,610	357,021	9,826,675
Vehicle Ownership	**[Cars/1,000 people]**	519	572	797
Annual Mileage	**[km]**	14,000	14,500	18,500
Motorway Density	**[m/km^2]**	15.46	34.63	7.79
Road Density	**[m/km^2]**	1,733	1,805	668

4.2.2. United Kingdom

At first glance, the often cited 'range anxiety' (i.e. the fear that the vehicle has insufficient range to reach its destination [151]) associated with electric vehicles seems unsubstantiated. An overwhelming majority (91%) of individual car journeys in the UK is shorter than 30 km as shown in figure 4.26. Thus, only about 9% of individual car journeys are equal to or longer than 30 km. However, further analysis shows that, if a car is used for private transportation, it is used for more than three (3.25) individual journeys per day on average. This is very relevant for EVs, which are typically only charged during night and driven (i.e. discharged) during day time. Consequently, the aggregated distance travelled per day is of greatest interest

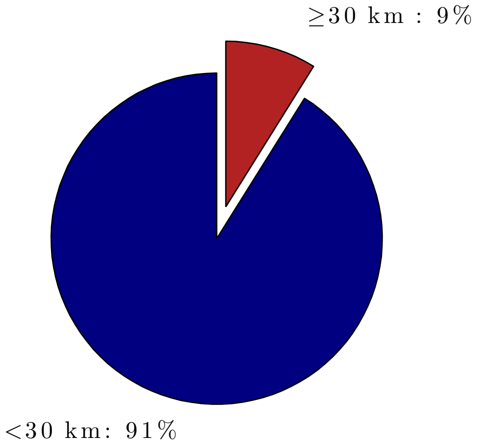

Figure 4.26.: Individual Trip Distances in the UK

for electric vehicles. Other authors including Offer et al. [152] also acknowledge the collective daily distance as the reference range value for electric vehicles. While their work mainly focuses on the relative share of the number of daily car trips with certain distance bounds compared with the total number of daily car trips, this work additionally considers the relative share of the cumulative distance of certain daily distance bounds compared with the total daily distance. The total distance approach is very important since energy use and emission abatement potential is roughly proportional to the total distance and not to the number of trips.

The results show that for the UK the mean daily driving distance is 43.35 km with a relatively high standard deviation of 58.70 km. The mode distance is 6.4 km. The minimum daily distance is 0.16 km while the maximum is 1,694 km, which is about 20% more than the traversal of the entire length of the island of Great Britain (Land's End to John o' Groats = 1,407 km). Most car activity, both in terms of the number of trips and the total distance driven, takes place on Fridays. Figure 4.27 relates car activity to day of week. It shows that car activity is roughly evenly spread across weekdays from Monday to Friday. There is a slight increase in activity towards the end of the week. Generally, during weekends there is less car activity and distances driven on Sundays tend to be longer than average. Family weekend trips most probably account for this.

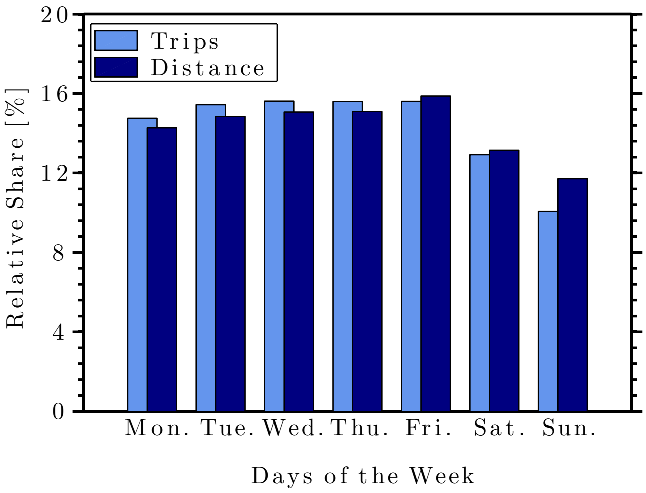

Figure 4.27.: Car Activity According to the Day of Week in the UK

Car activity may also be measured by vehicle category, as introduced in table 4.2 in the previous section of this chapter. Figure 4.28 demonstrates that more than 60% of all individual car trips made in the UK are either in a small (B) or a medium-sized car (C). Also, the aggregated distance covered with these vehicles is close to 60% of the total. Mini cars (A) only present a relatively small share of the car travel in the UK. As expected, their main activity is primarily associated with the number of trips rather than with the distance covered. Large cars (D) in contrast, cover longer distances than their relative trip number would suggest. In recent years, SUVs (M&J) have become more popular. However, their activity is lowest when compared to

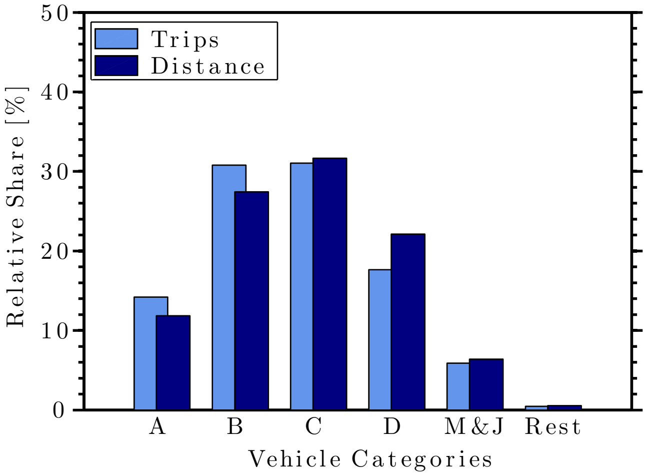

Figure 4.28.: Car Activity According to Vehicle Category in the UK

mini, small, medium-sized and large cars. Other cars' activity is negligible (≈0.5%).

Figure 4.29 shows that mini cars only account for about 2% of the current vehicle fleet, while 'other' vehicles account for about 17%. This maybe attributed to differences in the classification as well as to a significant share of vehicles, which are registered but not driven frequently. These typically include convertibles, vintage and veteran cars. Still, the range from mini cars up to SUVs covers 83% of all registered vehicles.

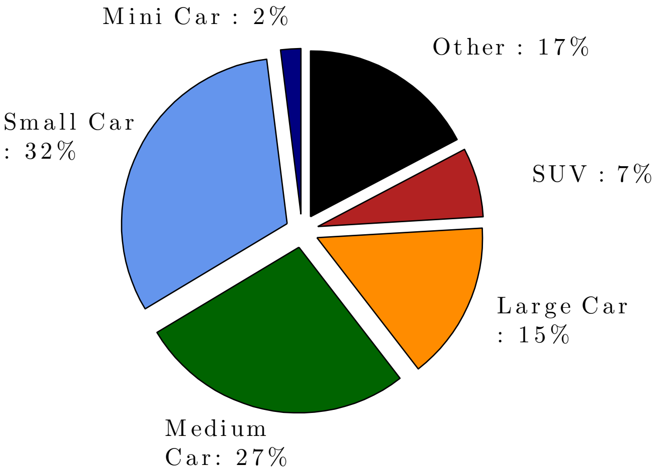

Figure 4.29.: UK Vehicle Registrations According to Vehicle Category [153]

Figure 4.30 confirms the assumption that an aggregate day analysis focussing on both the number of trips and the total distance results in more comprehensive findings compared with an individual trip analysis (figure 4.26). First, the light blue bars with the reference axis on the left hand-side show the frequency distribution of daily trips. The histogram is shown in terms of relative percentages and refers to bins of 25 km respectively. It demonstrates that almost half of cumulative daily distances are below 25 km. With an increasing daily driving distance, the

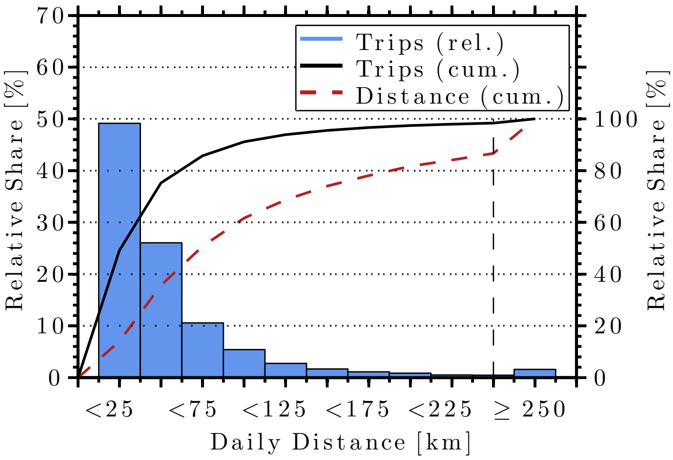

Figure 4.30.: Daily Driving Distances in the UK

relative share of 25 km bins reduces exponentially. Only about 1.6% percent of daily distances are longer than 250 km. The vertical dotted line in black indicates that trends below 250 km cannot linearly be extrapolated beyond 250 km.

Second, the black solid line in figure 4.30 refers to the right-hand ordinate and shows the cumulative share of daily distances. Consequently, a range of only 50 km covers more than 75% of all daily driving distances. With 100 km range a vehicle can cater for more than 91% of all daily driving distances in the UK. And a range of 150 km brings any vehicle into the 95^{th} percentile of daily distances, which is very important for engineering design in general. The numbers for the cumulative share of daily driving distances as well as the numbers of the corresponding survey respondents (NTS) are listed in table 4.16.

Third, the red dotted line in figure 4.30 also refers to the right-hand y-axis and shows the cumulative share of total vehicle kilometres. In the UK and in the US total vehicle kilometres are also known as vehicle miles travelled (VMT). Even though longer car journeys are relatively few in number, they represent a large share of total distance driven. Thus, the red line is significantly flatter (i.e. less sensitive) at low distances compared with the cumulative number of day distances. This also means that associated vehicle metrics such as running costs, emissions and wearing follow the red line rather than the black line. It also follows that in order to achieve a high share, more range is required from a total distance perspective than from the trip frequency perspective.

Table 4.16 lists the absolute and relative numbers corresponding to figure 4.30 up to a range of 500 km. In addition, mean and total distances for each distance band are tabulated. In total, 134,430 aggregated weighted daily distances (409,770 individual weighted journeys) have been included for this analysis. The mean daily distance for journeys longer than 500 km is 606.07 km. This is around fourteen times as long as the mean daily distance driven in the UK. The mean speed for different distance bands is calculated by dividing the total distance driven (sixth column) by the total journey time. As part of the UK National Travel Survey (NTS)

Table 4.16.: Daily Distance Statistics for the UK

Day Distance [km]	**Weighted Frequency [-]**	**Cumulative Share of Trips [%]**	**Mean Distance [km]**	**Mean Speed [km/h]**	**Total Distance [10^3 km]**	**Cumulative Share of Total Distance [%]**
0 < 25	66,063	49.14	12.19	22.54	804	13.97
25 < 50	35,048	75.21	35.70	33.05	1,251	35.68
50 < 75	14,176	85.76	61.10	40.92	866	50.73
75 < 100	7,271	91.17	86.47	47.07	629	61.65
100 < 125	3,647	93.88	111.60	52.32	407	68.72
125 < 150	2,234	95.54	136.27	56.54	304	74.01
150 < 175	1,466	96.63	161.65	59.63	237	78.12
175 < 200	1,107	97.46	186.63	63.71	206	81.70
200 < 225	655	97.94	211.27	64.35	138	84.11
225 < 250	626	98.41	237.06	67.26	148	86.69
250 < 275	430	98.73	261.93	69.43	113	88.65
275 < 300	345	98.99	287.20	70.76	99	90.37
300 < 325	268	99.19	313.32	72.96	84	91.83
325 < 350	209	99.34	336.89	74.14	71	93.05
350 < 375	168	99.47	362.06	74.15	61	94.11
375 < 400	155	99.58	387.10	77.88	60	95.16
400 < 425	135	99.68	412.31	74.88	56	96.12
425 < 450	90	99.75	436.69	78.74	39	96.81
450 < 475	85	99.81	460.48	76.01	39	97.49
475 < 500	53	99.85	485.57	80.70	26	97.94
≥ 500	196	100.00	606.07	82.66	119	100.00
	134,430	**-**	**43.35**	**40.47**	**5,758**	**-**

very detailed information is available on exact journey times and durations (see section 3.3.3). As expected, the mean speed increases with distance. Short distances are assumed to be driven in urban spaces, whereas long distances tend to occur in rural environments. The overall mean speed of 40.47 km/h coincides with the speed, at which energy consumption is minimised (see figure 4.6).

The table also highlights that a range of only 150 km is required in order to cover more than the 95^{th} percentile of all daily distances. However, a range of 400 km is required in order to cover 95% of the entire car distance driven (see two circles in table 4.16).

4.2.3. Germany

In Germany, the car travel is similar to that in the UK. If a car is used for private transportation, it is also used for more than three (3.43) individual journeys on average. As shown in figure 4.31, both the number of trips and the total distance driven is relatively evenly distributed during the week. There is also a slight increase of car activity towards the end of the week, while during weekends it is reduced. On Fridays, Saturdays and Sundays the share of the cumulative distance driven is higher than the share of the total number of trips. This means that during the week, individual trips are shorter than during weekends.

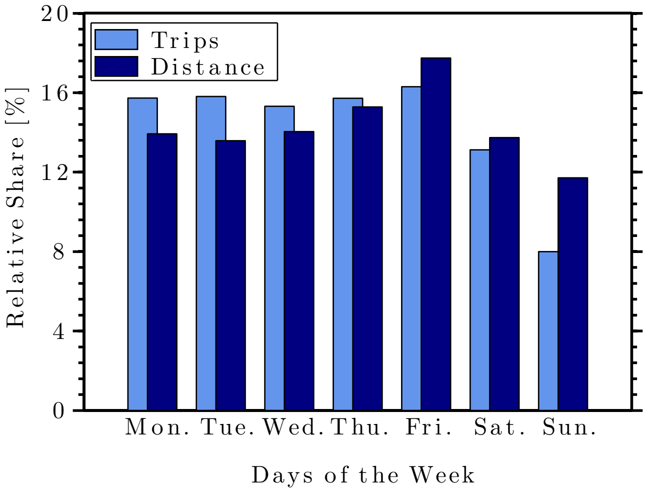

Figure 4.31.: Car Activity According to the Day of Week in Germany

Similarly, car travel can be assessed by vehicle category. Figure 4.32 shows that almost half of Germany's car activity derives from medium-sized cars (C). The vehicle classifications in the UK and in Germany are not exactly the same, which leads to a shift in the results. However, for both countries more than 60% of car activity stems from small (B) and medium-sized cars (C). Again, smaller vehicles are mainly used for frequent short trips while larger cars are used to cover longer distances. Large cars and multi-purpose vehicles together account for around 12% of car activity in Germany. In total, the selected vehicle categories (A, B, C, D, M&J) from table 4.2 account for around 90% of all car activity.

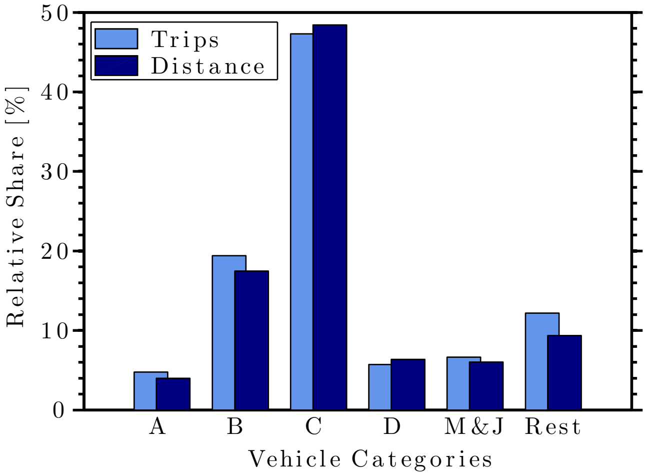

Figure 4.32.: Car Activity According to Vehicle Category in Germany

Figure 4.33 shows that in addition to car travel, travel behaviour in general in Germany is also very similar to that in the UK (see figure 4.30). First, almost half of cumulative daily distances are below 25 km (light blue bars). With an increasing daily driving distance, the relative share of 25 km bins reduces exponentially. A slightly bigger percentage of daily distances are longer than 250 km in Germany (2%) compared with the UK (1.6%).

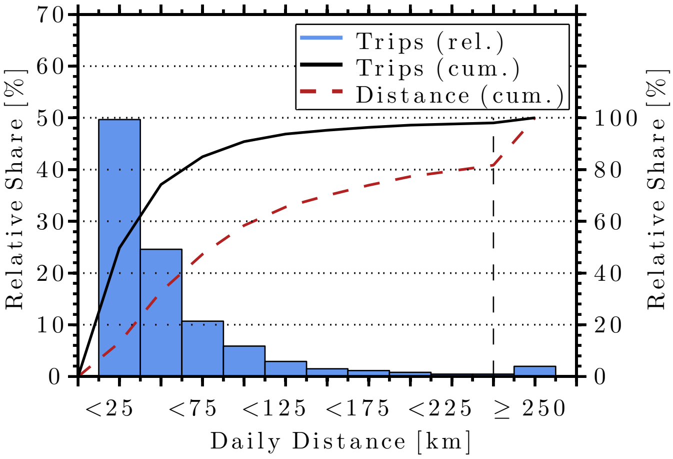

Figure 4.33.: Daily Driving Distances in Germany

Second, the black solid line in figure 4.30 shows that a range of only 50 km covers almost 75% of all daily driving distances. With 100 km range a vehicle can cater for more than 90% of all daily driving distances in Germany. And a range of 150 km brings any vehicle into the 95th percentile of daily distances. The numbers for the cumulative share of day driving distances as well as the numbers of the corresponding survey respondents are listed in table 4.17.

Third, the red dotted line in figure 4.33 is significantly flatter than that for the UK (figure 4.30). This means that the frequency distribution of daily distances is very similar for Germany and the UK. However, from a total distance point of view, daily distances in Germany are longer than in the UK. This can be explained by Germany's larger geographical area and its higher motorway density as shown in table 4.15.

Detailed results, listed in table 4.17, show that the mean daily driving distance for Germany (44.72 km) is almost identical to that of the UK (43.35 km). However, the standard deviation in Germany (70.11 km) is almost ⅕ bigger than in the UK (58.70 km). This indicates that daily distances driven with a car in Germany vary significantly more than in the UK. In total, 21,025 aggregated weighted daily distances (72,304 individual weighted journeys) have been included for this analysis. Like in the UK, a range of only 150 km is required in order to cover more than 95% of all daily distances in Germany (see circle in third column of table 4.17). The overall mean speed, like that in the UK is around 40 km/h. Again, this is the speed at which the energy consumption for various vehicle categories is minimised for a given distance (compare with figure 4.6).

Table 4.17.: Daily Distance Statistics for Germany

Day Distance [km]	**Weighted Frequency [-]**	**Cumulative Share of Trips [%]**	**Mean Distance [km]**	**Mean Speed [km/h]**	**Total Distance [10^3 km]**	**Cumulative Share of Total Distance [%]**
0 < 25	10,443	49.67	11.96	19.25	126	13.15
25 < 50	5,168	74.25	36.46	31.15	188	32.84
50 < 75	2,250	84.95	61.05	39.05	138	47.26
75 < 100	1,235	90.82	85.84	44.38	106	58.36
100 < 125	611	93.73	111.90	49.40	69	65.54
125 < 150	312	95.21	136.25	54.49	42	69.97
150 < 175	238	96.34	160.18	60.97	38	73.99
175 < 200	170	97.15	188.29	61.63	32	77.34
200 < 225	96	97.61	212.65	62.38	20	79.47
225 < 250	91	98.04	234.67	70.56	21	81.70
250 < 275	66	98.35	261.56	68.84	17	83.51
275 < 300	44	98.56	285.91	73.08	13	84.84
300 < 325	40	98.75	313.17	81.37	12	86.14
325 < 350	41	98.95	336.32	76.42	14	87.57
350 < 375	21	99.05	362.42	82.35	8	88.37
375 < 400	30	99.19	385.72	77.13	12	89.58
400 < 425	22	99.29	411.45	75.46	9	90.52
425 < 450	23	99.40	438.50	80.31	10	91.58
450 < 475	6	99.43	461.02	82.41	3	91.85
475 < 500	25	99.55	482.28	86.71	12	93.10
500 < 525	25	99.60	510.90	92.23	6	93.69
525 < 550	25	99.68	535.20	81.02	9	94.60
550 < 575	25	99.76	562.55	91.94	10	95.67
≥ 575	95	100.00	758.29	94.90	41	100.00
	21,025	**-**	**44.72**	**40.18**	**955**	**-**

Table 4.17 is longer compared with the equivalent one for the UK (table 4.16). This is because

from a total distance perspective, 95% of the cumulative daily distance driven is only covered with a range of 575 km compared with 400 km in the UK. Thus, long journeys (>250 km) in Germany are longer than in the UK. This also means that range requirements for EVs in Germany are higher than for EVs in the UK.

4.2.4. United States

As already mentioned in the introduction for this section, US car activity is higher compared with that of the UK and Germany. This is also reflected by the average number of individual car journeys per day, when the car is used. In the US, more than four (4.12) individual car journeys are undertaken on average, while in the UK this number is 3.25 and in Germany it is 3.43.

Car activity during the week is very similar to that in the UK and Germany as can be seen from figure 4.34 when compared with figures 4.27 and 4.31. During the week, car activity is relatively flat. Like in the UK and Germany, there is also an increasing trend of car activity towards the end of the week. There is also a significant drop of car activity during weekends. On Sundays, car drivers tend to be least active, however longer journeys are undertaken compared with other days.

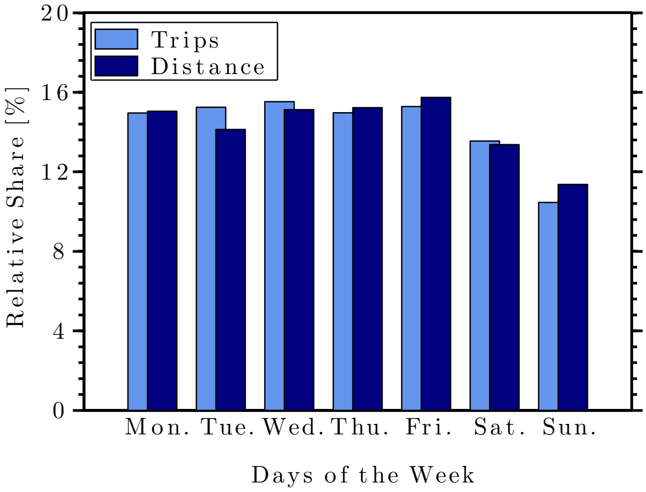

Figure 4.34.: Car Activity According to the Day of Week in the US

Unfortunately, travel survey data from the US does not relate travel behaviour with specific vehicle categories as detailed as in the UK or Germany. Figure 4.35 shows the vehicle activity in the US split into more generalised vehicle categories. Most road vehicle activity (53%) takes place by car, but a significant share also takes place by van (10%), SUVs (21%) and pickup vehicles (14%). Vans are used for shorter journeys compared with pick-ups. Other vehicles including recreational vehicles (RVs) and motorbikes are negligible (2%) in terms of overall road vehicle activity.

Figure 4.36 underlines that range requirements for the US are significantly higher than for

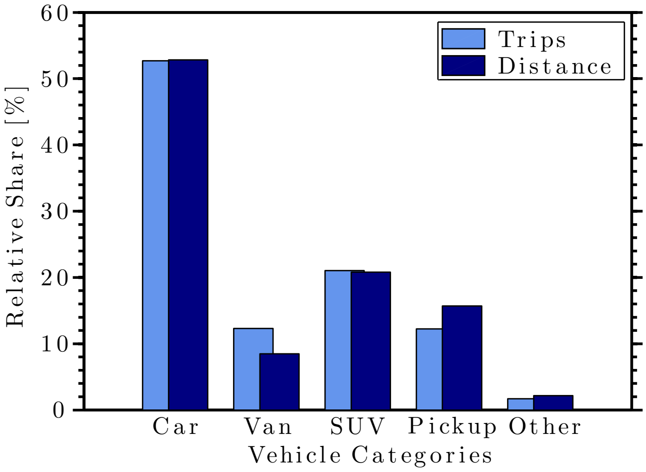

Figure 4.35.: Car Activity According to Vehicle Category in the US

the UK or Germany. First, the light blue bars with the reference y-axis on the left hand-side demonstrates that only about ⅓ of daily distances are shorter than 25 km. In the UK and Germany, this share is almost ½. The share of the relative number of trips decreases exponentially with distance. Almost 2.5% of daily distances are equal to or longer than 250 km.

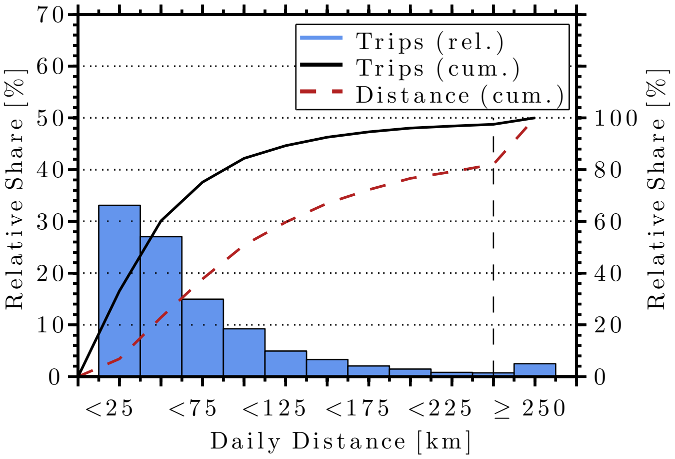

Figure 4.36.: Daily Driving Distances in the US

Second, this leads to a much flatter black solid line when compared with the UK (figure 4.30) or Germany (figure 4.33). It means that in the UK and Germany short car journeys are more frequent than long journeys when compared with the US. Therefore, in the US long daily distances present a higher share of all daily distances compared with Europe.

Third, also in terms of total distance US car activity is less dependent on short distances than Europe. The red dotted line, which indicates the share of the cumulative distance, is flatter when compared to figures 4.30 and 4.33.

Table 4.18 lists the numbers relating to figure 4.36. Due to a different weighting procedure, 53.9 billion aggregated weighted daily distances (720,903 unweighted individual journeys) have been included for this analysis.

By looking at the relative number of trips, a range of 200 km is sufficient to cover the 95th percentile of all daily distances (second column). Both in the UK and Germany a range of 150 km, or a 25% shorter range, satisfies this requirement. Less than one percent of all daily distances are above 400 km. The mean daily distance in the US is 59.60 km, which is about ⅓ more than both in the UK and Germany. The overall mean speed (59.60 km/h) is also higher than in Europe. In order to satisfy the 95th percentile of the cumulative distance driven, a range of 700 km is required.

Table 4.18.: Daily Distance Statistics for the US

Day Distance [km]	**Weighted Frequency [10^6]**	**Cumulative Share of Trips [%]**	**Mean Distance [km]**	**Mean Speed [km/h]**	**Total Distance [10^9 km]**	**Cumulative Share of Total Distance [%]**
0 < 25	17,958	33.12	12.88	25.56	229	6.87
25 < 50	14,583	60.17	36.35	37.05	531	22.81
50 < 75	8,062	75.13	61.59	44.88	498	37.77
75 < 100	4,974	84.36	86.78	51.52	433	50.77
100 < 125	2,666	89.31	111.66	56.09	297	59.70
125 < 150	1,765	92.58	136.29	60.18	241	66.96
150 < 175	1,094	94.61	161.62	63.45	176	72.27
175 < 200	767	96.03	187.03	66.40	144	76.59
200 < 225	417	96.81	211.26	68.99	88	79.23
225 < 250	394	97.54	236.40	69.37	93	82.02
250 < 275	231	97.97	261.95	72.47	60	83.84
275 < 300	155	98.26	287.20	73.29	44	85.18
300 < 325	107	98.46	313.41	77.07	34	86.18
325 < 350	118	98.67	336.53	77.49	40	87.37
350 < 375	120	98.90	363.12	78.46	44	88.68
375 < 400	88	99.06	387.06	80.40	34	89.71
400 < 425	67	99.18	411.06	82.19	27	90.53
425 < 450	40	99.26	437.31	81.57	18	91.06
450 < 475	73	99.39	462.00	82.88	33	92.06
475 < 500	28	99.45	487.48	80.69	14	92.48
500 < 525	28	99.50	512.43	85.81	15	92.91
525 < 550	21	99.54	536.66	87.42	11	93.26
550 < 575	17	99.57	561.98	86.88	10	93.55
575 < 600	23	99.61	586.62	88.51	13	93.94
600 < 625	16	99.64	613.29	89.94	10	94.24
625 < 650	21	99.68	638.55	91.25	13	94.64
650 < 675	15	99.71	661.04	94.30	10	94.94
675 < 700	7	99.72	686.47	87.33	5	95.07
≥ 700	150	100.00	1,087.26	111.16	164	100.00
	53,900	**-**	**59.60**	**51.81**	**3,329**	**-**

4.2.5. Interim Conclusion

The previous subsections have demonstrated that the distance which a vehicle can drive without having to refuel or to recharge, is an important factor. Especially for electric vehicles range is one of the key performance characteristics as charging them up may take up several hours. Despite the fact that an overwhelming majority of individual car journeys in the UK (91%) are relatively short (i.e. <30 km), range requirements for electric vehicles are significantly more challenging than this.

First, when in use, a car is typically driven three to four times a day for separate individual journeys. It is assumed that an EV is typically charged at night and discharged (i.e. driven) during the day. Second, the results have also shown that range requirements can be assessed both in terms of the number of trips and in terms of the total distance. The first focusses on the number of times the daily range is within a specific range band (e.g. 0-25 km, 25-50 km, etc.). This is also referred to as frequency distribution or histogram analysis. Based on the number of trips, a range of 150 km is required to cover at least 95% of all daily distances with a car in the UK and Germany. In the US, a range of 200 km satisfies the same requirement. The second assessment of range focusses on the share of the cumulative distance driven. There may be a high number of short distances driven during one day, but their cumulative distance may be shorter than one single long trip. Consequently, range requirements from a total distance perspective are higher than by just looking at the number of trips. For the UK, a range of 400 km satisfies the 95$^{\text{th}}$ percentile of the cumulative distance driven. In Germany, a range of 575 km and in the US a range of 700 km meet the same target.

4.3. Discussion & Summary

This section brings together the two previous sections about electric vehicle driving forces (section 4.1) and range requirements for electric vehicles (section 4.2). Based on these sections, it establishes nominal energy requirements for electric vehicles by vehicle category.

First, table 4.19 summarises the nominal electric vehicle driving forces, which were derived in section 4.1. It shows that on average SUVs require more than four times as much energy per unit distance of distance than mini cars. Medium-sized cars nominally require 140 Wh/km.

Table 4.19.: Summary of EV Driving Forces

Driving Force [Wh/km]				
Mini Car	**Small Car**	**Medium Car**	**Large Car**	**SUV**
70	110	140	200	290

Second, based on these driving forces and range requirements for the UK, Germany and the US (see section 4.2), initial battery capacity requirements may be established. Figures 4.37-4.39 display the results.

Each of the six figures is a plot of the cumulative share on the x-axis versus the theoretical EV battery capacity on the y-axis. Each row displays the information for a different country; UK, Germany or the US. Figures on the left hand-side (a) refer to the cumulative share of daily distances driven, while figures on the right hand-side (b) refer to the cumulative share of the total distance driven. Battery capacity requirements are higher from a total distance perspective than from a number of trips perspective. Obviously, the greater the battery capacity (i.e. those satisfying the 95% of the total distance requirement), the longer the range.

However, from an emission abatement perspective smaller battery capacities (i.e. those satisfying the 95% of all trips requirement) can be very effective as well. Because short trips (<30 km) involve more frequent stops and a smaller percentage of operation at high efficiency, the fuel efficiency for short trips is usually lower than for long trips. Figure 4.15 also gives empirical evidence for this correlation. Then, due to the linear relationship between fuel consumption and CO_2 emissions (see equation 1.1), emissions per unit of distance tend to be higher for short trips. Therefore, the CO_2 abatement potential for EVs with a relatively small battery capacity is already relatively high.

Table 4.20 concludes this chapter by listing the battery capacity requirements for EVs by driving force and range requirements in different countries. Battery capacity requirements range from 11 kWh for a mini car in the UK or Germany satisfying a 150 km range up to 203 kWh for a SUV in the US satisfying a 700 km range. As a reference, the energy content of a full fuel tank for a medium-sized ICEV (50 litres of petrol) is about 480 kWh. Individual capacities vary from the range of 95% of all trips to 95% of the total distance. The difference between these two is significant for all observed countries. Thus, some vehicle manufacturers offer their

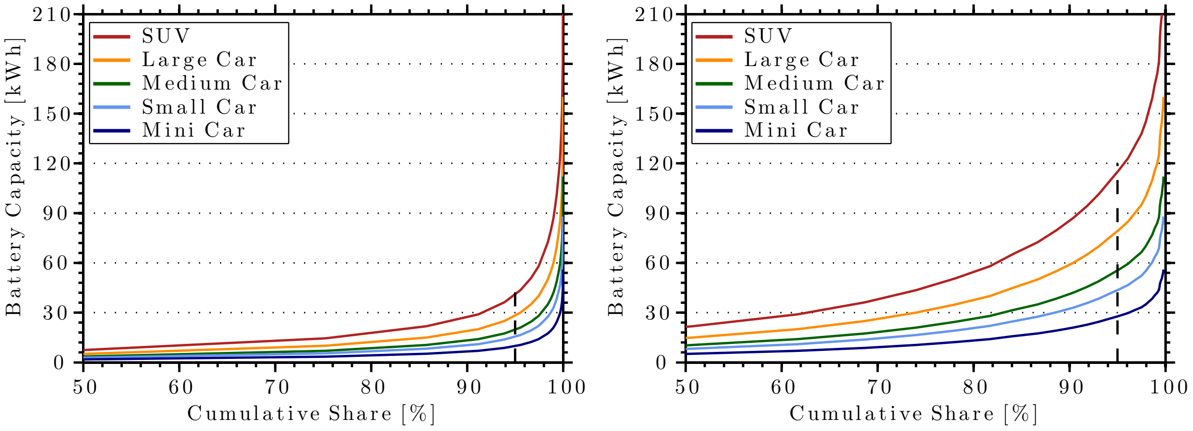

(a) Number of Trips **(b) Distance of Trips**

Figure 4.37.: Battery Capacity for Range Requirements in the UK

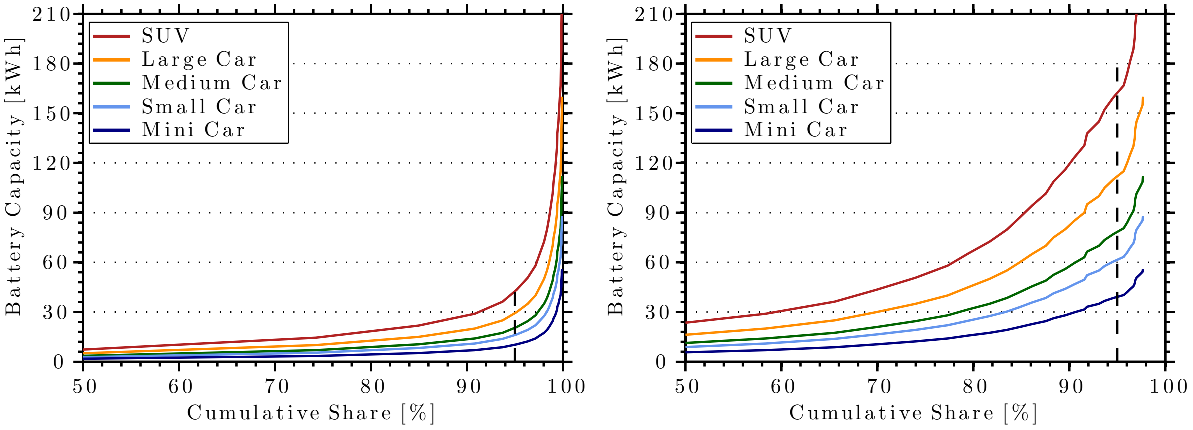

(a) Number of Trips **(b) Distance of Trips**

Figure 4.38.: Battery Capacity for Range Requirements in Germany

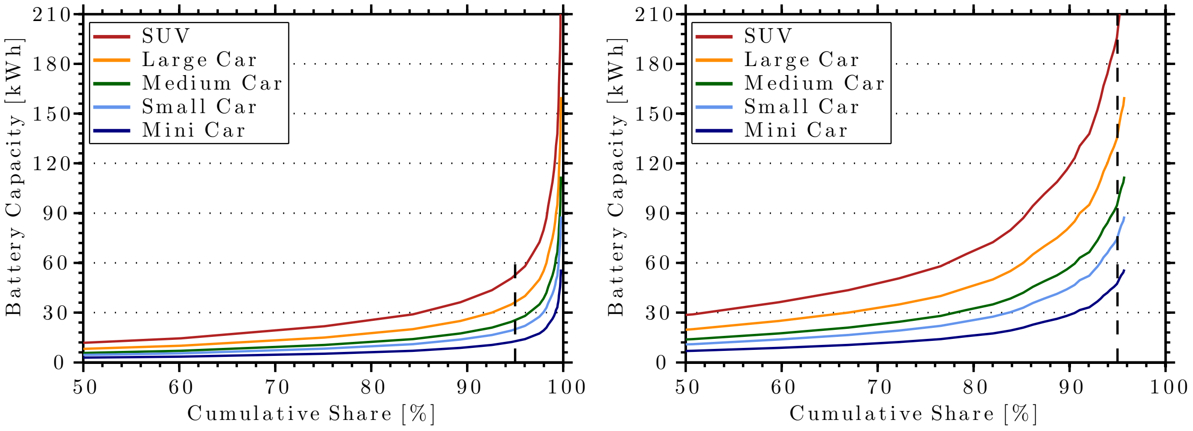

(a) Number of Trips **(b) Distance of Trips**

Figure 4.39.: Battery Capacity for Range Requirements in the US

electric vehicles with a range of battery capacities like e.g. the Tesla Model S.

Table 4.20.: EV Battery Capacity Requirements According to Driving Force and Range

Country	**95% Range [km]**		**Battery Capacity [kWh]**				
	Trips	**Dist.**	**Mini Car**	**Small Car**	**Medium Car**	**Large Car**	**SUV**
UK	150	400	11-28	17-44	21-56	30-80	44-116
Germany	150	575	11-40	17-63	21-81	30-115	44-167
US	200	700	14-49	22-77	28-98	40-140	58-203

5. Performance & Degradation Characteristics of EV Traction Batteries

This chapter extends the analysis of the optimum battery capacity for electric vehicles by considering battery performance and degradation behaviour. The previous chapter has come up with optimum energy requirements for various electric vehicle categories in three different countries. These energy requirements are based on nominal driving forces and daily travel distances associated with passenger vehicles. However, these nominal energy requirements cannot be converted 1:1 into optimum battery capacities. The reason for this is *battery degradation*, which alongside other consequences (see section 2.3.3) leads to capacity fade. This means that the optimum battery capacity for EVs needs to be larger than the optimum energy requirement. While the optimum energy requirement remains relatively constant (assuming no significant efficiency losses of the EV power train and steady travel patterns), battery capacity is reduced with time and use. Figure 5.1 illustrates this relationship. The optimum energy requirement from the previous chapter is shown in blue. It is constant with time and use. The spare capacity, which is shown in red, is diminished with time and use. Ideally, the battery capacity available at the end of the EV's lifetime is exactly equal to the optimum energy requirement. While chapter 4 has determined the magnitudes of the blue bar for various EV categories, this chapter is concerned with the characterisation of the red area. Note that the linear capacity fade shown in figure 5.1

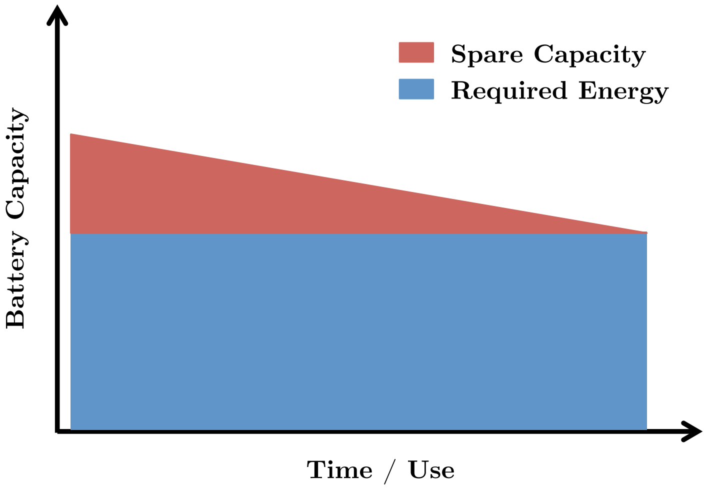

Figure 5.1.: Capacity Fade Schematic

is for demonstration purposes only.

In order to determine the long-term behaviour of an EV battery pack, an understanding of the short-term battery behaviour at cell level is essential. Therefore, this section is divided into three sections. Section 5.1 is devoted to EV battery performance parameters, while section 5.2 deals with battery degradation. Section 5.3 concludes this chapter.

5.1. Performance Characteristics of EV Traction Batteries

This section analyses performance characteristics of EV traction batteries. It is primarily concerned with the battery's power output given a particular power request. The first subsection deals with steady battery behaviour while the second subsection is devoted to dynamic battery performance characteristics. The third subsection provides an interim conclusion.

5.1.1. Steady Battery Behaviour

EV traction batteries are usually made up of a number of individual cells. Depending on the power and energy requirements, safety and cost considerations as well as design limitations, individual cells are often connected in series (S), in parallel (P) or a combination of both. For the SRZero (see section 3.3.1) for example, 164 $LiFePO_4$ cells with a nominal voltage of 3.3 V and a rated capacity of 100 Ah are connected in series. This 164S0P configuration results in a nominal battery pack voltage of 541.2 V and a rated capacity of 100 Ah (compare with section 2.3.2).

Published Discharge Behaviour

On the individual cell level, figure 5.2 shows the published discharge curves of the $LiFePO_4$ battery cells of the SRZero at steady discharge currents. The cell voltage is plotted against the

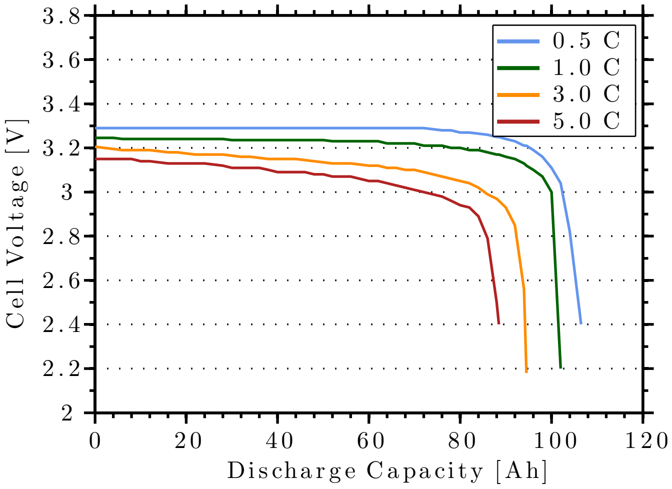

Figure 5.2.: Published Discharge Curves of SRZero Battery Cells (see appendix B)

discharge capacity for four different discharge rates at ambient temperatures. The light blue line shows the discharge characteristics at a constant discharge current of 50 A (i.e. 0.5 C for cells rated at 100 Ah), while the red line shows the discharge characteristics at a constant discharge current of 500 A (i.e. 5 C). Due to the capacity rate effect (see figure 2.23) high discharge rates result in a lower capacity compared with low discharge rates. Thus, the nominal discharge capacities at 0.5, 1, 3 and 5 C and a lower voltage limit of 2.5 V are 105, 101, 94 and 88 Ah respectively. Additionally, a higher load current (i.e. a higher C rating) leads to a lower cell voltage as well. This is because higher currents lead to higher diffusion resistances within the cell. Therefore, at 0.5 C the nominal cell voltage (i.e. the voltage, which occurs most frequently) is 3.29 V while at 5 C it is only 3.11 V. This means that at a discharge rate of 0.5 C, roughly 345 Wh should be available during discharge. At 5 C only about 80% of this energy is available according to the manufacturer.

Measured Charge and Discharge Behaviour

Figure 5.3 displays the results of initial charge and discharge tests of a single cell from the SRZero undertaken in early 2010, i.e. before the long test drive. Figure 5.3a on the left hand-side shows a galvanostatic charge at 20 A (0.2 C), while figure 5.3b on the right hand-side shows a galvanostatic discharge at 100 A (1 C). The nominal voltage during the charging process is around 3.4 V, while during discharge it is 3.1 V. Due to resistance losses during charging, the charging voltage is higher than the no-load open-circuit voltage (*OCV*). Thanks to resistance losses during discharge, the discharge voltage is lower than the *OCV*. It is also lower when compared with the green line in figure 5.2. Additionally, the shape of the discharge curve in figure 5.3b is less flat. It also features voltages of up to 3.8 V at very low discharge capacities, which figure 5.2 does not. The measured galvanostatic discharge characteristics (figure 5.3b) rather than the published discharge characteristics (figure 5.2) are taken as reference in order to

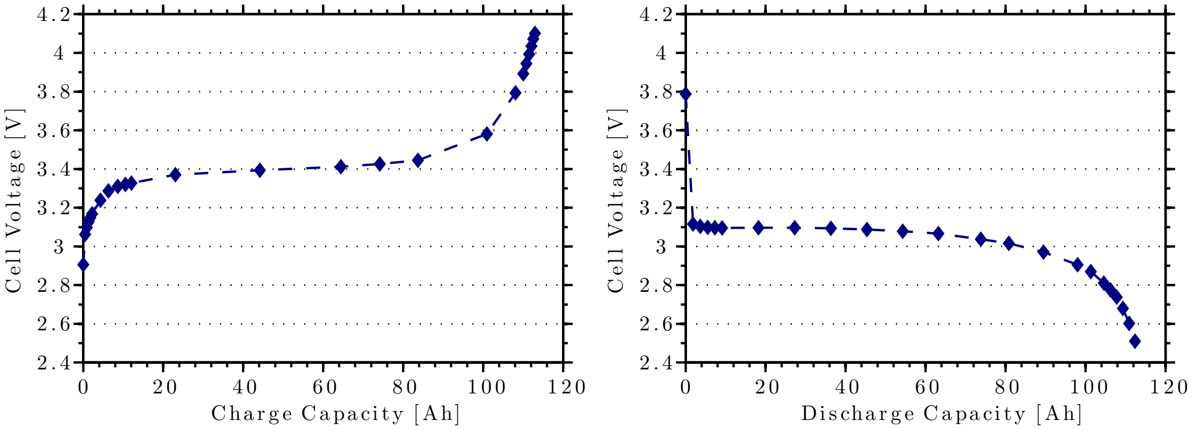

(a) Charge at 0.2 C **(b) Discharge at 1 C**

Figure 5.3.: Initial Charge and Discharge Curves of a Single SRZero Battery Cell

validate dynamic equivalent models first introduced in subsection 2.3.4. Differences between the two discharge curves may arise from varying environmental conditions (temperature, humidity, etc.), the experimental setup (contact resistances, measuring devices, etc.) as well as battery degradation.

Figures 5.2-5.3 show key characteristics of $LiFePO_4$ cells. First, the nominal cell discharge voltage is relatively high, 3.1-3.3 V. Second, the discharge profile is relatively flat. This is advantageous in terms of energy consumption as it results in relatively high discharge capacities at relatively high voltages. In other words, more energy can be withdrawn from a cell with a flat discharge voltage profile than from a cell with a sloped discharge voltage profile given the same nominal voltage. However, a flat discharge profile complicates the determination of the state of charge (SOC). A relatively high discharge capacity only corresponds to a minimal change in cell voltage. This also means that the available battery power is relatively stable with its state of charge. The available power can simply be calculated as the product of the (steady) current and the cell voltage at a particular SOC.

Derivation of OCV vs. SOC Relationship

Discharge curves vary with the discharge rate as illustrated in figure 5.2. However, only open-circuit voltage (OCV) values remain constant with different discharge currents. Therefore, the OCV value at a particular state of charge (SOC) is the only voltage reference value, which is not affected by the discharge rate. Following this, one would need to intermittently discharge a previously fully charged cell with a constant discharge rate. The interruptions, when no current is applied, would need to be long enough for the cell to reach its equilibrium (OCV) state. Figure 5.4 shows the cycling history for one of the SRZero battery cells as part of an galvanostatic electrochemical impedance spectroscopy (GEIS) measurement procedure. The detailed procedure for this is listed in table 3.6. As can be seen by the vertical blue bars, the discharge procedure is interrupted six times for each of the nine discharges. The interruptions

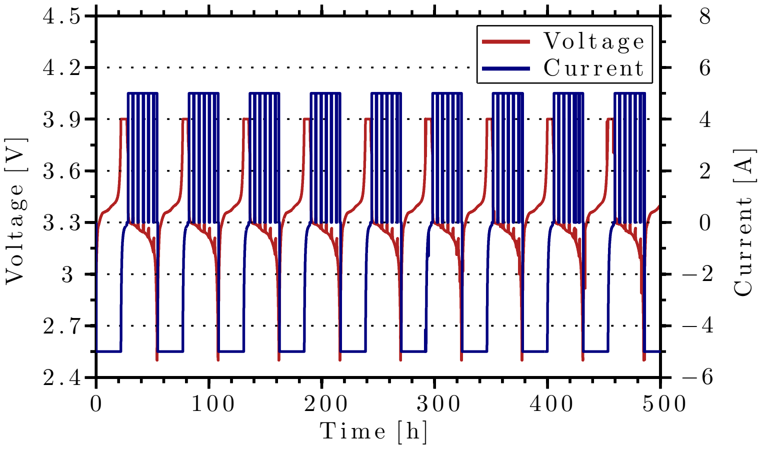

Figure 5.4.: GEIS Voltage and Current History

occur at 20 Ah intervals and last for 30 min each. Electric potential levels after 30 min rest are assumed to be in equilibrium state. Therefore, the peaks along the red voltage profiles represent OCV values at 100, 80, 60, 40, 20 and 0% SOC respectively.

Measured discharge data points from figure 5.3b and measured OCV values from figure 5.4 may then be taken as reference values in order to establish a generic OCV vs. SOC relationship for the SRZero cells. The rated discharge capacity (100 Ah) is equal to 100% depth of discharge (DOD) or 0% state of charge (SOC). Figure 5.3b is based upon 23 data points, while there are only seven OCV values per discharge from figure 5.4. Consequently, initial fitting was done with the the data from figure 5.3b and then the results were applied and modified for the data points in figure 5.4.

Furthermore, the first data point at zero discharge capacity was ignored for this analysis. The initial high voltage of 3.8 V measured during discharge is considered to be insignificant for the determination of the OCV vs. SOC relationship. This is because the capacity used from the beginning of the discharge until the voltage drops close to its nominal value is only 1.85 Ah at a discharge rate of 1C. In other words, for simplification purposes the initial high cell voltage is ignored without significant increase in error. Strictly speaking it is an OCV value. This also explains why the published discharge curves (figure 5.2) do not feature the initial high voltages. Also, for the charging process it is not essential to charge up to voltages way above the nominal charging voltage. Figure 5.3a shows that only about 4 Ah can be 'fed' into the cell above 3.8 V.

Various fitting models have been applied to these data points. These models and their goodness of fit parameters are listed in table 5.1. With the exception of the 1D exponential model the goodness of fit increases from left to right. Fitting a linear curve to the discharge data points yields a relatively high sum of squares due to error (SSE = 0.215) and a relatively low R^2 value (0.706). In contrast, a 2D exponential fit results in a very low SSE (0.003) and a very high R^2 value (0.996) and thus exhibits the best fit. However, this function can be simplified and still retain its goodness of fit:

Table 5.1.: Goodness of Fit for Various Models to Represent OCV vs. SOC Relationship

	Fitting Model					
Goodness of Fit Parameter	**Linear**	**Quadratic**	**Cubic**	**1D Exp.**	**2D Exp.**	**Custom**
Sum of squares due to error (SSE)	0.215	0.068	0.025	0.224	0.003	0.003
Coefficient of determination (R^2)	0.706	0.907	0.966	0.694	0.996	0.996
Root mean squared error (RMSE)	0.104	0.060	0.037	0.106	0.013	0.013

$$OCV(SOC) = a + b(100 - SOC) + ce^{d(100-SOC)} \tag{5.1}$$

The custom fitting model from table 5.1 relates to equation 5.1. It combines a linear model with a 1D exponential model. The coefficients are listed in table 5.2. The effect of these coefficients is illustrated in figure 5.5. Coefficient a determines the cell voltage at full SOC, while coefficient b determines the slope of the linear voltage drop with diminishing SOC down to about 20% SOC or 80% DOD. Coefficient c determines the starting point of the exponential decay, while coefficient d determines the slope of the exponential decay of the OCV at a SOC below 20%. Therefore, the cell voltage vs. SOC function can be divided into a linear function for SOC values above 20% and an exponential function for SOC values below 20%. Figure 5.5 shows that the cell voltage during discharge (1 C) shown in blue is shifted downwards by about 0.2 V from the OCV shown in green. Only at SOC values below 20%, i.e. when the exponential function is dominant, does the shape of the two functions differ.

Table 5.2.: Coefficients for Custom Model of OCV vs. SOC Relationship

Model	**Coefficient**			
	a	***b***	***c***	***d***
V_{term} vs. SOC	3.113	-8.66E-4	-3.49E-6	0.105
OCV vs. SOC	3.350	-8.66E-4	-2.00E-9	0.170

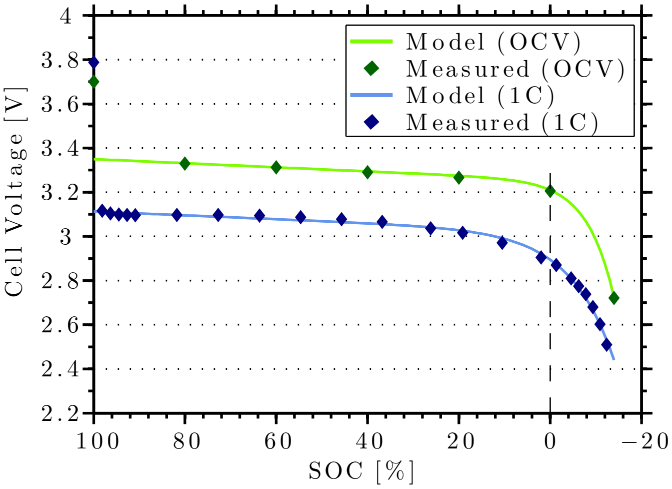

Figure 5.5.: Measured and Modelled Values for the OCV vs. SOC Relationship

Furthermore, the rated cell capacity (here 100 Ah) provides a good approximation of the 'true' electrical energy content, but does not provide an exact measure for mainly two reasons [101]. First, cell capacity ratings usually assume a lower discharge limit of 2.5-3 V for lithium-ion cells rather than 0 V. However, there is still electrical energy stored between 0 V and the lower discharge limit. Second, nominal capacity ratings are often based on expected ageing behaviour. Thus, initial cell capacity may exceed the nominal capacity rating, while end of life capacity is likely to fall below the nominal capacity rating. The spare capacity (see also figure 5.1) is shown on the right of the dotted line in figure 5.5.

5.1.2. Dynamic Battery Behaviour

The previous subsection looked at steady discharge behaviour. Many applications of lithium-ion cells including mobile phones, laptops and other portable electronic devices draw relatively steady currents from their cells. Therefore, power outputs are relatively predictable and *SOC* estimation may simply be based on galvanostatic discharge curves like those in figures 5.2 and 5.3b. In contrast, hybrid electric and pure electric vehicles present one of the most dynamic loads for lithium-ion batteries. This means that the standard deviation of a typical HEV or an EV traction battery load is significantly larger than that of a standard electronic portable device. The variation of the battery load for an EV is primarily due to EV driving forces (see section 4.1.1). To a lesser extent temperature and degradation effects also affect battery dynamic behaviour.

In the following, a representative battery load for the SRZero is derived from a sample drive cycle and a first principle analysis introduced in section 4.1.1. The following procedure follows the backward-forward-facing approach (see section 2.2.3) and is simplified here for the conditions of the SRZero as illustrated in figure 5.6. Two electric motors are mounted at the rear to propel the vehicle. While in traction mode, power is requested by each of the motor controllers from the battery pack. In this case the power flow is from right to left on the figure. During recuperation kinetic energy of the spinning rear wheels is converted back into electrical energy as the two electric motors act as generators. In this case the power flow is from left to right. The procedure mainly follows the backward-facing approach (i.e. from drive cycle to battery voltage), but also includes forward-facing component limits. It derives battery output voltages given current requests.

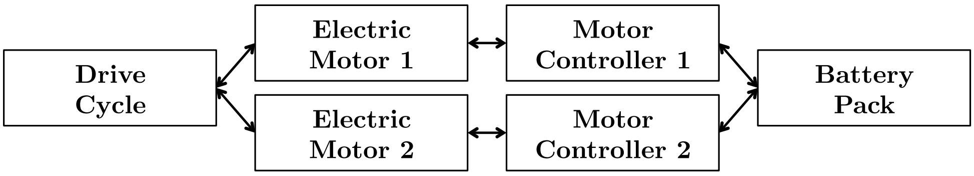

Figure 5.6.: Simplified Power Flow for EV Power Train

Sample Drive Cycle

Figure 5.7 shows a dynamic speed-time trace (drive cycle) of the SRZero. The vehicle speed is the arithmetic mean of the wheel speeds at the front left and front right. The drive cycle is taken from Anchorage in Alaska when the car was first picked up from the airport. Due to air cargo safety regulations [156], the state of charge of the battery pack was relatively low. Anchorage lies directly at the Gulf of Alaska of the Pacific Ocean and at the end of June 2010 ambient temperatures for this drive were around 20 °C. Consequently, neither cold nor hot temperature extremes affected the battery performance for this sample drive cycle. Also, ageing effects as well as road gradients are assumed to be negligible for this sample drive cycle.

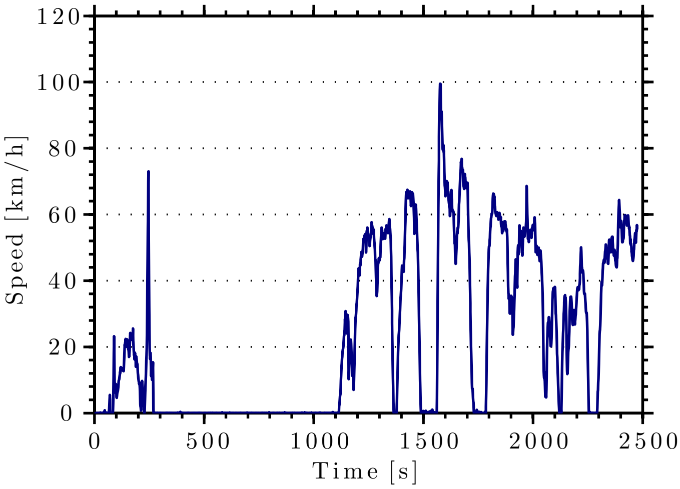

Figure 5.7.: Sample SRZero Drive Cycle

In this sample, the drive cycle is around 41 minutes long and begins with a low-speed drive within the airport premises. Then, the SRZero is accelerated up to around 73 km/h and subsequently decelerated to standstill. After this, the vehicle is not being driven for about 15 minutes before being driven in road traffic including several start and stop sequences for another 20 minutes. The rest period should give good indications about the battery's capacitative behaviour. In total, 13.64 km are covered for this drive cycle.

Taking the time derivative of speed yields acceleration. Figure 5.8 displays the corresponding acceleration profile with respect to figure 5.7. It shows that on average, the magnitudes of negative accelerations (decelerations) are larger than those of positive accelerations. Thus, more time is spent accelerating than decelerating. Peak accelerations as well as decelerations are relatively low.

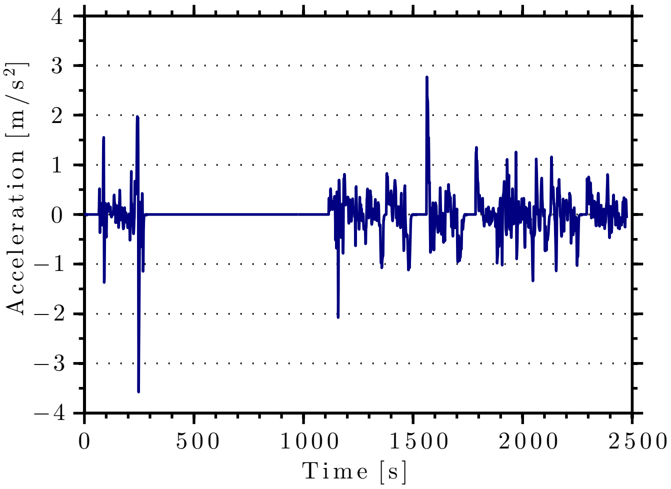

Figure 5.8.: Sample SRZero Acceleration Profile

Derivation of Torque Values

Based on the drive cycle in figure 5.7, a first principle analysis (see section 4.1.1) following a quasi-steady approach ($\Delta t = 1$ s) and the specifications of the SRZero (table 3.1), theoretical torque values for the left and right rear wheel are derived. The results are shown in figure 5.9, which also shows the measured torque values (via the torque constant K_T). Torque values for the left rear wheel are almost identical to those of the right rear wheel. Only in sharp bends when the outer wheel needs to travel a longer distance than the inner wheel, i.e. at a higher speed and when the grip between the two sides differs significantly, does the requested torque vary between left and right wheel. The mean measured torque is 27.72 Nm for the left hand-side and 27.70 Nm for the right hand-side. Figure 5.9 also shows that first principle considerations can yield relatively accurate results, because the coefficient of determination (R^2) for the modelled and measured values is 0.70 for the left hand-side and 0.73 for the right hand-side.

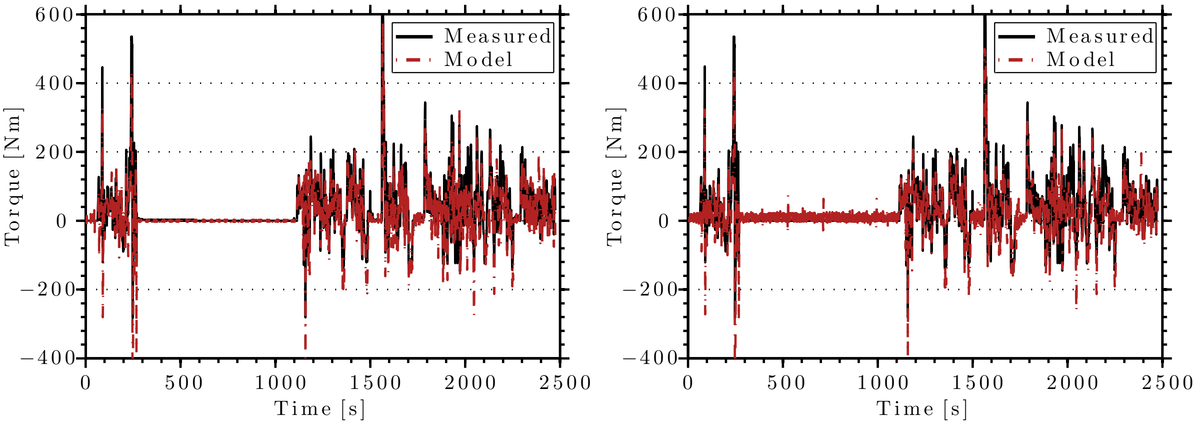

(a) Rear Left Wheel **(b) Rear Right Wheel**

Figure 5.9.: Theoretical and Measured Torque Values

Long-term measured requested torque values of the SRZero during the test drive from Alaska to Argentina are shown in figure 5.10. They put into perspective the derived torque values from figure 5.9. Figure 5.10a shows the combined requested torque values (i.e. left and right) against operation time. During the test drive, the SRZero was being driven for around 644 hours, i.e. for more than seven hours on average per drive cycle. The first observation from this figure is that the measured requested torque is highly dynamic. With a mean value of 55 Nm, its standard deviation of 137 Nm is very high. Due to control design the maximum requested torque cannot exceed the maximum possible output torque of 1.3 kNm. For safety purposes this was reduced to 95% of that value, i.e. 1.235 kNm. This means that at maximum each of the two motors can deliver 617.5 Nm. Therefore, maximum requested torque values appear to be flat at this value. The results of applying a low-pass filter (LPF shown in red) with a time constant of 1 hour however show that the moving average is relatively low.

In addition, figure 5.10b illustrates that combined torque values above 500 Nm are relatively

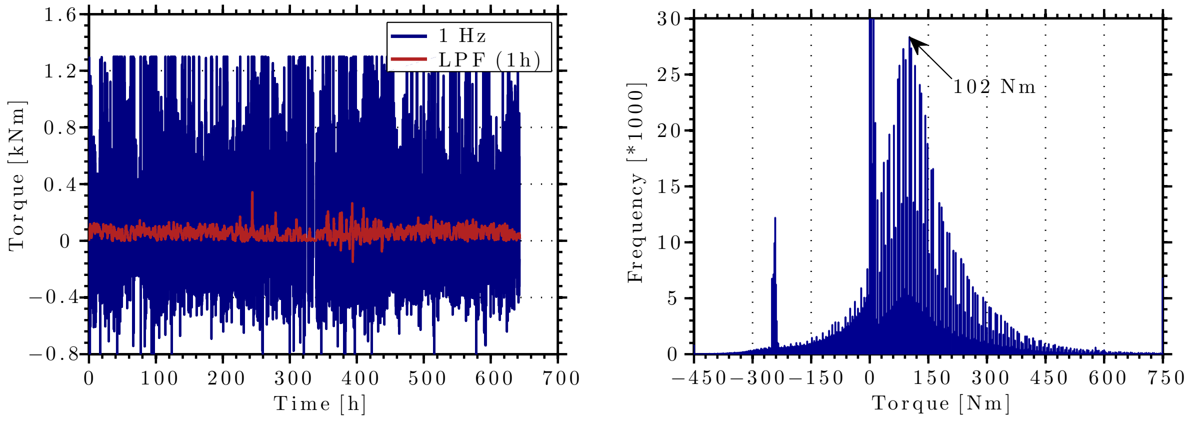

(a) Time Trend **(b) Histogram**

Figure 5.10.: Total Requested Torque Values of SRZero During Test Drive

rare. Less than 1% of all measured requested torque values are above 500 Nm. Leaving apart the peak at zero Nm (i.e. when the vehicle is on, but not requesting any torque), the nominal requested torque value is 102 Nm. A fast Fourier Transform (FFT) analysis did not reveal dominant frequencies for requested torque values.

Derivation of AC Motor Currents

The resulting requested AC current values from the motor controllers can be estimated via the torque constant ($|K_T| = 5.5$ Nm/A; see also equation 4.20) and the motor efficiency map (see figure 3.5). This means that during traction the torque constant is positive and during recuperation it is negative. Therefore, all AC currents are positive. The measured and modelled AC current values for the motor controllers are shown in figure 5.11. The mean measured current for this drive cycle at the left rear motor controller is 8.6 A with a relatively high

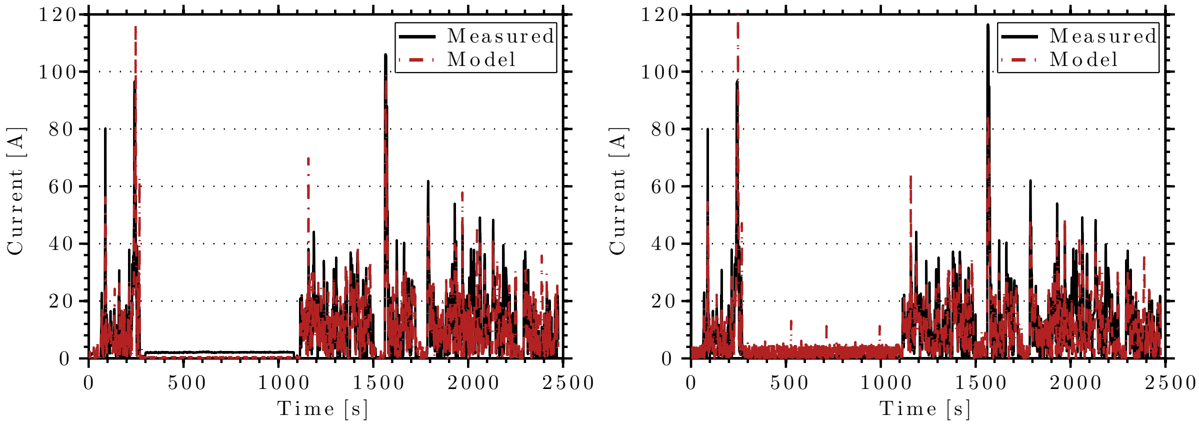

(a) Rear Left Wheel **(b) Rear Right Wheel**

Figure 5.11.: Theoretical and Measured AC Motor Controller Current Values

standard deviation of 12.1 A. The values for the rear right motor controller are 8.3 A and 12.6 A respectively. During the test drive along the Pan-American Highway the mean combined AC motor controller currents were 15.79 A, i.e. slightly less than the ones from the left and right side combined from the sample drive cycle. The maximum AC current for the motor controllers are 106.1 and 116.5 A. Here, the coefficient of determination (R^2) for the modelled and measured AC current values is 0.69 on the left hand-side and 0.73 on the right hand-side. This means that R^2 has only been reduced by 0.01 for the left side, while on the right side it remained constant.

Derivation of DC Motor Controller Characteristics

The DC motor controller input currents are the next element upstream along the EV power train. Analytically working out the DC input current from the motor controllers given the AC output current is not trivial. Figure 5.12 displays the empirical relationship between the DC motor controller input currents and the AC motor controller output currents. The input current and the direction of power flow determine the output current. At its linear edges on the far right hand-side and on the far left hand-side figure 5.12 shows the ideal inverting process. However, efficiency losses in both directions mean that input power is greater than output power. While the power is reduced along the direction of power flow, output currents may be greater than input currents provided the corresponding voltage is reduced. Figure 5.12 also shows that the inverter output current is limited to 223.5 A. This means that regardless of the DC input current, the AC output current will not exceed 223.5 A, which in combination with the torque constant ($|K_T| = 5.5$ Nm/A) leads to a maximum torque value of 1,230 Nm. Thus, the two inverters not only control the two AC motors, but also prevent overloading.

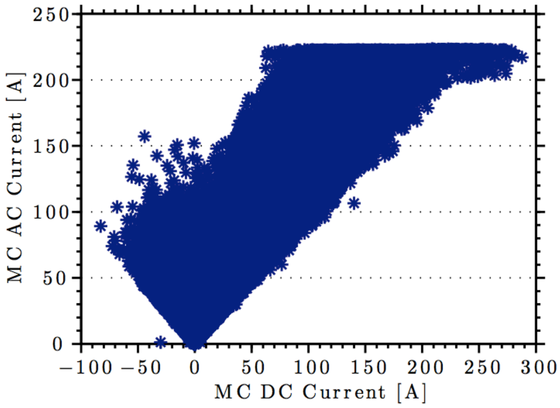

Figure 5.12.: SRZero Inverter AC Output Currents vs. DC Inverter Input Currents

Figure 5.13 shows the resulting DC motor controller currents as a function of time for the sample drive cycle. The mean DC motor controller current is 5.74 A with a relatively high standard deviation of 16.55 A. The minimum current is -36.8 A. The goodness of fit between the modelled and measured DC currents however is relatively low ($R^2 = 0.52$). Most probably this is due to inaccurate inverter efficiency mapping.

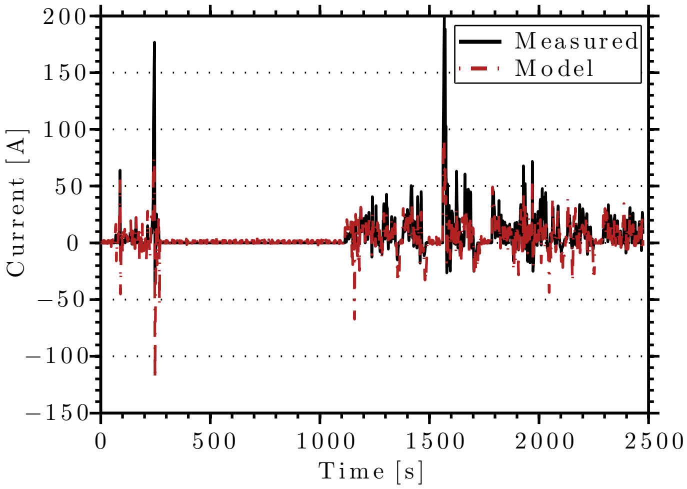

Figure 5.13.: Theoretical and Measured Requested MC DC Currents

During the test drive along the Pan-American Highway the mean DC motor controller currents were higher. On average, 7.1 A were drawn from the two motor controllers combined during the 644 operational hours of the SRZero as shown by the moving average in red in figure 5.14a. The maximum requested DC motor controller current was 287.7 A (i.e. 2.88 C). However, in accordance with the frequency distribution of torque values, high current values (i.e. >60 A) are very rare as shown in figure 5.14b. They constitute less than 1% of all MC DC current values. Neglecting the no-current condition, the nominal current drawn was 14.0 A. Again, a FFT analysis did not reveal dominant frequencies.

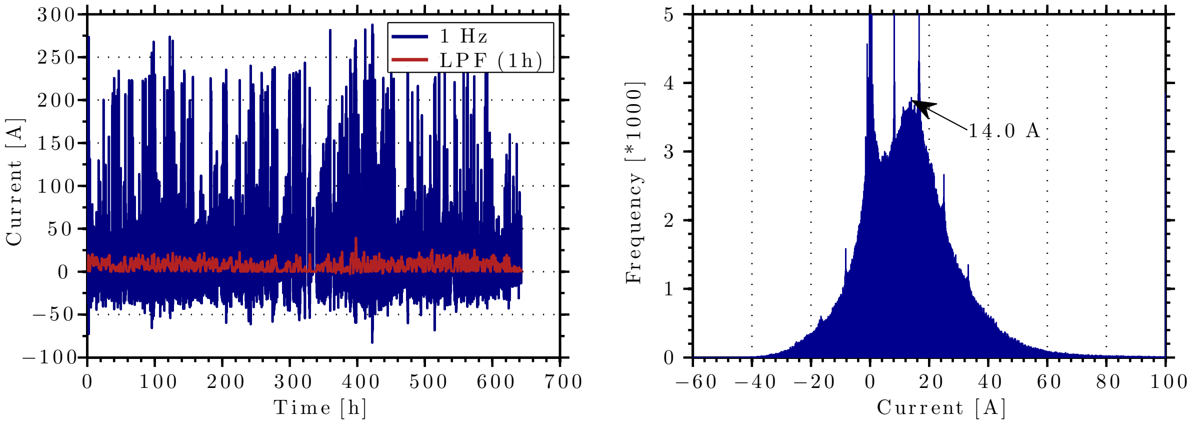

(a) Time Trend

(b) Histogram

Figure 5.14.: Combined SRZero DC Motor Controller Current Values

Derivation of Traction Battery Characteristics

The two motor controllers, which are connected in a parallel configuration, are directly linked to the battery terminals (see figure 2.8). Therefore, considering ohmic losses in the wires and at the connectors, the DC battery power is assumed to be proportional to the combined DC motor controller powers. A linear fit analysis between measured DC battery powers and measured DC motor controller powers reveals a linear coefficient of 0.87. The goodness of fit with $R^2 = 0.89$ is relatively high. Thus, DC battery powers on average are reduced by as much as 13% between the battery terminals and the motor controllers.

Figure 5.15 shows the measured DC traction battery currents of the SRZero as a function of time and frequency. The mean measured current is 7.21 A (0.07 C) with a standard deviation of 14.69 A (0.15 C). The maximum current measured was 264.73 A (2.64 C) and the minimum current was -88.56 A (-0.88 C). Figure 5.15b shows that the nominal current is 14.4 A (0.14 C) when ignoring the no-current condition. Thus, despite being highly dynamic, discharge rates were relatively low (i.e. < 3 C). 3 C is also the maximum recommended constant current discharge rate, while it is 20 C for impulse currents (see appendix B). This means that maximum impulse currents during the SRZero test drive were even lower than maximum recommended constant current discharge rates.

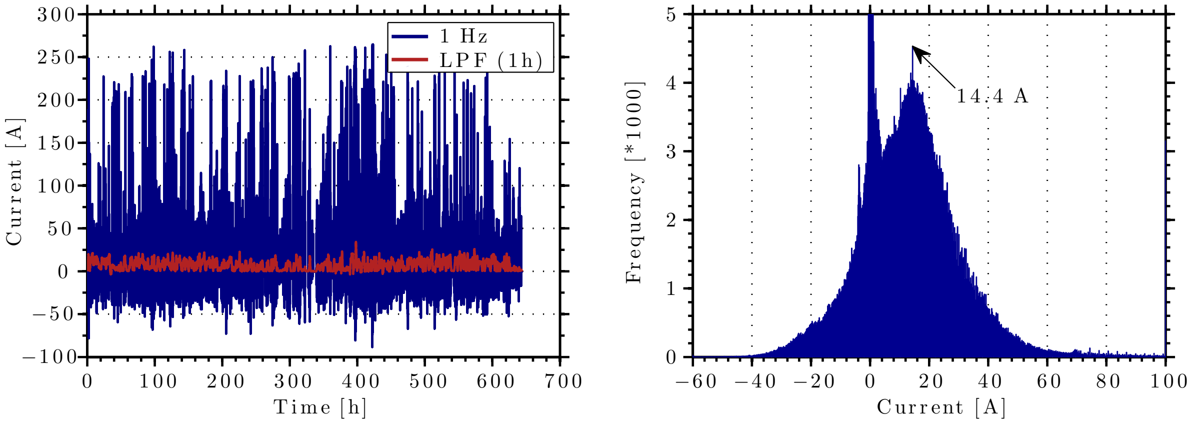

(a) Time Trend **(b) Histogram**

Figure 5.15.: SRZero Traction Battery Current

Derivation of Dynamic State of Charge (SOC) and Open-Circuit Voltage (OCV)

The battery current values present one important input parameter for a reliable and dynamic state of charge (*SOC*) estimation. As illustrated by figures 5.3b and 5.5 and supported by equations 2.5 and 2.7, the *SOC* is a function of current and time only for steady discharge procedures:

$$SOC_{const,I}(t) = 100\frac{Q_{nom} - I\sum \Delta t}{Q_{nom}} \tag{5.2}$$

In this case, it is the ratio of the instantaneous capacity divided by the rated or nominal capacity Q_{nom} multiplied by 100. Here, the instantaneous capacity left in the battery can be conveniently estimated by the difference of the rated capacity and the product of the constant current I and the total discharge time $\sum \Delta t$. Therefore, Coulomb counting is applied. The OCV at specific SOC values can then be estimated via equation 5.1.

For dynamic discharge rates however, the determination of the SOC is more complex. Here, the discharge current *I(t)* is no longer constant, but highly dynamic as illustrated by figure 5.13. Thus, in theory the SOC for dynamic discharges is determined by the following equation:

$$SOC_{dyn,I}(t) = 100\frac{Q_{nom} - \int I dt}{Q_{nom}} \tag{5.3}$$

It is the same as equation 5.2, but the capacity is no longer a product of the constant current and the total discharge time, but a time integral of the discharge current. The practical problem associated with this equation is that the current needs to be measured continuously, i.e. at infinitesimal short time steps. Typical current sensors however feature relatively low sampling frequencies (1-100 Hz). Certainly for the SRZero, the sampling frequency of 1 Hz is low. The main motivations for using current sensors with low sampling frequencies include low cost and a manageable data log size. Low sampling frequencies lead to the misleading assumption that the measured current is applied throughout the measured time step. Thus, the lower the sampling frequency, the lower the accuracy for SOC estimations.

Hence, an adaptive algorithm may be introduced. One way is to use the OCV as a means of regular correction. According to figure 5.5 and equation 5.1 the OCV reliably relates to specific SOC values. Because of intermittent charge periods through regenerative braking, resistance losses and the battery's capacitative behaviour, the traction voltage V_{trac} is not equal to the OCV for most of the time during a discharge process. However, at the very beginning of a new discharge cycle (i.e. when the EV is switched on) and after a rest period of 30 min (i.e. when the EV is parked for a stop) the traction voltage may be assumed to be in equilibrium ($V_{trac} = OCV$). This means that the SOC reading can be initialised by the initial traction voltage reading, which is taken as the OCV reading. The corresponding SOC is retrieved by solving equation 5.1 for SOC. Equation 5.4 shows that this solution is not explicit and therefore needs to be solved iteratively. For the 164 $LiFePO_4$ cells of the SRZero the solution is as follows:

$$SOC_{dyn,I,1}(OCV) = 164\left[100 - \frac{\ln(OCV - 3.350 + 8.66\text{E-}4(100 - SOC)) + \ln(-2\text{E-}9)}{0.170}\right] \tag{5.4}$$

Then, after initialising the SOC and at any time, when no OCV value is available, the SOC may be estimated using equation 5.5:

$$SOC_{dyn,I,2}(t) = SOC_{dyn,I,1} - \sum I\Delta t \tag{5.5}$$

Therefore, the determination of SOC values for dynamic discharge processes using this particular approach involves both *OCV* referencing and Coulomb counting. Figure 5.16 shows the results of *OCV* and *SOC* estimations for the sample SRZero drive cycle. The initial measured traction voltage is 537.95 V. From the previous paragraph (figure 5.13) we know that $I_{mc,dc}(0)$ is also equal to zero. In addition, the vehicle was switched off before for at least one week. Therefore,

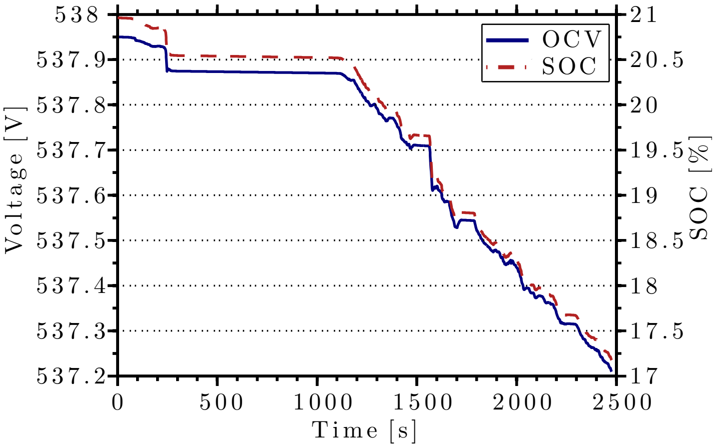

Figure 5.16.: OCV & SOC vs. Time for Sample Drive Cycle

the initial traction voltage must be the open-circuit voltage. The resulting *SOC* is 20.96%, i.e. relatively low. The measured capacity draw for the entire drive cycle is 3.79 Ah, i.e. 0.278 Ah/km. The rest period is only about 15 minutes, thus not long enough to take *OCV* readings. Therefore, the *SOC* at the end of the drive cycle is (20.96-3.79)% = 17.17%, which corresponds to a 'mileage' of 3.60 km/%*SOC*. The *OCV* values after the initial value are calculated using equation 5.1. Figure 5.16 also shows that *SOC* vs *OCV* relationship is still within its linear regime as the two move in parallel. If the drive cycle was longer, the *OCV* is expected to drop faster than the *SOC* as the exponential regime begins to dominate (compare with figure 5.5). After about 1,700 s *OCV* and *SOC* rise for a short period of time thanks to regenerative braking.

Derivation of Traction Voltage

Simulating and modelling the voltage response of a battery given a current request is probably the most important, yet also the most complicated aspect of battery modelling. It is crucial for the calculation of the output power, which is the product of the traction voltage V_{trac} and the battery current I. Given a current request from the motor controllers of an EV, an accurate battery model will determine whether battery operating limits are exceeded or are undercut. The two most significant battery operating limits are the minimum and maximum traction voltage ($V_{trac,min}$ & $V_{trac,max}$) respectively. These lead to several other battery operating limits including the maximum and minimum currents (I_{min} & I_{max}) at various levels of *SOC*. The battery model is usually an integral component of the battery management system (BMS).

A simple example illustrates the effectiveness of an accurate battery model. If, for instance, the state of charge of the EV traction battery is relatively low, than its open-circuit voltage is also relatively low. This means that at high states of charge higher maximum currents may be drawn compared with low states of charge assuming a minimum voltage limit and a voltage drop from the open-circuit voltage to the traction voltage. However, because of the non-linear I-V relationship, the traction voltage is difficult to accurately predict with mathematically simple battery models.

For the derivation of the traction voltage V_{trac}, five equivalent circuit models introduced in section 2.3.4 are applied and compared against each other. These include the internal resistance model, the Thévenin model, the PNGV model, the resistor capacitor (RC) model and the MATLAB/Simulink battery model.

The **Internal Resistance Model** is probably the least complex battery model. As equation 5.6 demonstrates, the traction voltage linearly depends upon the current request $I(t)$ and requires two input parameters:

$$V_{trac}(t) = OCV - R_{int}I(t) \tag{5.6}$$

While the internal resistance R_{int} is assumed to be constant, the open-circuit voltage (OCV) is a function of the state of charge (SOC) as illustrated in figure 5.5. Therefore, the accuracy of the internal resistance model highly depends on the accuracy of the $SOC(OCV)$ function as well. The optimum value for R_{int} can be found by regression.

The **Thévenin Model** is described by equations 2.14-2.15. Their solution can be written as:

$$\begin{aligned} V_{trac}(t) = OCV - R_{int}I(t) - R_{th} \Bigg[& \left(1 - \frac{\left(1-e^{-\Delta t/\tau}\right)}{\Delta t/\tau}\right) I(t) \\ & + \left(\frac{\left(1-e^{-\Delta t/\tau}\right)}{\Delta t/\tau} - e^{-\Delta t/\tau}\right) I(t-1) + e^{-\Delta t/\tau} I(t-1) \Bigg] \end{aligned} \tag{5.7}$$

Equation 5.7 shows that the Thévenin model is equal to the internal resistance model minus the Thévenin voltage V_{th}. V_{th} is the product of the constant Thévenin resistance R_{th} and the dynamic Thévenin current I_{th}. I_{th} itself is a function of the previous input current $I(t-1)$, the time step Δt (here 1 s) and the time constant τ. The time constant ($\tau = R_{th}C_{th}$) presents the time required to charge or discharge the battery through the resistance R_{th} by approximately 63% (= 1-e^{-1}) of the difference between the initial and final capacity value ΔC_{th}.

The **PNGV Model** is characterised by equations 2.16-2.18. Their solution can be written as shown in equation 5.8. It is the same as the solution for the Thévenin model (equation 5.7) minus a third voltage. This voltage is the product of the reciprocal of the bulk capacitance *OCV'* and its capacity.

$$\begin{aligned}V_{trac}(t) = OCV - R_{int}I(t) - R_{th} & \left[\left(1 - \frac{\left(1-e^{-\Delta t/\tau}\right)}{\Delta t/\tau} \right) I(t) \right. \\ & + \left. \left(\frac{\left(1-e^{-\Delta t/\tau}\right)}{\Delta t/\tau} - e^{-\Delta t/\tau} \right) I(t-1) + e^{-\Delta t/\tau} I(t-1) \right] \\ & - OCV' \left[\left(\sum I(t-1)\Delta t \right) + \frac{\left[I(t-1)+I(t)\right]\Delta t}{2} \right]\end{aligned} \tag{5.8}$$

The **RC Model** is characterised by equations 2.19-2.20. Equation 5.9 is the solution for these equations.

$$V_{trac}(t) = \frac{V_B R_C + V_C R_E}{R_E + R_C} + \left(-R_T - \frac{R_C R_E}{R_E + R_C} \right) I(t) \tag{5.9}$$

The standard battery model of the **MATLAB/Simulink Library** is characterised by equations 2.21-2.22. Equation 5.10 recalls the solution for the discharge process:

$$V_{trac}(t) = OCV - R_{int}I(t) - K \frac{Q}{Q - \int_0^t Idt} \left(\int_0^t Idt + I^* \right) + Ae^{B\int_0^t Idt} \tag{5.10}$$

It is similar, but uses a different methodology than most equivalent circuit models. Like all equivalent circuit models the MATLAB/Simulink battery model begins by calculating the ohmic voltage drop, which is simply the difference between the OCV and the product of the constant internal resistance R_{int} and the dynamic current *I(t)*. The third voltage term, which is deducted, presents the voltage drop caused by polarisation. Therefore, it is the product of the polarisation constant K [V/Ah], the reciprocal of the DOD and the sum of the integral of the input current *I(t)* and the filtered current I^*. I^* is the result of applying a first-order low-pass filter with an assumed time constant of 30 s to *I(t)*. In other words, it is the time average of *I(t)* for a duration of 30 s.

Figure 5.17 shows the results of each equivalent circuit model applied to the SRZero battery currents. The modelled traction voltages are shown as well as the measured traction voltages for the sample drive cycle. The model with the highest accuracy compared with the measured traction voltage values is the PNGV model with a coefficient of determination of 0.705. The goodness of fit parameters as well as the individual cell parameters for each model are listed in table 5.3.

The second most accurate model is the MATLAB model followed by the Thévenin model. The simple internal resistance model is the least accurate model for this application.

During the test drive, the SRZero showed similar voltage values as in figure 5.17. The filtered voltage alternated around 540 V as can be seen in figure 5.18a. Also, the mode traction voltage value was 541 V. The mean voltage was 533.60 V with a relatively low standard deviation of 12.03 V. The minimum voltage was 405.88 V, i.e. 2.47 V per cell. This is just below the recommended minimum cell voltage of 2.5 V (see appendix B). However, low traction voltages

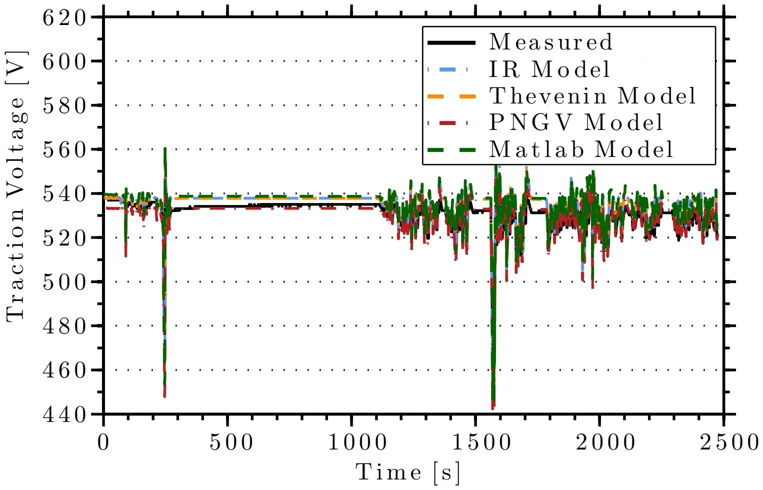

Figure 5.17.: Comparison of Various Battery Models Applied to SRZero Drive Cycle

Table 5.3.: Comparison of Various Battery Models Applied to SRZero Drive Cycle

Goodness of Fit Parameter (Battery Pack)	**Battery Model** **Internal Resistance**	**Thévenin**	**PNGV**	**RC**	**MATLAB**
Sum of squares due to error (SSE)	7.68E4	7.68E4	3.06E4	n/a	6.54E4
Coefficient of determination (R^2)	0.261	0.260	0.705	n/a	0.370
Root mean squared error (RMSE)	5.57	5.57	3.52	n/a	5.14
Battery Parameter (Single Cell)					
R_{int} [mΩ]	3	3	3	n/a	3
R_{th} [mΩ]	n/a	1.3	1.3	n/a	2.8
C_{th} [F]	n/a	54.35	n/a	n/a	n/a
τ [ms]	n/a	70.7	n/a	n/a	n/a
OCV' [1/F]	n/a	n/a	0.1	n/a	n/a

(i.e. <500 V; <3.05 V per cell) occured very rarely. They only accounted for less than 1% for all measured traction voltage values. The maximum measured voltage was 637.25 V (3.89 V per cell), just after the SRZero has been charged.

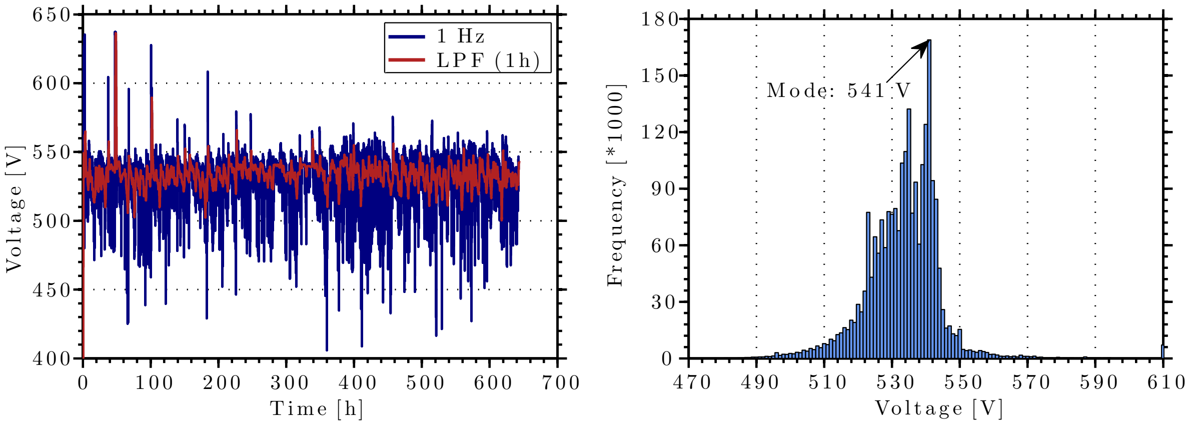

(a) Time Trend **(b) Histogram**

Figure 5.18.: SRZero Traction Voltage

Without any information on the corresponding current, no assumption is made about the corresponding state of charge. Therefore, figure 5.19 shows the combinations of current and voltage, which occurred most frequently. Colours range from dark blue (least frequent combination) to red (most frequent combination). The pair 1 A - 541 V occurs most frequently. The figure also shows that with increasing current, traction voltage nearly drops linearly.

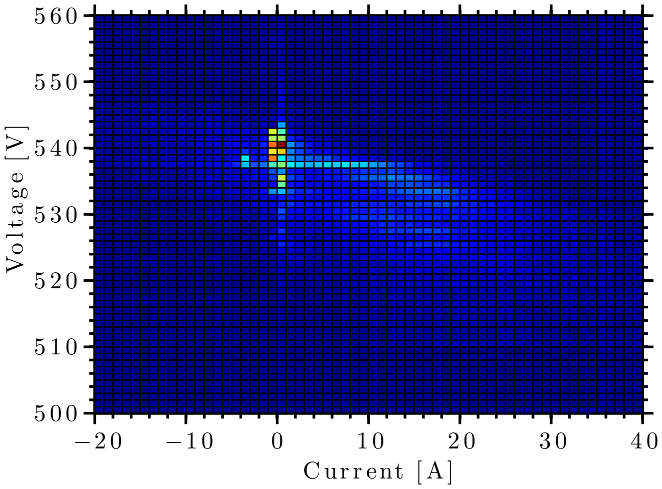

Figure 5.19.: SRZero Traction Voltage vs. Current

Derivation of Battery Power

The available battery power is the product of the battery current *I(t)* and the traction voltage $V_{trac}(t)$. Depending on the functionality of the BMS, current and voltage limits are implemented. The mean DC battery power is 3.75 kW with a relatively high standard deviation of 7.60 kW and a mode of 8.5 kW as can be see from figures 5.20a-5.20b.

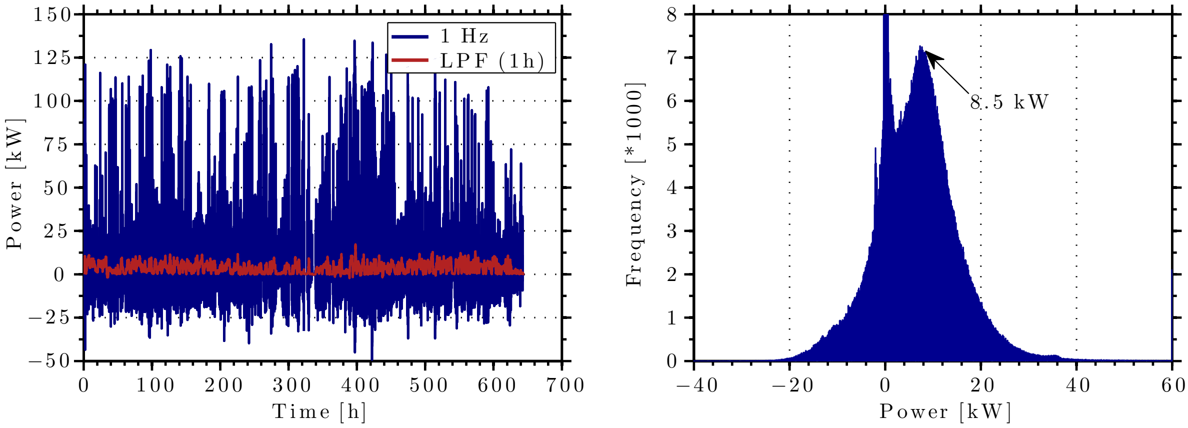

(a) Time Trend **(b) Histogram**

Figure 5.20.: SRZero Battery Power Output

5.1.3. Interim Conclusion

This section has demonstrated the most important short-term battery performance characteristics. Depending on the power and energy requirements, safety and cost considerations as well as design limitations, individual cells can be connected in series (S), in parallel (P) or a combination of both. Accordingly, the total voltage, capacity, and power levels can be adjusted. More detailed battery characteristics can be observed by looking at steady and dynamic discharge behaviour separately.

Steady discharge behaviour (V-Q curve) is usually published by the manufacturer for various discharge (C) rates. The capacity (C) rate is a measure of the constant current, at which the cell is discharged within one hour. Thus, for a cell rated at 100 Ah, 0.2 C is equivalent to a constant discharge current of 20 A, while 1 C is equivalent to 100 A. Due to the capacity rate effect high discharge rates result in a lower discharge capacity than lower discharge rates. Published and measured discharge curves are not necessarily the same as shown by figures 5.2 and 5.3b. Therefore, it is highly recommended to take own measurements before continuous use of the cells. $LiFePO_4$ cells feature a relatively high nominal voltage (3.1-3.3 V) and the voltage profile is relatively flat with its discharge capacity Q.

While cell voltage levels vary according to its steady discharge current, open-circuit voltage (OCV) levels remain constant irrespective of its C-rate. Therefore, exactly one depth of discharge (DOD) value can be allocated to exactly one OCV value. The state of charge is equal to 100 - *DOD*. It follows that the *OCV* can be described as an explicit function of *SOC* and vice versa. As figure 5.5 illustrates, this function can be divided into a linear regime (100-20% *SOC*) and an exponential regime (20% *SOC*-end of discharge).

Dynamic battery behaviour is also dominated by the voltage response given a current request. However, the output voltage function is not as simple as for steady discharge processes. First, battery current requests are derived. Following a backward-forward facing quasi-steady ($\Delta t = 1$ s) modelling approach, battery currents are derived from a sample drive cycle of the SRZero. The sample drive cycle (figure 5.7), SRZero specifications (table 3.1) and first principle assumptions (see section 4.1) lead to torque requests at the rear left and rear right wheel respectively. The accuracy for these values (R^2 = 0.70-0.73) is relatively high given the simplicity of the model.

It turns out that torque requests are dominated by the acceleration profile (figure 5.8). Therefore, most electric motors for EV applications are torque controlled, which in turn is a function of pedal position. Thus, AC motor currents may be estimated using the torque constant K_T. Considering efficiency losses in both directions of power flow (i.e. during discharge from the battery to the wheel and during recuperation from the wheel to the battery) the battery current may be estimated. Results show that the mean measured battery current is relatively low (7.21 A = 0.07 C), but very dynamic with a standard deviation of 14.69 A. Ignoring the no-load condition, the nominal current is 14.4 A, which is still relatively low. Maximum currents did not exceed 3 C.

After initialising, current requests were used to determine the *OCV* and *SOC* values for the sample drive cycle following the generic relationship established in equation 5.4. The resulting traction voltage primarily depends upon the current request, the internal resistance and the state of charge. Various equivalent circuit models have been applied and parametrised for this application. The PNGV model results in the highest accuracy with a relatively high coefficient of determination ($R^2 = 0.7$). This may be attributed to the additional capacitative element (see figure 2.33), which adjusts the open-circuit voltage V_{OC} according to the current drawn. Given the strong correlation between the terminal voltage and the open-circuit voltage and evidence that the dynamic OCV is strongly affected by capacitative effects, it is suggested to expand upon this. Specifically, this could involve a more sophisticated parametrisation and/or adding more capacitative elements.

5.2. Battery Degradation

The previous section looked at short-term battery behaviour, while this section is devoted to the long-term effects of battery behaviour, in particular battery degradation. This section is divided into three subsections. The first subsection analyses experimental long-term cycling data, while the second subsection builds an analytical model based on the experimental results. The third subsection summarises the main findings from this section.

5.2.1. Empirical Evidence of Battery Degradation

This subsection analyses empirical evidence of battery degradation on the basis of four different examples.

Long-Term Battery Cycling of Sample SRZero Cell

Figure 5.21 shows the results of long-term battery cycling applied to one of the SRZero battery cells. For each cycle the cell was first fully charged and then fully discharged. The exact experimental procedure is listed in table 3.5. The figure shows a clear trend, that of diminishing capacity with an increasing number of cycles. Capacity fade seems to be proportional to the number of cycles, however two linear regimes can be observed. For the first 64 cycles capacity fade is higher than for the remaining cycles. Applying a linear fit model to the data results in a capacity loss of 0.05 Ah (0.05%) per cycle for the first 62 cycles and a capacity loss of 0.03 Ah (0.03%) per cycle for the remaining 14 cycles. The total capacity fade for the 73 cycles is 3.32 Ah (3.32%).

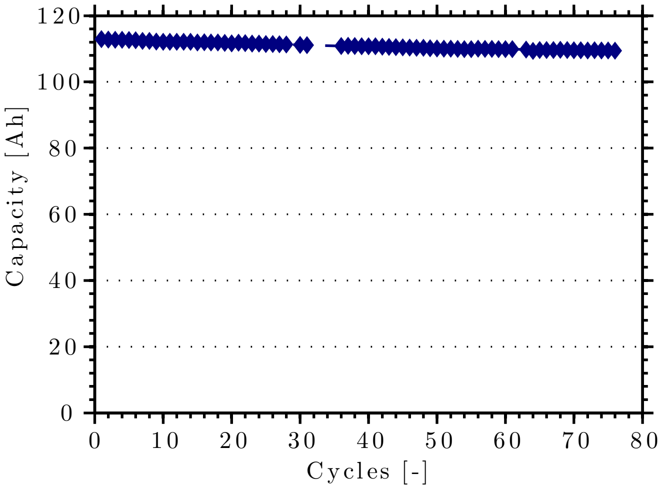

Figure 5.21.: Discharge Capacity as a Function of Battery Cycles for Sample SRZero Cell

The information from the previous figure (5.21) may also be displayed differently. Figure 5.22 shows typical voltage-capacity (V-Q) curves for the charge and discharge processes of the cycling procedure associated with figure 5.21. Figure 5.22a on the left hand-side shows the cell voltage as a function of capacity for the 73 charging processes, while figure 5.22b shows the the cell voltage as a function of capacity for the 73 discharging processes. The light blue lines indicate the data for all 73 cycles, while the dark blue line shows the respective process during the first cycle. The orange line shows the respective process during the 36th cycle, i.e. about halfway during the testing procedure. The red line indicates the charging or discharging process for the last cycle. Figure 5.22a shows a typical constant-current constant-voltage (CCCV) charging process. Up to 3.9 V the charging process is dominated by a constant current charge. Once that upper limit is reached, the voltage is kept constant and a current with a continuously decreasing magnitude is applied. This voltage plateau can be seen at the top right corner. The figure also shows that with an increasing number of cycles the charging capacity is reduced. Up to a charge capacity of 80 Ah, the profiles of the V-Q curves are almost identical. At charge capacities above 80 Ah, the profiles diverge. With an increasing number of cycles higher cell voltage values tend to be reached earlier, i.e. at lower charge capacities already.

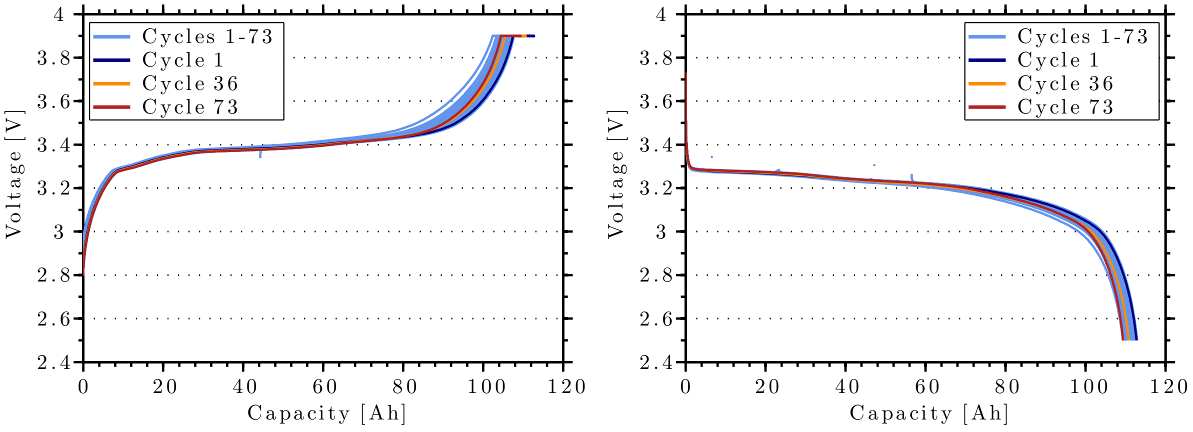

(a) Charge **(b) Discharge**

Figure 5.22.: Cell Voltage as a Function of Capacity During Long-Term Cycling

Similar observations can be made about the discharge process in figure 5.22b. With an increasing number of cycles the discharge capacity is reduced. Also, after about 80 Ah discharge capacity cell voltages tend to drop faster with an increasing number of cycles. This hypothesis is backed by the parametrisation of the custom model for the generic OCV vs SOC relationship (equation 5.1). Figure 5.23 shows the coefficients for the generic relationship derived in the previous section. Coefficient a, which determines the voltage at full charge (100% SOC), increases with the number of cycles by about 0.3%. Thus, this increase is small. Next, the magnitude of coefficient b, which governs the linear voltage drop from 100% down to about 80% SOC, increases with the number of cycles by about 15%. It follows that the voltage drop above 20% SOC is significantly accelerated with an increasing number of cycles. Coefficient c, which regulates the vertical shift of the exponential voltage drop at low SOC values, remains relatively level with the number of cycles. However, coefficient d, which controls the slope of the

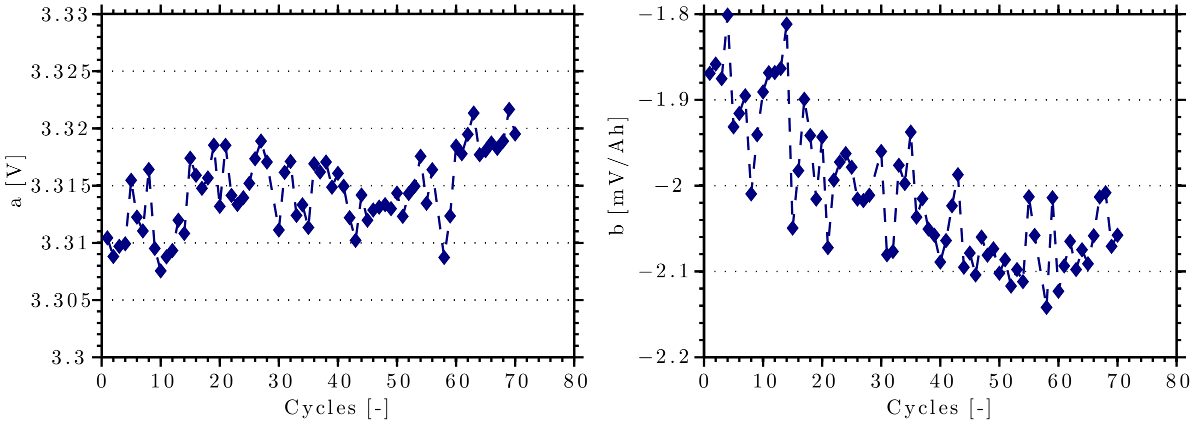

(a) Coefficient a

(b) Coefficient b

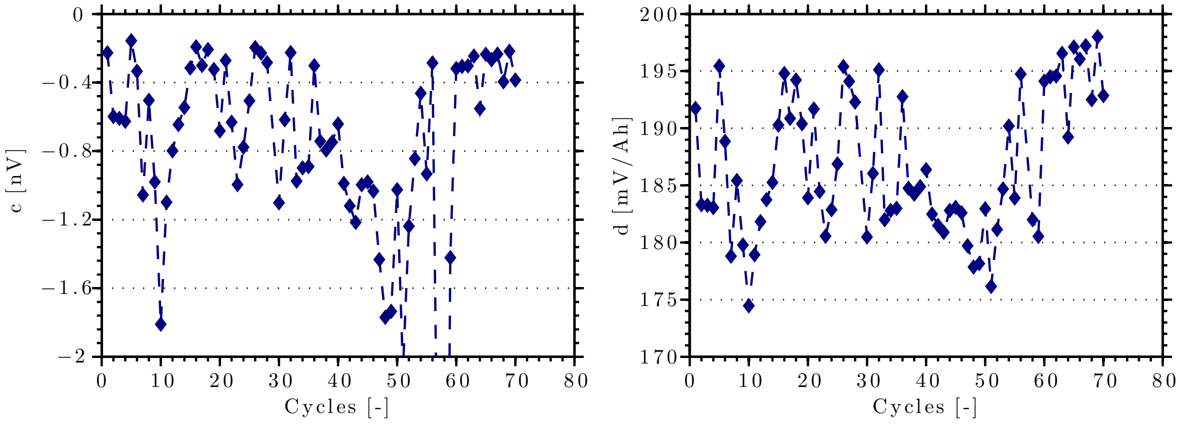

(c) Coefficient c

(d) Coefficient d

Figure 5.23.: Coefficients for Custom Model of OCV vs. SOC Relationship

exponential decay, increases by about 5% with the number of cycles. Therefore, both voltage drops during the linear and exponential discharge regime accelerate with the number of cycles.

Consequently, battery degradation affects both charge and discharge processes. For both processes, capacity is reduced with an increasing number of cycles. For the charging process above about 80% SOC the voltage increase is accelerated with an increasing number of cycles, while during the discharge process below about 20% SOC the voltage drop is accelerated with an increasing number of cycles. This means that the resistance of the cell is increased with an increasing number of cycles. Because capacity fade results in the diversion of voltage levels for a SOC range of 20%, we recommend a depth of discharge of 80%. This means that the optimum working capacity for these cells is 1.25 (=1/0.8) times the optimum nominal capacity. Considering a mean capacity fade of 0.045% and an expected lifetime of roughly 150-1,700 cycles (see section 5.2.2), the required spare capacity ranges between 7-125%.

Galvanostatic Electrochemical Impedance Spectroscopy Testing

The second empirical example of battery degradation is related to galvanostatic electrochemical impedance spectroscopy testing. The exact testing procedure is listed in table 3.6. Also, the cycling history is shown in figure 5.4. Here, for a relatively low number of cycles (9), impedance measurements are taken at different levels of state of charge. Figure 5.24 shows the characteristic V-Q curves for the charge and discharge processes. Like in in figure 5.22, the voltage increase during the charging process (figure 5.24a) is accelerated with an increasing number of cycles. Also, during the discharge process the voltage drop for the last cycle is fastest compared with earlier cycles and relative to the discharge capacity. The peaks along the discharge curve present rest periods of 30 min, during which the cell voltage is assumed to reach its equilibrium (OCV). The impedance spectroscopy test results shown in figure 5.25 are taken at these 20 Ah intervals.

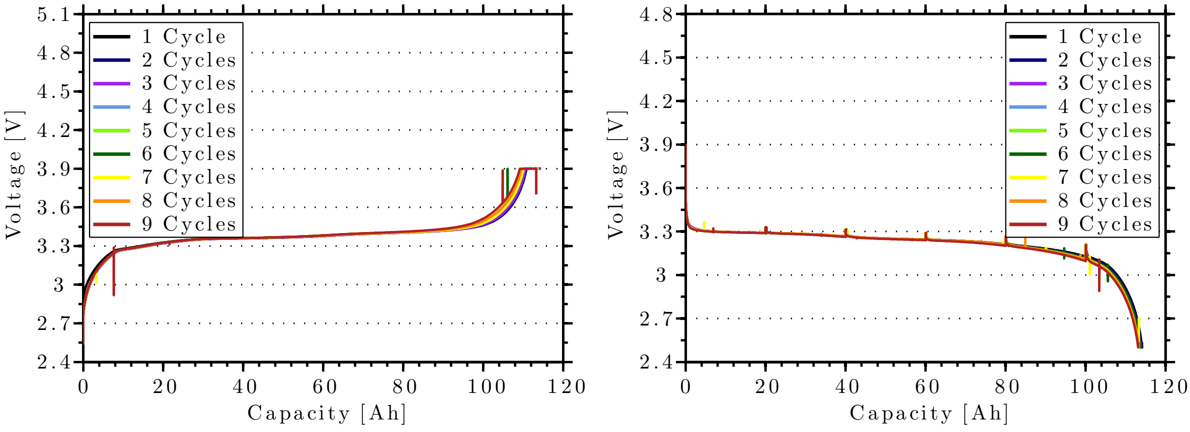

(a) Charge **(b) Discharge**

Figure 5.24.: Cell Voltage as a Function of Capacity During Short-Term Cycling

Figure 2.32 has demonstrated the significance and also gave an interpretation of electrochem-

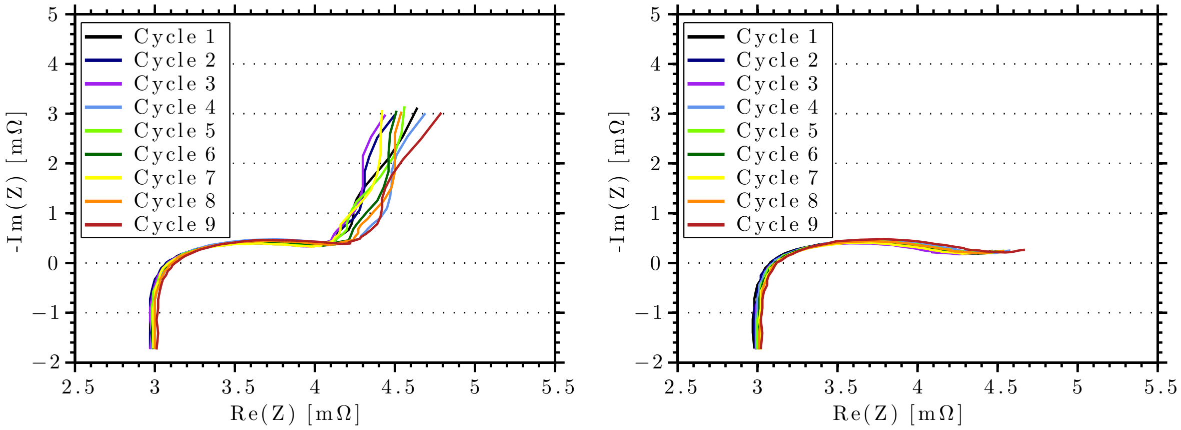

(a) 100% SOC **(b) 80% SOC**

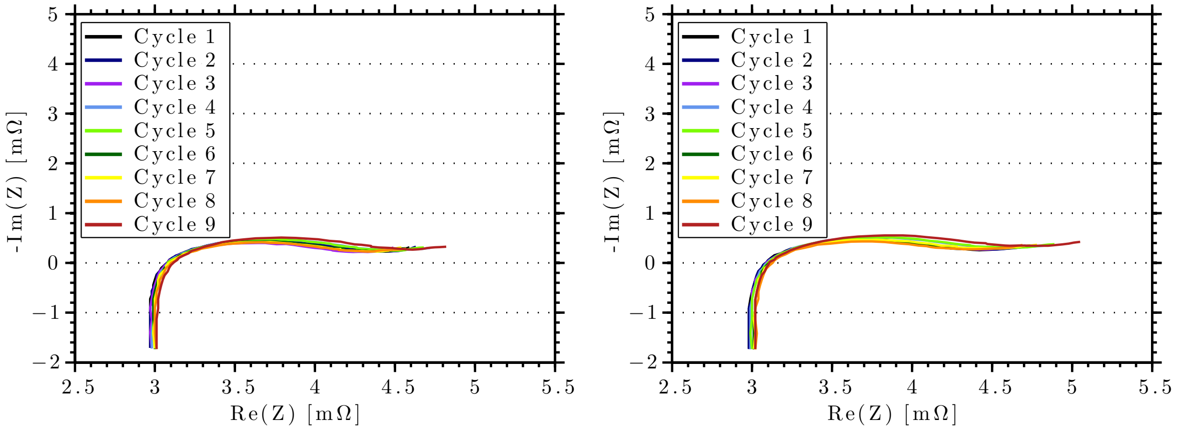

(c) 60% SOC **(d) 40% SOC**

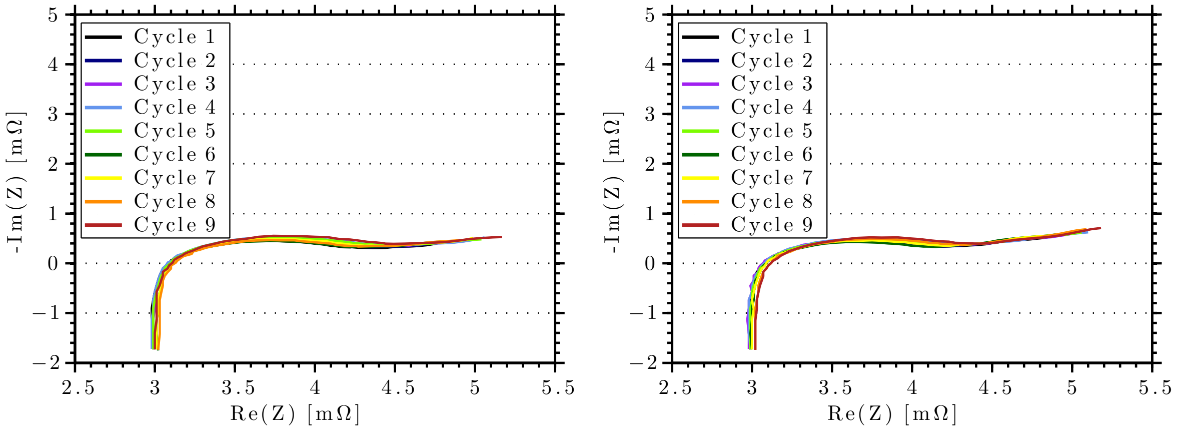

(e) 20% SOC **(f) 0% SOC**

Figure 5.25.: Galvanostatic Electrochemical Impedance Spectroscopy Test Results

ical impedance spectroscopy (EIS) for batteries. Therefore, the internal resistance of the cell at 100% *SOC* in figure 5.25a is about 3.1 mΩ while the polarisation resistance is about 1.0 mΩ. As explained in section 2.3.2, internal resistance refers to the series of ohmic resistance in the electrolyte, in the electrodes, and in the interconnections and battery terminals. The polarisation resistance refers to the depletion of reactants (electrons and ions) leading to a voltage drop.

Figure 5.26 shows both resistances as a function of battery cycles and *SOC* for the sample SRZero cell based on the results from figure 5.25. As expected, the internal resistance increases with the number of cycles, but not significantly (1.08% for all nine cycles; 0.13% per cycle). On average, the internal resistance increases by 4.76 $\mu\Omega$ per cycle. Thus, for the SRZero battery pack with 164 cells in series this would mean an increase of 0.78 mΩ per cycle. Also, internal resistance values remain relatively constant with different levels of state of charge as can be seen from figure 5.26a.

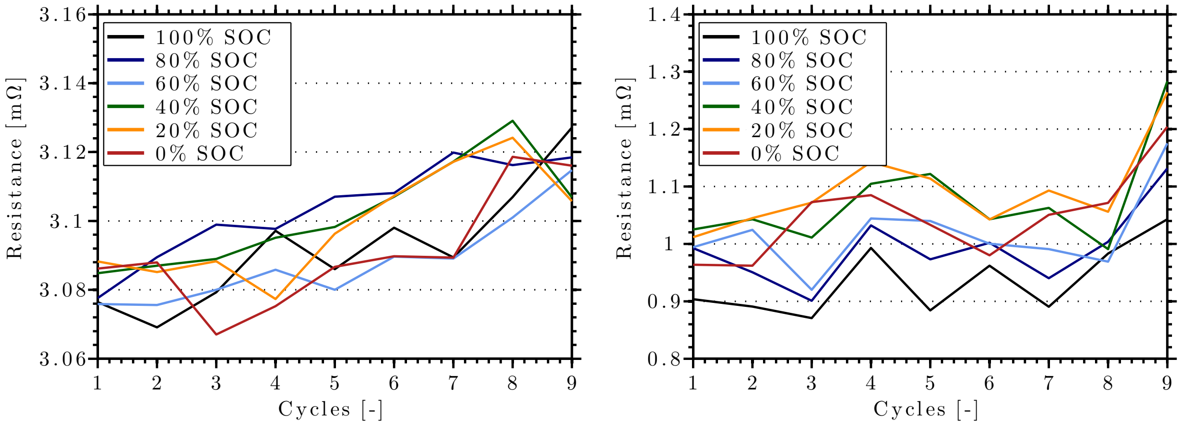

(a) Internal Resistance **(b) Polarisation Resistance**

Figure 5.26.: Resistance Values as a Function of Battery Cycles for Sample SRZero Cell

Polarisation resistance (figure 5.26b) in contrast increases significantly with the number of cycles (20.5% for all nine cycles; 2.44% per cycle). This compares to an average capacity fade of 0.06% per cycle, i.e. slightly higher than in the previous example. On average, the polarisation resistance increases by 14.74 mΩ per cycle. This means that for the SRZero battery pack the polarisation resistance would increase by as much as 2.42 Ω per cycle if cycled under the same conditions. The polarisation resistance also shows a second trend. As expected, the polarisation resistance increases with a decreasing state of charge. Thus, polarisation resistance is highest, when the cell is almost 'empty'. Internal resistance values on average are more than three times as large as polarisation resistances.

Long-Term Battery Cycling of Low-Capacity Cell at Low DOD (20%)

A third example of capacity fade is illustrated in figure 5.27. Here, the cell is a low-capacity (2.3 Ah) A123 26650 cylindrical (i.e. 26 mm diameter × 65 mm length) cell. The data was

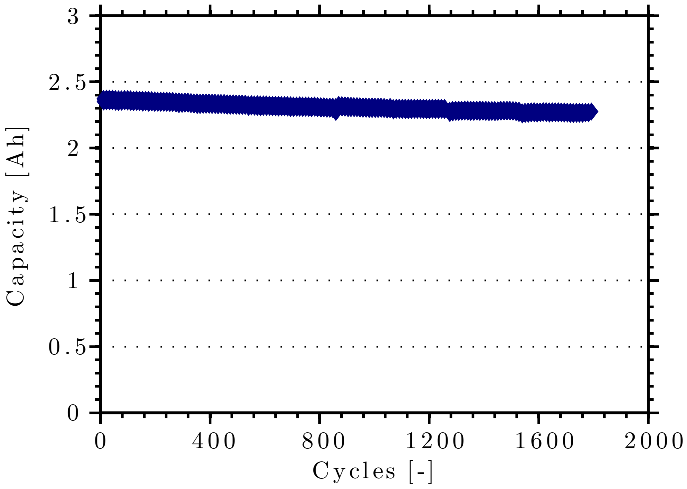

Figure 5.27.: Discharge Capacity as a Function of Battery Cycles for Low-Capacity Cell

kindly provided by Dr. Vladmir Yufit, research associate at Imperial College's Earth Science & Engineering Department. Again, the figure clearly shows the effect of capacity fade. The number of tested cycles (1,793) is significantly larger than in the previous examples, however the cell has not been discharged completely like in the previous examples. For this particular test, a depth of discharge of 20% was applied. The maximum discharge capacity was determined by applying a full discharge followed by a full charge for every 11$^{\text{th}}$ cycle.

Four regions with distinct linear capacity fade can be identified. The first region, from the beginning up to around 900 cycles, has a decay coefficient of 6.9E-5 Ah per cycle. The second regime, from around 900 cycles up to 1,300 cycles, the factor is reduced to 5.7E-5 Ah per cycle. During the third region, from 1,300 cycles up to 1,500 cycles, the decay coefficient is further reduced to 1.1E-5 Ah per cycle. During the last regime, from 1,500 cycles to the end the decay coefficient rises again to 2.2E-5 Ah per cycle when modelled linearly. Thus, for this example the capacity fades between 0.05-0.3‱ per cycle, which is 1-2 orders of magnitude lower compared with the capacity fade observed at the previous two examples.

Long-Term Battery Cycling with Dynamic Discharge Currents

The last empirical example of capacity fade refers to the long-term battery cycling of the SRZero cells during the test drive along the Pan-American Highway. In this example, discharge currents are no longer steady like in the previous examples, but highly dynamic (see figure 5.15a). In addition, charge capacities as well discharge capacities varied markedly as figure 5.28 points out. The figure shows the SOC range calculated on the basis of equation 5.4 for each of the 87 cycles. The first discharge (analysed in detail in subsection 5.1.2) is very short compared to other discharges. The mean ΔSOC is 53.37% with a relatively high standard deviation of 32.07%.

Figure 5.29 shows the characteristic V-Q curves for the 87 cycles of the Racing Green En-

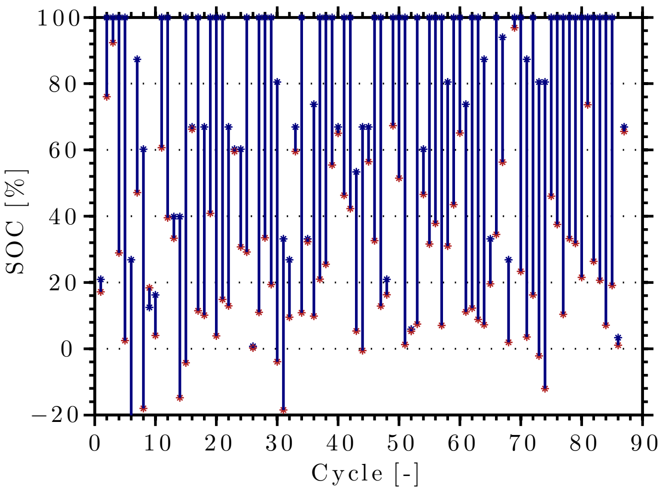

Figure 5.28.: Initial and Final SOC Values Individual Cycles along SRZero Trip

durance trip. Light blue lines highlight all cycles. Dark blue lines show an early cycle, orange lines show a cycle approximately half way between all all cycles and red lines show a cycle towards the end. The total battery statistics from the Racing Green Endurance Trip are listed in appendix F. When analysing all cycles in detail no clear trend with an increasing number of cycles can be observed. This means that both the dynamic character of the discharge current as well as the varying discharge capacities result in a much more complex environment in order to determine capacity fade compared with the previous examples, where the discharge current was steady.

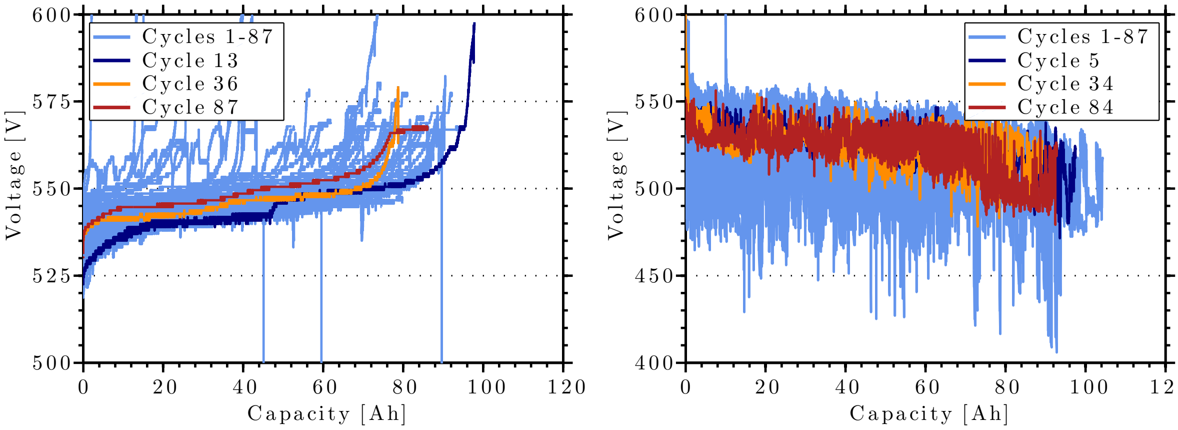

(a) Charge

(b) Discharge

Figure 5.29.: Traction Voltage as a Function of Capacity for SRZero Battery Pack

5.2.2. Empirical Modelling of Battery Degradation

The previous subsections have led to the conclusion that steady battery behaviour (I-V characteristics) is relatively easy to model and simulate, while dynamic battery behaviour is markedly more complicated to model. The same applies to the modelling of capacity fade for varying charge/discharge magnitudes. This subsection proposes the use of the rainflow-counting algorithm in order to model capacity fade for varying charge/discharge magnitudes.

Boundary Conditions

Here, the main motivation for studying the effects of battery degradation and in particular those of capacity fade is to be able to predict the required spare capacity necessary at the beginning of an EV's lifetime. Figure 5.1 illustrates how the spare capacity diminishes with time and use due to capacity fade.

First, the terms 'time' and 'use' need to be defined. The life time of a passenger vehicle in general is a function of its design, its mileage, its periodic maintenance, its handling and its natural environment. Therefore, life times of passenger vehicles can vary considerably, even those of the same make and model. However, there are relatively stable indicators for the minimum lifetime requirements of passenger vehicles such as warranties and annual mileages.

In the European Union (EU), car manufacturers are legally bound to offer warranties for at least two years for their new cars. Typical warranties, which cover wear and tear for passenger cars, range between three to eight years. Some warranties are also defined in terms of mileage, ranging between 100,000-150,000 km. Obviously, these numbers are only minimum reference values. Figure 5.30 shows annual mileage ranges and the corresponding relative share of all annual mileages in Germany and the UK. The data was retrieved from the travel surveys introduced in chapter 3. For the UK, the data was only available in terms of miles, which leads to a different scale compared with Germany. Figure 5.30a shows that 98% of annual mileages are

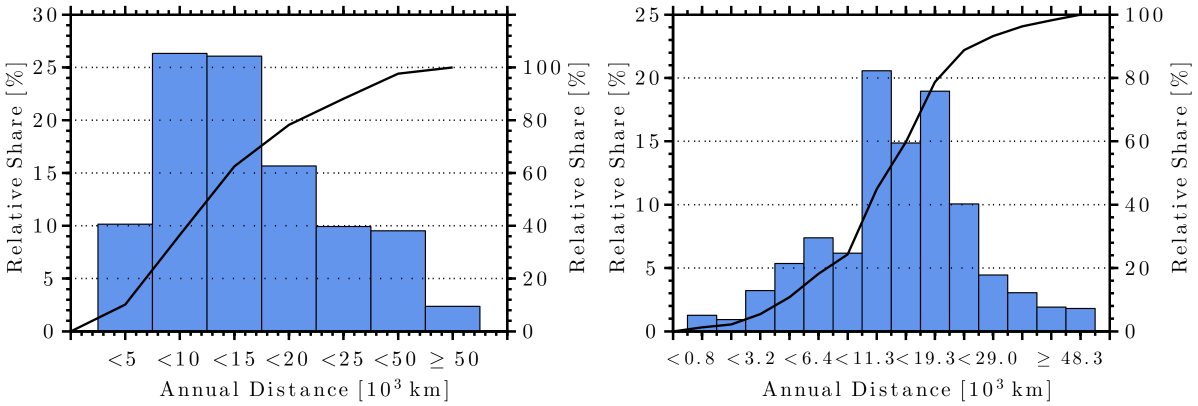

(a) **Germany** (b) **United Kingdom**

Figure 5.30.: Annual Mileages in Germany and the UK

below 50,000 km and 88% of annual mileages are below 25,000 km in Germany. Most drivers (63%) cover less than 15,000 km per year. The mean annual mileage in Germany is 14,500 km.

In the UK (see figure 5.30b), more than 96% of annual mileages are below 34,000 km, while almost 89% of annual mileages are below 25,000 km. The mean annual mileage in the UK is 14,000 km. Annual mileages in Germany and the UK are therefore very similar.

Assuming an annual mileage of 15,000-25,000 km and a lifespan of 7-10 years, the total vehicle mileage ranges between 105,000-250,000 km. This figure is in line with industry figures [13]. Based on these total vehicle mileages and the daily ranges from the previous chapter, table 5.4 lists the total battery cycle requirements. The third and fourth column also distinguish between full and half discharges. This accounts for drivers who choose to recharge their EV although the *SOC* is still around 50%.

Table 5.4.: Battery Cycle Requirements[1]

Country	**Range [km]**	**Number of Cycles [-]** **Full Discharge**	 **Half Discharge**
UK	150-400	250-1,667	500-3,333
Germany	150-575	174-1,667	348-3,333
US	200-700	142-1,250	284-2,500

Consequently, the total number of consecutive charge/discharge cycles for EVs can vary between around 150-1,700 full cycles, where the numbers have been rounded.

Rainflow-Counting Algorithm

This subsection introduces the rainflow-counting algorithm and applies it to the highly dynamic and non-uniform battery cycling data of the SRZero.

The rainflow-counting algorithm is mainly used in the context of material science in order to reduce a spectrum of varying stress into a set of simple stress reversals. The problem is that for most of the time, (tensile) peaks have a different magnitude of stress than the corresponding (compressive) troughs (see figure 5.31). Thus, consecutive peaks and troughs of a complex stress history do not constitute a full cycle. In 1968 Matsuishi & Endo [157] developed an algorithm, which '*allows the application of Miner's rule in order to assess the fatigue life of a structure subject to complex loading*' [158]. Miner's rule, also called the Palmgren-Miner linear damage hypothesis, predicts the number of cycles to failure given k different stress magnitudes in a spectrum $S_i (1 \leq i \leq k)$ each contributing $n_i(S_i)$ cycles.

$$\sum_{i=1}^{k} \frac{n_i}{N_i} = C \tag{5.11}$$

---

[1] based on a total mileage of 100,000-250,000 km

$N_i(S_i)$ is the number of cycles to failure of a constant stress reversal S_i and C is a constant, usually assumed to be 1. Figure 5.31 shows a random stress fluctuation with time. It is important to note that only (tensile) peaks and (compressive) troughs are shown. Intermediate values are not relevant for the rainflow-counting algorithm. Then, the time history of stress may be rotated clockwise by 90 degrees. The results are shown in figure 5.32. Now, each tensile peak (numbered numerically) may be thought of as a water source, from which water drops down the pagoda (numbered alphanumerically). A pagoda is a tiered tower, most frequently found in the Far East. There are three possibilities for each single rainflow to reach the the end of a half-cycle:

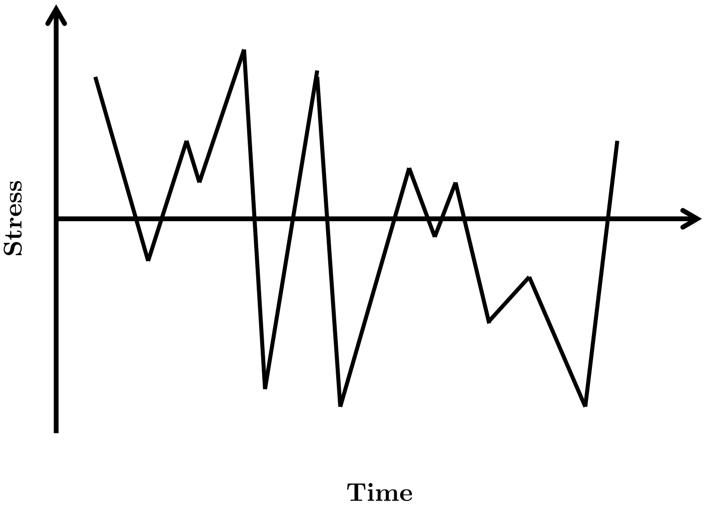

Figure 5.31.: Random Stress Fluctuation with Time

- It flows opposite a tensile peak of greater magnitude (1, 2)
- It merges with a flow that started at an earlier tensile peak (7)
- It directly reaches the end of the time history (4)

The magnitude of each half cycle is the difference along the horizontal axis between the initial value and the final value from figure 5.32. The same procedure is applied to compressive troughs in order to find the corresponding other half cycles. The resulting full and half cycles are shown in figure 5.33. The figure shows how consecutive and non-consecutive peaks and troughs are connected in order to build equivalent full cycles. Both amplitude and period of these equivalent cycles may vary significantly.

The idea of reducing a spectrum of varying stress into a set of simple stress reversals may also be applied to varying charge/discharge magnitudes of batteries. Like for a complex time history of stress, consecutive charge and discharge magnitudes are not equal in magnitude for most of the time. Therefore, consecutive charge and discharge magnitudes of a typical 'real-life cycling' history do not constitute full cycles according to the strictest interpretation of 'full cycle'. Figure

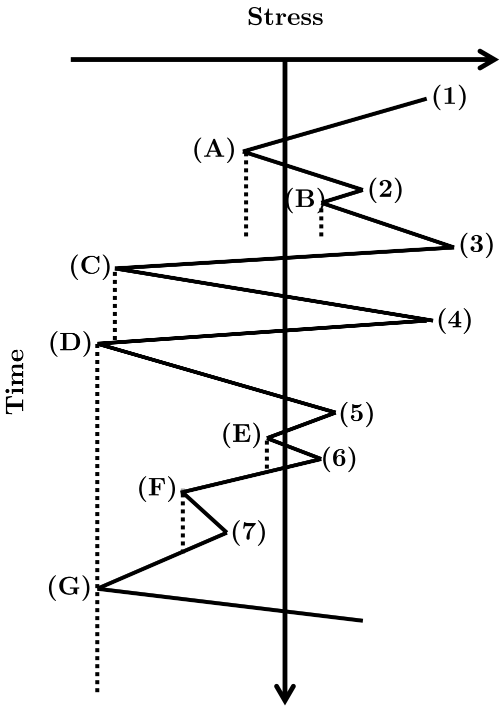
Stress
Time
(1)
(A)
(2)
(B)
(3)
(C)
(4)
(D)
(5)
(E)
(6)
(F)
(7)
(G)

Figure 5.32.: Rainflow Pagoda Roof

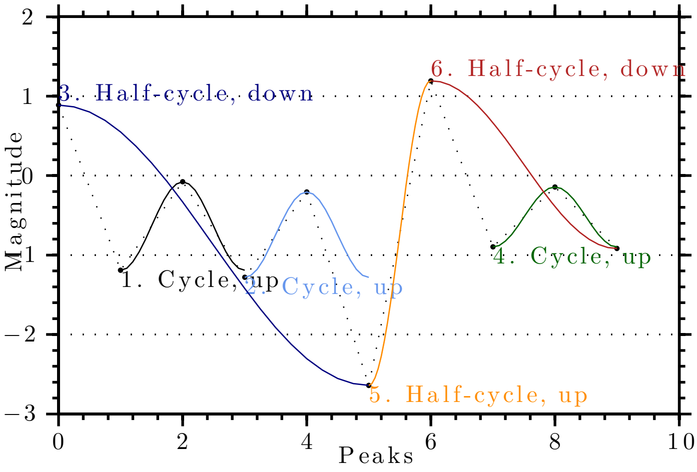

Figure 5.33.: Sample Rainflow-Counting Cycles

5.34 shows the magnitudes of both capacity and energy extreme values from the SRZero test drive. Positive values refer to discharge and negative values refer to charge values. Blue stars refer to energy values, while red stars refer to capacity values.

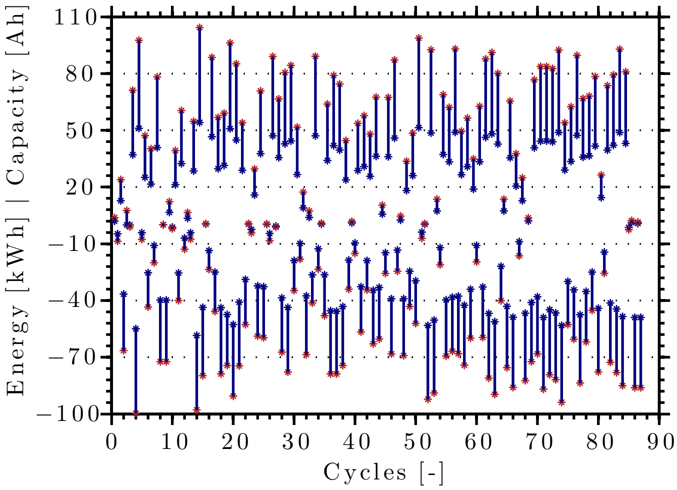

Figure 5.34.: SRZero Energy and Capacity Extreme Values

Applying the rainflow-counting algorithm to the capacity values from figure 5.34 gives the results in table 5.5. The rainflow-counting algorithm used for this work is based on the work by [160]. The algorithm can be thought of assessing what proportion of capacity fade is caused by charging/discharging at each magnitude and then forming a linear combination of their aggregate. Thus, the rainflow-counting algorithm creates equivalent cycles for non-uniform charge/discharge magnitudes. Equivalent cycles may be equal to or longer than one measured cycle. Also, residual half cycles are possible if no corresponding equivalent half cycle is found. Corresponding half cycles need to have the same amplitude, but opposite directions.

The table counts 91 individual half or full cycles, which together account for 30 equivalent uniform cycles at full capacity. The mean amplitude of the equivalent cycles is 54.78 Ah (i.e. 54.78% SOC) with a relatively high standard deviation of 28.64 Ah. The maximum equivalent cycle amplitude is 101.95 Ah and the minimum is 2.40 Ah. The mean of the equivalent cycles, which is expected to be around zero, is -0.4616 Ah. This means that on average charge capacities are higher than discharge capacities. The reason for this is the Coulombic efficiency of the battery. The mean of the equivalent cycles has a standard deviation of 10.66 Ah. More than 90% of the counted equivalent cycles are full cycles (1.0) as shown in the fourth column. There are only nine half cycles (0.5) out of the 91 total cycles. The start times of each equivalent cycle are listed in the fifth column. The last column shows the cycle period. Most equivalent cycles (70%) have a period of one, i.e. they are made up of exactly one charge and one discharge per real cycle. The longest equivalent cycle has a period of 119 real cycles, which means that each of the real charge/discharge cycles contributes exactly $1/119$ to this equivalent cycle.

The information from table 5.5 may also displayed graphically. Figure 5.35 shows the am-

Table 5.5.: Rainflow-Counting Equivalent Cycles of SRZero Charge/Discharge History

Counter	Amplitude [Ah]	Mean [Ah]	Full or Half Cycle [-]	Start Time [-]	Cycle Period [-]
1	6.22	-2.44	0.5	0.0	1
2	16.30	7.64	0.5	0.5	1
3	4.33	3.26	1.0	2.0	1
4	45.17	-21.23	0.5	1.0	1
5	68.75	2.36	0.5	1.5	3
6	85.36	-14.26	0.5	3.0	1
7	27.46	19.77	1.0	4.5	1
8	30.14	10.16	1.0	6.0	1
9	60.81	17.44	1.0	5.5	3
10	36.19	-36.16	1.0	7.5	1
11	7.18	5.07	1.0	9.0	1
12	39.67	-0.33	1.0	10.0	1
13	7.06	-0.54	1.0	12.0	1
14	33.74	20.92	1.0	11.5	3
15	66.39	-5.95	1.0	8.5	5
16	97.69	-0.14	1.0	4.0	19
17	12.12	-11.45	1.0	15.0	1
18	51.26	5.54	1.0	16.5	1
19	66.71	-7.60	1.0	18.0	1
20	83.69	4.86	1.0	16.0	3
21	87.96	8.18	1.0	14.5	9
22	2.52	-1.82	1.0	22.0	1
23	41.13	-11.61	1.0	21.5	3
24	56.39	-2.41	1.0	21.0	5
25	4.45	-3.93	1.0	25.0	1
26	65.20	5.60	1.0	24.0	1
27	79.86	5.27	1.0	20.0	1
28	33.89	32.65	1.0	26.5	1
29	73.92	6.69	1.0	27.5	1
30	17.72	-0.39	1.0	30.5	1
31	43.21	8.44	1.0	29.5	1
32	24.35	-16.96	1.0	32.0	1
33	76.47	7.87	1.0	29.0	5
34	83.41	5.61	1.0	26.0	5
35	12.14	-11.28	1.0	33.5	1
36	55.98	7.94	1.0	34.5	1
37	8.47	-6.61	1.0	39.0	1
38	39.31	5.25	1.0	38.0	1
39	55.10	-1.43	1.0	40.0	1
40	41.18	6.80	1.0	41.5	1
41	60.30	-2.59	1.0	41.0	3
42	18.08	-7.63	1.0	44.0	1
43	63.85	3.54	1.0	43.5	3
44	67.86	-0.39	1.0	43.0	5
45	74.40	0.08	1.0	37.0	1

Counter	**Amplitude [Ah]**	**Mean [Ah]**	**Full or Half Cycle [-]**	**Start Time [-]**	**Cycle Period [-]**
46	78.89	0.13	1.0	36.0	1
47	14.62	-9.93	1.0	46.5	1
48	38.45	-4.73	1.0	48.0	1
49	50.33	-1.81	1.0	49.0	1
50	78.16	8.99	1.0	46.0	3
51	83.99	5.15	1.0	33.0	5
52	3.85	-3.24	1.0	50.5	1
53	94.65	4.09	1.0	19.5	61
54	17.35	-3.72	1.0	53.0	1
55	64.46	-2.33	1.0	55.0	1
56	69.10	-0.32	1.0	54.0	1
57	90.74	1.82	1.0	52.0	1
58	58.81	-9.33	1.0	56.5	1
59	27.25	7.65	1.0	59.0	1
60	58.18	-1.66	1.0	58.0	1
61	61.11	1.56	1.0	60.0	1
62	80.99	6.75	1.0	57.5	7
63	86.09	5.07	1.0	61.5	1
64	26.87	-13.30	1.0	63.5	1
65	70.53	-5.03	1.0	64.5	1
66	20.65	4.24	1.0	66.5	1
67	37.99	-34.30	1.0	68.0	1
68	59.98	-22.29	1.0	66.0	3
69	72.44	4.19	1.0	69.0	1
70	83.04	-2.96	1.0	63.0	5
71	80.97	1.69	1.0	71.5	1
72	82.78	0.98	1.0	71.0	3
73	85.33	-1.54	1.0	70.0	1
74	91.06	1.42	1.0	62.5	21
75	92.57	0.40	1.0	51.5	9
76	53.35	0.62	1.0	74.0	1
77	61.48	1.02	1.0	75.0	1
78	64.33	2.44	1.0	77.0	1
79	56.64	11.52	1.0	78.0	1
80	25.95	0.42	1.0	80.0	1
81	73.16	0.47	1.0	81.0	1
82	78.10	0.36	1.0	79.0	1
83	78.69	0.62	1.0	82.0	1
84	86.60	3.01	1.0	76.0	1
85	2.40	-0.08	1.0	84.5	1
86	82.95	-2.06	1.0	83.5	1
87	43.81	-42.30	1.0	85.5	1
88	101.95	2.33	0.5	3.5	21
89	99.05	5.23	0.5	14.0	119
90	93.35	-0.46	0.5	73.5	19
91	89.50	3.39	0.5	83.0	7

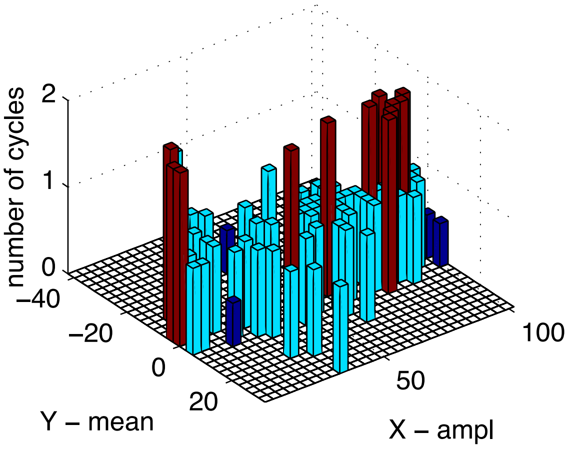

Figure 5.35.: Rainflow-Counting Histogram of SRZero Charge/Discharge History

plitudes as well as mean values for the equivalent cycles calculated with the rainflow-counting algorithm.

The results of the rainflow-counting algorithm may then be taken as input for a simple and generic empirical capacity fade function similar to equation 5.11. The previous subsection (figure 5.21) has demonstrated that 73 reference full charge/discharge cycles led to a total capacity fade of 3.11%. The cumulative capacity for these 73 cycles is 8,094 Ah. It follows that the cell has experienced 8,094 reference 'Amp-Hour-Cycles', which led to a capacity fade of 3.11%. The proportion of equivalent 'Amp-Hour-Cycles' can be calculated by the following equation:

$$\frac{\sum \left(iC_{Amp}\right)/T}{NC_{Amp}} = C \tag{5.12}$$

One equivalent 'Amp-Hour-Cycle' is equal to the product of its magnitude (2^{nd} column of table 5.5) with the identifier i (4^{th} column) divided by its period T. The sum of all equivalent cycles is then divided by the reference 'Amp-Hour-Cycles'. The result shows that despite more charges and discharges during the SRZero test drive (87) compared with the number charges/discharges during lab testing (73), the number of equivalent 'Amp-Hour-Cycles' for the test drive (3,187) is actually only about 39% of the reference 'Amp-Hour-Cycles' (8,094). Thus, assuming linear capacity fade, the capacity fade for the SRZero battery cells during the test drive was about 0.39*3.11 = 1.21%.

5.2.3. Interim Conclusion

This section has analysed battery degradation, both empirically and analytically.

Subsection 5.2.1 brought together empirical evidence of battery degradation from four different examples. First, the lab based testing of a sample SRZero cell undergoing 73 full charge/discharge cycles has shown a linear capacity fade of 0.03-0.05% per cycle. The capacity fade is most visible by showing the available discharge capacity as a function of time or by plotting the characteristic V-Q curves. Voltage drops during the linear and exponential discharge regime accelerate with the number of cycles.

Second, impedance spectroscopy testing of a sample SRZero cell in a lab environment cycling at full capacity has shown that internal resistance as well as polarisation resistance increase with the number of cycles. Polarisation resistance refers to the increasing resistance with decreasing SOC, while internal resistance refers to the series of ohmic resistance in the electrolyte, in the electrode, and in the interconnections and battery terminals. Polarisation resistance ($\approx$1.0 mΩ per cell), which is about three times smaller than internal resistance, increases markedly with the number of cycles (2.44% per cycle). In contrast, the larger internal resistance ($\approx$3.1 mΩ per cell) only increases by about 0.13% per cycle.

Third, long term cycling of a low-capacity cylindrical cell at 20% depth of discharge has shown a capacity fade of 0.05-0.3‰ per cycle, i.e. 1-2 orders of magnitude lower compared with SRZero cells cycled at full capacity.

Fourth, long-term cycling of SRZero battery cells at highly dynamic discharge currents and non-uniform charge/discharge magnitudes has shown that capacity fade is very complex to evaluate without further assumptions.

The second subsection (5.2.2) looked at battery degradation from an analytical perspective. First, boundary conditions were established. Depending on the design, periodic maintenance, its handling, annual mileage and the natural environment typical total vehicle mileages range between 100,000-250,000 km. Subject to range, this translates into approximately 150-1,700 full capacity cycles for an EV. Assuming half capacity cycles, the number of consecutive charge/discharge processes is doubled.

Second, the rainflow-counting algorithm is introduced as a means of working out equivalent cycles. In contrast to a lab environment, charge/discharge capacities of 'real' EVs vary significantly between 'cycles'. The problem is that these consecutive and non-uniform charge/discharge capacities cannot be considered equal cycles. The rainflow-counting algorithm, which is most often used in stress analysis, offers one way of assessing what proportion of capacity fade is caused by charging/discharging at each capacity level and then forming a linear combination of their aggregate.

Applying the algorithm to the capacity history of the SRZero reveals that 87 consecutive non-uniform charge/discharge processes only correspond to about 30 equivalent uniform cycles at full capacity. This means that the number of equivalent cycles is markedly lower than the number of cumulative charge/discharge processes during 'real operation'. As figure 5.34 points out, some charge/discharge processes have an extremely low magnitude compared with the nominal capacity of the cell. Therefore, simply counting battery cycles as the cumulative number of charge/discharge processes is misleading. Following this logic, intermittent charging processes from regenerative braking and the subsequent discharge process should theoretically also be counted as a cycle, but it is not. In contrast, the rainflow-counting algorithm, which only depends upon local maximum and minimum capacity values, proportionately takes into account these very low amplitude cycles. Therefore, battery cycle requirements should be calculated according to the equivalent cycle number rather than the cumulative number of charge/discharge processes.

Assuming a linear capacity fade of 0.03-0.05% per cycle for the SRZero cells, the capacity would be reduced to 80% after 1,100-650 cycles already. An EV traction is considered dead once its remaining capacity drops below 80% of its nominal capacity. This means a spare capacity of 5-134% is required in order satisfy range requirements after 150-1,700 full capacity cycles.

5.3. Discussion & Summary

This chapter has analysed battery performance and degradation characteristics of EV traction batteries. The first section (5.1) looked at battery performance characteristics.

Depending on the power and energy requirements, safety and cost considerations as well as design limitations, individual cells can be connected in series (S), in parallel (P) or a combination of both. Accordingly, the total voltage, capacity, and power levels can be adjusted. More detailed battery characteristics can be observed by looking at steady and dynamic discharge behaviour separately.

Steady discharge behaviour can be best described by V-Q curves. Due to the capacity rate effect (figure 5.2) high discharge rates result in a lower discharge capacity than lower discharge rates. Published and measured discharge curves are not necessarily the same as shown by figure 5.2 and 5.3b. Therefore, it is highly recommended to take measurements before the continuous use of the cells.

The open-circuit voltage (OCV) presents an independent indicator of state of charge (SOC). Therefore, SOC values may be determined given reliable OCV values and vice versa. Equations 5.1-5.5 illustrate the corresponding dependencies. Figure 5.5 shows that the OCV vs SOC function can be divided into a linear regime (100-20% SOC) and an exponential regime (20% SOC - end of discharge).

Dynamic battery behaviour is also controlled by the voltage response given a current request. However, it is a more complex function compared with that of steady currents. Following a backward-forward facing quasi-steady (Δt = 1 s) modelling approach, battery currents are derived given a sample drive cycle of the SRZero. The sample drive (figure 5.7), SRZero specifications (table 3.1) and first principle assumptions (see section 4.1.1) lead to torque requests at the rear wheels. Torque requests are dominated by the acceleration profile. Therefore, most electric motors for EV applications are torque controlled, which in turn is a function of pedal position. It turns out that the mean requested battery current is relatively low (7.21 A = 0.07 C). However, the battery current is highly dynamic. The resulting traction voltage primarily depends upon the current request, the internal resistance and the state of charge. Various equivalent circuit models have been applied and parametrised for this application. The PNGV model results in the highest accuracy with a relatively high coefficient of determination.

The second section (5.2) has analysed battery degradation, both empirically and analytically. It has gathered empirical evidence of battery degradation from four different examples. The first example refers to lab based testing of a sample SRZero cell undergoing 73 full charge/discharge cycles. This experiment has shown a linear capacity fade of 0.03-0.05% per cycle. Plotting the available discharge capacity as a function of time and/or charting the characteristic V-Q curves allows for the best visual interpretation. Voltage drops during the linear and exponential discharge regime accelerate with the number of cycles.

The second experiment relates to impedance spectroscopy testing of a sample SRZero cell in a lab environment cycling at full capacity. The results have shown that internal resistance as well as polarisation resistance increase with the number of cycles. Polarisation resistance refers to the increasing resistance with a decreasing amount of reactants, i.e. a decreasing SOC. Internal resistance in contrast refers to the series of ohmic resistance in the electrolyte, in the electrode, and in the interconnections and battery terminals. Polarisation resistance (≈1.0 mΩ per cell), which is about three times smaller than internal resistance, increases markedly with the number of cycles (2.44% per cycle). In contrast, the larger internal resistance (≈3.1 mΩ per cell) only increases by about 0.13% per cycle.

The third experiment is concerned with the long term cycling of a low-capacity cylindrical cell at 20% depth of discharge. The results have shown a capacity fade of 0.05-0.3‱ per cycle, i.e. 1-2 orders of magnitude lower compared with SRZero cells cycled at full capacity.

The last experiment is about the long-term cycling of SRZero battery cells at highly dynamic discharge currents and non-uniform charge/discharge magnitudes. It has shown that capacity fade is very complex to evaluate without further assumptions.

The second subsection (5.2.2) looked at battery degradation from an analytical perspective. First, boundary conditions were established. Depending on the design, periodic maintenance, its handling, annual mileage and the natural environment typical total vehicle mileages range between 100,000-250,000 km. Subject to range, this translates into approximately 150-1,700 full capacity cycles for an EV. For half capacity cycles, the number of consecutive charge/discharge processes is doubled.

Second, the rainflow-counting algorithm is introduced as a means of working out equivalent cycles. In contrast to a lab environment, charge/discharge capacities of 'real' EVs vary significantly between 'cycles'. The problem is that these consecutive and non-uniform charge/discharge capacities cannot be considered equal cycles. The rainflow-counting algorithm, which is most often used in stress analysis, offers one way of assessing what proportion of capacity fade is caused by charging/discharging at each capacity level and then forming a linear combination of their aggregate.

Applying the rainflow-counting algorithm to the capacity history of the SRZero reveals that 87 consecutive non-uniform charge/discharge processes only correspond to about 30 equivalent uniform cycles at full capacity. This means that the number of equivalent cycles is markedly lower than the number of cumulative charge/discharge processes during 'real operation'. As figure 5.34 points out, some charge/discharge processes have an extremely low magnitude compared with the nominal capacity of the cell. Therefore, simply counting battery cycles as the cumulative number of charge/discharge processes is misleading. Following this logic, intermittent charging processes from regenerative braking and the subsequent discharge process should theoretically also be counted as a cycle, but they are not. In contrast, the rainflow-counting algorithm, which only depends upon local maximum and minimum capacity values, proportionately takes into account these very low amplitude cycles. Therefore, battery cycle requirements should be calculated using the equivalent cycle number rather than the cumulative number of charge/discharge processes.

Assuming a linear capacity fade of 0.03-0.05% per cycle for the SRZero cells, the capacity would be reduced to 80% after 1,100-650 cycles already. An EV traction battery is considered 'dead' once its remaining capacity drops below 80% of its nominal capacity. This means an initial spare capacity of 5-134% is required in order satisfy range requirements after 150-1,700 full capacity cycles.

6. Discussion

This work has shown that the optimum battery capacity for electric vehicles taking into account battery degradation is about 1.25-1.75 times the optimum nominal battery capacity. Chapter 4 has derived optimum nominal battery capacities for different electric vehicle classes, while chapter 5 has derived the additional capacity required in order to account for battery degradation. The connection between the two chapters is best explained by figure 5.1. The findings of both chapters are summarised, connected and discussed in the following two sections (6.1-6.2). Section 6.3 deals with the limitations of this work.

6.1. Optimum Nominal Battery Capacity

The optimum nominal battery capacity mainly depends upon two factors: mean driving force $\bar{F}_d$ and range d. These are discussed in turn in the following two subsections.

6.1.1. Mean Driving Force

The mean driving force, which is the total energy consumption normalised by the distance covered, can vary significantly due to a number of factors.

Vehicle Parameters and Representative Vehicle Classes

First, the mean driving force primarily depends upon vehicle parameters such as the vehicle's mass m_v, the aerodynamic drag coefficient C_d, the vehicle's frontal area A_f, the rolling resistance coefficient C_r, the mean auxiliary power $\bar{P}_{aux}$ and losses. Table 6.1 summarises the main vehicle parameters for five representative vehicle classes.

Table 6.1.: Vehicle Classes and Representative Parameter Values

	Mini Car	**Small Car**	**Medium Car**	**Large Car**	**SUV**
Euro Car Segment	A	B	C	D	J
m_v [kg]	750	1,000	1,200	1,500	2,000
C_dA_f [m^2]	0.3	0.6	0.7	0.8	1.2
C_r [-]	0.008	0.01	0.011	0.012	0.013
$\bar{P}_{aux}$ [W]	500	750	1,000	2,000	3,000

Operating Modes

Second, the magnitude of the mean driving force depends on whether the vehicle is in traction mode or not. During traction, when the driver puts down his/her foot on the accelerator, the motors apply a propulsion force to the wheels. Thus, the mean driving force of a vehicle is reduced to its auxiliary load only, when the vehicle is not in traction mode. The traction ratio TR as a measure of the time spent in traction mode relative to driving time is derived for dynamic speed conditions and varying road grades (equations 4.9-4.11). In practice, traction ratios range between 55-75%. All else being equal, the mean driving force almost linearly depends upon TR (see table 4.13).

Speed and Acceleration

Third, the mean driving force is influenced by the driving parameters speed $v(t)$ and acceleration $a(t)$. For steady speeds, the energy consumption per unit of distance is smallest at low medium speeds ($\approx$40 km/h) and ranges between 35 Wh/km for mini cars and 170 Wh/km for SUVs. At medium steady speeds (20-100 km/h) the mean driving force does not change markedly with speed, which can be observed in figure 4.6.

However, at very low speeds (<20 km/h) driving force increases exponentially with decreasing speed due to the mean auxiliary power $\bar{P}_{aux}$. At high speeds (>100 km/h) the mean driving force increases quadratically with speed due to aerodynamic drag. Owing to road speed limits, congestion and the assumption that most car journeys are relatively short (i.e. <50 km), we expect the variation of the mean driving force to be relatively small between different journeys. Dynamic driving involves a constant change of the vehicle's inertia. Nominal accelerations don't exceed 2 m/s^2.

Regenerative Braking

Fourth, the mean driving force of an EV heavily depends upon its ability to recuperate kinetic energy. The lighter the vehicle, the greater the relative effect of regenerative braking. The relative recuperation gain G_r introduced with equation 4.12 applied to various drive cycles across different vehicle classes proves this point (see table 4.10). Furthermore, a sensitivity analysis (equations 4.13-4.17) has shown that for a vehicle with ideal recuperation the impact of vehicle mass on the mean driving force is greatly reduced compared to that of a vehicle without a regenerative braking system. Thus, a regenerative braking system reduces both the distance-specific energy consumption as well as its dependence on the vehicle's mass.

Journey Distance

Fifth, the journey distance also affects the mean driving force. There is an empirical correlation that with longer journey distances, distance-specific energy consumption tends be smaller (see figure 4.15).

Driving Behaviour

Sixth, the individual driving style has profound implications on the mean driving force. As evidenced by table 4.13 the mean driving force can vary up to 23% between different drivers who follow exactly the same route at comparable traffic conditions and driving another vehicle of exactly the same make and model.

Interim Conclusion

Subsection 4.1.2 about 'real' driving forces has broadly confirmed the assumptions made in the subsection about theoretical driving forces 4.1.1. These are corroborated by the published literature about the energy consumption of electric vehicles ([147]-[149]). The resulting reference values of table 6.2 are rounded values based on table 4.9, an overall vehicle efficiency of 90% and a regenerative braking efficiency of 50%.

Table 6.2.: Mean Driving Forces for Different Vehicle Categories

	Driving Force [Wh/km]				
	Mini Car	**Small Car**	**Medium Car**	**Large Car**	**SUV**
Analytical[1]	61.81-74.61	103.15-119.01	129.25-148.04	185.89-210.24	272.72-304.56
RGE SRZero	n/a	n/a	95.47-310.73	n/a	n/a
2010 FCC	146.18	125.19-146.94	124.32-157.66	n/a	n/a
2011 FCC	68.63-166.72	105.79-119.51	86.95-134.12	n/a	n/a
2012 FCC	53.85-62.33	128.81	140.25-143.01	n/a	n/a
Reference Values	**70.00**	**110.00**	**140.00**	**200.00**	**290.00**

6.1.2. Range

The subsections on range requirements for electric vehicles (4.2.1-4.2.4) have demonstrated that the distance, which a vehicle can drive without having to refuel or to recharge, is an important factor. Especially for electric vehicles range is one of the key performance characteristics as charging it up may take several hours. Despite the fact that an overwhelming majority of individual car journeys in the UK (91%) are relatively short (i.e. <30 km), range requirements for electric vehicles are significantly more challenging than this.

First, when in use, a car is typically driven three to four times a day for separate individual journeys. It is assumed that an EV is typically charged at night and discharged (i.e. driven) during the day. Second, the results have also shown that range requirements can be assessed both in terms of the number of trips and in terms of the total distance. The first focusses on the number of times the daily range is within a specific range band (e.g. 0-25 km, 25-50 km, etc.). This is also referred to as frequency distribution or histogram analysis. Based on the number of trips, a range of 150 km is required to cover more than 95% of all daily distances with a car in the UK and Germany. In the US, a range of 200 km satisfies the same requirement. The second assessment of range focusses on the share of the cumulative distance driven. There may be a high number of short distances driven in one day, but their cumulative distance may be shorter than one single long trip. Consequently, range requirements from a total distance perspective are higher than by just looking at the number of trips. For the UK, a range of 400 km satisfies the 95^{th} percentile of the cumulative distance driven. In Germany, a range of 575 km and in the US a range of 700 km meet the same target.

---

[1] ranging from full recuperation to no recuperation with an energy efficiency of 90% (see table 4.9)

6.1.3. Conclusion

Based on the mean driving forces (see table 6.2) and range requirements for the UK, Germany and the US, initial battery capacity requirements may be established. Battery capacity requirements are higher from a total distance perspective than from a number of trips perspective. Obviously, the bigger the battery capacity (i.e. those satisfying the 95% of the total distance requirement), the longer the range.

However, from an emission abatement perspective smaller battery capacities (i.e. those satisfying the 95% of all trips requirement) can be very effective as well. Because short trips (<30 km) involve more frequent stops and a higher percentage of operation at low efficiency, fuel efficiency for short trips is usually lower than for long trips. Figure 4.15 also gives empirical evidence for this correlation. Then, due to the linear relationship between fuel consumption and CO_2 emissions (see equation 1.1), emissions per unit of distance tend to be higher for short trips. Therefore, the CO_2 abatement potential for EVs with a relatively small battery capacity is already relatively high.

Table 6.3 concludes this section by listing the optimum nominal battery capacity requirements for EVs according to driving force and range requirements in different countries. Battery capacity requirements range from 11 kWh for a mini car in the UK or Germany satisfying a 150 km range up to 203 kWh for a SUV in the US satisfying a 700 km range. As a reference, the energy content of a full fuel tank for a medium-sized ICEV (50 litres of petrol) is about 480 kWh.

Table 6.3.: EV Battery Capacity Requirements According to Driving Force and Range

Country	**95% Range [km]**		**Battery Capacity [kWh]**				
	Trips	**Dist.**	**Mini Car**	**Small Car**	**Medium Car**	**Large Car**	**SUV**
UK	150	400	11-28	17-44	21-56	30-80	44-116
Germany	150	575	11-40	17-63	21-81	30-115	44-167
US	200	700	14-49	22-77	28-98	40-140	58-203

6.2. Battery Performance & Degradation

This section summarises the fifth chapter on battery performance and degradation, which aims at characterising the red area in figure 5.1. In order to determine the long-term behaviour of an EV battery pack, an understanding of the short-term battery behaviour at cell level is essential. Thus, this section is divided into three subsections. The first subsection is devoted to EV battery performance, while the consecutive subsection deals with battery degradation. The last subsection summarises this section.

6.2.1. Battery Performance

Steady discharge behaviour (V-Q curve) is usually published by the manufacturer for various discharge (C) rates. Due to the capacity rate effect high discharge rates result in a lower discharge capacity than lower discharge rates. Published and measured discharge curves are not necessarily the same as shown by figures 5.2 and 5.3b. Therefore, it is highly recommended to take measurements before continuous use of the cells.

While cell voltage levels vary according to its steady discharge current, open-circuit voltage (OCV) levels remain constant irrespective of its C-rate. Therefore, exactly one depth of discharge (DOD) value can be allocated to exactly one OCV value. It follows that the OCV can be described as a function of SOC and vice versa. As figure 5.5 shows, this function can be divided into a linear regime (100-20% SOC) and an exponential regime (20% SOC-end of discharge).

Following a backward-forward facing quasi-steady ($\Delta t = 1$ s) modelling approach, battery dynamic currents are derived given a sample drive cycle of the SRZero. The sample drive cycle (figure 5.7), SRZero specifications (table 3.1) and first principle assumptions (see section 4.1) lead to torque requests at the rear left and rear right wheel respectively.

It turns out that torque requests are dominated by the acceleration profile (figure 5.8). Therefore, most electric motors for EV applications are torque controlled, which in turn is a function of pedal position. Thus, AC motor currents may be estimated using the torque constant K_T. Considering efficiency losses in both directions of power flow the battery current may be estimated. Results show that the mean measured battery current is relatively low (7.21 A).

After initialising, current requests were used to determine the OCV and SOC values for the sample drive cycle following the generic relationship established in equation 5.4. The resulting traction voltage primarily depends upon the current request, the internal resistance and the state of charge. Various equivalent circuit models have been applied and parametrised for this application. The PNGV model results in the highest accuracy.

6.2.2. Battery Degradation

This subsection summarises both empirical as well as analytical results of battery degradation considerations.

Empirical Evidence for Battery Degradation

Subsection 5.2.1 has gathered empirical evidence of battery degradation from four different examples. First, the lab based testing of a sample SRZero cell undergoing 73 full charge/discharge cycles has shown a linear capacity fade of 0.03-0.05% per cycle. The capacity fade is most visible by showing the available discharge capacity as a function of time or by plotting the characteristic V-Q curves. Voltage drops during the linear and exponential discharge regime accelerate with the number of cycles. Second, impedance spectroscopy testing of a sample SRZero cell in a lab environment cycling at full capacity has shown that internal resistance as well as polarisation resistance increase with the number of cycles. Polarisation resistance ($\approx$1.0 mΩ per cell), which is about three times smaller than internal resistance, increases markedly with the number of cycles (2.44% per cycle). In contrast, internal resistance ($\approx$3.1 mΩ per cell) only increases by about 0.13% per cycle. Third, long term cycling of a low-capacity cylindrical cell at 20% depth of discharge has shown a capacity fade of 0.05-0.3‱ per cycle, i.e. 1-2 orders of magnitude lower compared with SRZero cells cycled at full capacity. Fourth, long-term cycling of SRZero battery cells at highly dynamic discharge currents and non-uniform charge/discharge magnitudes has shown that capacity fade is very complex to evaluate without further assumptions.

Battery Degradation Modelling

First, boundary conditions were established. Depending on the design, periodic maintenance, its handling, annual mileage and the natural environment typical total vehicle mileages range between 100,000-250,000 km. Subject to range, this translates into approximately 150-1,700 full capacity cycles for an EV. Second, the rainflow-counting algorithm is introduced as a means of working out equivalent cycles. In contrast to a lab environment, charge/discharge capacities of 'real' EVs vary significantly between 'cycles'. The problem is that these consecutive and non-uniform charge/discharge capacities cannot be considered equal cycles. The rainflow-counting algorithm, which is most often used in stress analysis, offers one way of assessing what proportion of capacity fade is caused by charging/discharging at each capacity level and then forming a linear combination of their aggregate. Applying the algorithm to the capacity history of the SRZero reveals that 87 consecutive non-uniform charge/discharge processes only correspond to about 30 equivalent uniform cycles at full capacity. This means that the number of equivalent cycles is markedly lower than the number of cumulative charge/discharge processes during 'real operation'. As figure 5.34 illustrates, some charge/discharge processes have an extremely low magnitude compared with the nominal capacity of the cell. Therefore, simply counting battery cycles as the cumulative number of charge/discharge processes is misleading. Following this logic, intermittent charging processes from regenerative braking and the subsequent discharge process should theoretically also be counted as a cycle, but they are not. In contrast, the rainflow-counting algorithm, which only depends upon local maximum and minimum capacity values, proportionately takes into account these very low amplitude cycles. Therefore, battery cycle requirements should be calculated using the equivalent cycle number rather than the cumulative number of charge/discharge processes.

Assuming a linear capacity fade of 0.03-0.05% per cycle for the SRZero cells, the capacity would be reduced to 80% after 1,100-650 cycles already. This means a spare capacity of 5-134% is required in order satisfy range requirements after 150-1,700 full capacity cycles. For a battery pack discharged at a recommended depth of discharge of 80% the required spare capacity is assumed to be up to 40% of the ratio of the optimum nominal battery capacity and the recommended depth of discharge. Therefore, the optimum battery capacity for electric vehicles with particular focus on battery degradation is about 1.25-1.75 times the optimum nominal battery capacity.

6.3. Limitations

This section briefly discusses the limitations of this work. First, potential problems with some of the assumptions made are highlighted. Second, the shortcomings associated with the validation methods are summarised. Third, physical limitations regarding the optimum battery capacity, namely weight and volume, are outlined. Finally, financial limitations are briefly discussed.

6.3.1. Assumptions

Section 3.1 has introduced some of the major assumptions made in this work. First, vehicle dynamics are only assessed along the longitudinal axis, i.e. transverse vehicle dynamics such as sideslip are ignored for this analysis. Consequently, vehicle dynamics are simplified for the purpose of quickly assessing the mean driving force of a particular vehicle class. Still, mean theoretical driving forces are relatively accurate when compared with empirical driving forces. Second, vehicle as well as battery dynamics are assumed to be steady for the duration of one second. Therefore, for simplicity reasons the so-called quasi-steady approach ignores medium to high frequency (f >1 Hz) events. This means that highly dynamic processes, especially electrochemical ones, are much simplified in order to develop long-term trends. The third major assumption is linked to the previous one. This work takes a mechanical engineering viewpoint of the battery sizing problem. Thus, electrochemical details certainly affecting the functionality of batteries are mostly ignored or greatly simplified. Again, this work aims to describe the long-term effects rather than the short-term ones of battery behaviour. Fourth, the terminal voltage is assumed to be equal to the open-circuit voltage after a minimum of 30 minutes under the no-load condition. Realistically, depending upon the discharge rate and temperature effects, this settling time will vary.

6.3.2. Validation Methods

There are shortcomings related to the validation techniques of this work. First, the SRZero was designed as an endurance high performance sports car for long-distance driving. It was not designed for 'everyday' driving. Without space for more than two passengers, the lack of a boot and no real auxiliaries it was also never intended for that. However, its parameters (m_v, $C_d A_f$ and C_r) are very close to that of a medium-sized car. Also, its mean driving force (131.43 Wh/km) is within the theoretical range of that of a medium-sized car with an efficiency of 90% (129.25-148.04 Wh/km). Second, no large EV and no electric SUV competed in any of the FCCs, against which theoretical driving force values could be compared. Third, the FCC encourages low-energy driving. Thus, mean driving forces from the FCC tend to be an underestimation of 'real' values. Fourth, there is no direct empirical evidence of the accuracy of the rainflow-counting algorithm.

6.3.3. Physical Limitations

This subsection briefly discusses physical limitations regarding the optimum battery capacity. Considerations about weight and volume restrictions are briefly discussed.

Weight

For ICEVs the heaviest single component is usually either the motor or the gearbox. Downsizing and the use of alternative materials aims to reduce this. In contrast, for EVs the traction battery pack tends to be the heaviest single component. The ratio of battery pack weight to total vehicle kerb weight for the SRZero for instance is just below 50% (see table 3.1), while for the Nissan Leaf and the Tesla Roadster these values are 20% and 36% respectively. The mass of the battery pack m_{bat} is the product of the battery's specific energy density ρ_{bat} and the battery's capacity Q_{bat} in kWh as shown equation 6.1:

$$m_{bat} = \rho_{bat} Q_{bat} \tag{6.1}$$

Thus, maximising the specific energy density and minimising the capacity results in a lower battery pack weight and thus in a lower kerb weight of the vehicle.

First, specific energies for commercial lithium-ion batteries range between 100-250 Wh/kg [12] (see also figure 2.26). Following this and the battery capacity range from table 4.20, table 6.4 lists the battery pack mass as function of specific energy and capacity. Thus, the mass of battery packs can vary significantly depending on the specific energy density and battery capacity. The factor between the heaviest and the lightest battery pack is 50. Considering that typical total vehicle mass range between 750-2,000 kg (see table 4.2), battery packs with capacities above 100 kWh exceed ⅓ of a medium-sized vehicle's kerb mass (1,200 kg) with the current state of technology. Based on specific energy densities for traction batteries of 100-250 Wh/kg and a

Table 6.4.: Battery Pack Mass According to Specific Energy and Capacity

	Battery Capacity [kWh]						
	10	**20**	**40**	**60**	**80**	**100**	**200**
Mass [kg]	40-100	80-200	160-400	240-600	320-800	400-1,000	800-2,000

maximum battery mass to kerb mass ratio of ⅓, table 6.5 lists the maximum battery capacities for each vehicle class. It follows that there is a trade-off between a small battery capacity, which minimises weight and thus reduces the EV's driving force (see section 4.1), and a large battery capacity, which can give a longer range (see section 4.2).

Table 6.5.: Upper Battery Capacity Limits According to Weight[1]

	Mini Car	**Small Car**	**Medium Car**	**Large Car**	**SUV**
Q_{bat} [kWh]	25-62.5	33-83	40-100	50-125	67-167

Unfortunately, battery mass to total kerb mass ratios are unavailable for most commercially available EVs. Most commercial EV manufacturers do not reveal the chemistry and the associated specific energy density of their battery pack. However, information about battery capacities for most commercially available EVs is public and listed in table 2.1 and appendix E. The capacity ratio CR relates the battery capacity Q_{bat} to the vehicle's kerb mass m_v (see equation 6.2).

$$CR = \frac{Q_{bat}}{m_v} \tag{6.2}$$

Effectively this is a measure of the electrical energy that can be stored on board with respect to the total mass of the vehicle. Applying this equation to table 2.1 and appendix E gives the results in figure 6.1. The figure shows that currently battery capacity ratios range between 10.5-47.0 Wh/kg for currently available EVs. The mean capacity ratio is around 21.7 Wh/kg with a relatively low standard deviation of 9.5 Wh/kg. This means that the variability between capacity ratios is relatively small. Sports cars tend to have a larger CR than other vehicle classes. This may be attributed to their design focus on performance rather than on safety or entertainment.

Volumetric Limitations

Volumetric energy densities for lithium-ion battery cells range between 330-630 Wh/L (see table 2.3). Thus, battery packs with battery capacities ranging between 10-100 kWh can take up around 15-300 litres (0.015-0.3 m^3) of space. Typical passenger car volumes range between 2,400 and 3,400 litres. Thus, the volume of a battery pack can take up a considerable amount

---

[1] based on a maximum battery mass to kerb mass ratio of ⅓

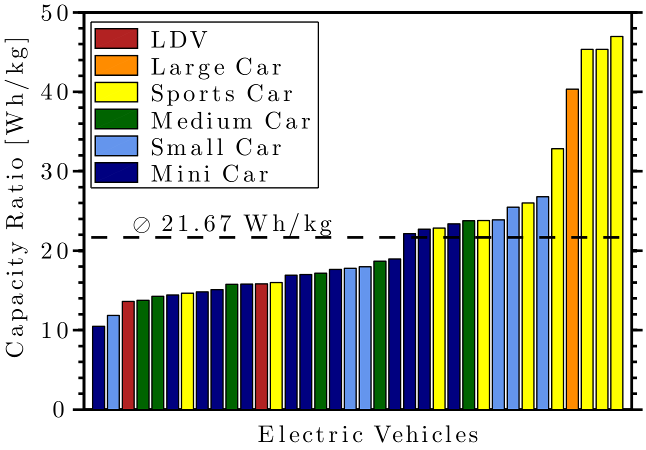

Figure 6.1.: Battery Capacity Ratio for Various EVs[2]

of space in absolute terms, but relative to the vehicle's total volume the share is relatively small (<15%). It follows that the total weight of battery packs for EVs presents a more significant limitation to optimum battery capacities introduced earlier than the total volume.

6.3.4. Financial Limitations

Battery cost is a contentious subject, driven by differing views on material costs, rate of technical improvement, permissible depth of discharge (DOD), range, and so on. Therefore, only general remarks are made. Rechargeable traction batteries are usually the most expensive components of electric vehicles, comprising about half of the retail cost of the car [165]. Due to relatively high raw material costs (including copper and lithium) current electric vehicle battery prices range between 400-800 $/kWh [166]. Thus, currently the price range for EV traction packs is $4,000-$80,000.

---

[2] based on table 2.1, appendix E and equation 6.2

7. Conclusions & Further Work

This chapter concludes this work. In the first section (7.1), the main research questions posed in section 1.3 are addressed. The final section 7.2 suggests potential further work, which could be built upon this work.

7.1. Conclusions

The problem statement of this work (section 1.3) concluded with five main research questions. Thanks to the research, analysis, deduction, abduction and discussion done in the preceding chapters, these questions can be answered in a relatively concise way:

- *What does 'optimum battery capacity' mean in the electric vehicle context?*
  Optimum battery capacity in the electric vehicle context refers to the capacity of the traction battery (measured in amp-hours (Ah) or kilowatt-hours (kWh)) optimised according to nominal energy requirements and battery degradation.

- *Which are the main factors that affect the optimum battery size and how?*
  From a mechanical engineering point of view these include the mean driving force $\bar{F}_d$, range d, and battery degradation. The product of the mean driving force and range yields the optimum nominal battery capacity, which is assumed to be static. In contrast, battery degradation is assumed to affect the optimum battery capacity linearly with time.

- *What is the expected lifetime of an EV and therefore of its battery pack?*
  Assuming an annual mileage of 15,000-25,000 km and a lifespan of 7-10 years, the total vehicle mileage ranges between 105,000-250,000 km. For all-electric ranges between 150-700 km this translates into 150-1,700 full battery cycles.

- *What does battery degradation mean?*
  Battery degradation and ageing describe electrochemical phenomena, which modify a cell's inherent properties with time and use. The three most problematic symptoms of a degraded cell are capacity loss, power loss and loss of integrity (i.e. cell damage or leakage). These are mainly caused by the effects of increased internal resistance, polarisation, corrosion and passivation.

- *How does battery degradation affect the sizing of a traction battery for EVs?*
  Amongst other consequences battery degradation leads to capacity fade. Empirical evi-

dence has shown that capacity fade is mostly linear and ranges between 0.05-0.3‱ per cycle for low-capacity cells discharged at 20% depth of discharge (DOD) up to 0.03-0.05% per cycle for high-capacity cells discharged at full capacity. Therefore, first it is recommended to reduce the depth of discharge (DOD) to 80% at minimum when the battery is in use. Second, a spare capacity at the beginning of life of around 20-40% is recommended in order to satisfy range and power requirements also towards the end of the EVs lifetime. It follows that the optimum actual battery capacity is around 1.25-1.75 times the optimum nominal battery capacity for an EV.

7.2. Further Work

This work has presented a novel software model for the determination of the optimum battery capacity for electric vehicles with particular focus on battery degradation. It contributes towards the goal of reducing cost, weight and complexity of EVs. In order to have an even better understanding of the effects of battery degradation on the optimum battery capacity, long-term dynamic cycling (e.g. with a NEDC load) using similar Li-ion cells and applying different levels of depth of discharge is proposed. In particular, it is recommended to compare the long-term battery behaviour (V-Q characteristics) of identical dynamic loads from 'real-world' driving and from a lab environment. This way the long-term effects of 'real' loads on battery behaviour can be monitored and analysed comprehensively.

On top of analysing the effect of dynamic charge/discharge cycles it is suggested to monitor the effect of varying charge/discharge capacities (see figure 5.28). By this means, battery degradation for consecutive, dynamic and varying charge/discharge capacities can be quantified and compared against the results of the rainflow-counting algorithm. This process could result in the validation of the rainflow-counting algorithm or the opposite. The rainflow-counting algorithm may be validated not only for batteries, but also for other electrochemical energy storage/conversion systems such as supercapacitors or fuel cells.

Furthermore, for a more comprehensive view on the battery sizing problem, more detailed analysis about the physical and financial limitations is desirable.

Bibliography

[1] Wards Auto. (2011) *World Vehicle Population Tops 1 Billion Units.* [Online]. Available from: http://wardsauto.com/ar/world_vehicle_population_110815 [Accessed 7th July 2012]

[2] BP. (2012) *Statistical Review of World Energy.* [Online]. Available from: http://www.bp.com/content/dam/bp/excel/Statistical-Review/statistical_review_of_world_energy_2013_workbook.xlsx [Accessed 19th July 2013]

[3] Shafiee, S. & Topal, E. (2010) *A long-term view of worldwide fossil fuel prices.* Applied Energy. [Online]. 87 (3), 988-1000. Available from: http://dx.doi.org/10.1016/j.apenergy.2009.09.012 [Accessed 7th July 2012]

[4] Uherek, E. et al. (2010) *Transport impacts on atmosphere and climate: Land transport.* Atmospheric Environment. [Online]. 44 (37), 4772-4816. Available from: http://dx.doi.org/10.1016/j.atmosenv.2010.01.002 [Accessed 7th July 2012]

[5] Yim, S. & Barrett, S. (2012) *Public Health Impacts of Combustion Emissions in the United Kingdom.* Environmental Science & Technology. [Online]. 46 (8), 4291-4296. Available from: http://dx.doi.org/10.1021/es2040416 [Accessed 7th July 2012]

[6] Odgen, J. & Anderson, L. (2011) *Sustainable Transportation Energy Pathways.* [Online]. 304. Available from: http://steps.ucdavis.edu/STEPS.Book [Accessed 7th July 2012]

[7] International Energy Agency (iea). (2011) *CO_2 Emissions from Fuel Combustion - Highlights.* [Online]. 9-10, 67. Available from: http://www.iea.org/co2highlights/co2highlights.pdf [Accessed 12th July 2012]

[8] International Council on Clean Transportation (ICCT). (2011) *Car CO_2 Standard Data.* [Online]. Available from: http://www.theicct.org/sites/default/files/GlobalPVStd_Aug2011_datasheet_web.xls [Accessed 13th July 2012]

[9] World Bank. (2011) *Motor Vehicles (per 1,000 people).* [Online]. Available from: http://data.worldbank.org/indicator/IS.VEH.NVEH.P3 [Accessed 7th August 2012]

[10] United Nations (UN). (2012) *World Urbanization Prospects.* [Online]. Available from: http://esa.un.org/unup/ [Accessed 2nd August 2012]

[11] Gao, D., Mi, C. & Emadi A. (2007) *Modeling and Simulation of Electric and Hybrid Vehicles.* Proceedings of the IEEE 95 (4), 729-745 [Online]. Available from: http://dx.doi.org/10.1109/JPROC.2006.890127 [Accessed 13th August 2012]

[12] Scrosati, B. & Garche, J. (2010) *Lithium Batteries - Status, Prospects and Future.* Journal of Power Sources [Online]. Available from: http://dx.doi.org/10.1016/j.jpowsour.2009.11.048 [Accessed 2nd August 2012]

[13] Dreves, F. (2011) Audi AG, Personal Conversation, 23rd September.

[14] Fritzson, P. (2004) *Principles of Object Oriented Modelling and Simulation with Modelica 2.1.* Piscataway (US), IEEE Press.

[15] Gartner, Inc. (2009) *Gartner's Hype Cycle Special Report for 2009.* [Online]. Available from: http://www.gartner.com/id=1108412 [Accessed 30th July 2012]

[16] Wikipedia (2012) *Jedlik's Electric Car.* [Online]. Available from: http://en.wikipedia.org/wiki/File:Jedlik%27s_electric-car.PNG [Accessed 31st July 2012]

[17] Wakefield, E. (1993) *History of the Electric Automobile - Battery-Only Powered Cars.* Warrendale (US), Society of Automotive Engineers.

[18] General Motors (GM). (2012) *History of the Automobile.* [Online]. Available from: http://www.gm.ca/inm/gmcanada/english/about/OverviewHist/hist_auto.html [Accessed 30th July 2012]

[19] Kirsch, D. (2000) *The Electric Vehicle and the Burden of History.* New Brunswick (US), Rutgers University Press.

[20] Gatsby Passions (2012) *Nikolas Tesla, un poète fou de science....* [Online]. Available from: http://www.gatsbyonline.com/main.aspx?page=text&id=109&cat=passions [Accessed 31st July 2012]

[21] Encyclopædia Britannica. (2012) *Automobile.* [Online]. Available from: http://www.britannica.com/EBchecked/topic/44957/automobile/259061/Early-electric-automobiles#ref=ref918099 [Accessed 31st July 2012]

[22] About Inventors. (2012) *History of Electric Vehicles.* [Online]. Available from: http://inventors.about.com/od/estartinventions/a/Electric-Vehicles.htm [Accessed 31st July 2012]

[23] Høyer, K. (2008) *The History of Alternative Fuels in Transportation: The Case of Electric and Hybrid Cars.* Utilities Policy 16 (2), 63-71 [Online]. Available from: http://dx.doi.org/10.1016/j.jup.2007.11.001 [Accessed 1st August 2012]

[24] Wikipedia. (2012) *Milk Float South Kensington.* [Online]. Available from: http://en.wikipedia.org/wiki/File:Milk_float_South_Kensington_2.jpg [Accessed 1st August 2012]

[25] Air Resources Board (ARB). (2012) *History of Air Resources Board.* [Online]. Available from: http://www.arb.ca.gov/knowzone/history.htm [Accessed 1st August 2012]

[26] Public Broadcasting Service (PBS). (2012) *California Air Quality in the Courts - Zero-Emission Vehicles.* [Online]. Available from: http://www.pbs.org/now/science/caautoemissions2.html [Accessed 1st August 2012]

[27] United Nations Framework Convention on Climate Change (UNFCCC). (2012) *Full Text of the Convention.* [Online]. Available from: http://unfccc.int/essential_background/convention/background/items/1353.php [Accessed 1st August 2012]

[28] Pike Research. (2011) *695,000 Neighborhood Electric Vehicles to be on the Road by 2017.* [Online]. Available from: http://www.pikeresearch.com/newsroom/695000-neighborhood-electric-vehicles-to-be-on-the-road-by-2017 [Accessed 8th August 2012]

[29] Society of Motor Manufacturers and Traders (SMMT). (2012) *Motor Industry Facts 2012.* [Online]. Available from: http://www.smmt.co.uk/2012/03/motor-industry-facts-2012/ [Accessed 8th August 2012]

[30] Various Car Manufacturers. (2012) *Vehicle Manufacturer Data.*

[31] Department of Energy & Climate Change (DECC). (2011) *2011 Guidelines to Defra / DECC's GHG Conversion Factors for Company Reporting* . [Online]. Available from: http://archive.defra.gov.uk/environment/business/reporting/pdf/110819-guidelines-ghg-conversion-factors.xls [Accessed 8th August 2012]

[32] Ricardo plc. (2009) *Reducing Carbon Emissions from Road Transport.* [Online]. Available from: http://www.foundation.org.uk/events/pdf/20090429_jackson.pdf [Accessed 9th August 2012]

[33] Massachusetts Institute of Technology (MIT). (2008) *On the Road in 2035.* [Online]. Available from: http://web.mit.edu/sloan-auto-lab/research/beforeh2/otr2035/ [Accessed 9th August 2012]

[34] Lorf, C. (2011) *Optimum Battery Capacity for Electric Vehicles with Particular Focus on Battery Degradation.* MPhil/PhD Transfer Report.

[35] Hayes, J. et al. (2011) *Simplified Electric Vehicle Power Train Models and Range Estimation.* Proceedings of the Vehicle Power and Propulsion Conference (VPPC) [Online]. Available from: http://dx.doi.org/10.1109/VPPC.2011.6043163 [Accessed 11th August 2012]

[36] Transportation Research Board (TRB) (2006) *Tires and Passenger Vehicle Fuel Economy*. Special Report 286 [Online]. Available from: http://www.trb.org/publications/sr/sr286.pdf [Accessed 11th August 2012]

[37] Miller, M. et al. (2011) *The GM 'Voltec'*. Proceedings of the SAE 2011 World Congress [Online]. Available from: http://dx.doi.org/10.4271/2011-01-0887 [Accessed 10th August 2012]

[38] Chae, H. et al. (2011) *3.3 kW On Board Charger for Electric Vehicle*. Proceedings of the 8th International Conference on Power Electronics - ECCE Asia [Online]. Available from: http://dx.doi.org/10.1109/ICPE.2011.5944762 [Accessed 10th August 2012]

[39] Gautam, D., Musavi, F. & Eddington, M. (2011) *An Automotive On-Board 3.3 kW Battery Charger for PHEV Application*. Proceedings of the Vehicle Power and Propulsion Conference (VPPC) [Online]. Available from: http://dx.doi.org/10.1109/VPPC.2011.6043192 [Accessed 10th August 2012]

[40] Sever, G. & Fliess, R. (1899) *Operating Costs of Horse and Electric Delivery Wagons in New York City*. Proceedings of the 16th General Meeting of the American Institute of Electrical Engineers [Online]. Available from: http://dx.doi.org/10.1109/T-AIEE.1899.4764098 [Accessed 9th August 2012]

[41] Sun, L. Bai, W. & Sun, F. (2002) *State-of-the-Art Electric Vehicle Simulation Technology*. EVS19 Conference Proceedings, Busan, South Korea.

[42] Wilkins, S. (2005) *The Development of an Object-Oriented Tool for the Modelling and Simulation of Hybrid Powertrains for Vehicular Applications*. PhD Thesis. Imperial College London.

[43] National Instruments (2012) *LabVIEW System Design Software*. [Online]. Available from: http://www.ni.com/labview/ [Accessed 13th August 2012]

[44] MathWorks (2012) *Simulink - Simulation and Model Based Design*. [Online]. Available from: http://www.mathworks.co.uk/products/simulink/ [Accessed 13th August 2012]

[45] Autonomie (2012) *Autonomie Overview*. [Online]. Available from: http://www.autonomie.net/overview/overview4.html [Accessed 11th August 2012]

[46] AVL (2012) *AVL CRUISE - Vehicle and Driveline System Analysis for Conventional and Future Vehicle Concepts*. [Online]. Available from: https://www.avl.com/cruise1/ [Accessed 10th August 2012]

[47] Dassault Systèmes (2012) *Dymola - Multi-Engineering Modeling and Simulation*. [Online]. Available from: http://www.3ds.com/products/catia/portfolio/dymola [Accessed 10th August 2012]

[48] Modelica (2012) *Modelica and the Modelica Association.* [Online]. Available from: https://modelica.org/ [Accessed 10th August 2012]

[49] Argonne National Laboratory (2012) *PSAT (Powertrain System Analysis Toolkit).* [Online]. Available from: http://www.transportation.anl.gov/modeling_simulation/PSAT/index.html [Accessed 10th August 2012]

[50] MathWorks (2012) *SimDriveline.* [Online]. Available from: http://www.mathworks.co.uk/products/simdrive/description1.html [Accessed 11th August 2012]

[51] Shukla, A. (2012) *Modelling and Simulation of Hybrid Electric Vehicles.* PhD Thesis. Imperial College London.

[52] Wipke, K. , Cuddy, M. & Burch, S. (1999) *ADVISOR 2.1: A User-Friendly Advanced Powertrain Simulation Using a Combined Backward/Forward Approach.* IEEE Transactions on Vehicular Technology 48,6,1751-1761 [Online]. Available from: http://dx.doi.org/10.1109/25.806767 [Accessed 11th August 2012]

[53] Cuddy, M. (1995) *A Comparison of Modeled and Measured Energy Use in Hybrid Electric Vehicles.* SAE Technical Paper 950959 [Online]. Available from: http://dx.doi.org/10.4271/950959 [Accessed 12th August 2012]

[54] Mechanical Simulation (2012) *CarSim - Maths Models.* [Online]. Available from: http://www.carsim.com/downloads/pdf/CarSim_Math_Models.pdf [Accessed 13th August 2012]

[55] Bumby, J. Clarke, P. & Forster, I. (1985) *Computer modelling of the automotive energy requirements for internal combustion engine and battery electric-powered vehicles.* IEE Proceedings 132 (5) [Online]. Available from: http://dx.doi.org/10.1049/ip-a-1:19850059 [Accessed 11th August 2012]

[56] Marr, W. & Walsh, W. (1992) *Life-cycle Cost Evaluations of Electric/Hybrid Vehicles.* Energy Conversion and Management 33 (9), 849-853 [Online]. Available from: http://dx.doi.org/10.1016/0196-8904(92)90013-M [Accessed 11th August 2012]

[57] Guzzella, L. & Sciarretta, A. (2007) *Vehicle Propulsion Systems.* Berlin (Germany), Springer Verlag.

[58] Swiss Federal Institute of Technlogy Zurich (ETH) - Institute for Dynamic Systems and Control *QSS Toolbox.* [Online]. Available from: http://www.idsc.ethz.ch/Downloads/qss [Accessed 15th August 2012]

[59] Cole, G. (1991) *SIMPLEV: A Simple Electric Vehicle Simulation Program - Version 1.0.* [Online]. Available from: http://www.osti.gov/bridge/servlets/purl/10167537-sw6BZA/native/10167537.pdf [Accessed 11th August 2012]

[60] Big Ladder Software (2012) *ADVISOR*. Software. [Online]. Available from: http://bigladdersoftware.com/advisor/ [Accessed 13th August 2012]

[61] Markel, T. et al. (2002) *ADVISOR: A Systems Analysis Tool for Advanced Vehicle Modelling.* Journal of Power Sources 110 (2), 255-266 [Online]. Available from: http://dx.doi.org/10.1016/S0378-7753(02)00189-1 [Accessed September 10th 2012]

[62] National Renewable Energy Laboratory (NREL) (2012) *Future Automotive Systems Technology Simulator*. Software. [Online]. Available from: http://www.nrel.gov/vehiclesandfuels/vsa/fastsim.html [Accessed 13th August 2012]

[63] Butler, K., Ehsani M. & Kamath, P. (1999) *A Matlab-Based Modelling and Simulation Package for Electric and Hybrid Electric Vehicle Design.* [Online]. Available from: http://dx.doi.org/10.1109/25.806769 [Accessed 15th August 2012]

[64] University of South Carolina (USC) (2010) *Virtual Test Bed - Overview.* [Online]. Available from: http://vtb.engr.sc.edu/vtbwebsite/#/Overview [Accessed 15th August 2012]

[65] Powersim Inc. (2012) *PSIM - Overview.* [Online]. Available from: http://www.powersimtech.com/index.php?name=psim [Accessed 15th August 2012]

[66] Ganji, B. & Kouzani, A. (2012) *Combined Quasi-Static Backward Modelling and Look-Ahead Fuzzy Control of Vehicles.* Expert Systems with Applications 39 (1), 223-233 [Online]. Available from: http://dx.doi.org/10.1016/j.eswa.2011.07.012 [Accessed 11th August 2012]

[67] British Broadcasting Corporation (BBC). (2003) *Riddle of 'Baghdad's batteries'.* [Online]. Available from: http://news.bbc.co.uk/1/hi/sci/tech/2804257.stm [Accessed 4th October 2012]

[68] Wikipedia. (2012) *Baghdad Battery.* [Online]. Available from: http://en.wikipedia.org/wiki/File:Ironie_pile_Bagdad.jpg [Accessed 4th October 2012]

[69] Educational Technology Clearinghouse. (2012) *Voltaic Pile.* [Online]. Available from: http://etc.coedu.usf.edu/clipart/4200/4286/voltaic-pile_1_lg.gif [Accessed 4th October 2012]

[70] Vincent, C. & Scrosati B. (1997) *Modern Batteries.* London (UK), Arnold.

[71] Mizushima, K. et al. (1980) *Li_xCoO_2 (0 <x <-1): A New Cathode Material for Batteries of High Energy Density.* Materials Research Bulletin 15 (6), 783-789 [Online]. Available from: http://dx.doi.org/10.1016/0025-5408(80)90012-4 [Accessed 8th October 2012]

[72] Hamwi, A. et al. (1989) *New Graphite Fluorides as Electrode Materials in Lithium Batteries.* Journal of Power Sources 27 (1), 81-87 [Online]. Available from: http://dx.doi.org/10.1016/0378-7753(89)80107-7 [Accessed 8th October 2012]

[73] Battery University. (2012) *Global Battery Markets.* [Online]. Available from: http://batteryuniversity.com/learn/article/global_battery_markets [Accessed 8th October 2012]

[74] Linden, D & Reddy T. (2002) *Handbook of Batteries.* London (UK), McGraw-Hill.

[75] Newman, J. & Thomas-Alyea, K. (2004) *Electrochemical Systems.* Hoboken (US), John Wiley & Sons.

[76] Besenhard, J. (1999) *Handbook of Battery Materials.* Wiley-VCH, Weinheim.

[77] Ozawa, K. (2009) *Lithium Ion Rechargeable Batteries.* Weinheim (D), Wiley-VCH.

[78] Schalkwijk, W. & Scrosati B. (2002) *Advances in Lithium-Ion Batteries.* New York (US), Kluwer.

[79] Goodenough, J. & Kim, Y. (2010) *Challenges for Rechargeable Batteries.* Journal of Power Sources 196 (16), 6688-6694 [Online]. Available from: http://dx.doi.org/10.1016/j.jpowsour.2010.11.074 [Accessed 8th October 2012]

[80] Spotnitz, R. (2005) *Battery Modelling.* The Electrochemical Society - Interface 14 (4), 39-42 [Online]. Available from: http://www.electrochem.org/dl/interface/wtr/wtr05/wtr05_p39-42.pdf [Accessed 9th October 2012]

[81] Heaviside, O. (1893) *A Gravitational and Electromagnetic Analogy.* The Electrician Part I (31), 281-282 [Online]. Available from: http://serg.fedosin.ru/Heavisid.htm [Accessed 9th October 2012]

[82] Wikipedia. (2012) *Hydraulic Analogy.* [Online]. Available from: http://en.wikipedia.org/w/index.php?title=File:Electronic-hydraulic_analogy.svg&page=1 [Accessed 10th October 2012]

[83] Jongerden, M. & Haverkort, B. (2008) *Battery Modelling.* Report. [Online]. Available from: http://purl.utwente.nl/publications/64556 [Accessed 20th October 2012]

[84] Wikipedia. (2012) *Periodic Table of Elements.* [Online]. Available from: http://en.wikipedia.org/w/index.php?title=File:Periodic_table.svg&page=1 [Accessed 17th October 2012]

[85] Electropaedia. (2012) *Rechargeable Lithium Batteries.* [Online]. Available from: http://www.mpoweruk.com/lithiumS.htm#lto [Accessed 18th October 2012]

[86] Moura, S. (2011) *Techniques for Battery Health Conscious Power Management via Electrochemical Modelling and Optimal Control.* PhD Thesis. University of Michigan.

[87] Hassoun, J., Reale, P. & Scrosati, B. (2007) *Recent Advances in Liquid and Polymer Lithium-Ion Batteries.* Journal of Materials Chemistry 17 (35), 3668-3677. [Online]. Available from: http://dx.doi.org/10.1039/b707040n [Accessed 20th October 2012]

[88] Abraham, K. & Jiang, Z. (1996) *A Polymer Electrolyte-Based Rechargeable Lithium/Oxygen Battery.* Journal of the Electrochemical Society 143 (1), 1-5. [Online]. Available from: http://dx.doi.org/10.1149/1.1836378 [Accessed 20th October 2012]

[89] Padbury, R. & Zhang, X. (2011) *Lithium-Oxygen Batteries - Limiting Factors that affect Performance.* Journal of Power Sources 196 (10), 4436-4444 [Online]. Available from: http://dx.doi.org/10.1016/j.jpowsour.2011.01.032 [Accessed 1st August 2012]

[90] Frost *&* Sullivan (2012) *Analysis of the Global Hybrid Electric and Electric Vehicle Lithium-Ion Battery Market.* Market report N9E7-27. Mountain View (US).

[91] Wikipedia. (2012) *Battery Recycling.* [Online]. Available from: http://en.wikipedia.org/wiki/Battery_recycling [Accessed 21st October 2012]

[92] Stiftung Gemeinsames Rücknahmesystem (GRS) Batterien. (2007) *Die Welt der Batterien - Funktion, Systeme, Entsorgung.* [Online]. Available from: http://www.grs-batterien.de/fileadmin/user_upload/Download/Wissenswertes/welt_bat.pdf [Accessed 21st October 2012]

[93] Broussely, M. et al. (2005) *Main Aging Mechanisms in Li-ion Batteries.* Journal of Power Sources 146 (1-2), 90-96. [Online]. Available from: http://dx.doi.org/10.1016/j.jpowsour.2005.03.172 [Accessed 19th October 2012]

[94] Broussely, M. et al. (2005) *Identify Capacity Fading Mechanism in a Commercial* $LiFePO_4$ *Cell.* Journal of Power Sources 194 (1), 541-549. [Online]. Available from: http://dx.doi.org/10.1016/j.jpowsour.2009.05.036 [Accessed 19th October 2012]

[95] AutoBlogGreen (2012) *Nissan's Andy Palmer discusses Leaf Battery Degradation Crisis.* [Online]. Available from: http://green.autoblog.com/2012/10/10/nissan-andy-palmer-leaf-battery-degradation-crisis-video/ [Accessed 11th October 2012]

[96] Markovsky, B. et al. (2003) *The Study of Capacity Fading Processes of Li-ion batteries: Major Factors that Play a Role.* Journal of Power Sources 119-121, 504-510. [Online]. Available from: http://dx.doi.org/10.1016/S0378-7753(03)00274-X [Accessed 19th October 2012]

[97] Peterson, S., Apt, J. & Whitacre, J. (2010) *Lithium-ion Battery Cell Degradation Resulting from Realistic Vehicle and Vehicle-to-Grid Utilization.* Journal of Power Sources 195 (8), 2385-2392. [Online]. Available from: http://dx.doi.org/10.1016/j.jpowsour.2009.10.010 [Accessed 20th October 2012]

[98] Zhang, Y., Wang, C. & Tang, X. (2011) *Cycling Degradation of an Automotive* $LiFePO_4$ *lithium-ion battery.* Journal of Power Sources 196 (3), 1513-1520. [Online]. Available from: http://dx.doi.org/10.1016/j.jpowsour.2010.08.070 [Accessed 20th October 2012]

[99] Blaiszik, B. et al. (2012) *Autonomic Restoration of Electrical Conductivity.* Advanced Materials 24 (3), 398-401. [Online]. Available from: http://dx.doi.org/10.1002/adma.201102888 [Accessed 20th October 2012]

[100] Fergus, J. (2010) *Recent Developments in Cathode Materials for Lithium Ion Batteries.* Journal of Power Sources 195 (4), 939-954. [Online]. Available from: http://dx.doi.org/10.1016/j.jpowsour.2009.08.089 [Accessed 20th October 2012]

[101] Exponent Failure Analysis Associates, Inc. (2011) *Lithium-Ion Batteries Hazard and Use Assessment.* Final Report prepared for the Fire Protection Research Foundation. [Online]. Available from: http://www.nfpa.org/assets/files/pdf/research/rflithiumionbatterieshazard.pdf [Accessed 21st October 2012]

[102] Shepherd, C. (1965) *Design of Primary and Secondary Cells II. - An Equation Describing battery Discharge.* Journal of The Electrochemical Society 112 (7), 657-664. [Online]. Available from: http://dx.doi.org/10.1149/1.2423659 [Accessed 23rd October 2012]

[103] Doerffel, D. & Sharkh S. (2006) *A Critical Review of Using the Peukert Equation for Determining the Remaining Capacity of Lead-acid and Lithium-ion Batteries.* Journal of Power Sources 155 (2), 395-400. [Online]. Available from: http://dx.doi.org/10.1016/j.jpowsour.2005.04030 [Accessed 23rd October 2012]

[104] Doyle, M., Fuller, T. & Newman, J. (1993) *Modelling of Galvanostatic Charge and Discharge of the Lithium/Polymer/Insertion Cell.* Journal of The Electrochemical Society 140 (6), 1526-1533 [Online]. Available from: http://dx.doi.org/10.1149/1.2221597 [Accessed October 22nd 2012]

[105] Fuller, T., Doyle, M. & Newman, J. (1994) *Simulation and Optimization of the Dual Lithium Ion Insertion Cell.* Journal of The Electrochemical Society 141 (1), 1-10 [Online]. Available from: http://dx.doi.org/10.1149/1.2054684 [Accessed October 22nd 2012]

[106] Fuller, T., Doyle, M. & Newman, J. (1994) *Relaxation Phenomena in Lithium-Ion-Insertion Cells.* Journal of The Electrochemical Society 141 (4), 982-990 [Online]. Available from: http://dx.doi.org/10.1149/1.2054868 [Accessed October 22nd 2012]

[107] Newman, J. (1998) *FORTRAN Programs for the Simulation of Electrochemical Systems.* Software. [Online]. Available from: http://www.cchem.berkeley.edu/jsngrp/fortran.html [Accessed October 22nd 2012]

[108] Millner, A. (2010) *Modelling Lithium Ion Battery Degradation in Electric Vehicles.* 2010 IEEE Conference on Innovative Technologies for an Efficient and Reliable Electricity Supply (CITRES). [Online]. Available from: http://dx.doi.org/10.1109/CITRES.2010.5619782 [Accessed 23rd October 2012]

[109] Lai, W. (2011) *Electrochemical Modelling of Single Particle Intercalation Battery Materials with Different Thermodynamics.* Journal of Power Sources 196 (15), 6534-6553. [Online]. Available from: http://dx.doi.org/10.1016/j.jpowsour.2011.03.055 [Accessed 23rd October 2012]

[110] Schmidt, A. et al. (2010) *Experiment-driven Electrochemical Modelling and Systematic Parametrisation for a Lithium-Battery Cell.* Journal of Power Sources 195 (15), 5071-5080. [Online]. Available from: http://dx.doi.org/10.1016/j.jpowsour.2010.02.029 [Accessed 23rd October 2012]

[111] Smith, K. & Wang C. (2006) *Power and Thermal Characterisation of a Lithium-ion Battery Pack for Hybrid-electric Vehicles.* Journal of Power Sources 160 (1), 662-673. [Online]. Available from: http://dx.doi.org/10.1016/j.jpowsour.2006.01.038 [Accessed 23rd October 2012]

[112] University of California, San Diego (UCSD) (2012) *New Sophisticated Control Algorithms Poised to Revolutionize Electric Battery Technology.* [Online]. Available from: http://www.jacobsschool.ucsd.edu/news/news_releases/release.sfe?id=1271 [Accessed 12th October 2012]

[113] Hu, X., Li, S. & Peng H. (2012) *A Comparative Study of Equivalent Circuit Models for Li-ion Batteries.* Journal of Power Sources 198, 359-367 [Online]. Available from: http://dx.doi.org/10.1016/j.jpowsour.2011.10.013 [Accessed September 11th 2012]

[114] Johnson, V. (2002) *Battery Performance Models in ADVISOR.* Journal of Power Sources 110 (2), 321-329 [Online]. Available from: http://dx.doi.org/10.1016/S0378-7753(02)00194-5 [Accessed September 11th 2012]

[115] He, H., Xiong, R. & Fan J. (2011) *Evaluation of Lithium-Ion Battery Equivalent Circuit Models for State of Charge Estimation by an Experimental Approach.* Energies 4 (4), 582-598 [Online]. Available from: http://dx.doi.org/10.3390/en4040582 [Accessed October 25th 2012]

[116] Liaw, B. et al. (2004) *Modelling of Lithium-Ion cells - A Simple Equivalent Circuit Approach.* Solid State Ionics 175 (1-4), 835-839 [Online]. Available from: http://dx.doi.org/10.1016/j.ssi.2004.09.049 [Accessed October 25th 2012]

[117] Tremblay, O. & Dessaint, L. (2009) *Experimental Validation of a Battery Dynamic Model for EV Applications.* World Electric Vehicle Journal 3 [Online]. Available from: http://www.evs24.org/wevajournal/php/download.php?f=vol3/WEVJ3-2230080.pdf [Accessed 8th September 2012]

[118] Pop, V. et al. (2005) *State-of-the-Art of Battery State-of-Charge Determination.* Measurement Science and Technology 16 (12), 93-110 [Online]. Available from: http://dx.doi.org/10.1088/0957-0233/16/12/R01 [Accessed October 26th 2012]

[119] Bergveld, H., Krujit, W. & Notten, P. (2002) *Battery Management Systems - Design by Modelling.* Boston (US), Kluwer.

[120] Plett, G. (2004) *Extended Kalman Filtering for Battery Management Systems of LiPB-Based HEV Battery Packs: Part 1. Background.* Journal of Power Sources 134 (2), 252-261 [Online]. Available from: http://dx.doi.org/10.1016/j.jpowsour.2004.02.031 [Accessed October 26th 2012]

[121] Plett, G. (2004) *Extended Kalman Filtering for Battery Management Systems of LiPB-Based HEV Battery Packs: Part 2. Modelling and Identification.* Journal of Power Sources 134 (2), 262-276 [Online]. Available from: http://dx.doi.org/10.1016/j.jpowsour.2004.02.032 [Accessed October 26th 2012]

[122] Plett, G. (2004) *Extended Kalman Filtering for Battery Management Systems of LiPB-Based HEV Battery Packs: Part 3. State and Parameter Estimation.* Journal of Power Sources 134 (2), 277-292 [Online]. Available from: http://dx.doi.org/10.1016/j.jpowsour.2004.02.033 [Accessed October 26th 2012]

[123] Wang, J. (2002) *Cycle-life model for graphite-$LiFePO_4$ cells.* Journal of Power Sources 196 (8), 3942-3948 [Online]. Available from: http://dx.doi.org/10.1016/j.jpowsour.2010.11.134 [Accessed September 11th 2012]

[124] Li, Z. et al. (2011) *Modeling the Capacity Degradation of $LiFePO_4$/Graphite Batteries Based on Stress Coupling Analysis.* Journal of Power Sources 196 (22), 9757-9766 [Online]. Available from: http://dx.doi.org/10.1016/j.jpowsour.2011.07.080 [Accessed September 11th 2012]

[125] Ning, G., White, R. & Popov, B. (2006) *A Generalized Cycle Life Model of Rechargeable Li-Ion Batteries.* Electrochimica Acta 51 (10), 2012-2022 [Online]. Available from: http://dx.doi.org/10.1016/j.electacta.2005.06.033 [Accessed September 11th 2012]

[126] Choi, S. & Lim, H. (2002) *Factors that affect Cycle-Life and Possible Degradation Mechanisms of a Li-Ion Cell Based on $LiCoO_2$*. Journal of Power Sources 111 (1), 130-136 [Online]. Available from: http://dx.doi.org/10.1016/S0378-7753(02)00305-1 [Accessed September 11th 2012]

[127] ANSYS, Inc. (2013) *Designing Batteries for Electrical Vehicles.* [Online]. Available from: http://www.ansys.com/Resource+Library/Technical+Briefs/Designing+Batteries+for+Electrical+Vehicles [Accessed January 3rd 2013]

[128] COMSOL (2013) *Electrochemistry Specification Chart.* [Online]. Available from: http://www.comsol.com/products/specifications/electrochemistry/ [Accessed January 3rd 2013]

[129] Lorf, C., Martínez-Botas R. & Brandon, N. (2012) *26,500 km Down The Pan-American Highway in an Electric Vehicle - A Battery's Perspective.* SAE International Journal of Alternative Powertrains 1 (1), 19-26 [Online]. Available from: http://dx.doi.org/10.4271/2012-01-0123 [Accessed 24th September 2012]

[130] Howey, D., Martínez-Botas R., Cussons, B. & Lytton, L. (2011) *Comparative Measurements of the Energy Consumption of 51 electric, hybrid and internal combustion engine vehicles.* Transportation Research Part D: Transport and Environment 16 (6) [Online]. Available from: http://dx.doi.org/10.1016/j.trd.2011.04.001 [Accessed 23rd December 2012]

[131] Lorf, C., Martínez-Botas R., Howey, D.A., Lytton, L. & Cussons, B. (2013) *Comparative Analysis of the Energy Consumption and CO_2 Emissions of 40 Electric, Plug-in Hybrid Electric, Hybrid Electric and Internal Combustion Engine Vehicles.* Transportation Research Part D: Transport and Environment 23 [Online]. Available from: http://dx.doi.org/10.1016/j.trd.2013.03.004 [Accessed 1st May 2013]

[132] The Royal Automobile Club (RAC) (2012) *RAC Future Car Challenge - Official Entry Regulations* [Online]. Available from: http:www.futurecarchallenge.com/downloads/2011-downloads/Participate%20-%20Document%20Downloads/RAC%20FCC%202012%20Regulations%2015%20June.pdf [Accessed 23rd December 2012]

[133] Commission of the European Communities (EC) (1999) *Regulation (EEC) No 4064/89* [Online]. Available from: http://ec.europa.eu/competition/mergers/cases/decisions/m1406_en.pdf [Accessed 23rd December 2012]

[134] Department of Energy & Climate Change (DECC) (2011) *Digest of United Kingdom Energy Statistics (DUKES), Annex A - Energy and Commodity Balances, Conversion Factors and Calorific Values* [Online]. Available from: http://www.decc.gov.uk/assets/decc/11/stats/publications/dukes/2293-dukes-2011-annex-a.pdf [Accessed 23rd December 2012]

[135] US Department of Energy (DOE) (2012) *Transportation Energy Data Book, Appendix B - Table B.4 Heat Content for Various Fuels* [Online]. Available from: http://cta.ornl.gov/data/tedb31/Spreadsheets/TableB_04.xls [Accessed 28th December 2012]

[136] Department for Transport (DfT) (2012) *National Travel Survey: 2011.* [Online]. Available from: https://www.gov.uk/government/publications/national-travel-survey-2011 [16th January 2013]

[137] Economic and Social Data Service (ESDS) (2013) *SN: 5340 National Survey, 2002-2010.* [Online]. Available from: https://www.esds.ac.uk/ [16th January 2013]

[138] Clearing House of Transport Data at the Institute of Transport Research (DLR) (2013) *Mobilitätspanel Deutschland (MOP) 1994-2011.* [Online]. Available from: http://www.dlr.de/cs/en/desktopdefault.aspx/1177_read-2160/ [7th February 2013]

[139] U.S. Department of Transportation, Federal Highway Administration (2013) *2009 National Household Travel Survey.* [Online]. Available from: http://nhts.ornl.gov [20th January 2013]

[140] Wikipedia. (2012) *Measured Drag Coefficients.* [Online]. Available from: http://en.wikipedia.org/wiki/File:14ilf1l.svg [Accessed 30th December 2012]

[141] Robert Bosch GmbH. (2007) *Automotive Handbook.* 7th Edition. Chichester (UK), John Wiley & Sons.

[142] Franke, R., Terwiesch, P. & Meyer, M. (2000) *An Algorithm for the Optimal Control of the Driving of Trains.* Proceedings of the 39th IEEE Conference on Decision and Control [Online]. Available from: http://dx.doi.org/10.1109/CDC.2000.914108 [Accessed 31st December 2012]

[143] U.S. Environmental Protection Agency (EPA) (2013) *Dynamometer Drive Schedules* [Online]. Available from: http://www.epa.gov/nvfel/testing/dynamometer.htm [January 6th June 2013]

[144] Google Inc. (2013) *Google Maps.* [Online]. Available from: https://maps.google.com [Accessed 27th February 2013]

[145] GPS Visualizer (2013) *Draw a Profile.* [Online]. Available from: http://www.gpsvisualizer.com/profile_input [Accessed 27th February 2013]

[146] von Srbik, M. et al (2013) *The 2012 RAC Future Car Challenge - The impact of hybridisation on energy consumption.* Hybrid and Electric Vehicles Conference (HEVC), London (UK).

[147] Blair, P. (1978) *Modelling Energy and Power Requirements of Electric Vehicles.* Energy Conversion 18 (3), 127-134 [Online]. Available from: http://dx.doi.org/10.1016/0013-7480(78)90011-16 [Accessed 1st April 2013]

[148] Wang, G. (2011) *Advanced Vehicles: Costs, Energy Use and Macroeconomic Impacts.* Journal of Power Sources 196 (1), 530-540 [Online]. Available from: http://dx.doi.org/10.1016/j.jpowsour.2010.07.009 [Accessed 1st April 2013]

[149] International Energy Agency (2011) *Technology Roadmap - Electric and Plug-In Hybrid Electric Vehicles.* [Online]. Available from: http://www.iae.org/publications/freepublications/publication/EV_PHEV_Roadmap.pdf [Accessed 1st April 2013]

[150] The Economist (2012) *Seeing the Back of the Car.* [Online]. Available from: http://www.economist.com/node/21563280 [Accessed 6th March 2013]

[151] Wikipedia (2013) *Range Anxiety.* [Online]. Available from: http://en.wikipedia.org/wiki/Range_anxiety [Accessed 4th March 2013]

[152] Offer, G.J. et al. (2011) *Techno-Economic and Behavioural Analysis of Battery Electric, Hydrogen Fuel Cell and Hybrid Vehicles in a Future Sustainable Road Transport System in the UK.* Energy Policy 39 (4), 1939-1950 [Online]. Available from: http://dx.doi.org/10.1016/j.enpol.2011.01.006 [18th January 2013]

[153] Society of Motor Manufacturers and Traders (SMMT) (2013) *2012 UK Vehicle Registration Statistics*

[154] Department for Transport (DfT) (2009) *Low Carbon Transport: A Greener Future.* Report [Online]. Available from: http://webarchive.nationalarchives.gov.uk/+/http:/www.dft.gov.uk/pgr/sustainable/_analysis.pdf [1st May 2013]

[155] Rinehart Motion Systems LLC (RmS) (2010) *PM100DZ Data Sheet - AC Traction Controller for Electric and Hybrid Vehicles.*

[156] International Air Transport Association (IATA) (2013) *Lithium Battery Guidance Document - Transport of Lithium Ion Batteries.* Report [Online]. Available from: http://www.iata.org/whatwedo/cargo/dgr/Documents/Lithium-Battery-Guidance-2013-V1.1.pdf [3rd June 2013]

[157] Matsuishi, M. & Endo, T. (1968) *Fatigue of Metals Subjected to Varying Stress.* Fukuoka (Japan), Japan Society of Mechanical Engineers.

[158] Wikipedia (2013) *Rainflow-Counting Algorithm.* [Online]. Available from: http://en.wikipedia.org/wiki/Rainflow-counting_algorithm [Accessed 10th June 2013]

[159] Sandia National Laboratories (1991) *User's Guide for LIFE2's Rainflow Counting Algorithm.* Report [Online]. Available from: http://prod.sandia.gov.techlib/access-control.cgi/1990/902259.pdf [Accessed 3rd June 2013]

[160] Nieslony, A. (2003) *Rainflow Counting Algorithm* [Software] Available from: http://www.mathworks.com/matlabcentral/fileexchange/3026-rainflow-counting-algorithm [Accessed 11th June 2013]

[161] Gao, L., Liu, S. & Dougal, R. (2002) *Dynamic Lithium-Ion Battery Model for System Simulation.* IEEE Transactions on Components and Packaging Technologies 25 (3) [Online]. Available from: http://dx.doi.org/10.1109/TCAPT.2002.803653 [Accessed 8th September 2012]

[162] Chen, M. & Rincón-Mora, R. (2006) *Accurate Electrical Battery Model Capable of Predicting Runtime and I-V Performance.* IEEE Transactions on Energy Conversion 21 (2) [Online]. Available from: http://dx.doi.org/10.1109/TEC.2006.874229 [Accessed 8th September 2012]

[163] Burke, A. (2007) *Batteries and Ultracapacitors for Electric, Hybrid, and Fuel Cell Vehicles.* Proceedings of the IEEE 95 (4) [Online]. Available from: http://dx.doi.org/10.1109/JPROC.2007.892490 [January 3rd January 2013]

[164] The Boston Consulting Group (BCG) (2011) *Powering Autos to 2020 - The Era of the Electric Car?* Report [Online]. Available from: http://www.bcg.com/documents/file80920.pdf [January 6th January 2013]

[165] McKinsey & Company (2011) *A Portfolio of Power-Trains for Europe - A Fact Based Analysis.* Report [Online]. Available from: http://ec.europa.eu/research/fch/pdf/a_portfolio_of_powertrains_for_europe_a_fact_based_analysis.pdf [January 6th June 2013]

[166] Bloomberg New Energy Finance (BNEF) (2012) *Q1 2012 Electric Vehicle Battery Price Index.* Report.

Appendices

A. Publications

Journal Articles

- Lorf, C., Martínez-Botas R., Howey, D., Lytton, L. & Cussons, B. (2013) *Comparative analysis of the energy consumption and CO_2 emissions of 40 electric, plug-in hybrid electric, hybrid electric and internal combustion engine vehicles.* Transportation Research Part D: Transport and Environment 23 [Online]. Available from: http://dx.doi.org/10.1016/j.trd.2013.03.004

- Lorf, C., Martínez-Botas R. & Brandon, N. (2012) *26,500 km Down The Pan-American Highway in an Electric Vehicle - A Battery's Perspective.* SAE International Journal of Alternative Powertrains 1 (1), 19-26 [Online]. Available from: http://dx.doi.org/10.4271/2012.01.0123

Conference Presentations

- Lorf, C. (2012) *26,500 km down the Pan-American Highway in an Electric Vehicle - A Battery's Perspective.* SAE World Congress, Detroit (US).

- Lorf, C. (2010) *Optimum Battery Capacity for Electric Vehicles with Particular Focus on Battery Degradation.* International Conference on Sustainable Mobility (ICSM), Kuala Lumpur (Malaysia).

Report

- Lorf, C. & Lytton, L. (2011) *The Green Charge - Analysis of energy and CO_2 emissions data from the 2011 RAC Future Challenge.* [Report]. Available from: http://www.racfoundation.org/assets/rac_foundation/content/downloadables/the_green_charge-lorf_lytton-270312.pdf

Other

- Lorf, C. (2012) *16,000 Miles down the Pan-American Highway in an Electric Vehicle.* The Institution of Engineering and Technology (IET). [Presentation]

B. SRZero Battery Specifications

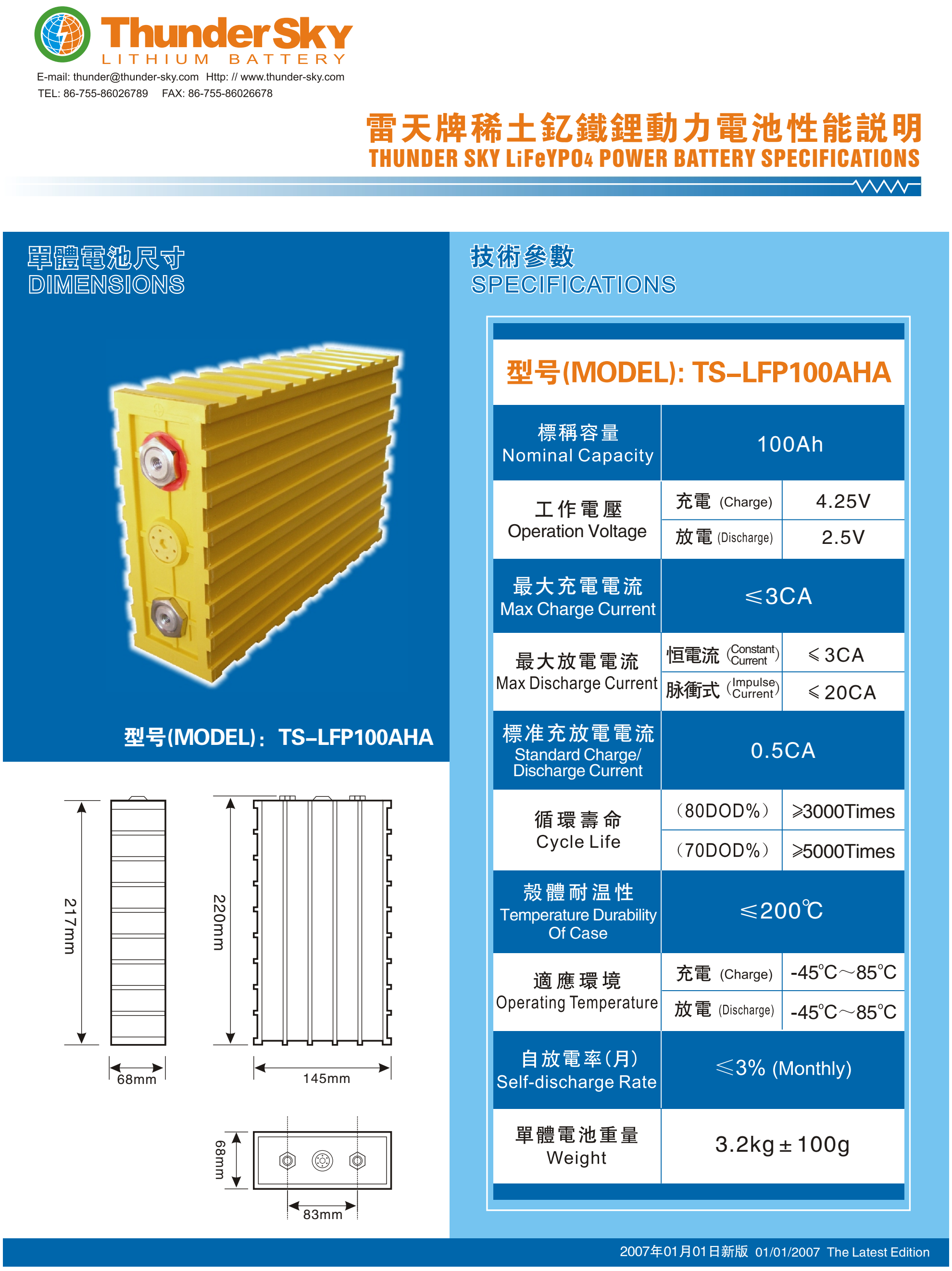

ThunderSky
LITHIUM BATTERY
E-mail: thunder@thunder-sky.com Http: // www.thunder-sky.com
TEL: 86-755-86026789 FAX: 86-755-86026678

雷天牌稀土釔鐵鋰動力電池性能説明
THUNDER SKY LiFeYPO4 POWER BATTERY SPECIFICATIONS

單體電池尺寸
DIMENSIONS

型号(MODEL)：TS–LFP100AHA

217mm
220mm
68mm
145mm
68mm
83mm

技術參數
SPECIFICATIONS

型号(MODEL): TS–LFP100AHA

標稱容量 Nominal Capacity	100Ah	
工作電壓 Operation Voltage	充電 (Charge)	4.25V
	放電 (Discharge)	2.5V
最大充電電流 Max Charge Current	≤3CA	
最大放電電流 Max Discharge Current	恒電流 (Constant Current)	≤ 3CA
	脉衝式 (Impulse Current)	≤ 20CA
標准充放電電流 Standard Charge/ Discharge Current	0.5CA	
循環壽命 Cycle Life	（80DOD%）	≥3000Times
	（70DOD%）	≥5000Times
殼體耐温性 Temperature Durability Of Case	≤200℃	
適應環境 Operating Temperature	充電 (Charge)	-45℃～85℃
	放電 (Discharge)	-45℃～85℃
自放電率(月) Self-discharge Rate	≤3% (Monthly)	
單體電池重量 Weight	3.2kg ± 100g	

2007年01月01日新版 01/01/2007 The Latest Edition

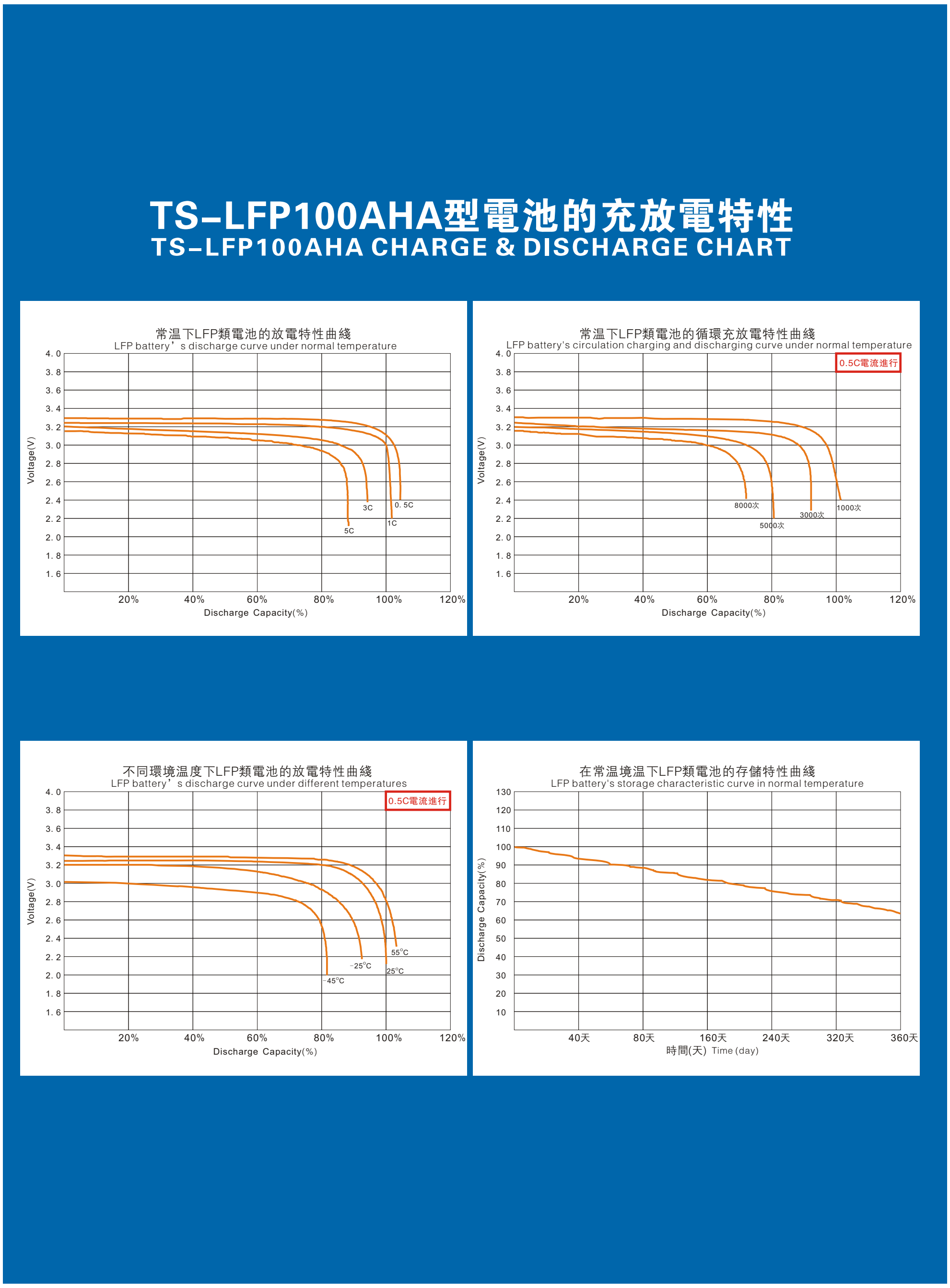

TS–LFP100AHA型電池的充放電特性

TS–LFP100AHA CHARGE & DISCHARGE CHART

常温下LFP類電池的放電特性曲綫
LFP battery’s discharge curve under normal temperature

常温下LFP類電池的循環充放電特性曲綫
LFP battery's circulation charging and discharging curve under normal temperature

不同環境温度下LFP類電池的放電特性曲綫
LFP battery’s discharge curve under different temperatures

在常温境温下LFP類電池的存儲特性曲綫
LFP battery's storage characteristic curve in normal temperature

Voltage(V)
4. 0
3. 8
3. 6
3. 4
3. 2
3. 0
2. 8
2. 6
2. 4
2. 2
2. 0
1. 8
1. 6
20%
40%
60%
80%
100%
120%
Discharge Capacity(%)
5C
3C
1C
0. 5C
0.5C電流進行
8000次
5000次
3000次
1000次
-45°C
-25°C
25°C
55°C
Discharge Capacity(%)
130
120
110
100
90
80
70
60
50
40
30
20
10
40天
80天
160天
240天
320天
360天
時間(天) Time (day)

C. Racing Green Endurance Itinerary

Leg	**Date (2010)**	**Route**	**Country**	**Distance [km]**
1	July 1st	Anchorage to Chena Hotsprings	US	673
2	July 3rd	Chena Hotsprings to Tok	US	402
3	July 4th	Tok to Beaver Creek	US & Canada	176
4	July 5th	Beaver Creek to Whitehorse	Canada	451
5	July 7th	Whitehorse to Watson Lake	Canada	415
6	July 8th	Watson Lake to Iskut	Canada	315
7	July 9th	Iskut to Smithers	Canada	518
8	July 10th	Smithers to Prince George	Canada	371
9	July 11th	Prince George to Clinton	Canada	404
10	July 12th	Clinton to Vancouver	Canada	357
11	July 17th	Vancouver to Seattle	Canada & US	237
12	July 18th	Seattle to Wilsonville	US	307
13	July 19th	Wilsonville to Yreka	US	493
14	July 20th	Yreka to Santa Rosa	US	467
15	July 21st	Santa Rosa to San Francisco	US	184
16	July 24th	San Francisco to San Luis Obispo	US	441
17	July 25th	San Luis Obispo to Helendale	US	421
18	July 27th	Helendale to Las Vegas	US	282
19	July 28th	Las Vegas to Flagstaff	US	408
20	July 30th	Flagstaff to Santa Rosa	US	708
21	July 31st	Santa Rosa to Snyder	US	467
22	August 1st	Snyder to Austin	US	467
23	August 8th	Austin to Eagle Pass	US	356
24	August 10th	Eagle Pass to Saltillo	US & Mexico	450
25	August 11th	Saltillo to San Luis Potosi	Mexico	464
26	August 12th	San Luis Potosí to Mexico City	Mexico	410
27	August 17th	Mexico City to Oaxaca	Mexico	470
28	August 18th	Oaxaca to La Ventosa	Mexico	305
29	August 19th	La Ventosa to Tapachula	Mexico	423
30	August 20th	Tapachula to Guatemala City	Mexico & Guatemala	300
31	August 22nd	Guatemala City to San Salvador	Guatemala & El Salvador	263
32	August 25th	San Salvador to Lufassa	El Salvador & Honduras	308
33	August 26th	Lufassa to Managua	Honduras & Nicaragua	292
34	August 27th	Managua to Liberia	Nicaragua & Costa Rica	244
35	August 28th	Liberia to San José	Costa Rica	202
36	August 31st	San José to David	Costa Rica & Panama	392
37	September 1st	David to Panama City	Panama	466
38	September 4th	Panama City to Colon	Panama	90

Leg	**Date (2010)**	**Route**	**Country**	**Distance [km]**
39	September 25th	Cartagena to Montería	Colombia	253
40	September 26th	Montería to Medellín	Colombia	393
41	September 28th	Medellín to Bogotá	Colombia	414
42	October 3rd	Bogotá to Armenia	Colombia	290
43	October 4th	Armenia to Cali	Colombia	200
44	October 5th	Cali to Pasto	Colombia	385
45	October 6th	Pasto to Ibarra	Colombia & Ecuador	105
46	October 7th	Ibarra to Quito	Ecuador	115
47	October 14th	Quito to Machala	Ecuador	518
48	October 15th	Machala to Piura	Ecuador & Peru	393
49	October 16th	Piura to Chiclayo	Peru	214
50	October 17th	Chiclayo to Chimbote	Peru	350
51	October 18th	Chimbote to Lima	Peru	424
52	October 21st	Lima to Ica	Peru	300
53	October 22nd	Ica to Nazca	Peru	150
54	October 23rd	Nazca to Camaná	Peru	388
55	October 24th	Camaná to Tacna	Peru	463
56	October 25th	Tacna to Iquique	Peru & Chile	360
57	October 26th	Iquique to Mejillones	Chile	356
58	October 27th	Mejillones to ESO	Chile	330
59	October 28th	ESO to Copiapó	Chile	363
60	October 29th	Copiapó to Tongoy	Chile	400
61	October 31st	Tongoy to Santiago	Chile	438
62	November 4th	Santiago to Taica	Chile	269
63	November 5th	Taica to Los Angelos	Chile	269
64	November 6th	Los Angelos to Osorno	Chile	409
65	November 7th	Osorno to Bariloche	Chile & Argentina	250
66	November 8th	Bariloche to Esquel	Argentina	310
67	November 10th	Esquel to Sarmiento	Argentina	441
68	November 11th	Sarmiento to Puerto San Julián	Argentina	581
69	November 12th	Puerto San Julián to Río Gallegos	Argentina	359
70	November 15th	Río Gallegos to Río Grande	Argentina	220
71	November 16th	Río Grande to Ushuaia	Argentina	258

D. International Driving Cycles

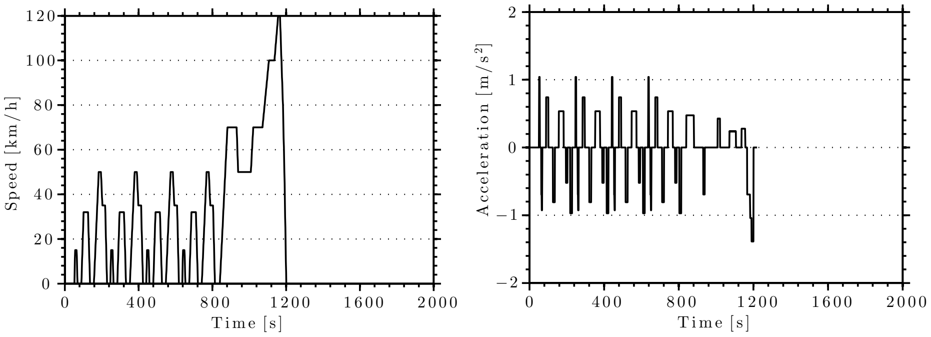

Figure D.1.: New European Driving Cycle (NEDC) [143]

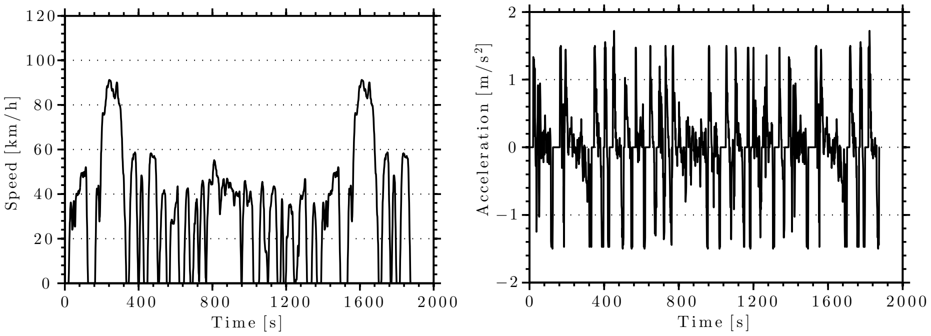

Figure D.2.: US Federal Testing Procedure (FTP-75) [143]

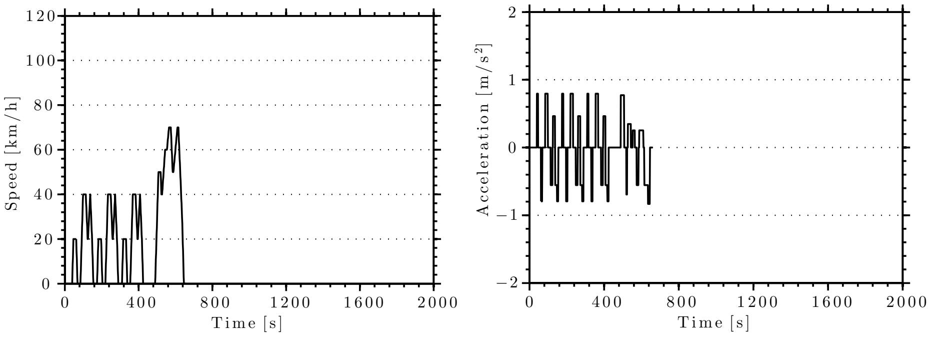

Figure D.3.: Japanese 10-15 Mode [143]

E. 2011 FCC - EV Specifications

Make	**Model**	**Start Number**	**Veh. Mass [kg]**	**Peak Power [kW]**	**Driving Force[1] [Wh/km]**	**Range[1] [km]**	**Battery Capacity [kWh]**
VW	Golf Blue e-motion	1	1,545	85	150	145	26.5
Smart	fortwo coupé E	2	870	30	120	135	16.5
Nissan	Leaf	3	1,521	80	220	160	24.0
Delta	E4	4	975	160	n/a	225	32.0
Lotus	Elise S1 EV	8	1,000	30	125	96	16.0
Radical	SRZero	9	1,150	300	110	500	54.0
Nissan	Leaf	12	1,521	80	220	160	24.0
MG	F-EV	16	1,230	54	n/a	128	18.0
Tesla	Roadster	18	1,235	225	135	356	56.0
G. Murray	T27	27	680	25	80	160	12.0
Nissan	Leaf	30	1,521	80	220	160	24.0
Nissan	Leaf	36	1,521	80	220	160	24.0
Lightning	GT	38	1,850	300	n/a	240	44.0
VW	Lupo EV	40	1,060	50	130	200	27.0
VW	Golf Blue e-motion	43	1,545	85	150	145	26.5
Delta	E4	44	975	160	n/a	225	32.0
Proton	Saga	51	1,148	52	n/a	120	13.6
Jaguar	E-Type EV	54	1,230	150	n/a	215	32.0
Nissan	Leaf	56	1,521	80	220	160	24.0
Smart	fortwo coupé E	57	870	30	120	135	16.5
BMW	Mini E	60	1,465	150	125	160	35.0
Citroën	Nemo Van Electric	62	1,176	26	100	90	16.0
Smart	fortwo coupé E	63	870	30	120	135	16.5
Smart	fortwo coupé E	66	870	30	120	135	16.5
Smart	fortwo coupé E	70	870	30	120	135	16.5
		∅	**1,209**	**96**	**147.63**	**179.20**	**25.72**

---

[1] based on NEDC & US EPA

F. Battery Statistics from the RGE Trip

Battery Cycle	$\bar{I}_{charge}$ **[A]**	$\bar{P}_{charge}$ **[kW]**	C_{charge} **[Ah]**	E_{charge} **[kWh]**	$\bar{I}_{discharge}$ **[A]**	$\bar{P}_{discharge}$ **[kW]**	$C_{discharge}$ **[Ah]**	$E_{discharge}$ **[kWh]**
1	n/a	n/a	n/a	n/a	5.50	2.83	3.82	1.99
2	3.71	2.05	74.31	47.36	16.20	8.59	23.97	12.78
3	6.85	3.73	77.80	43.65	11.51	6.01	7.74	4.11
4	3.65	1.99	34.06	18.65	11.38	5.97	71.01	37.13
5	2.65	1.46	43.18	24.48	10.69	5.57	97.75	51.07
6	3.97	2.19	59.84	33.98	9.58	5.00	47.28	25.07
7	7.02	3.86	72.29	41.05	9.46	4.93	40.41	21.56
8	3.57	1.96	43.13	24.93	12.21	6.35	78.18	40.81
9	4.65	2.56	86.11	48.90	0.81	0.43	1.54	0.82
10	4.67	2.54	8.66	4.72	6.75	3.50	12.26	6.62
11	3.56	1.98	2.11	1.27	4.03	2.11	39.18	21.16
12	3.80	2.09	40.00	25.49	4.31	2.27	60.42	32.34
13	2.25	1.22	12.82	6.97	5.20	2.68	6.48	3.49
14	3.12	1.69	7.61	4.13	12.02	6.15	54.52	28.51
15	5.05	2.76	97.83	58.47	10.33	5.35	104.32	54.15
16	5.86	3.17	79.78	43.67	5.00	2.66	0.69	0.37
17	6.65	3.67	23.57	13.57	12.62	6.59	88.79	46.56
18	7.45	4.04	45.72	24.98	6.27	3.21	56.60	29.63
19	7.25	3.95	78.83	43.76	8.08	4.15	58.84	31.46
20	6.14	3.33	66.40	36.57	7.12	3.69	96.31	50.79
21	5.88	3.21	90.56	52.74	9.99	5.23	85.03	44.81
22	4.50	2.44	74.59	40.81	9.14	4.79	54.45	28.88
23	2.62	1.42	52.74	28.80	4.18	2.21	0.79	0.37
24	2.73	1.49	4.34	2.37	7.29	3.86	29.50	15.80
25	3.86	2.09	58.79	32.25	11.41	6.00	70.71	37.68
26	7.74	4.21	59.60	32.75	1.45	0.72	0.49	0.27
27	6.36	3.40	8.38	4.51	8.44	4.44	89.35	47.03
28	2.10	1.11	1.24	0.66	9.60	5.08	66.59	35.53
29	5.49	2.99	67.23	38.56	8.08	4.26	80.52	42.89
30	3.77	2.05	1.08	0.59	9.73	5.11	84.35	44.37
31	2.41	1.30	34.77	18.87	9.55	4.91	51.86	26.59
32	3.51	1.88	18.11	9.79	8.33	4.25	17.21	9.01
33	3.69	2.00	68.60	37.55	7.92	4.14	7.43	3.98
34	1.90	1.05	41.31	26.33	7.03	3.65	89.12	47.03
35	1.76	0.95	23.42	12.65	0.82	0.44	0.96	0.46
36	7.88	4.31	48.04	26.43	6.78	3.51	63.88	34.01
37	7.13	3.90	78.84	45.37	10.73	5.63	79.10	41.91
38	7.74	4.23	78.76	45.63	6.39	3.33	74.66	39.57

Battery Cycle	$\bar{I}_{charge}$ **[A]**	$\bar{P}_{charge}$ **[kW]**	C_{charge} **[Ah]**	E_{charge} **[kWh]**	$\bar{I}_{discharge}$ **[A]**	$\bar{P}_{discharge}$ **[kW]**	$C_{discharge}$ **[Ah]**	$E_{discharge}$ **[kWh]**
39	4.27	2.34	74.32	43.13	4.65	2.44	44.79	23.84
40	6.19	3.40	99.62	54.88	0.83	0.44	1.92	1.00
41	0.99	0.55	15.08	9.61	5.68	2.97	54.08	28.75
42	4.36	2.38	56.53	32.68	4.18	2.20	57.58	30.88
43	5.48	2.99	34.37	18.85	3.79	1.98	48.28	25.63
44	5.93	3.23	62.89	34.62	10.15	5.26	67.15	36.21
45	3.96	2.16	60.31	33.08	0.99	0.53	10.40	5.65
46	6.77	3.74	25.71	14.69	4.31	2.25	67.39	35.99
47	7.09	3.88	68.25	39.02	9.17	4.76	87.49	45.87
48	1.76	0.95	24.55	13.33	1.27	0.67	4.79	2.50
49	5.95	3.25	69.17	39.08	1.80	0.94	33.67	18.20
50	3.53	1.88	7.69	4.13	4.40	2.34	48.30	26.05
51	5.58	3.07	52.14	29.61	8.34	4.30	98.67	51.41
52	0.50	0.27	7.09	3.82	0.16	0.09	0.62	0.32
53	7.26	4.00	92.17	53.20	6.46	3.33	92.24	48.54
54	5.98	3.27	88.92	50.41	2.17	1.13	13.68	7.37
55	1.46	0.81	21.07	12.09	7.47	3.85	69.06	37.20
56	6.39	3.51	69.43	39.69	13.98	7.07	62.08	33.32
57	3.40	1.86	66.78	38.24	7.01	3.60	93.31	48.90
58	5.59	3.05	68.14	37.64	5.57	2.84	49.38	26.56
59	6.71	3.70	74.25	42.52	5.86	2.99	56.52	30.78
60	16.88	9.48	43.37	25.33	9.55	4.95	34.85	18.88
61	7.80	4.29	19.60	10.83	6.62	3.40	62.22	33.29
62	8.04	4.39	59.55	32.84	6.59	3.44	87.77	46.27
63	5.80	3.19	101.22	57.75	7.05	3.67	91.18	48.13
64	6.32	3.47	89.65	51.16	7.35	3.80	79.92	42.67
65	3.89	2.12	40.17	21.96	8.31	4.34	13.60	7.35
66	6.71	3.70	75.55	43.05	8.69	4.55	65.51	35.38
67	7.62	4.18	86.00	48.83	13.47	7.09	37.67	20.53
68	7.92	4.29	16.41	8.91	10.80	5.56	24.76	12.76
69	7.32	4.02	82.27	46.72	2.04	1.08	3.75	2.00
70	3.52	1.90	19.98	10.81	8.38	4.40	76.56	40.78
71	4.85	2.65	68.25	37.97	10.42	5.36	83.75	44.21
72	5.32	2.92	86.88	48.91	9.58	4.96	83.58	44.33
73	6.85	3.76	79.28	44.79	9.46	4.92	82.69	43.90
74	3.23	1.77	81.80	46.56	12.28	6.34	92.45	48.78
75	6.53	3.58	93.81	53.18	5.77	3.03	53.81	28.93
76	3.82	2.09	52.74	29.89	13.36	7.04	62.47	33.50
77	4.48	2.46	60.46	34.35	11.36	5.88	89.48	47.34
78	5.43	3.00	83.58	47.54	8.43	4.36	66.76	35.79
79	4.33	2.39	61.88	35.20	10.92	5.61	68.26	36.47
80	7.62	4.19	72.34	39.75	8.16	4.25	78.49	41.68
81	7.54	4.14	77.75	44.15	6.98	3.72	26.25	14.44
82	8.00	4.41	25.53	14.41	9.37	4.91	73.60	39.50
83	6.45	3.55	72.69	41.35	11.31	5.92	79.41	42.13
84	4.61	2.53	78.07	44.48	5.93	3.07	92.95	48.83
85	2.13	1.17	85.00	48.51	3.81	1.96	81.23	43.02
86	0.18	0.10	2.47	1.31	1.19	0.62	2.33	1.22
87	4.65	2.56	86.11	48.90	1.22	0.65	3.57	1.94
$\oslash$	**5.12**	**2.80**	**56.13**	**31.83**	**7.39**	**3.84**	**53.53**	**28.39**